

**LA-7195-PR**  
Progress Report

NRC-4, NRC-7, NRC-8

**Nuclear Reactor Safety**  
**Quarterly Progress Report**  
**October 1—December 31, 1977**

120555003954 1 R4R7R8AN  
US NRC  
ADM LIBRARY BRANCH  
BRANCH CHIEF  
160  
WASHINGTON DC 20555

Issued: April 1978

  
**los alamos**  
**scientific laboratory**  
of the University of California  
LOS ALAMOS, NEW MEXICO 87545

An Affirmative Action/Equal Opportunity Employer

UNITED STATES  
DEPARTMENT OF ENERGY  
CONTRACT W-7409-ENG. 38

Previous reports in this series, unclassified, are LAPR-NUREG-6233, LAPR-NUREG-6317, LA-NUREG-6447-PR, LA-NUREG-6579-PR, LA-NUREG-6698-PR, LA-NUREG-6842-PR, LA-NUREG-6934-PR, and LA-7039-PR.

This work was supported by the US Nuclear Regulatory Commission's Office of Nuclear Regulatory Research, Division of Reactor Safety Research, Office of Nuclear Reactor Regulation, Division of Systems Safety, and the US Department of Energy, Division of Reactor Development and Demonstration.

Printed in the United States of America. Available from  
 National Technical Information Service  
 U.S. Department of Commerce  
 5285 Port Royal Road  
 Springfield, VA 22161

Microfilm \$ 3.00

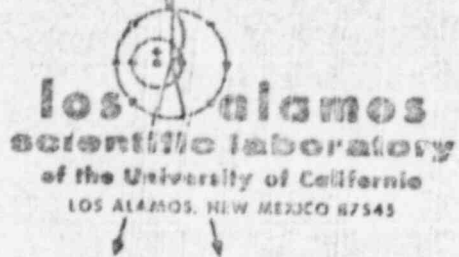
001-025	4.00	126-150	7.25	251-275	10.75	376-400	13.00	501-525	15.25
026-050	4.50	151-175	8.00	276-300	11.50	401-425	13.25	526-550	15.50
051-075	5.25	176-200	9.00	301-325	11.75	426-450	14.00	551-575	16.25
076-100	6.00	201-225	9.25	326-350	12.00	451-475	14.50	576-600	16.50
101-125	6.50	226-250	9.50	351-375	12.50	476-500	15.00	601 up	--1

1. Add \$2.50 for each additional 100-page increment from 601 pages up.

#### NOTICE

This report was prepared as an account of work sponsored by the United States Government. Neither the United States nor the United States Nuclear Regulatory Commission, nor any of their employees, nor any of their contractors, subcontractors, or their employees, makes any warranty, express or implied, or assumes any legal liability or responsibility for the accuracy, completeness or usefulness of any information, apparatus, product or process disclosed, or represents that its use would not infringe privately owned rights.

LA-7105-PII  
Progress Report  
NRC-4, NRC-7, NRC-8



**Nuclear Reactor Safety**  
**Quarterly Progress Report**  
**October 1—December 31, 1977**

Compiled by

James F. Jackson  
Michael G. Stevenson

Manuscript completed: February 1978  
Issued: April 1978

Prepared for the US Nuclear Regulatory Commission  
Office of Nuclear Regulatory Research

## CONTENTS

	ABSTRACT -----	xvi
I.	INTRODUCTION ----- (J. P. Jackson and M. G. Stevenson, Q-DO)	1
II.	LWR SAFETY RESEARCH ----- (J. F. Jackson, Q-EO)	2
	A. TRAC Code Development and Verification ----- (J. C. Vigil and R. J. Pryor, Q-6)	2
	1. TAC Code Development ----- (R. J. Pryor, Q-6)	3
	a. Steady-State Capabilities ----- (J. M. Sicilian, Q-6)	4
	b. FILL Module Improvements ----- (R. J. Pryor, Q-6)	4
	c. Coding Standardizations ----- (R. J. Harper, Q-6)	4
	d. TRAC Overlay Structure ----- (R. J. Pryor, Q-6)	5
	e. Production of Movies for TRAC ----- (J. C. Ferguson, Q-6)	5
	2. Fluid Mechanics Methods ----- (D. R. Liles and J. H. Mahaffy, Q-6)	7
	a. Differential Equations -----	9
	b. Finite Difference Equations -----	10
	c. Constitutive Equations -----	17
	3. Heat Transfer Methods ----- (W. L. Kirchner, Q-6)	22
	a. Radiation Heat Transfer to Liquid -----	23
	b. Reflood Heat Transfer -----	23
	4. TRAC Developmental Verification ----- (K. A. Williams, Q-6)	24
	a. TRAC Analysis of Downcomer Effects in the Creare 1/15-Scale Vessel ----- (K. A. Williams, Q-6)	26
	b. Analysis of PSR Standard Problem No. 5 ----- (J. W. Bolstad, Q-6)	27
	c. Analysis of LOFT Nonnuclear Test 11-4 (RSR Stan- dard Problem No. 7) ----- (J. J. Pyun, Q-6)	31

CONTENTS (cont)

5.	Statistical Sensitivity Analysis - - - - -	34
	(M. D. McKay, Q-12)	
B.	TRAC Applications - - - - -	35
	(J. C. Vigil and P. B. Eleiweis, Q-6)	
1.	PKL Demonstration Problem - - - - -	36
	(P. B. Eleiweis, Q-6)	
2.	U.S. PWR TRAC Model and Steady-State Calculation - - -	46
	(P. B. Eleiweis and J. R. Ireland, Q-6)	
3.	Preliminary Noding of the INEL Air-Water Injection Tests - - - - -	57
	(D. Dobranich, Q-6)	
4.	TRAC Noding for the Japanese Reflood Experiment - - -	59
	(D. Dobranich and P. B. Eleiweis, Q-6)	
5.	Analysis Support for Japanese Slab Core Tests - - - -	59
	(F. H. Harlow and A. A. Amsden, T-3; and P. B. Eleiweis, Q-6)	
C.	Thermal-Hydraulic Research for Reactor Safety Analysis - -	63
	(T. D. Butler, T-3)	
1.	The Effect of the Throat Length to Throat Diameter Ratio in Critical Nozzle Flows - - - - -	63
	(J. R. Travis, C. W. Hirt, and W. C. Rivard, T-3)	
2.	Slab Vessel Reflood Calculations - - - - -	66
	(P. H. Harlow and A. A. Amsden, T-3)	
3.	Numerical Study of Downcomer Steam-Water Flows - - - -	69
	(A. A. Amsden, B. J. Daly, and F. H. Harlow, T-3)	
4.	HDR Core Barrel Dynamics - - - - -	72
	(J. K. Dienes, W. C. Rivard, L. R. Stein, and M. D. Torrey, T-3)	
D.	LMR Safety Experiments - - - - -	80
	(H. H. Helmick, Q-8)	
1.	Storz Lens -- Video System - - - - -	80
	(C. R. Mansfield, J. Spalding, and P. F. Bird, Q-8)	
	a. Storz Lens Development - - - - -	81
	b. Data Reduction Techniques - - - - -	81
2.	Upper Plenum De-entrainment Experiment - - - - -	82
	(P. F. Bird, Q-8 and W. L. Kirchner, Q-6)	
3.	Hot-Fil Anemometer - - - - -	82
	(P. F. bird, Q-8)	
4.	Unwrapped Downcomer Experiment - - - - -	83
	(V. S. Starkovich, Q-8)	

CONTENTS (cont)

III.	LWFR SAFETY RESEARCH - - - - -	84
	(M. G. Stevenson, Q-DO and J. E. Boudreau, Q-7)	
A.	SIMMER Code Development and Applications - - - - -	84
	(L. L. Smith, Q-7)	
	1. SIMMER-II Phase Transition Methods - - - - -	85
	(W. R. Bohl, Q-7)	
	2. SIMMER-II Postdisassembly Expansion Analysis - - - - -	88
	(W. R. Bohl, Q-7)	
	3. Application of Probabilistic Methods to Work-Energy Partition Calculations with SIMMER-II - - - - -	91
	(R. D. Burns, III and L. B. Luck, Q-7)	
B.	Modeling of Phenomena and Studies on the Limits and Control of CDA Energetics - - - - -	95
	(C. R. Bell, Q-7)	
	1. Evaluation of Nonuniform Expansion Phenomenon in the Postdisassembly Core Expansion - - - - -	97
	(C. R. Bell, P. J. Blewett, and G. P. DeVault, Q-7)	
	2. Analysis of Multicomponent Condensation Experiments - -	105
	(A. J. Suo-Anttila, Q-7)	
C.	SIMMER Model Development and Verification Experiments - - -	108
	(J. H. Scott, Q-7 and H. H. Helmick, Q-8)	
	1. Interfacial Area and Drag Experiment - - - - -	108
	(P. E. Rexroth, Q-7 and V. S. Starkovich, Q-8)	
	2. Statistical Analysis of the Interfield Area and Drag Experiment - - - - -	110
	(R. D. Burns, III and P. E. Rexroth, Q-7)	
	3. Multicomponent Condensation Experiment - - - - -	114
	(W. M. Hughes, Q-8 and A. J. Suo-Anttila, Q-7)	
	4. Flow Coastdown Simulation Experiments - - - - -	115
	(H. M. Forehand, Q-7 and J. P. Davis, Q-8)	
D.	Safety Test Facilities Study - - - - -	118
	(M. G. Stevenson, Q-DO)	
	1. Hodoscope Diagnostic System Evaluations - - - - -	118
	(A. E. Evans, Q-14)	
	2. Flash X-Ray Monitoring of Reactor Fuel Motion - - - - -	136
	(W. E. Stein, P-DOR)	
IV.	HTR SAFETY RESEARCH - - - - -	141
	(M. G. Stevenson and J. F. Jackson, Q-DO)	
A.	Fission Product Release and Transport - - - - -	141
	(C. E. Apperson, Jr., Q-13)	

CONTENTS (cont)

1.	Fission Product Release Experiments - - - - -	141
	(R. G. Behrens and M. A. David, CMB-2)	
2.	Fuel Failure and Fission Gas Release Experiments - - -	144
	(J. L. Lansford, CMB-8)	
3.	Fission Product Transport Calculations - - - - -	146
	(J. L. Lansford, CMB-8)	
a.	Fission Product Kinetics - - - - -	146
b.	Gaseous Fission Product Release - - - - -	147
	(C. E. Apperson, Jr., Q-13)	
B.	Structural Evaluation - - - - -	147
	(C. A. Anderson, Q-13)	
1.	Seismic Program - - - - -	148
	(R. C. Dove and J. G. Bennett, Q-13)	
2.	Code Development for Analysis of PCRVs - - - - -	153
	(P. D. Smith, W. A. Cook, and C. A. Anderson, Q-13)	
a.	Status of NONSAP-C, INGEN, and MOVIE.LASL - - - - -	153
b.	Concrete Constitutive Relations - - - - -	154
3.	Reliability Assessment of a Prestressed Concrete Reactor Vessel - - - - -	157
	(C. A. Anderson and P. D. Smith, Q-13)	
C.	Phenomena Modeling, Systems Analysis, and Accident Delineation - - - - -	161
	(P. A. Secker, Q-6)	
1.	Relative Hazard Indexing - - - - -	163
	(P. G. Bailey, Q-6 and B. W. Washburn, Q-13)	
2.	LASAN Numerical Integration Technique - - - - -	163
	(R. B. Lazarus, C-3 and P. A. Secker, Q-6)	
3.	LASAN Frequency Response Capability - - - - -	171
	(P. A. Secker, Q-6 and M. L. Stein, C-3)	
4.	Fort St. Vrain Modeling - - - - -	177
	(P. A. Secker and G. J. E. Willcutt, Jr., Q-6; and T. J. Merson, WX-4)	
a.	Steam Generator/Reheater Modeling - - - - -	177
b.	Modifications to Core and Reflector Models - - - - -	178
c.	Improved Lower Plenum Module - - - - -	179
d.	Plenum Dynamics - - - - -	179
e.	Modifications to Kinetics Module - - - - -	179

CONTENTS (cont)

V.	GCPR CORE DISRUPTIVE TEST PROGRAM - - - - -	180
	(D. L. Hanson, Q-8)	
A.	Program Planning - - - - -	180
	(D. L. Hanson, Q-8)	
B.	Analysis - - - - -	182
	(A. J. Giger, Q-13; D. L. Hanson, Q-8; and J. C. Miller, E-2)	
	1. Heater Rod Grinder - - - - -	181
	2. Guarded Core Module (GCM) - - - - -	181
C.	Design - - - - -	184
	(A. J. Giger, Q-13 and B. C. Cone, SD-2)	
	1. Full-length Subgroup (FLS) - - - - -	184
	2. Guarded Core Module (GCM) - - - - -	184
D.	Procurement and Fabrication - - - - -	185
	(A. J. Giger, Q-13 and B. Cone, SD-2)	
	FLS - - - - -	185
E.	Assembly, Installation, and Checkout - - - - -	187
	(A. J. Giger, Q-13; D. L. Hanson, Q-8, W. G. Hansen, E-4; and J. C. Miller, E-2)	
	1. Heater Rod Grinder - - - - -	187
	2. FLS - - - - -	188
F.	Testing - - - - -	190
VI.	CONTAINMENT SYSTEMS EVALUATION AND STUDIES - - - - -	191
	(R. G. Gido, Q-6)	
A.	COMPARE-Mod 2 - - - - -	191
	1. Method of Characteristics - - - - -	191
	(R. G. Gido, Q-6)	
	2. User-Convenience Development - - - - -	192
	(G. J. E. Willcutt, Jr., Q-6)	
	3. Tree Representation Capability - - - - -	193
	(R. W. Meier, WX-4)	
B.	Hydrogen Concentrations in Containment Compartments - - - - -	195
	(G. J. E. Willcutt, Jr., Q-6 and A. Koestel, LASL Consultant)	
C.	Containment Subcompartment Analysis - - - - -	196
	1. Standard Modeling Procedures - - - - -	196
	(J. S. Gilbert, Q-6)	

CONTENTS (cont)

2.	Calculation of the Comparative Analysis Standard Problem (CASP) - - - - -	197
	(W. S. Gregory, WX-8)	
D.	Main Steam Line Break Inside Containment - - - - -	198
	(D. E. Larkin, Q-6 and A. Koestel, IASL Consultant)	
1.	Introduction - - - - -	198
2.	Prediction of Containment Atmosphere Temperature Response - - - - -	199
a.	Heat Transfer Coefficient for Energy Absorption by Heat Sinks - - - - -	199
b.	Condensate Revaporization - - - - -	200
c.	Liquid Entrainment in the Break Effluent - - - - -	201
3.	Prediction of Equipment Thermal Response - - - - -	201
a.	Temperature Variation Within Containment Atmosphere - - - - -	201
b.	Heat Transfer Coefficient for Equipment - - - - -	201
	REFERENCES - - - - -	203

FIGURES

Fig. 1.	TRAC overlay structure. - - - - -	5
Fig. 2.	Three-dimensional mesh-cell velocities. - - - - -	12
Fig. 3.	Flow regime map for three-dimensional hydrodynamics. - - - - -	19
Fig. 4.	Calculated and experimental mass flow rate (cold-leg side of break) for Semiscale Test S-02-8. - - - - -	28
Fig. 5.	Calculated and experimental mass flow rate (hot-leg side of break) for Semiscale Test S-02-8. - - - - -	28
Fig. 6.	Calculated and experimental lower plenum pressure for Semiscale Test S-02-8. - - - - -	29
Fig. 7.	Calculated and experimental lower plenum fluid temperature for Semiscale Test S-02-8. - - - - -	29
Fig. 8.	Calculated and experimental pump differential pressure for Semiscale Test S-02-8. - - - - -	30
Fig. 9.	Calculated and experimental pump inlet mass flow rate for Semiscale Test S-02-8. - - - - -	30

FIGURES (cont)

Fig. 10.	Calculated and experimental steam generator outlet density for Semiscale Test S-02-8. - - - - -	32
Fig. 11.	Calculated and experimental pressure at the steam generator outlet for Semiscale Test S-02-8. - - - - -	32
Fig. 12.	TRAC noding diagram for RSR Standard Problem No. 7. - - - - -	33
Fig. 13.	TRAC model schematic for PKL system. - - - - -	37
Fig. 14.	TRAC noding for PKL vessel (side view). - - - - -	38
Fig. 15.	TRAC noding for PKL vessel (top view). - - - - -	39
Fig. 16.	PKL initial fuel rod temperatures. - - - - -	40
Fig. 17.	PKL vapor volume fractions and quench front positions at $t = 1.5$ s. - - - - -	42
Fig. 18.	PKL vapor volume fractions and quench front positions at $t = 5$ s. - - - - -	43
Fig. 19.	PKL vapor volume fractions and quench front positions at $t = 10$ s. - - - - -	44
Fig. 20.	PKL vapor volume fractions and quench front positions at $t = 25$ s. - - - - -	45
Fig. 21.	TRAC schematic of a typical PWR. - - - - -	47
Fig. 22.	TRAC noding for unbroken cold legs. - - - - -	48
Fig. 23.	TRAC noding for pressurizer hot leg. - - - - -	49
Fig. 24.	TRAC noding for broken cold leg. - - - - -	51
Fig. 25.	TRAC noding for pressure vessel. - - - - -	52
Fig. 26.	Cold-leg mixture velocities at vessel entrance. - - - - -	53
Fig. 27.	Hot-leg and pressurizer velocities. - - - - -	54
Fig. 28.	Cold- and hot-leg pressures at vessel. - - - - -	54
Fig. 29.	Pressure in vessel. - - - - -	55
Fig. 30.	Steady-state cold- and hot-leg temperatures. - - - - -	55
Fig. 31.	Liquid temperature in vessel. - - - - -	56
Fig. 32.	Preliminary TRAC noding for INEL air-water injection tests. - - - - -	59
Fig. 33.	TRAC model for Japanese reflood experiment. - - - - -	60
Fig. 34.	TRAC noding for Japanese vessel. - - - - -	62
Fig. 35.	Effect of throat-length-to-diameter ratio on the calculated flow multiplier. - - - - -	65
Fig. 36.	Volume-fraction-weighted velocity vectors of the water and steam flow, contours of volume fraction, and contours of water temperature and structure temperature. - - - - -	68

FIGURES (cont)

Fig. 37. K-TIP computation region for unwrapped downcomer studies. The top and bottom boundaries are rigid, free-slip walls. The left and right boundaries are periodic. ECC water is injected into the system through the intact cold legs (A cells), while steam enters through the entire lower plenum region. Both steam and water exit through the broken leg (B cell), but only steam enters the system through this port. The hot-leg obstacles (X) are included only in the fine-resolution calculations. - - - - - 70

Fig. 38. Comparison of calculated (solid lines) and experimental (short-dashed lines) water delivery curves for 60-gpm water injection rate and four different steam ramp rates (long-dashed lines). The heavy solid line in the Creare H-1 comparison shows calculated results obtained with a fine-scale mesh. - - - - - 71

Fig. 39. Comparison of calculated and experimental water delivery curves for three different ECC injection rates and approximately the same steam ramp rate. The curves are as indicated in Fig. 38. - - - - - 73

Fig. 40. Comparison of calculated and experimental water delivery curves for 60-gpm ECC injection rate, two different steam ramp rates and superheated (350°F) vessel walls. The light solid line in the Creare H157 experiment shows the effect of including a critical heat flux transition in the wall heat transfer model. Otherwise, the curves are as indicated in Fig. 38. - - - - - 74

Fig. 41. Core barrel radial deflection profiles at the circumferential (a-d) location of the broken pipe at 10, 20, 30, and 40 ms after pipe rupture. - - - - - 75

Fig. 42. Sectional view of the cylindrical HDR single-loop vessel (dimensions in meters). - - - - - 79

Fig. 43. Sodium vapor mass -- maximum, minimum, and average for 10 SIMMER-II calculations. - - - - - 95

Fig. 44. Impulse on vessel head -- maximum, minimum, and average for 10 SIMMER-II calculations. - - - - - 96

Fig. 45. Geometric model and initial conditions for the standard case SIMMER-I calculation. - - - - - 98

Fig. 46. Geometric model and initial conditions for the standard case WONDY calculation. - - - - - 99

Fig. 47. Dependence of pressure on density of the fuel-steel mixture for WONDY calculations. - - - - - 101

Fig. 48. Slug displacement as a function of time for an ideal gas,  $\alpha = 1.06$ . - - - - - 103

FIGURES (cont)

Fig. 49.	Kinetic energy of the system at slug impact as a function of slug mass. - - - - -	104
Fig. 50.	Temperature rise of a 0.025 m diam copper sphere in a 408 K steam environment with variable amounts of air present under natural convection conditions. - - - - -	107
Fig. 51.	Variation in the predictions with respect to thermophysical property evaluation. - - - - -	107
Fig. 52.	Fluidized bed rise height -- maximum, minimum, and average of 12 SIMMER-I calculations. - - - - -	111
Fig. 53.	Fluidized bed rise/collapse cycle time -- maximum, minimum, and average of 12 SIMMER-I calculations. - - - - -	112
Fig. 54.	Schematic of multicomponent condensation experiment apparatus. - - - - -	116
Fig. 55.	Flow coastdown simulation experiment. - - - - -	117
Fig. 56.	Photograph of the PARKA facility showing increased shielding. -	121
Fig. 57.	Plan view of the PARKA facility as used for hodoscope evaluation. - - - - -	122
Fig. 58.	Neutron hodoscope scans of a single simulated FFTF pin in PARKA. The asymmetry in the background radiation is believed to be caused by scattering from temporary shielding between the hodoscope and the reactor. - - - - -	123
Fig. 59.	Results of gamma-ray scan of a single simulated FFTF pin in PARKA. - - - - -	125
Fig. 60.	Results of neutron and gamma scans of a 37-pin assembly intact and with the center pin missing. Direction of scan was across flats of the hexagon. These data, which were taken during a 3-h run that commenced immediately after reaching operating reactor power, are uncorrected for buildup of fission and activation products. - - - - -	126
Fig. 61.	Sensitivity of the hodoscope to removal of fuel as a function of position of the void in the test bundle. The center (20 mm) points have been corrected for a known 15% power-distribution depression in the center of the test bundle. Indicated errors are from counting statistics only. - -	129
Fig. 62.	Results of linearity test for neutrons. Errors are statistical only. - - - - -	130
Fig. 63.	Results of linearity test for gamma rays. - - - - -	131
Fig. 64.	Results of single-pin and background gamma scans with a NaI (Tl) detector, with various energy discriminator settings. - - - - -	132
Fig. 65.	Results of single-pin and background gamma scans with an NE102 plastic scintillator. - - - - -	133

FIGURES (cont)

Fig. 66.	Results of 37- and 36-pin gamma scans with a NaI(Tl) detector. - - - - -	134
Fig. 67.	Results of 37- and 36-pin gamma scans with a NE102 plastic scintillator. - - - - -	135
Fig. 68.	Density of film radiograph and calculated x-ray transmission for a 37-pin array viewed perpendicularly to the hexagonal flats and surrounded by a steel cylinder with 25.4 mm radial thickness. The densitometer data and transmission calculations are for a trace taken perpendicularly to the array axis and through the void in the central pin. The intensity of the x-ray flash was 34 R at 1 m. - - - - -	138
Fig. 69.	Density of film radiograph for a 169-pin array viewed perpendicularly to the hexagonal flats and surrounded by a steel cylinder with 38 mm radial thickness. The densitometer data were taken perpendicularly to the array axis and through the void in the central pin. The intensity of the x-ray flash was 80 R at 1 m. - - - - -	139
Fig. 70.	Density of film radiograph and measured video signal for a 37-pin array viewed perpendicularly to the hexagonal flats and surrounded by a steel cylinder with 25.4 mm radial thickness. The densitometer data and the video signal are for a track taken perpendicularly to the array axis and through the void in the central pin. The intensity of the x-ray flash was 34 R at 1 m. - - - - -	140
Fig. 71.	Time dependence of desorption flux from cesium-doped H-451 graphite at constant temperatures between 765-996 K for Experiment 6. - - - - -	143
Fig. 72.	Time dependence of desorption flux from cesium-doped H-451 graphite at constant temperatures between 1180-1267 K for Experiment 3. - - - - -	145
Fig. 73.	Effect of clearance gap on the four-block prototype system response. - - - - -	149
Fig. 74.	Effect of excitation frequency on the four-block prototype system response. - - - - -	149
Fig. 75.	Effect of the initial configuration -- gap at right end. - - - -	150
Fig. 76.	Effect of the initial configuration -- gap between blocks 3 and 4. - - - - -	151
Fig. 77.	Flow chart illustrating the coupling between the PCRV analysis codes INGEN, NONSAP-C, and MOVIE.LASL. - - - - -	155
Fig. 78.	Experimental and computed head load-deflection behavior of PV-27. - - - - -	156
Fig. 79.	Failure and initial discontinuity surfaces in principal stress space. - - - - -	156

FIGURES (cont)

Fig. 80.	Histogram for concrete compressive strengths. - - - - -	157
Fig. 81.	Prestressed concrete cylinder model. - - - - -	159
Fig. 82.	Prestressed concrete cylinder at failure. - - - - -	160
Fig. 83.	Normal probability plot for failure pressure of the pre-stressed concrete cylinder. - - - - -	161
Fig. 84.	IOIF solutions for a tenth-order linear system. - - - - -	169
Fig. 85.	Prompt power for a one dollar reactivity insertion using IOIF. - - - - -	170
Fig. 86.	Rapid depressurization accident. - - - - -	172
Fig. 87.	Power-to-flow-ratio for a rapid PCRV depressurization. - - - -	173
Fig. 88.	Closed loop frequency response of prompt power vs power demand. - - - - -	176
Fig. 89.	Open loop frequency response prompt power vs rod reactivity. -	177
Fig. 90.	Control rod rate logic diagram. - - - - -	178
Fig. 91.	Core heater rod profile. - - - - -	182
Fig. 92.	GCM conceptual schematic. - - - - -	193
Fig. 93.	Heat loss from DMFT insulation. - - - - -	184
Fig. 94.	FLS lower electrical assembly adjacent to the tube bundle. - -	185
Fig. 95.	FLS parts above the tube bundle. - - - - -	186
Fig. 96.	FLS pressure vessel, tube bundle assembly, and duct. - - - -	186
Fig. 97.	Fully assembled Heater Rod Grinder. - - - - -	187
Fig. 98.	Cladding surface temperature thermocouple installation. - - - -	188
Fig. 99.	Assembled cladding tube bundle. - - - - -	189
Fig. 100.	Blanking segments installation at Spacer Grid No. 9. - - - -	189
Fig. 101.	Volume and junction geometry and initial conditions used in tee flow calculation. - - - - -	194
Fig. 102.	Static pressure drop through a tee (points with symbols are calculated values). - - - - -	195
Fig. 103.	Total pressure loss coefficients through a tee (dots are calculated values). - - - - -	195

TABLES

I.	TRAC Overlays - - - - -	6
II.	Nomenclature for 3-D Two-Fluid Equations - - - - -	7

TABLES (cont)

III.	Comparison of Initial Conditions for LOFT Nonnuclear Test LI-4 - - - - -	35
IV.	Component Identification for Japanese Reflood Experiment - - -	61
V.	Input Uncertainty for the Interfield Area and Drag Experiment -	113
VI.	Summary of Events for Case 1 - - - - -	119
VII.	Summary of Events for Case 2 - - - - -	119
VIII.	Summary of On-center Hodoscope Counting Rates for 37-, 36-, 1-, and 0-Pin Scans, with and without 200 mm Lucite Plugs in Collimator - - - - -	127
IX.	Summary of Experimental Conditions for Desorption Measurements on H-451 Graphite - - - - -	142
X.	Maximum Strain Produced in Four-Block Systems During Simulated Earthquake Tests - - - - -	152
XI.	Input and Output Data for the Prestressed Concrete Cylinder - -	162
XII.	Nuclides Included in Hazard Decay Chains - - - - -	164

## ABSTRACT

The initial release version of the TRAC code (TRAC-P1) was transmitted to NRC with draft documentation. This version is designed to analyze LOCAs in PWRs, but is sufficiently versatile to also treat a broad range of experiments. A number of improvements were made to TRAC including an upgraded steady-state capability, time- and pressure-dependent fill boundary conditions to better simulate ECC injection systems, improved core heat transfer features, and a better movie production program. In the TRAC developmental verification area, the CREARE refill experimental comparisons were extended to cases having high ECC subcooling, improved agreement between calculation and experiment was obtained for a heated core Semiscale blowdown test, and steady-state calculations were completed for a LOFT nonnuclear blowdown experiment. In the TRAC applications area, earlier PKL calculations were extended to include subcooled hot-leg injection, reflood heat transfer, and quench front motion; a steady-state calculation was performed for a typical four-loop U.S. PWR; modeling of the four-loop cylindrical core Japanese reflood facility was completed; and preliminary calculations were performed for the INEL air-water injection tests. The thermal-hydraulic research effort focused on determining the appropriate critical flow multipliers for different nozzle or break geometries, the development of a two-dimensional (slab geometry) computer code to analyze the proposed Japanese reflood experiments, the analysis of a broad range of ramped steam flow CRFARE downcomer experiments with the K-TIF code, and the comparison of 2-D and 3-D techniques for treating fluid-structure interaction problems. In the LWR safety experiments and instrumentation area, progress was made on developing a Storz lens video system and coupled data reduction capability to examine two-phase flow conditions.

In the LMFB area, the analysis of postdisassembly expansion previously performed with SIMMER-I was repeated with SIMMER-II. A comparable calculation with nominal parameters predicted the system kinetic energy was about a factor of 10 lower than that calculated with SIMMER-I. A one-dimensional, two-phase expansion dynamics study was performed with SIMMER-I and results compared to similar calculations with the WORDY Lagrangian hydrodynamics code. The ability of SIMMER-I to predict the hydrodynamics of a nonuniform expansion process was confirmed by this study. Initial results from multicomponent condensation experiments are in good agreement with predictions by the new model recently implemented in SIMMER-II. In other work in the SIMMER verification experiment activity, diagnostics development for and statistical analysis of the inter-field drag (air-particle) experiments were completed. Also, initial flow coastdown simulation experiments were performed. In fuel motion diagnostic systems evaluation work in the LMFB safety test facilities project, initial analyses were completed of densitometer traces of film radiographs taken of 37 and 169 fuel pin arrays at the PHEMEX flash x-ray facility. The analyses indicate that the information contained in the transmitted x-rays is sufficient to provide about 1 mm spatial resolution

and a mass density sensitivity of about  $1 \text{ g/cm}^2$  and about  $2 \text{ g/cm}^2$  for the 37- and 169-pin arrays, respectively. This is about 6% sensitivity in each case.

In the fission product task area of the HTGR safety research program, the cesium desorption kinetics studies reported last quarter were repeated and the initial results were verified. Analytical work concentrated on optimizing the direct search algorithm in QUIL/QUIC, modifying the evaluation of burst release in SUVIUS, and preparing a preprocessor for SUVIUS. Data reduction for the seismic model tests in the structural evaluation task was completed. A new elastic-plastic constitutive model for concrete was developed for implementation in NONSAP-C. A probabilistic reliability assessment of a single-cavity PCRV was performed. In work with the CHAP series of HTGR system transient analysis codes, an improved lower plenum module was developed for the Ft. St. Vrain version (CHAP-2), reverse helium flow heat transfer was added to all primary loop modules, a general one-dimensional tube and shell heat exchanger subroutine was developed for FSV emergency cooling problems, and a module for calculating fuel particle failure and nuclide release during accident transients was developed. Rapid depressurization accidents using the FSV model were also studied during this period.

Progress continued in planning and developing the hardware for the GCFR subassembly disruption experiments. Delivery was completed on most of the parts required to assemble the 37-rod full-length test fixture and its first test assembly. The heater rod grinder is now fully operational and an initial set of graphite heater rods produced for the first 37-rod test assembly. A test plan for the first 37-rod test was outlined.

In the reactor containment evaluation program, progress was made in the areas of improving the COMPARE code, providing a better analysis of hydrogen concentration distributions within containment structures, establishing standard modeling procedures for subcompartment analyses, and predicting the consequence of a main steam line break within a containment structure.

## NUCLEAR REACTOR SAFETY

Compiled by

James F. Jackson  
and  
Michael G. Stevenson

### I. INTRODUCTION

(J. F. Jackson and M. G. Stevenson, Q-D0)

The Los Alamos Scientific Laboratory (LASL) is conducting a broad-based nuclear reactor safety research program. A key facet of this program concentrates on providing a detailed understanding of the behavior of reactor systems under postulated accident conditions. Both analytical and experimental efforts are included. This report summarizes the technical progress from this work in that area.

The report is mainly organized according to reactor type. Major sections deal with Light Water Reactors (LWRs), Liquid Metal Fast Breeder Reactors (LMFBRs), High-Temperature Gas-Cooled Reactors (HTGRs), and Gas-Cooled Fast Reactors (GCFRs). The last section of the report discusses work in the area of LWR reactor containment evaluation.

The research discussed in this report was performed by a number of divisions and groups at LASL. The names and group affiliations of the individual staff members responsible for the work are given at the beginning of each section. Most of the work was performed in the Energy (Q) Division. Other divisions contributing to the program were the Theoretical (T) Division, The Chemistry-Materials Science (CMB) Division, the Design Engineering (WX) Division, and the Dynamic Testing (M) Division.

The bulk of this research was funded by the U.S. Nuclear Regulatory Commission (NRC), with certain projects being funded by the U.S. Department of Energy (DOE).

## II. LWR SAFETY RESEARCH

(J. F. Jackson, Q-DO)

Progress from three projects in LASL's LWR safety research program is reported in this section. These related projects are supported by the Division of Reactor Safety Research of the NRC (RSR/NRC). The first project focuses on the development, verification, and application of the Transient Reactor Analysis Code (TRAC). The second concentrates on thermal-hydraulic research related to LWR safety problems and the development of component codes. The third supports the above analytical efforts with model development and verification experiments and also develops advanced instrumentation techniques for use in LWR safety experiments. An additional project that encompasses LWR containment system analysis and evaluation is reported in Sec. VI.

### A. TRAC Code Development and Verification

(J. C. Vigil and R. J. Pryor, Q-6)

The TRAC code is an advanced, best estimate computer program for LWR accident analyses. It provides an improvement over previous system codes both in structure and in the more accurate treatment of key thermal-hydraulic phenomena. The modular structure of TRAC permits the efficient development and maintenance of more detailed models of system components. The treatment of multidimensional, two-phase flow in the vessel more accurately models the important phenomena that occur during accident conditions.

The first release version of TRAC, called TRAC-P1, was transmitted to NRC in December 1977. This version is directed toward loss-of-coolant accidents (LOCAs) in pressurized water reactors (PWRs). Because of its versatility, however, TRAC-P1 can also be applied to a wide variety of analyses ranging from blowdowns in simple pipes to integral LOCA tests in multiloop facilities. Later versions of the code will treat boiling water reactors (BWRs) and will provide capabilities for Anticipated Transient Without Scram (ATWS) and Reactivity Insertion Accident (RIA) analyses.

In conjunction with the TRAC development effort and as a part of a closely coupled verification effort, the code is being applied to a broad range of reduced-scale water-reactor safety experiments. These experiments are designed

to study separate and integral effects that occur during all stages of a LOCA. TRAC predictions are compared with the experimental results to verify the thermal-hydraulic models in the code.

Major accomplishments during the past quarter in the areas of TRAC development and verification include:

1. release of TRAC-P1 with draft documentation to NRC,
2. completion of generalized and PWR steady-state capabilities for TRAC-P1,
3. incorporation of time- and pressure-dependent fill boundary conditions,
4. completion of an improved movie production program,
5. incorporation of several improvements to the core heat transfer package,
6. extension of CREARE refill calculations to cases having high emergency core cooling (ECC) water subcooling,
7. resolution of previous discrepancies between calculated and measured flow rates and pressures for RSR Standard Problem 5 (heated Semiscale blowdown test),
8. completion of steady-state calculations for RSR Standard Problem 7 (LOFT nonnuclear blowdown test), and
9. completion of the first draft of a report that discusses methods for statistical sensitivity analysis.

#### 1. TRAC Code Development

(R. J. Pryor, Q-6)

A major milestone was met during the past quarter with the release of the TRAC-P1 code to NRC along with draft documentation. Documentation transmitted with the code consists of Volume I of the TRAC-P1 User's Manual. This volume contains a complete description of the TRAC models and methods, a user's guide, a programmer's information section, and a sample PWR input deck. Volume II contains the results of the verification problems and is now being prepared. Work continued on completing a public release version of TRAC-P1, which will be sent to the Argonne Code Center as soon as the required developmental verification is completed. Several improvements related to preparing the code for this release are described below.

a. Steady-State Capabilities

(J. M. Sicilian, Q-6)

The TRAC steady-state capabilities have been completed and tested in a preliminary manner. Two options are available to the user: a generalized calculation that applies to any type of system geometry and a FWR initialization calculation. Both calculations use the component iteration subroutines to advance the system condition to its steady state. Both also employ the convergence test algorithms which compare system variable derivatives with corresponding natural time scales.

The FWR initialization calculation adjusts the pump speeds and steam generator fouling factors in each coolant loop to obtain a steady-state condition which matches loop flow rates and vessel inlet temperatures specified by the user. The evaluation of system parameters is performed in an iterative manner. An approximate steady-state condition is evaluated for a particular set of pump speeds and steam generator areas. A simple set of balance equations is then solved for new values of the system parameters, using the flow and thermal conditions obtained previously. These new values are used to evaluate a new steady state. The process continues until the loop flow rates and vessel inlet temperatures obtained match the user-specified values within the convergence criterion.

b. FILL Module Improvements

(R. J. Pryor, Q-6)

The FILL module was modified to allow the user additional flexibility in specifying boundary conditions. A FILL is used to specify a velocity boundary condition at an end of a one-dimensional component, such as a pipe. Before this modification, only a fixed velocity could be specified. The additional options permit specification of velocity vs time or velocity vs pressure with the possibility of trip control. These options can be used to model transient emergency core cooling (ECC) injection by the high- and low-pressure injection systems. Testing of the options was completed successfully.

c. Coding Standardizations

(R. J. Harper, Q-6)

Even though an effort was made during the development of the TRAC code to keep usage of nonstandard FORTRAN at a minimum, a certain number of

system-dependent features were introduced. In order to prepare the code for release, these nonstandard usages have been removed.

d. TRAC Overlay Structure

(R. J. Pryor, Q-6)

A new overlay, PWRSS, containing PWR initialization coding was added to the steady-state segment of the overlay calling tree. The new code overlay structure is summarized in Fig. 1 and Table I. This finalizes the overlay structure of the release version of the code except that overlays STEADY and TRANS will be combined with overlay MAIN. This will be done to reduce the number of overlay levels to three, which is the maximum allowed by the CDC standard loader. Since these two overlays are small, the increase in the load module size will be minimal.

e. Production of Movies for TRAC

(J. C. Ferguson, Q-6)

A new version of the POST program<sup>1</sup> has been written and tested. POST reads the TRAC movie output file and produces 16 mm color movies of the two-phase flow patterns in a three-dimensional reactor vessel. The display uses isometric projection of all geometric objects involved including all vessel boundaries and ports. The flow is visualized by the motion of tracer particles whose velocity, density, and color are functions of the local vapor and liquid properties.

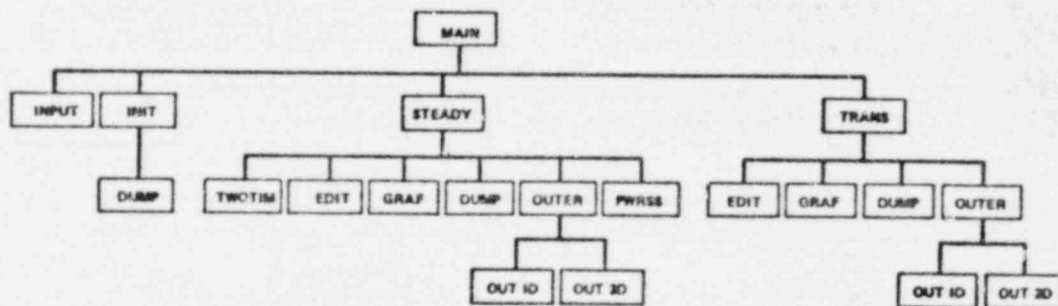


Fig. 1.  
TRAC overlay structure.

TABLE I  
TRAC OVERLAYS

<u>Overlay</u>	<u>Description</u>
MAIN	Controls overall flow of calculation. (The MAIN overlay also contains many service routines used throughout the code.)
INPUT	Reads input and restart files, assigns LCM storage space and saves input data there, and analyzes PWR loops for PWR initialization calculations.
INIT	Initializes component data and graphics tables.
STEADY	Performs a steady-state calculation, using either the generalized or the PWR initialization option.
TRANS	Performs a transient calculation.
OUTER	Performs one complete outer iteration.
OUT1D	Performs all the inner iterations for a single one-dimensional component during one outer iteration.
OUT3D	Performs all the inner iterations for a VESSEL during one outer iteration.
TWOTIM	Evaluates maximum normalized rates of change throughout the system.
PWRSS	Evaluates new parameter values for the PWR initialization option.
DUMP	Adds a dump at the current time to the TRCDMP file.
EDIT	Adds an edit at the current time to the TROUT file.
GRAF	Adds a graphics edit at the current time to the TROGRF file.

Specific features of the new version of POST, which were not handled by the original version, include:

1. Pipe connections can occur at any mesh cell face.
2. The user can select the type of port outline (e.g., the cell face perimeter or an ovular image).

3. Particle flow display can be restricted to certain r- $\theta$ -z intervals within the vessel (all particles having r- $\theta$ -z coordinates outside these intervals are not plotted).
4. Vessel geometry allows both lower and upper plenum definitions.
5. Vessel rotation (for display enhancement), can be time-coordinated with previous POST runs. This is used to merge files from different runs.

Formal checkout of POST is complete, and the program is successfully being applied to the CREATE downcomer calculations described later in this report.

## 2. Fluid Mechanics Methods

(D. R. Liles and J. H. Mahaffy, Q-6)

Most of the past quarter was used to debug and refine the TRAC code before release and to write the appropriate parts of the user's manual. The one-dimensional drift-flux model used for the loop components in TRAC-P1 was discussed in the previous quarterly report.<sup>2</sup> The three-dimensional, two-fluid model used in the vessel module is described below. The nomenclature used in this section is defined in Table II.

TABLE II  
NOMENCLATURE FOR 3-D TWO-FLUID EQUATIONS

### Independent Variables

t	Time.
r	Radial coordinate in cylindrical geometry.
$\theta$	Azimuthal coordinate in cylindrical geometry.
x	Coordinate for one-dimensional geometry.
z	Axial coordinate in cylindrical geometry.

### Other Variables

A	Area.
c	Shear or friction coefficient in two-fluid equations.
D	Diameter.
e	Specific internal energy.
FA	Flow area.

TABLE II (cont)

Other Variables (cont)

$h$	Specific enthalpy or heat transfer coefficient.
$h_{M}$	Latent heat of vaporization.
$Nu$	Nusselt number.
$p$	Pressure.
$q$	Heat generation rate.
$Re$	Reynolds number.
$T$	Temperature.
$V$	Velocity.
$vol$	Hydrodynamic cell volume.
$We$	Weber number.
$\alpha$	Vapor volume fraction or absorptivity.
$\Gamma$	Net volumetric vapor production rate due to phase change.
$\Delta$	Increment.
$\mu$	Viscosity.
$\rho$	Microscopic density.
$\sigma$	Surface tension.

Subscripts

$b$	Bubble.
$d$	Droplet.
$g$	Vapor (gas) field.
$h$	Hydraulic.
$i$	Interface (liquid-vapor) quantity.
$lg$	Liquid field.
$l$	Liquid to vapor.
$m$	Mixture quantities.
$r$	Relative quantities.
$r, \theta, z$	Cylindrical coordinate directions.
$r \pm 1/2$	Mesh cell boundary indices.
$\theta \pm 1/2$	
$z \pm 1/2$	
$s$	Saturation quantities.
$w$	Wall quantities.

### a. Differential Equations

The field equations<sup>3,4</sup> describing the two-phase, two-fluid flow are given below.

#### Mixture Mass Equation

$$\frac{\partial \rho_m}{\partial t} + \nabla \cdot [\alpha \rho_g \mathbf{V}_g + (1-\alpha) \rho_l \mathbf{V}_l] = 0 \quad (1)$$

#### Vapor Mass Equation

$$\frac{\partial (\alpha \rho_g)}{\partial t} + \nabla \cdot (\alpha \rho_g \mathbf{V}_g) = \Gamma \quad (2)$$

#### Vapor Equation of Motion

$$\begin{aligned} \frac{\partial \mathbf{V}_g}{\partial t} + \mathbf{V}_g \cdot \nabla \mathbf{V}_g = & - \frac{c_i}{\alpha \rho_g} \mathbf{V}_r |\mathbf{V}_r| - \frac{1}{\rho_g} \nabla p - \frac{\Gamma}{\alpha \rho_g} (\mathbf{V}_g - \mathbf{V}_{ig}) \\ & - \frac{c_{wg}}{\alpha \rho_g} \mathbf{V}_g |\mathbf{V}_g| \end{aligned} \quad (3)$$

#### Liquid Equation of Motion

$$\begin{aligned} \frac{\partial \mathbf{V}_l}{\partial t} + \mathbf{V}_l \cdot \nabla \mathbf{V}_l = & \frac{c_i}{(1-\alpha) \rho_l} \mathbf{V}_r |\mathbf{V}_r| - \frac{1}{\rho_l} \nabla p + \frac{\Gamma}{(1-\alpha) \rho_l} (\mathbf{V}_l - \mathbf{V}_{il}) \\ & - \frac{c_{wl}}{(1-\alpha) \rho_l} \mathbf{V}_l |\mathbf{V}_l| \end{aligned} \quad (4)$$

#### Mixture Energy Equation

$$\begin{aligned} \frac{\partial [(1-\alpha) \rho_l e_l + \alpha \rho_g e_g]}{\partial t} + \nabla \cdot [(1-\alpha) \rho_l e_l \mathbf{V}_l + \alpha \rho_g e_g \mathbf{V}_g] \\ = - p \nabla \cdot [(1-\alpha) \mathbf{V}_l + \alpha \mathbf{V}_g] + q_{wg} + q_{wl} \end{aligned} \quad (5)$$

### Vapor Energy Equation

$$\frac{\partial(\alpha \rho_g e_g)}{\partial t} + \nabla \cdot (\alpha \rho_g V_g e_g) = -p \frac{\partial \alpha}{\partial t} - p \nabla \cdot (\alpha V_g) + q_{wg} + q_{lg} + \dot{m}_{sg} \quad (6)$$

where

$$\rho_m = \alpha \rho_g + (1 - \alpha) \rho_l \quad (7)$$

and

$$V_r = V_g - V_l \quad (8)$$

### b. Finite Difference Equations

The momentum equations are separated into the three coordinate components. Only the vapor equation will be discussed with the understanding that the liquid momentum equation is treated in an analogous manner. The three components of the vapor-momentum differential equation are:

#### Axial (z) Component

$$\begin{aligned} \frac{\partial v_{gz}}{\partial t} = & - \left( v_{gr} \frac{\partial v_{gz}}{\partial r} + \frac{v_{gz}}{r} \frac{\partial v_{gz}}{\partial \theta} + v_{gz} \frac{\partial v_{gz}}{\partial z} \right) - \frac{1}{\rho_g} \frac{\partial p}{\partial z} \\ & - \frac{c_{iz}}{\alpha \rho_g} (v_{gz} - v_{lz}) |v_{gz} - v_{lz}| - \frac{\Gamma}{\alpha \rho_g} (v_{gz} - v_{igr}) - \frac{c_{wgrz}}{\alpha \rho_g} v_{gz} |v_{gz}| \quad (9) \end{aligned}$$

#### Radial (r) Component

$$\begin{aligned} \frac{\partial v_{gr}}{\partial t} = & - \left( v_{gr} \frac{\partial v_{gr}}{\partial r} + \frac{v_{g\theta}}{r} \frac{\partial v_{gr}}{\partial \theta} - \frac{v_{g\theta}^2}{r} + v_{gz} \frac{\partial v_{gr}}{\partial z} \right) - \frac{1}{\rho_g} \frac{\partial p}{\partial r} \\ & - \frac{c_{ir}}{\alpha \rho_g} (v_{gr} - v_{lr}) |v_{gr} - v_{lr}| - \frac{\Gamma}{\alpha \rho_g} (v_{gr} - v_{igr}) - \frac{c_{wgr}}{\alpha \rho_g} v_{gr} |v_{gr}| \quad (10) \end{aligned}$$

Azimuthal ( $\theta$ ) Component

$$\begin{aligned} \frac{\partial v_{g\theta}}{\partial t} = & - (v_{gr} \frac{\partial v_{g\theta}}{\partial r} + \frac{v_{g\theta}}{r} \frac{\partial v_{g\theta}}{\partial \theta} + \frac{v_{gr} v_{g\theta}}{r} + v_{gz} \frac{\partial v_{g\theta}}{\partial z}) - \frac{1}{\rho_g} \frac{\partial p}{\partial \theta} \\ & - \frac{c_{i\theta}}{\alpha \rho_g} (v_{g\theta} - v_{l\theta}) |v_{g\theta} - v_{l\theta}| - \frac{r}{\alpha \rho_g} (v_{g\theta} - v_{ig\theta}) - \frac{c_{wq\theta}}{\alpha \rho_g} v_{g\theta} |v_{g\theta}|. \end{aligned} \quad (11)$$

Velocities are defined on the mesh-cell surfaces as shown in Fig. 2 where subscript "a" stands for either l or g.

In the staggered scheme<sup>5,6</sup> used in TRAC, the velocities are located on the mesh-cell surfaces at the locations shown in Fig. 2 while the volume properties,  $p$ ,  $\alpha$ ,  $T$ ,  $e$ ,  $\rho$ , etc., are located at the mesh-cell centers. The scalar field equations are written over a given mesh cell while the momentum equations are staggered between mesh cells in the three component directions.

To write out the difference scheme for each of the momentum equations is a rather lengthy process due to the cross-derivative terms. Therefore, only the vapor z-direction finite difference equations for a typical mesh cell are given to illustrate the procedure used. The time levels are indicated by the superscript  $n$  (old time) or  $n+1$  (new time). The subscript  $g$  (for vapor) will be dropped except where it is needed for clarity of the presentation. Using these conventions, the finite difference vapor momentum equation in the z-direction is:

$$\begin{aligned} v_z^{n+1}(r, \theta, z+\frac{1}{2}) = & v_z^n(r, \theta, z+\frac{1}{2}) - \Delta t \left\{ \frac{v_r(r, \theta, z+\frac{1}{2})}{\Delta r} \left[ v_z(r+\frac{1}{2}, \theta, z+\frac{1}{2}) - v_z(r-\frac{1}{2}, \theta, z+\frac{1}{2}) \right]^n \right. \\ & + \frac{v_\theta(r, \theta, z+\frac{1}{2})}{r\Delta\theta} \left[ v_z(r, \theta+\frac{1}{2}, z+\frac{1}{2}) - v_z(r, \theta-\frac{1}{2}, z+\frac{1}{2}) \right]^n \\ & + \frac{v_z(r, \theta, z+\frac{1}{2})}{\Delta z} \left[ v_z(r, \theta, z+1) - v_z(r, \theta, z) \right]^n \\ & \left. - \frac{[p(r, \theta, z+1) - p(r, \theta, z)]^{n+1}}{\rho^n(r, \theta, z+\frac{1}{2}) \Delta z} \right\} \end{aligned}$$

$$\begin{aligned}
& \frac{c_{iz}^n(r, \theta, z + \frac{1}{2}) \left| V_{gz}(r, \theta, z + \frac{1}{2}) - V_{lz}(r, \theta, z + \frac{1}{2}) \right|^{n+1}}{\alpha^n(r, \theta, z + \frac{1}{2}) \rho^n(r, \theta, z + \frac{1}{2})} \\
& \cdot \left| V_{gz}(r, \theta, z + \frac{1}{2}) - V_{lz}(r, \theta, z + \frac{1}{2}) \right|^n \\
& \frac{\Gamma^n(r, \theta, z + \frac{1}{2}) \left| V_z(r, \theta, z + \frac{1}{2}) - V_{iz}(r, \theta, z + \frac{1}{2}) \right|^{n+1}}{\alpha^n(r, \theta, z + \frac{1}{2}) \rho^n(r, \theta, z + \frac{1}{2})} \\
& \left. \frac{c_{wz}^n(r, \theta, z + \frac{1}{2}) V_z^{n+1}(r, \theta, z + \frac{1}{2}) \left| V_z^n(r, \theta, z + \frac{1}{2}) \right|}{\alpha^n(r, \theta, z + \frac{1}{2}) \rho^n(r, \theta, z + \frac{1}{2})} \right\}, \tag{12}
\end{aligned}$$

where  $\Delta t$  is the time-step size.

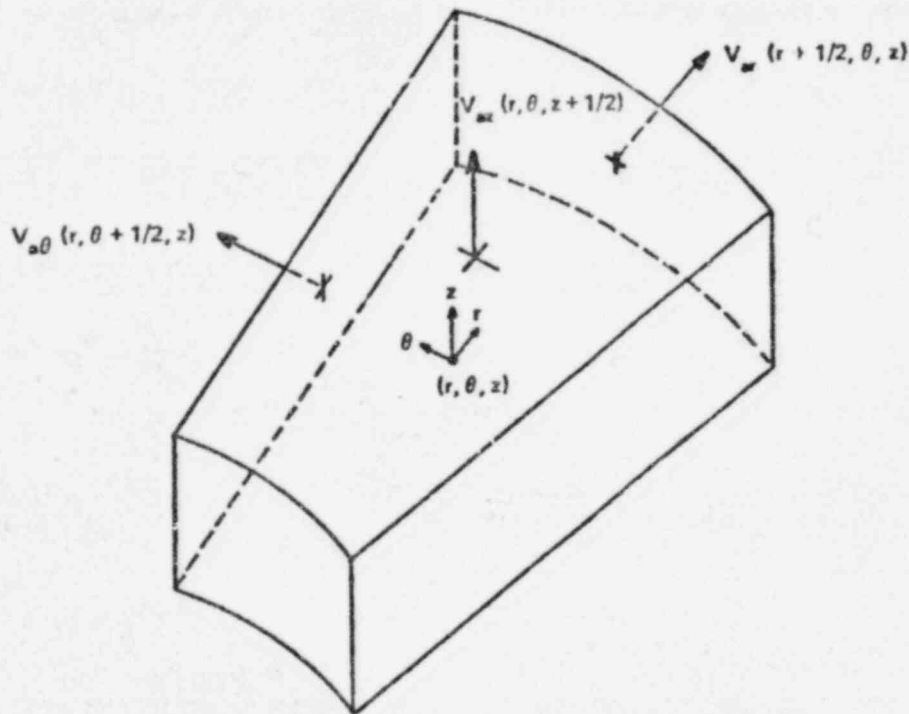


Fig. 2.  
Three-dimensional mesh-cell velocities.

As with any finite difference scheme, certain quantities are required at locations where they are not formally defined so that additional relations are needed. The volume properties,  $\Gamma$ ,  $\alpha$ , and  $\rho_g$  are donor celled, depending on the direction of  $V_z(r, \theta, z+\frac{1}{2})$ . For example,

$$\begin{aligned} \alpha(r, \theta, z+\frac{1}{2}) &= \alpha(r, \theta, z) && \text{if } V_z(r, \theta, z+\frac{1}{2}) \geq 0 \\ &= \alpha(r, \theta, z+1) && \text{if } V_z(r, \theta, z+\frac{1}{2}) < 0. \end{aligned} \quad (13)$$

The radial component of velocity at axial location  $z+\frac{1}{2}$  is obtained from

$$\begin{aligned} V_r(r, \theta, z+\frac{1}{2}) &= \frac{1}{2} [V_r(r+\frac{1}{2}, \theta, z) + V_r(r-\frac{1}{2}, \theta, z) + V_r(r+\frac{1}{2}, \theta, z+1) \\ &\quad + V_r(r-\frac{1}{2}, \theta, z+1)] \end{aligned} \quad (14)$$

with a similar expression applying to  $V_\theta(r, \theta, z+\frac{1}{2})$ . The spatial differences for  $V_z$  are also donor celled. For example, in the  $r$ -direction,

$$V_z(r+\frac{1}{2}, \theta, z+\frac{1}{2}) - V_z(r-\frac{1}{2}, \theta, z+\frac{1}{2}) = V_z(r, \theta, z+\frac{1}{2}) - V_z(r-1, \theta, z+\frac{1}{2})$$

if  $V_r(r, \theta, z+\frac{1}{2}) \geq 0$ , or

$$= V_z(r+1, \theta, z+\frac{1}{2}) - V_z(r, \theta, z+\frac{1}{2})$$

if  $V_r(r, \theta, z+\frac{1}{2}) < 0$ .

(15)

The finite difference relations for the scalar field equations are written in conservation form, noting, of course, that internal energy is not a conserved quantity. The finite difference form of the overall mixture mass equation is

$$\begin{aligned} \rho_m^{n+1} &= \rho_m^n + (\Delta t / \text{vol}) \left\{ FA_{z-\frac{1}{2}} \left[ \left( (1-\alpha)\rho_\ell \right)^n V_\ell^{n+1} + (\alpha\rho_g)^n V_g^{n+1} \right]_{z-\frac{1}{2}} \right. \\ &\quad - FA_{z+\frac{1}{2}} \left[ \left( (1-\alpha)\rho_\ell \right)^n V_\ell^{n+1} + (\alpha\rho_g)^n V_g^{n+1} \right]_{z+\frac{1}{2}} + FA_{r-\frac{1}{2}} \left[ \left( (1-\alpha)\rho_\ell \right)^n V_\ell^{n+1} \right. \\ &\quad \left. \left. + (\alpha\rho_g)^n V_g^{n+1} \right]_{r-\frac{1}{2}} - FA_{r+\frac{1}{2}} \left[ \left( (1-\alpha)\rho_\ell \right)^n V_\ell^{n+1} + (\alpha\rho_g)^n V_g^{n+1} \right]_{r+\frac{1}{2}} \right\} \end{aligned}$$

$$\begin{aligned}
& + FA_{\theta-\frac{1}{2}} \left[ \left( (1-\alpha)\rho_l \right)^n V_l^{n+1} + (\alpha\rho_g)^n V_g^{n+1} \right]_{\theta-\frac{1}{2}} \\
& - FA_{\theta+\frac{1}{2}} \left[ \left( (1-\alpha)\rho_l \right)^n V_l^{n+1} - (\alpha\rho_g)^n V_g^{n+1} \right]_{\theta+\frac{1}{2}}
\end{aligned} \tag{16}$$

where vol is the hydrodynamic cell volume and FA is the flow area at the mesh-cell edge. The other scalar equations are differenced similarly.

All of the field equations (1-6) have additional source terms to allow piping to be connected anywhere in the mesh. These sources in the scalar equations contain both an explicit and an implicit term. The implicit term is iterated with the rest of the new time variables in order to provide a consistent (in terms of time differencing) procedure for providing one-dimensional connections to the vessel. The source terms appearing in the mass and energy equations are given below. Subscripts p and v refer to pipe and vessel quantities, respectively, and  $V_m$  and  $e_m$  are given by

$$V_m = \frac{\alpha\rho_g V_g + (1-\alpha)\rho_l V_l}{\rho_m} \tag{17}$$

and

$$e_m = \frac{\alpha\rho_g e_g + (1-\alpha)\rho_l e_l}{\rho_m} \tag{18}$$

#### Overall Mass Continuity Source Term

$$(\rho_m^n FA V_m^{n+1})_p$$

#### Vapor Mass Continuity Source Term

$$[(\alpha\rho_g)^n FA V_m^{n+1}]_p + [\alpha(1-\alpha) \frac{\rho_g \rho_l}{\rho_m} FA V_x]_p^n$$

Overall Energy Source Term

$$\begin{aligned} & [(\rho_m e_m)^n FA V_m^{n+1}]_p + [\alpha(1-\alpha) \frac{\rho_l \rho_g}{\rho_m} (e_g - e_l) FA V_r]_p^n \\ & + P_v (V_m^{n+1} FA)_p + P_v [\alpha(1-\alpha) \frac{(\rho_l - \rho_g)}{\rho_m} FA V_r]_p^n \end{aligned}$$

Vapor Energy Source Term

$$\begin{aligned} & [(\alpha \rho_g e_g)^n FA V_m^{n+1}]_p + [\alpha(1-\alpha) \frac{\rho_l \rho_g}{\rho_m} e_g FA V_r]_p^n \\ & + P_v (\alpha^n FA V_m^{n+1})_p + P_v [\alpha(1-\alpha) \frac{\rho_l}{\rho_m} FA V_r]_p^n \end{aligned}$$

The momentum source terms are complicated due to the staggered differencing and the fact that pipes may enter at an arbitrary angle. For the present code version, we have assumed that the pipe enters normal to the vessel mesh-cell face. The basic forms for the liquid and vapor momentum source terms are:

Liquid Momentum Source Term

$$(V_l^2 \frac{FA}{\Delta x})_p^n / FA_v$$

Vapor Momentum Source Term

$$(V_g^2 \frac{FA}{\Delta x})_p^n / FA_v$$

where

$$V_l = V_m - \frac{\alpha \rho_g}{\rho_m} V_r \quad (19)$$

and

$$V_g = V_m + (1-\alpha) \frac{\rho_l}{\rho_m} V_r \quad (20)$$

If structure exists in the mesh cell, the hydrodynamic flow areas and volumes are reduced from their geometric mesh-cell values. Thus, FA may be less than or equal to the geometric mesh-cell area, and vol may be less than or equal to the geometric mesh-cell volume. Flow areas may also be set identically equal to zero. If this is the case, all fluxes across that plane are suppressed along with the individual velocities of each phase. This procedure allows large obstacles such as the downcomer walls to be properly modeled. The user is allowed complete freedom to specify the flow and volume restrictions.

The finite difference equations thus formed are semi-implicit, since the pressure gradient terms in the vapor and liquid momentum equations are treated at the new time. A Courant stability criterion of the form

$$\frac{|V| \Delta t}{L} < 1$$

is necessary, where

$$\frac{|V|}{L} = \max \left( \frac{V_{gz}}{\Delta z}, \frac{V_{g\theta}}{\Delta \theta}, \frac{V_{gr}}{\Delta r}, \frac{V_{lz}}{\Delta z}, \frac{V_{l\theta}}{\Delta \theta}, \frac{V_{lr}}{\Delta r} \right).$$

In order to solve the system of finite difference equations, a linearization procedure is carried out. All of the scalar equations are reduced to a linear system in  $V_l$ ,  $V_g$ ,  $T_l$ ,  $T_g$ ,  $\alpha$ , and  $p$ . This is accomplished by using the thermal equations of state:

$$\rho_l = \rho_l(p, T_l)$$

$$\rho_g = \rho_g(p, T_g),$$

the caloric equations of state:

$$e_l = e_l(p, T_l)$$

$$e_g = e_g(p, T_g),$$

and the definitions for  $\rho_m$  and  $e_m$ .

A further reduction in the system is accomplished by observing that the finite difference vapor and liquid momentum equations yield equations of the form

$$V^{n+1} = V^n + [\text{conv}^n + \frac{1}{\rho_l} V_p^{n+1} + \text{FRIC}] \Delta t, \quad (21)$$

where conv designates the explicit convection terms and FRIC includes both the wall and interfacial shears. Equation (21) indicates that changes in  $V$  are linearly dependent (after an explicit pass on the explicit parts of the momentum equations) on changes in pressure. The system of variables may therefore be further reduced to  $T_l$ ,  $T_g$ ,  $p$ , and  $\alpha$  and solved by a Block Gauss-Seidel method. Reference 7 provides a much more detailed description of the basic Newton Block Gauss-Seidel numerical technique.

One improvement to the method proposed in Ref. 7 has been implemented to reduce the computing cost. The linear system that results from this method is a block seven-strip matrix. In performing the Gauss-Seidel operation, if the nonlinear terms are not updated, the matrix coefficients remain constant for the time step. In this case, a Gauss elimination technique can be applied once at each time step to the seven-stripe block array, which allows its reduction to a seven-stripe single-element array. This results in a much faster iteration (after the first iteration) for the pressure. When the vessel pressures are obtained to a specified convergence criterion, a back-substitution is performed to unfold  $T_l$ ,  $T_g$ , and  $\alpha$  and the velocities for each phase. The thermodynamic properties and their derivatives are then updated in preparation for the next time step.

### c. Constitutive Equations

The field equations (1-6) require certain auxiliary or constitutive equations to effect closure. It has already been mentioned that thermal and caloric equations of state for each phase are required. In addition, the liquid and vapor wall shear, interfacial drag, wall heat transfer, interfacial heat transfer, the net vaporization rate, and a specification for the interfacial velocities are necessary.

The wall heat transfers  $q_{wg}$  and  $q_{wl}$  are accounted for in the standard way, as described previously.<sup>8</sup> The wall shear coefficients  $c_{wg}$  and  $c_{wl}$  are defined as

$$c_{wg} = \alpha \rho_g \frac{c_{fg}}{2} \quad (22)$$

and

$$c_{wl} = (1-\alpha) \rho_l \frac{c_{fl}}{2}, \quad (23)$$

where  $c_{fg}$  and  $c_{fl}$  are, respectively, the vapor and liquid wall friction factors. The standard Harwell correlation<sup>9</sup> is employed to provide the wall friction factors. The average cell vector velocity is used to define the mesh-cell Reynolds number, and the two-phase multiplier is calculated using cell-centered quantities. A total friction factor is calculated from the information above and is ascribed completely to the liquid momentum equation until a vapor fraction of 0.9 is reached. From  $\alpha$  of 0.9 to 0.9999, the shear is assigned with linear weighting to both the liquid and vapor. Beyond a vapor fraction of 0.9999, a pure vapor drag coefficient is calculated (laminar or Blasius) and assigned totally to the vapor momentum equation. If the vapor fraction is less than 0.0001, a single-phase liquid correlation (laminar or Blasius) is used.

A single friction coefficient is generated for both the outer radial and upper axial cell face from this procedure. However, the hydraulic diameter used in the radial and axial directions will, in general, vary depending on the geometry. These hydraulic diameters are calculated from

$$D_h = 4FA_i/P_i, \text{ where } i = \theta, z, r$$

and where the wetted perimeter ( $P_i$ ) normal to direction  $i$  includes the surface area of any rods, wall heat slabs, or flow boundaries. If there is no solid material in a mesh cell, the wall shear is zero. A similar procedure is used to arrive at a wall shear in the theta direction. In this case, however, vector velocities and properties on the appropriate theta face (rather than the cell-centered averages) are used in order to achieve theta symmetry, where such symmetry should exist.

The basic finite difference scheme will properly calculate classical Bourda losses at an expansion but overpredicts the losses at a contraction. At present, no additional correction at a contraction is supplied automatically by the code, but an additional constant hydraulic loss factor can be specified by the user in any of the coordinate directions and at any mesh face.

The flashing rate  $\Gamma$  is determined from a simplified thermal energy jump condition.<sup>8</sup> In both the vapor continuity equation and the vapor thermal energy equation, the potentials  $T_s - T_g$  and  $T_s - T_l$  are evaluated at the new time level while  $h_{ig}A_i$  and  $h_{il}A_i$  are evaluated at the old time.

The interfacial heat transfers during boiling and the interfacial shear are calculated in conjunction with a simple flow regime map.<sup>10</sup> Figure 3 illustrates the manner in which the flow map is implemented in the code.

If the void fraction is less than or equal to 0.25, a bubbly flow is assumed. The interfacial surface area in this regime is calculated in conjunction with a critical bubble Weber number  $We_b$  (100 is used in the present code):

$$\frac{\rho_l V_r^2 D_b}{\sigma} = We_b$$

or

$$D_b = \frac{We_b \sigma}{\rho_l V_r^2} \quad (24)$$

where  $D_b$  is the bubble diameter. For this diameter, and assuming a uniform bubble distribution within the mesh-cell volume (vol), the number of bubbles is

$$CNB = \frac{6 \alpha \text{ vol}}{\pi D_b^3} \quad (25)$$

and the interfacial area is

$$A_i = 6 \alpha \text{ vol} \rho_l V_r^2 / We_b \sigma \quad (26)$$

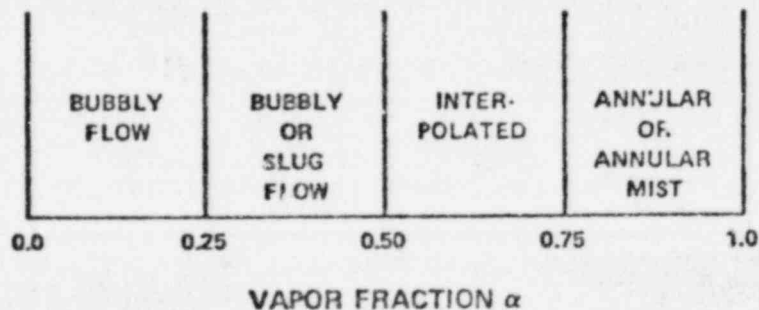


Fig. 3.  
Flow regime map for three-dimensional hydrodynamics.

The liquid side interfacial heat transfer coefficient is taken as the larger of an approximate formulation of the Plesset-Zwick bubble growth model<sup>9,11</sup>

$$Nu = 0.95493(T_l - T_s) \rho_l \frac{\partial \rho_l}{\partial T_l} / [\rho_g (h_{s g} - h_{s l})] \quad (27)$$

and a sphere convection coefficient<sup>12</sup>

$$Nu = 2.0 + 0.74 Re_D^{0.5}, \quad (28)$$

where

$$Re_D = \rho_l V_c D_b / \mu_l.$$

The interfacial shear coefficient is provided by a rather standard set of formulas for a sphere:<sup>13</sup>

$$c_i = \frac{c_b \alpha \rho_l}{2 D_b} \quad (29)$$

where

$$\begin{aligned} c_b &= 240 \text{ for } Re_D < 0.1, \\ &= 24/Re_D \text{ for } 0.1 \leq Re_D \leq 2, \\ &= 9.35/Re_D^{0.68} \text{ for } Re_D > 2. \end{aligned}$$

If the cell-average mass flux is less than 2000 and the vapor fraction is between 0.25 and 0.5, the flow enters the slug regime. At the maximum  $\alpha$  of 0.5, 40% of the vapor is assumed to exist in the form of trailing bubbles with the remainder contained in the slug. These bubbles probably contribute the majority of the interfacial heat transfer, and the liquid side coefficient is calculated from the relations for the entrained bubbles. If the mass flux is greater than 2700, all of the vapor is assumed to exist in bubble form. Linear interpolation in mass flux is used in the range 2000 to 2700. In the slug regime the interfacial drag is volume-averaged between the slug and the trailing bubbles with a constant drag coefficient of 0.44 used for the slug.

In the vapor fraction range of 0.75 to 1.0, an annular or annular mist regime is employed. An approximation to the Wallis entrainment correlation<sup>14</sup> is used to estimate the fraction of liquid that is in droplet form:

$$E = 1 - \exp[-0.125(J'_g - 2.1)] \quad (30)$$

where

$$J'_g = 10^4 \alpha \frac{V_g \mu_g}{\sigma} \left(\frac{\rho_g}{\rho_l}\right)^{\frac{1}{2}}$$

The remainder of the liquid is in a film or sheet. The wetted surface area of the mesh cell is determined from the rod or slab heat transfer area in the cell and that portion of the geometric flow area which is blocked off. If the cell is in a region devoid of any structure, the geometric surface area is employed as a scaling factor. This is, of course, artificial but in a realistic PWR simulation very few, if any, of the mesh cells are completely free of metal structure. The total interfacial surface area is determined by the sum of the areas contained in the wetted film and the droplets. A critical Weber number equal to 12 for the drops is used with a calculation procedure that is similar to that for bubbly flow. The liquid side heat transfer coefficient is simply

$$h_{i,l} = c k_l / D_d \quad (31)$$

where  $c$ , a constant, has been adjusted to drive the drops to equilibrium under a variety of flow conditions. In the present code,  $c = 15000$  which implies a thermal boundary layer in the drops that is about a thousandth of the drop diameter. In the film a correlation

$$Nu = 0.0073 Re \quad (32)$$

is employed to predict  $h_{i,l}$ . The Wallis annular flow model<sup>14</sup> determines the shear for a wavy film while the same drag correlations used for a bubble are employed if droplets exist. The droplet Reynolds number is defined as

$$Re_d = \frac{\rho_g V_{rd} D_d}{\mu_g} \quad (33)$$

Since the actual relative velocity calculated is based on a shear that has been averaged between the film and drop correlations, a separate function<sup>15</sup> is used for  $V_{rd}$ :

$$V_{rd} = 1.4 \alpha [9.8 \sigma (\rho_l - \rho_g) / \rho_g^2]^{\frac{1}{2}} \quad (34)$$

In the interpolated regime defined in Fig. 3, a linear interpolation in vapor fraction is made between the conditions that would exist if the vapor fraction were at 0.75 in the annular or annular mist topology, and the conditions that would exist if the flow were in the bubbly or bubbly slug regime at a void fraction of 0.5. This makes the correlation for the interfacial shear, interfacial heat transfer, and surface area a continuous function of vapor fraction, relative velocity, mass flux, and the various fluid thermodynamic and transport properties.

We now discuss the vapor-side heat transfer coefficient and the liquid heat transfer coefficient during condensation. The vapor heat transfer coefficient is the simple function  $h_{ig} = c$ , where  $c = 1 \times 10^4$ . This implies that the rate for boiling or condensation is determined principally by the liquid side coefficient with a vapor coefficient designed to drive the vapor toward the saturation temperature. The formulation for the total liquid heat transfer coefficient  $h_{iL}A_i$  used for boiling seems to provide too high a coefficient during condensation. It is anticipated that a condensation rate based on a film model might be more appropriate. Therefore, for condensation the interfacial area is calculated from

$$A_i = (\text{vol}/\Delta z)c,$$

where the coefficient  $c$  accounts for a rough interface and is equal to 10. The specific heat transfer coefficient is the same as the film coefficient used in the annular boiling regime. This model for condensation is admittedly simple and may be improved in future versions of the code if additional testing indicates that this is desirable.

### 3. Heat Transfer Methods

(W. L. Kirchner, Q-6)

Several modifications and improvements have been made to the heat transfer packages in the TRAC code. The conduction solutions have been updated to allow specification of either implicit or semi-implicit boundary conditions. The addition of the former allows rapid convergence of the temperature field calculation for steady-state solutions. A rudimentary dynamic gap conductance calculational method has been added and tested. The conductance is calculated as a function of gap gas conductivity and radiation terms. Provision for future incorporation of a contact conductance term has been made. Radiation

heat transfer from wall to liquid in the film boiling regimes and a major improvement in the reflood heat transfer nodalization have been added.

a. Radiation Heat Transfer to Liquid

The radiation heat transfer coefficient is based on Bromley's<sup>16</sup> analysis:

$$h_{\text{RAD}} = \sigma F (T_w^4 - T_l^4) / (T_w - T_l), \quad (35)$$

where

$$F = \frac{1}{\frac{1}{\epsilon} + \frac{1}{\alpha} - 1}, \quad (36)$$

and

- $\epsilon$  = emissivity of the wall,
- $\alpha$  = absorptivity of the liquid, and
- $\sigma$  = Stefan-Boltzmann constant.

Since this method is only strictly applicable to parallel wall configurations, the value obtained is weighted by one minus the vapor fraction  $(1 - \alpha)$ . This model will be improved as a more sophisticated dispersed flow film boiling regime analysis is added.

b. Reflood Heat Transfer

Limitations on computer running times required TRAC fluid cells in the core region to be on the order of a half meter in length in the axial direction. However, under reflood conditions, significant variations in transport processes may take place in a much shorter axial length. To allow improved modeling of these processes, without incurring prohibitive computer costs, a renodalization of the fuel rod conduction calculation was made available. Based on user-supplied input, the coarse axial mesh corresponding to the fluid cell is subdivided into an arbitrary number of fine-mesh intervals. The radial conduction solution is then applied in each fine-mesh interval.

Material properties and gap heat transfer coefficients continue to be based on coarse-mesh values, but heat transfer coefficients are now evaluated for each fine mesh. To better approximate actual temperature profiles, a temperature interpolation scheme has been added to initially fill the fine-mesh temperature fields. A Lagrangian interpolation scheme<sup>17</sup> is used:

$$T(z) = \sum_{i=0}^n \ell_i T_i, \quad (37)$$

where

$$\ell_i = \frac{(z-z_0) \dots (z-z_{i-1})(z-z_{i+1}) \dots (z-z_n)}{(z_i-z_0) \dots (z_i-z_{i-1})(z_i-z_{i+1}) \dots (z_i-z_n)} \quad (38)$$

and  $T_i$  are the coarse-mesh temperatures. The quadratic equation obtained by fitting three adjoining coarse-mesh temperatures at a time yields the fine-mesh profile.

To ensure conservation of energy, and taking advantage of constant properties within a coarse mesh, the fine-mesh temperatures ( $T_j$ ) are normalized as follows:

$$T_j = N_f T_i \bar{T}_j / \sum_{j=1}^{N_f} \bar{T}_j, \quad (39)$$

where

$N_f$  = number of axial fine meshes in coarse mesh  $i$ ,

$\bar{T}_j = az_j^2 + bz_j + c$ ,

and  $a$ ,  $b$ , and  $c$  are obtained from Eq. (38).

A second procedure incorporated in the reflood initialization is a search to locate quench fronts. Rather than assume the core is dry at the beginning of reflood, which may not be the case, a pattern search of each average rod is made for the combined condition of clad surface temperature less than the Leidenfrost temperature and sufficient liquid available to form a film on the rod. Two quench fronts per rod are accounted for: a falling film from the top and a bottom quench front.

#### 4. TRAC Developmental Verification

(K. A. Williams, Q-6)

The verification problems that will be included with the documentation of the first public release version of TRAC have been selected. These problems are now being run with the code version recently released to NRC. The problems were selected to provide verification of the code over the large class of problems on which the TRAC code can be employed. These problems range from

simple unheated pipe blowdown experiments to the large-scale experiments that are prototypical of full-sized reactor systems.

Verification problems selected for TRAC documentation include:

1. Edwards horizontal pipe blowdown,
2. CISE unheated pipe blowdown (100% break area),
3. CISE heated pipe blowdown (100% break area),
4. RSR Standard Problem 2 (Semiscale isothermal blowdown)
5. RSR Standard Problem 5 (Semiscale heated blowdown),
6. CREARE refill experiments,
7. FLECHT reflood experiment,
8. Semiscale blowdown/reflood experiment (Test S-05-1), and
9. RSR Standard Problem 7 (LOFT nonnuclear blowdown experiment -- Test L1 4).

In addition to reference calculations of these problems, the documentation will include the results of parametric studies and a blowdown/reflood calculation of a typical PWR with ECC injection.

The pipe blowdown problems and Standard Problem 2 have all been rerun with the release version of the code, TRAC-Pl. Results from these calculations are similar to or better than those previously reported.

Calculational results from Standard Problem 5 are now in much better agreement with experimental data on mass flow rates and pressures. This improvement was due to the correction of an error in the geometrical input data. The calculated rod temperatures are in good agreement with the data, as they were before.

The CREARE refill calculations have been extended to include cases having the highest ECC water subcooling that was tested (80 K). This case also had the highest reverse core steam flow rate.

FLECHT reflood calculations are continuing and have identified a problem area; that is, the overprediction of liquid above the quench front. Possible solutions to this problem are currently being investigated.

An initial steady-state calculation has been performed for LOFT nonnuclear blowdown Test Ll-4. The results are in very good agreement with the experimentally measured steady-state values. Calculation of the actual blowdown is currently in progress.

a. TRAC Analysis of Downcomer Effects in the Creare 1/15-Scale Vessel

(K. A. Williams, Q-6)

During the previous quarter, TRAC was used to analyze downcomer experiments conducted by Creare with a 1/15-scale vessel. The purpose of this experiment was to better understand how delivery to the lower plenum of ECC water is affected by reverse core steam flow rate, ECC water subcooling, and superheated walls. The previous calculations had included only cases having low subcooling and low reverse core steam flow rate. This quarter TRAC was used to analyze cases having the highest ECC water subcooling as well as the highest reverse core steam flow rate reported by the Creare experimenters. The same modeling of the Creare vessel (as discussed last quarter) was used in the current analyses.

The lowest ECC water temperature used in the Creare countercurrent flow experiments is 303 K (85°F). A case using this water temperature and operating near the complete bypass point (thus having the highest reverse steam flow rate) was computed. The dimensionless countercurrent steam flow,  $J_{gc}^*$ , is equal to 0.30 for this case. This steam flow results in complete bypass of the ECC water injected at a rate of  $3.785 \times 10^{-3} \text{ m}^3/\text{s}$  (60 gpm). The TRAC calculation also resulted in complete bypass of the ECC water.

Another case was analyzed having an intermediate value of ECC water temperature. This case was at an ECC water temperature of 339 K (150°F) and an injection rate of  $3.785 \times 10^{-3} \text{ m}^3/\text{s}$  (60 gpm). The dimensionless reverse core steam flow was  $J_{gc}^* = 0.17$ , producing partial delivery of ECC water to the lower plenum and partial bypass. From the reported penetration curve,<sup>18</sup> this should result in a dimensionless water flow delivered,  $J_{fd}^*$ , of approximately 0.01. This means that about 18% of the injected ECC water is delivered to the lower plenum. TRAC computed a value of 0.008; if the point is plotted on the penetration curve, it is seen to fall within the range of uncertainty for this curve, which is estimated to be about  $\pm 5\%$ .

Finally, the original penetration curve that was analyzed last quarter<sup>2</sup> was recomputed to see if recent minor changes to the three-dimensional, two-fluid hydrodynamic package produced any effect. Three cases were computed such that the entire range from complete bypass to complete delivery was covered. These calculations again produced good agreement with the experimental penetration curve.

b. Analysis of RSR Standard Problem No. 5

(J. W. Bolstad, Q-6)

Both steady-state and transient verification calculations have been performed for RSR Standard Problem No. 5, a Semiscale blowdown experiment with an active core and steam generator. The calculated cladding temperature response for this experiment was presented in the last quarterly progress report.<sup>2</sup> Comparisons with experimental results of the other calculated thermal-hydraulic output variables have been made and a representative sampling of these comparisons is presented here.

The calculated break flow rates are shown in Figs. 4 and 5; the agreement with experiment is good. The prediction of the cold-leg side break mass flow rate is slightly high for the first portion of the transient. However, it is believed that the measurement is on the low side during this time period.<sup>19</sup> Error bars in these and other figures are estimates of the uncertainties in the experimental measurements.

A comparison of the calculated and experimental lower plenum pressure is shown in Fig. 6. The agreement is quite good except for the first six seconds. The cause of this discrepancy is currently being investigated.

The calculated and experimental fluid temperatures are shown in Fig. 7. The core flow is negative for the first five seconds, and the effect of the hot core fluid being swept into the lower plenum is evident in both the calculation and experiment.

Comparisons of the pump differential pressure and mass flow rate are shown in Figs. 8 and 9. Both quantities show good agreement between the predicted and experimental values. It is noted that the initial pump differential pressure is smaller than experiment; this is due to the fact that the initial experimental pump head and flow rate do not agree with the given pump homologous curves.

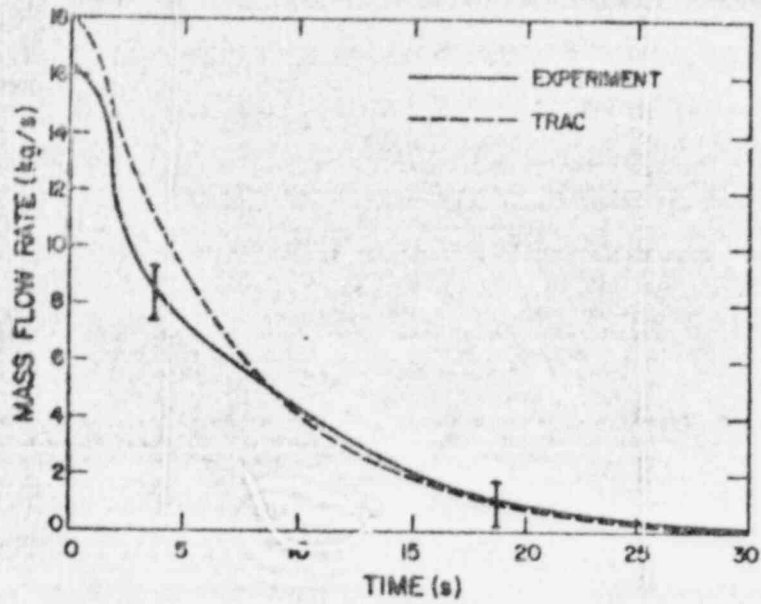


Fig. 4.  
 Calculated and experimental mass flow rate (cold-leg side of break)  
 for Semiscale Test S-02-8.

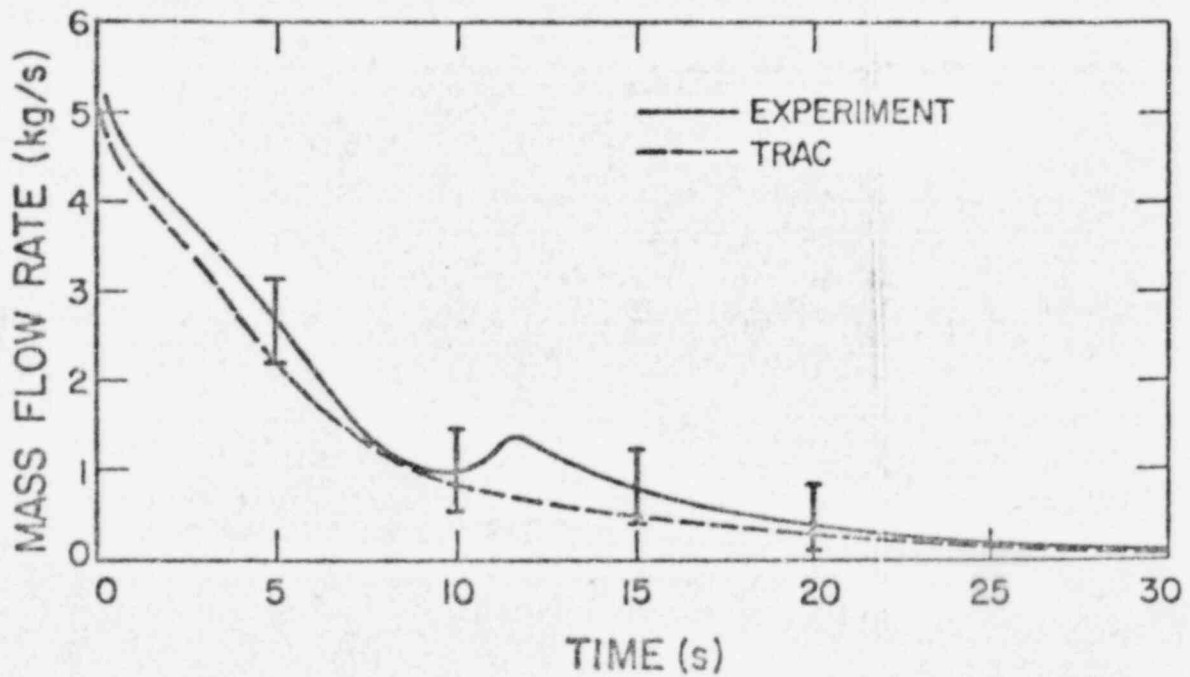


Fig. 5.  
 Calculated and experimental mass flow rate (hot-leg side of break)  
 for Semiscale Test S-02-8.

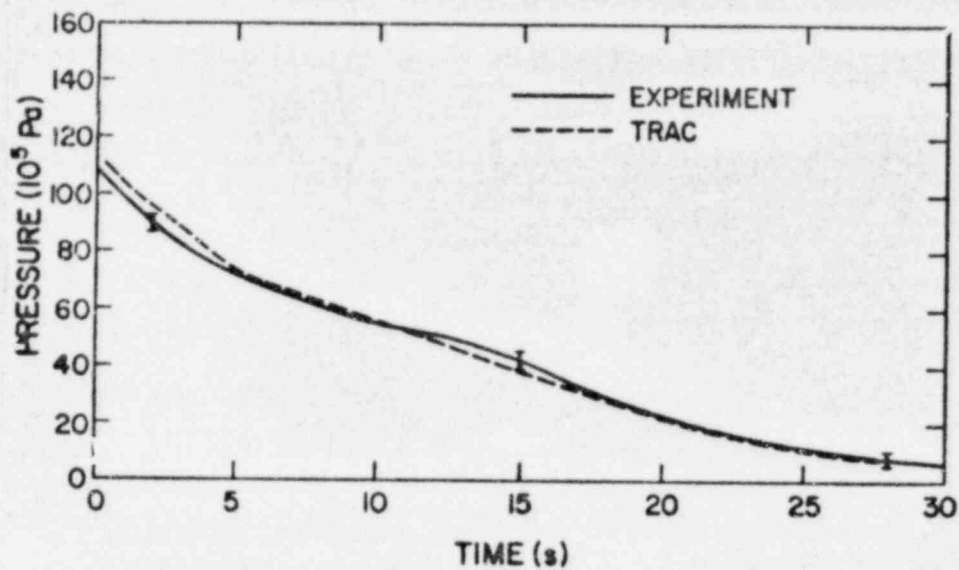


Fig. 6.  
 Calculated and experimental lower plenum pressure for  
 Semiscale Test S-02-8.

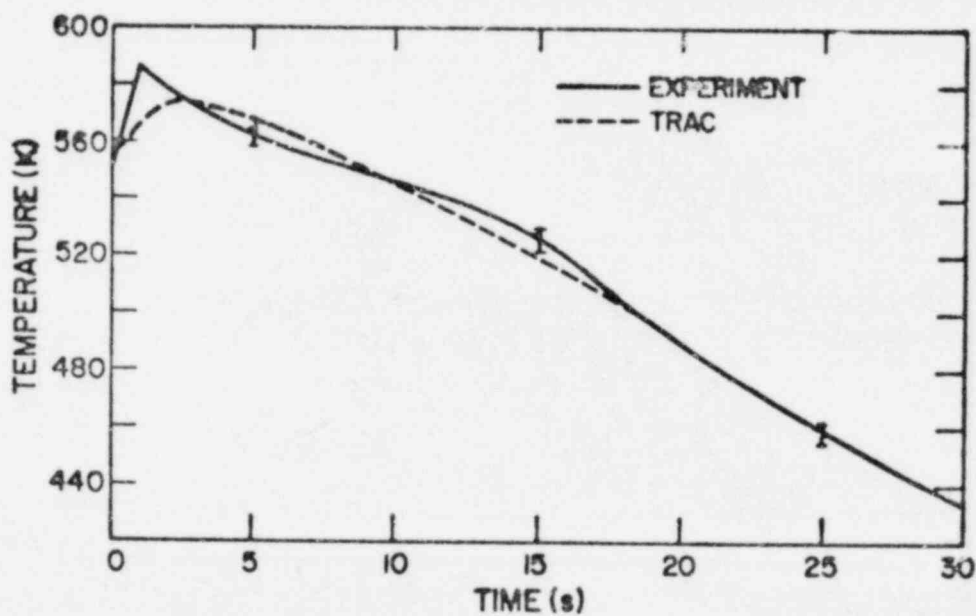


Fig. 7.  
 Calculated and experimental lower plenum fluid temperature for  
 Semiscale Test S-02-8.

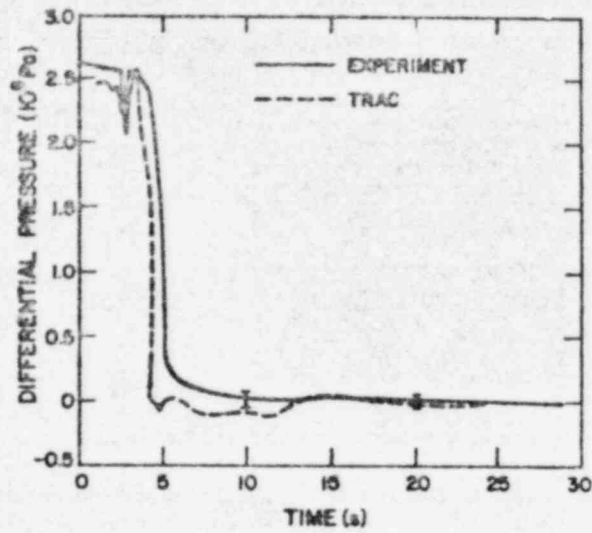


Fig. 8.  
 Calculated and experimental pump differential pressure for  
 Semiscale Test S-02-8.

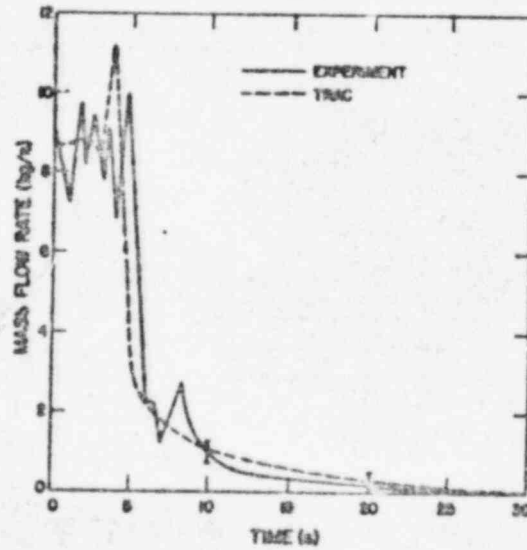


Fig. 9.  
 Calculated and experimental pump inlet mass flow rate for  
 Semiscale Test S-02-8.

Comparisons for the steam generator (primary side) outlet density and pressure are shown in Figs. 10 and 11. The predicted density compares favorably with experiment while the steam generator outlet pressure is slightly overpredicted for the first 10 s.

The overprediction of the pressures in Figs. 6 and 11 has been traced to the fact that the calculated pressurizer pressure decreased too rapidly. This occurred because the experimental apparatus has a very high resistance in the pressurizer surge line, and this high resistance was not reflected in the TRAC calculation. The calculation is currently being repeated with the correct surge line hydraulic resistance.

c. Analysis of LOFT Nonnuclear Test L1-4 (RSR Standard Problem No. 7)

(J. J. Pyun, Q-6)

Test L1-4 is the fourth in a series of five nonnuclear isothermal blowdown tests performed by the Loss-of-Fluid Test (LOFT) program<sup>20</sup> and is designated as RSR Standard Problem No. 7. The LOFT facility was designed to simulate the major components and system responses of a large pressurized water reactor during a LOCA. A hydraulic core simulator assembly was installed in place of the nuclear core. Test L1-4 was performed from initial conditions of 552 K and 15.75 MPa (absolute pressure) and had a 200% (100% break area in each leg) double-ended offset shear break in the simulated cold leg. The purpose of this test was to provide system thermal-hydraulic data to compare with predictions and other experimental data for code verifications, and to provide comparison of delayed HPIS (high-pressure injection system) and LPIS (low-pressure injection system) injection to the cold leg and the lower plenum. The TRAC model of this system, and the calculated results for steady-state conditions, are described here.

Figure 12 shows a detailed noding diagram for this problem, along with a TRAC arrangement of components and junctions. The system is modeled using 21 junctions and 20 components containing 176 fluid cells. The reactor vessel is modeled using the three-dimensional VESSEL module containing 56 fluid cells. Except near the break, the cell dimensions are approximately 0.2-2.0 m long. The cell length for the fully implicit PIPE modules near the breaks (components 15 and 16) varies from 0.02-0.1 m.

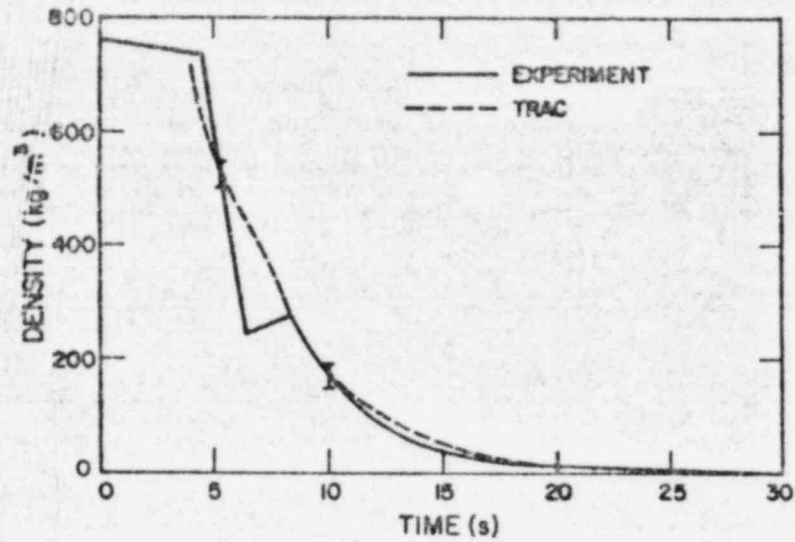


Fig. 10.  
 Calculated and experimental steam generator outlet density for  
 Semiscale Test S-02-8.

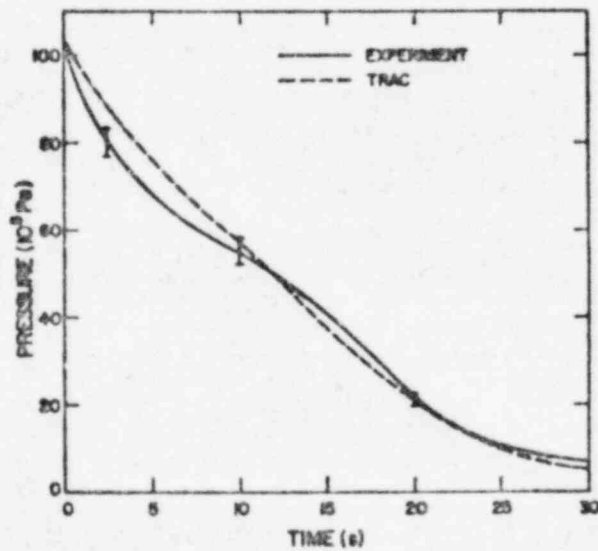


Fig. 11.  
 Calculated and experimental pressure at the steam generator outlet for  
 Semiscale Test S-02-8.

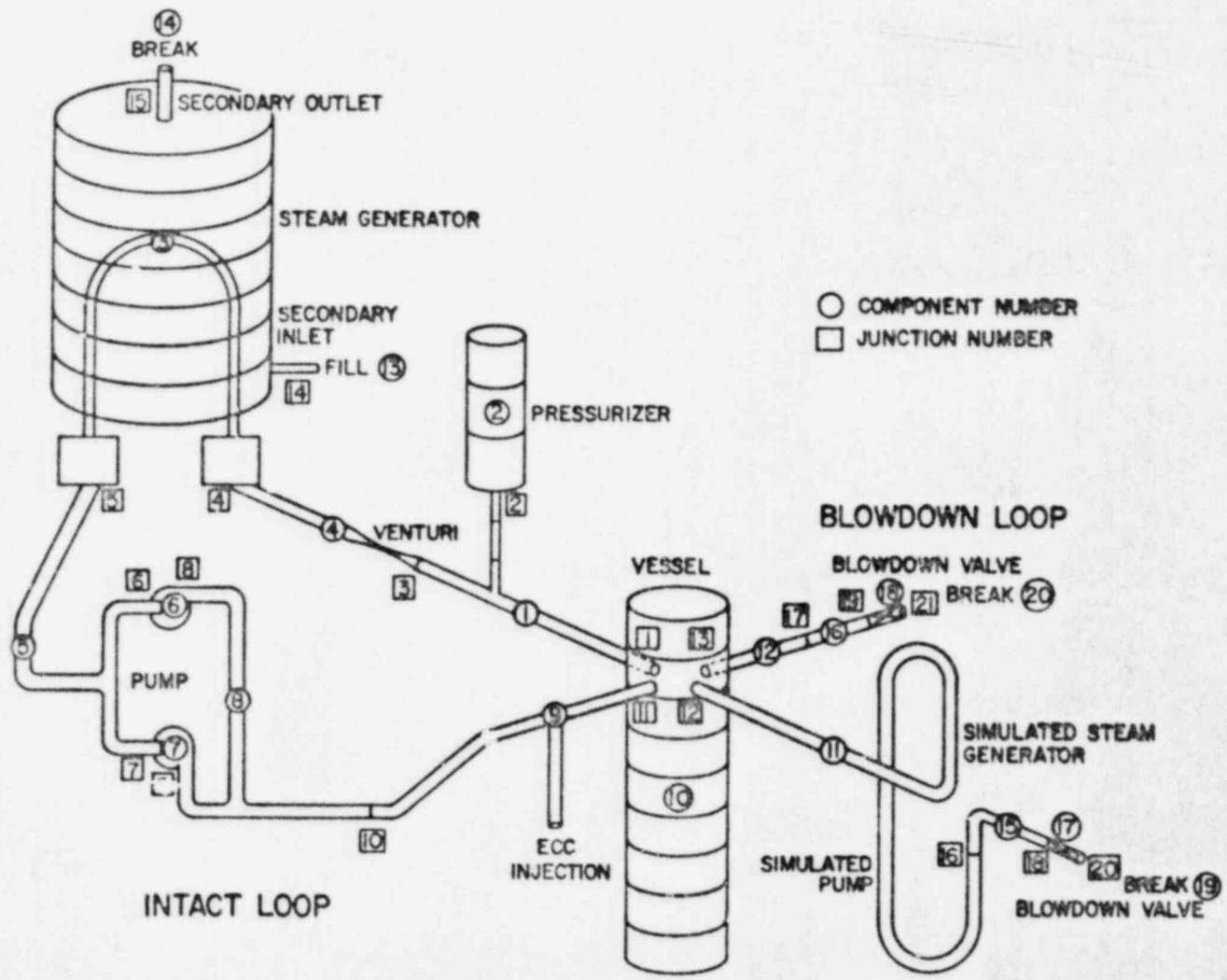


Fig. 12.  
TRAC noding diagram for RSR Standard Problem No. 7.

The steady-state conditions were calculated with TRAC by running a transient calculation with initial conditions<sup>21</sup> of zero flow rate, uniform pressure, and temperature distributions. At time zero, the pumps were started and the transient was initiated. The system flow rates, pressure, and temperature approach their steady-state distributions after one loop cycle time (~ 3-4 s) because the whole system is under isothermal conditions, and heat transfer among components and within a component are negligibly small. In addition, no heat is generated within the reactor core. This steady-state calculation required approximately 30 s of CPU time on the CDC-7600.

Table III shows the comparison between calculated and measured initial conditions. In general, the agreement is very good (i.e., within 0.1%) except for the differential pressure across the primary pumps in the intact loop. The disagreement in the pump differential pressure is probably due to the fact that the measured value is not always consistent with the corresponding mass flow rate generated by the homologous pump characteristic curves used in TRAC.

Transient calculations, based on calculated steady-state initial conditions, are being performed for the system depressurization transient with ECC injection to the intact loop cold leg.

#### 5. Statistical Sensitivity Analysis

(M. D. McKay, Q-12)

The first draft of a report that discusses four methods of sensitivity analysis was completed. The report examines the partial derivative, the partial derivative of a response surface, an averaged partial derivative technique, and the partial rank correlation coefficient as measures of sensitivity. The measures are studied relative to the local view of sensitivity analysis, which is concerned with output variability in a neighborhood of a single point in the input space, and with respect to the global view, which is concerned with output variability over the entire range of inputs.

An investigation into the matter of minimum sample size requirements for sensitivity analysis was initiated. Tentative indications are that sample size must be at least one (and more often two) larger than the number of inputs under study. This lower limit will hold for most analysis techniques unless restrictive assumptions on the relationships among inputs and outputs are made. The investigation is continuing.

TABLE III  
COMPARISON OF INITIAL CONDITIONS FOR LOFT NONNUCLEAR TEST LI-4

<u>Parameter</u>	<u>Calculated</u>	<u>Measured</u>
Loop Mass Flow Rate (kg/s)	268.00	268.40
Pressurizer Pressure (MPa)	15.73	15.5
Pressurizer Water Mass (kg)	414.80	418.80
Pressurizer Water Level (m)	1.15	1.16
Steam Generator Primary Side Pressure (MPa)	15.70	15.75
Steam Generator Primary Side Inlet Temperature (K)	552.30	554.00
Steam Generator Primary Side Outlet Temperature (K)	553.20	552.00
Steam Generator Secondary Side Pressure (MPa)	6.65	6.65
Steam Generator Secondary Side Temperature (K)	553.00	552.00
Core Inlet Temperature (K)	552.20	552.00
Total System Mass (kg)	7677.80	7652.2
Differential Pressure in Intact Loop Across Primary Pumps 1 and 2 (MPa)	0.10	0.13

A method for measuring the sensitivity of an output to a group of inputs taken collectively is being implemented in the analysis code. If successful, the method will enable the detection of joint importance of inputs, which may have a very low degree of importance when taken separately.

#### B. TRAC Applications

(J. C. Vigil and P. B. Bleiweis, Q-6)

The scope of the work described in this section includes the application of TRAC to full-scale light water reactor (LWR) transients and to the large-scale German and Japanese reflood tests. These applications provide design assistance, pretest predictions, and posttest analyses for the experimental programs. In general, they are used to help with the planning and coordination of the large-scale reflood experiments. TRAC applications to these experiments also help validate the code for use on full-scale LWR systems. Applications of TRAC to full-scale LWR systems provide best estimate predictions of the consequences of postulated transients.

Effort in the TRAC applications area during the past quarter has concentrated on an extension of a PKL calculation reported in the last quarterly<sup>2</sup> and on the nodding and steady-state calculation of a typical U.S. PWR in preparation for the first complete TRAC PWR LOCA calculation. The PKL demonstration problem described below extends an earlier calculation by the inclusion of subcooled hot-leg injection, reflood heat transfer and quench front motion. The calculation was also extended over a longer time period. The results serve to demonstrate some of the important multidimensional capabilities of TRAC. A detailed model for a typical U.S. PWR has been completed and the model and results of a steady-state calculation are also described below. In addition to these two major projects, a TRAC model of the Idaho National Engineering Laboratory (INEL) air-water injection tests has been completed and preliminary test calculations performed. The four-loop Japanese cylindrical core reflood test facility was also modeled during the past quarter. Finally, initial contact with the SAM code developers regarding its use for design-related calculations and test analyses of the Japanese slab core experiment has been made.

#### 1. PKL Demonstration Problem

(P. B. Bleiweis, Q-6)

As a prelude to actual PKL posttest analyses, an extension of the preliminary PKL calculation reported in the last quarterly<sup>2</sup> was performed. The preliminary calculation was a short simulation of a hot-leg break with hot- and cold-leg injection at saturation and no reflood heat transfer. The new calculation extends the previous PKL preliminary calculation to include subcooled hot-leg injection, reflood heat transfer, quench front motion, and a much longer simulation time. The main purpose of this particular PKL calculation is to demonstrate some of the multidimensional capabilities of TRAC such as liquid pool formation above the upper core support plate (UCSP), penetration into the core from this pool, hot-leg injection with subcooled liquid, reflood heat transfer, and quench front motion. In addition, such a calculation serves to test TRAC on a large, complicated problem.

Figure 13 shows a schematic of the TRAC PKL arrangement. Figures 14 and 15 show a side and top view, respectively, of the TRAC nodding for the PKL vessel. The PKL schematic and nodding diagrams were presented previously but are repeated here for the convenience of the reader. Note that the

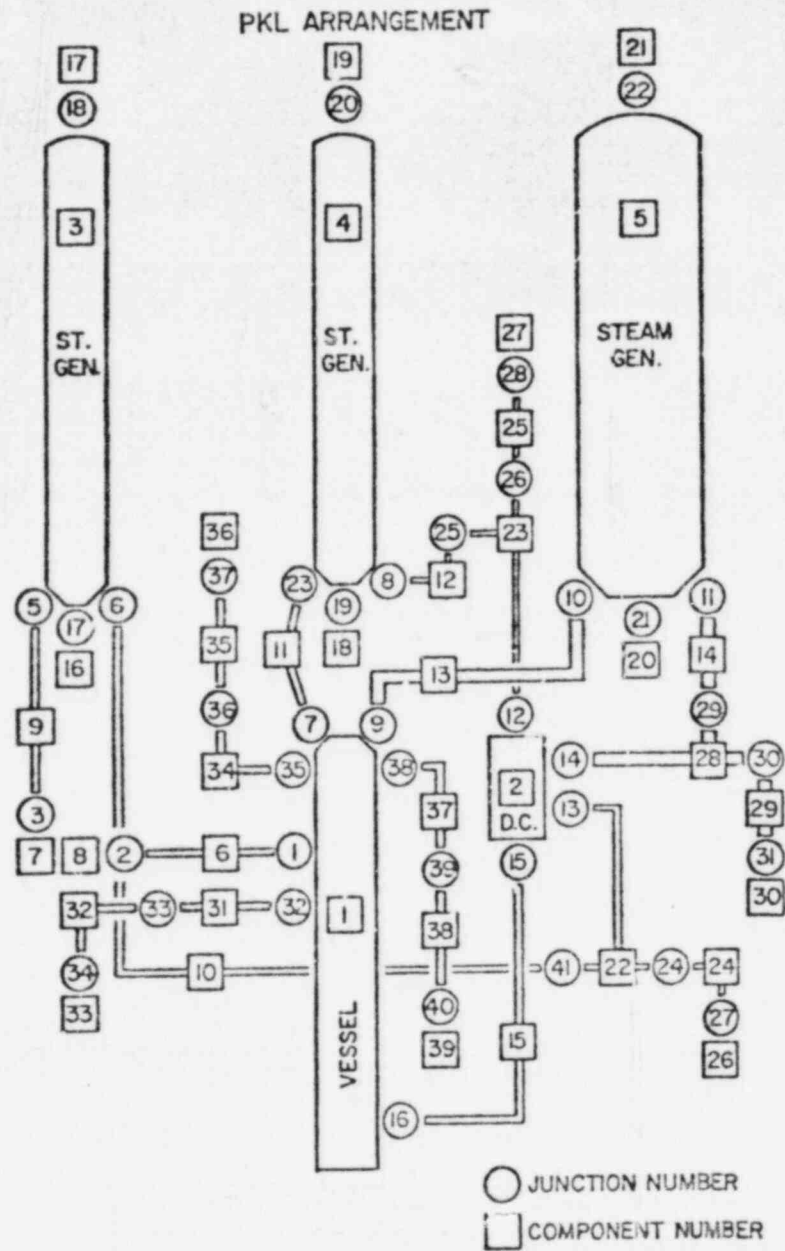


Fig. 13.  
TRAC model schematic for PKL system.

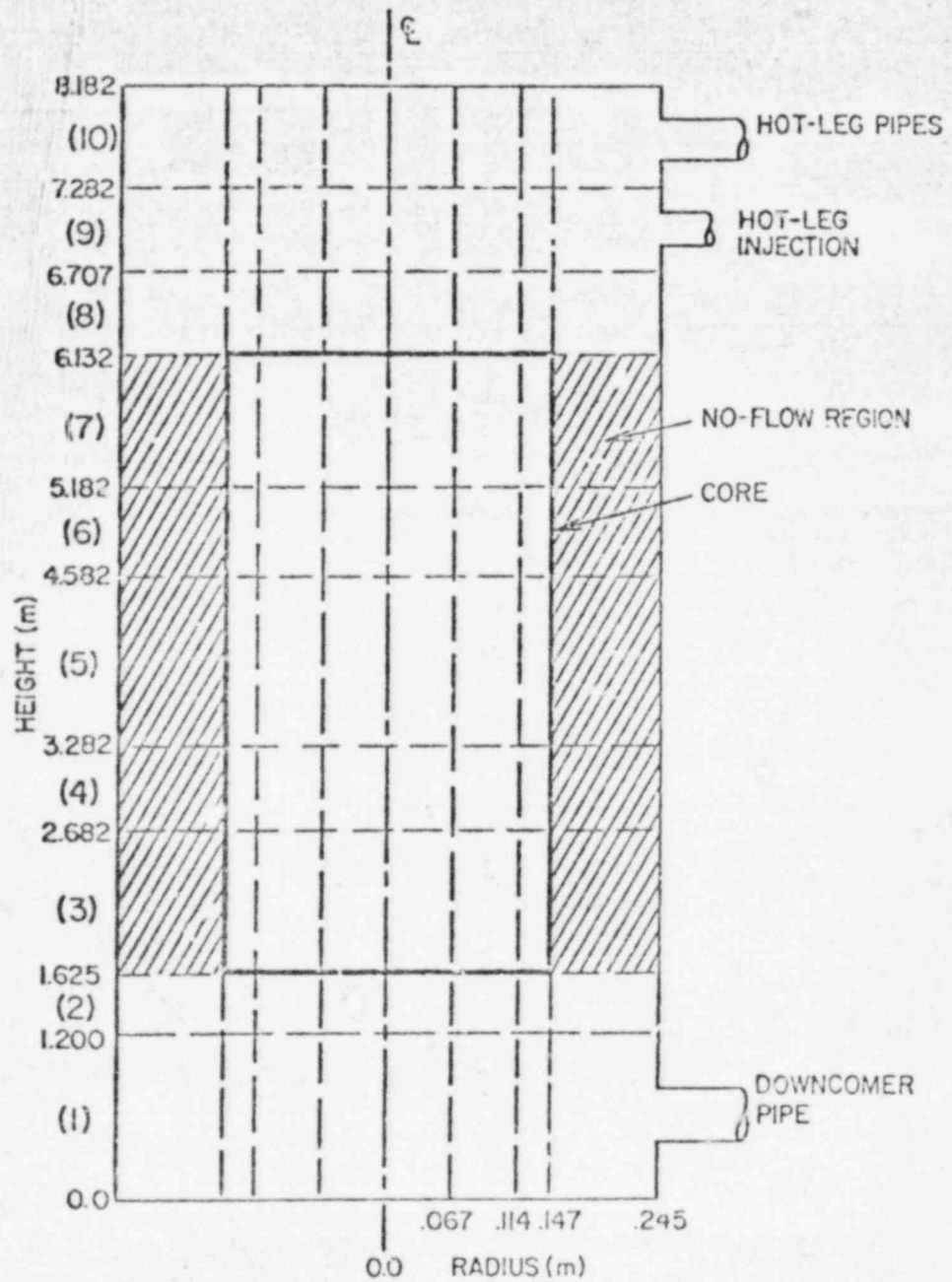
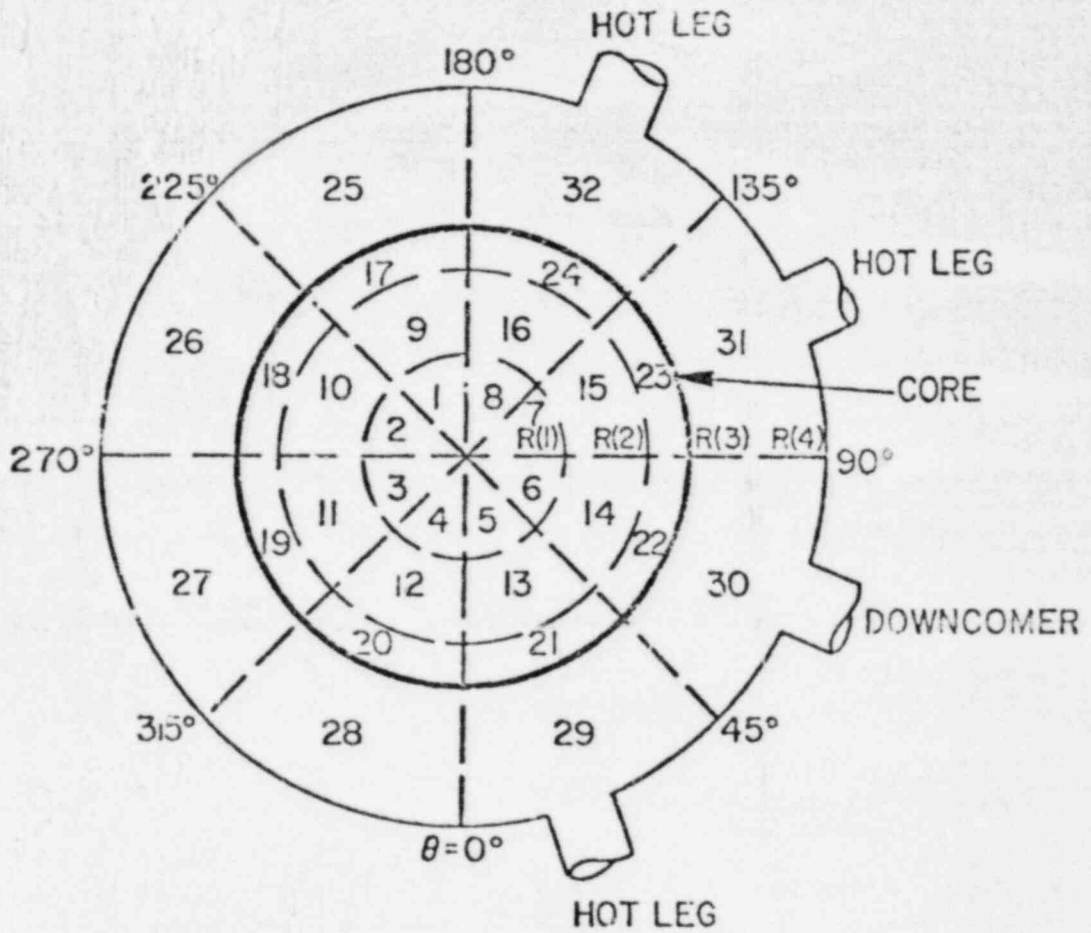


Fig. 14.  
TRAC noding for PKL vessel (side view).



$R(1) = 0.067 \text{ m}$   
 $R(2) = 0.114 \text{ m}$   
 $R(3) = 0.147 \text{ m}$   
 $R(4) = 0.245 \text{ m}$

Fig. 15.  
TRAC noding for PKL vessel (top view).

cross-hatched area shown in Fig. 14 is a no-flow region which, in the real system, is blocked off by metal plates. As can be seen from Figs. 14 and 15, there are 8 angular segments, 4 radial rings, and 10 axial levels totalling 320 TRAC mesh cells. In addition, five fine-mesh cells per coarse-mesh are included in the noding for the reflood heat transfer calculation. As shown in Fig. 14, the hot-leg injection pipes enter at the same angular locations as the hot legs themselves but at one axial level lower than the hot legs.

As mentioned previously, the calculation is a hot-leg break beginning with an all vapor system at a pressure of  $4.2 \times 10^5$  Pa. The power curve employed is 1.2 times the ANS standard decay heat curve.<sup>22</sup> Initial vapor temperatures are at saturation (417.4 K) and the initial fuel rod temperatures are shown in Fig. 16. At time = 0.0 s, the hot-and cold-leg injection systems begin to operate with the hot-leg ECC liquid entering at an initial temperature of 308 K and the cold-leg ECC liquid at 400 K. This was done to separate the effects of the subcooled hot-leg injection. For this demonstration problem the ECC systems were modeled by constant pressure breaks at  $6.2 \times 10^5$  Pa. Because of a lack of detailed experimental information, exact ECC flow rates were not available. The  $2 \times 10^5$  Pa pressure differential forces the ECC water in at much higher velocities than were present in the actual test.

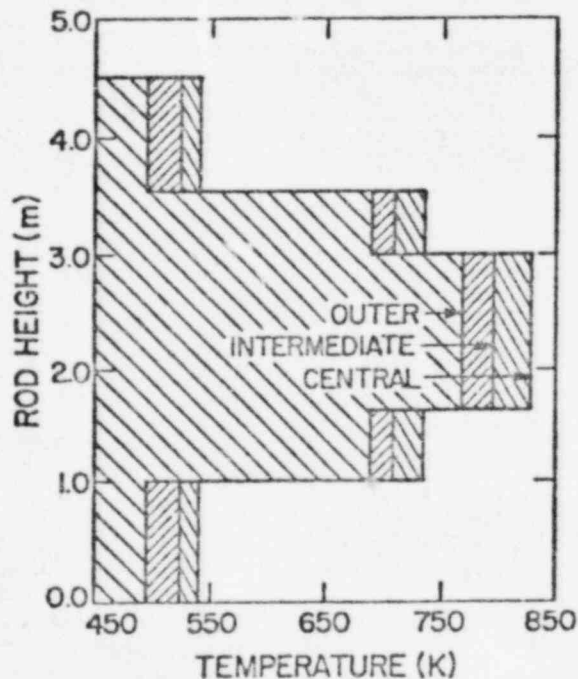


Fig. 16.  
PKL initial fuel rod temperatures.

Thus, the sequence of events, such as pool formation and lower plenum filling, is accelerated, compared to a normal test.

Since qualitative, rather than quantitative, trends were desired and since this particular calculation does not match an actual test, the results are displayed in a semiquantitative manner. Referring back to Figs. 14 and 15, the important parameters that demonstrate the phenomena mentioned above include time-dependent void fractions and quench front positions for cuts in the  $r, z$  plane directly across the hot leg (double-loop leg) entering at Cell 29. The time-dependent behavior in the  $r, z$  plane across from the other hot legs is similar.

Figure 17 shows void fractions (four different shade regions) and quench front positions (lines in the core) for mesh-cell segments 29, 21, 13, 5, 1, 9, 17, and 25 in the  $r, z$  plane at 1.5 s after the transient has begun. At this time, a small pool on the UCSP (axial level 8) has begun to form (the void fractions are between 0.75 and 0.0). A quench front has formed on the rod in segment 21 because of the low initial temperatures for the outside rods. At this point in time, there is between 0 and 25% liquid in this cell so that immediate quenching can occur. Figure 18 shows the same plane at 5.0 s after the beginning of the transient. At this point in time, the pool on the UCSP has spread to all the segments shown and liquid has begun to penetrate into the core. Thus, all of the rods in the segments shown have formed falling films (quench fronts), while the two outer rods have formed both top and bottom quench fronts. Again, even a small amount of liquid (between 0 and 25%) is enough to quench the lower, colder portions of the outside rods. At the same point in time the cold-leg ECC water has also begun to enter the vessel from the simulated downcomer.

Figures 19 and 20 show the middle and end stages of this particular calculation. Figure 19 shows the void fractions and quench front positions at 10.0 s into the calculation. As can be seen, the lower plenum has begun to fill and some of the hot- and cold-leg ECC water has started to quench all the rods on the bottom. Finally, Fig. 20 shows the results at the end of the calculation (25.0 s). At this point, all of the bottom and top quench fronts have moved to the next coarse axial level and the core is beginning to fill with liquid. In addition, a fairly stable pool has formed on the UCSP. The calculation was stopped at 25.0 s because it was felt that the important physical

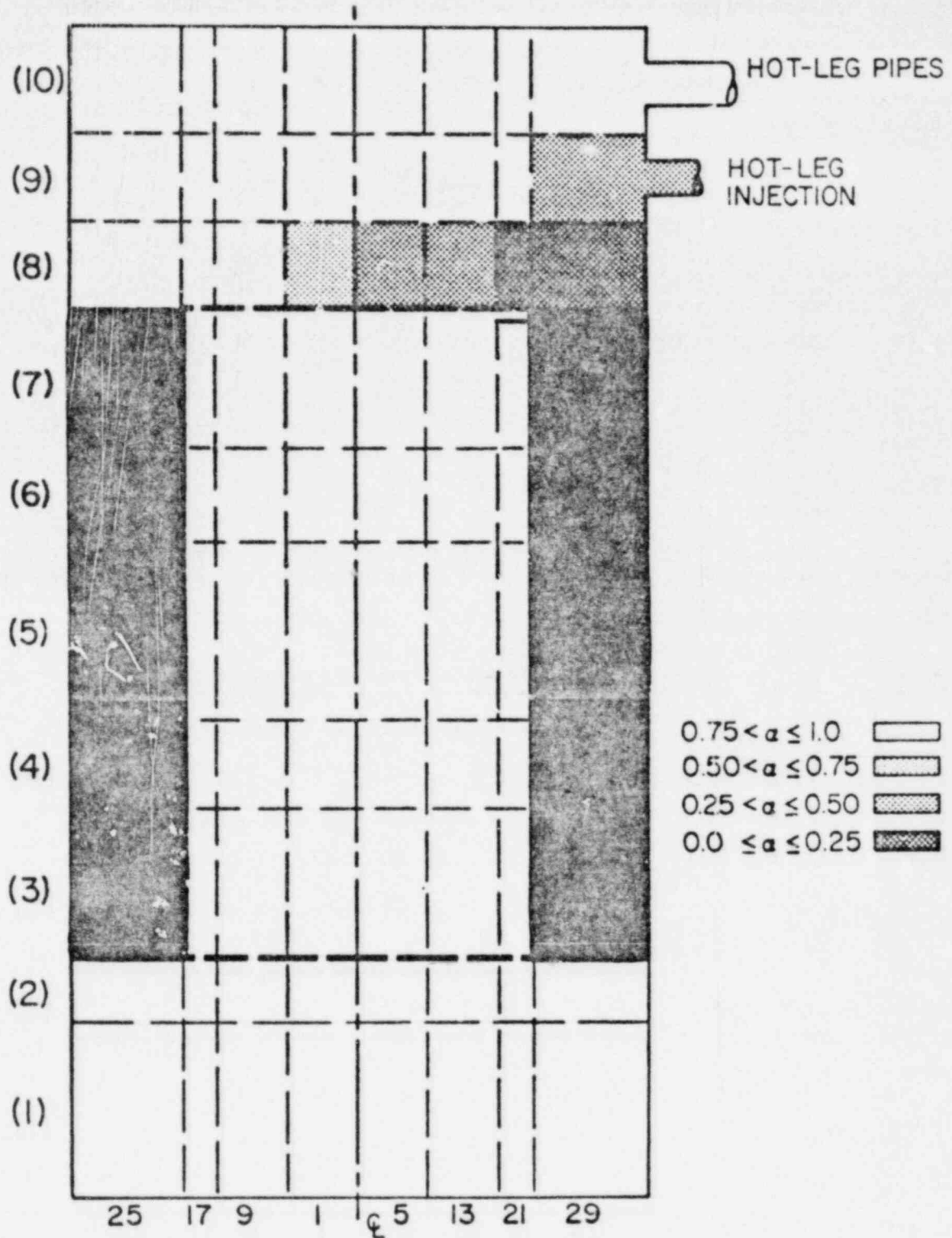


Fig. 17.  
PKL vapor volume fractions and quench front positions at  $t = 1.5$  s.

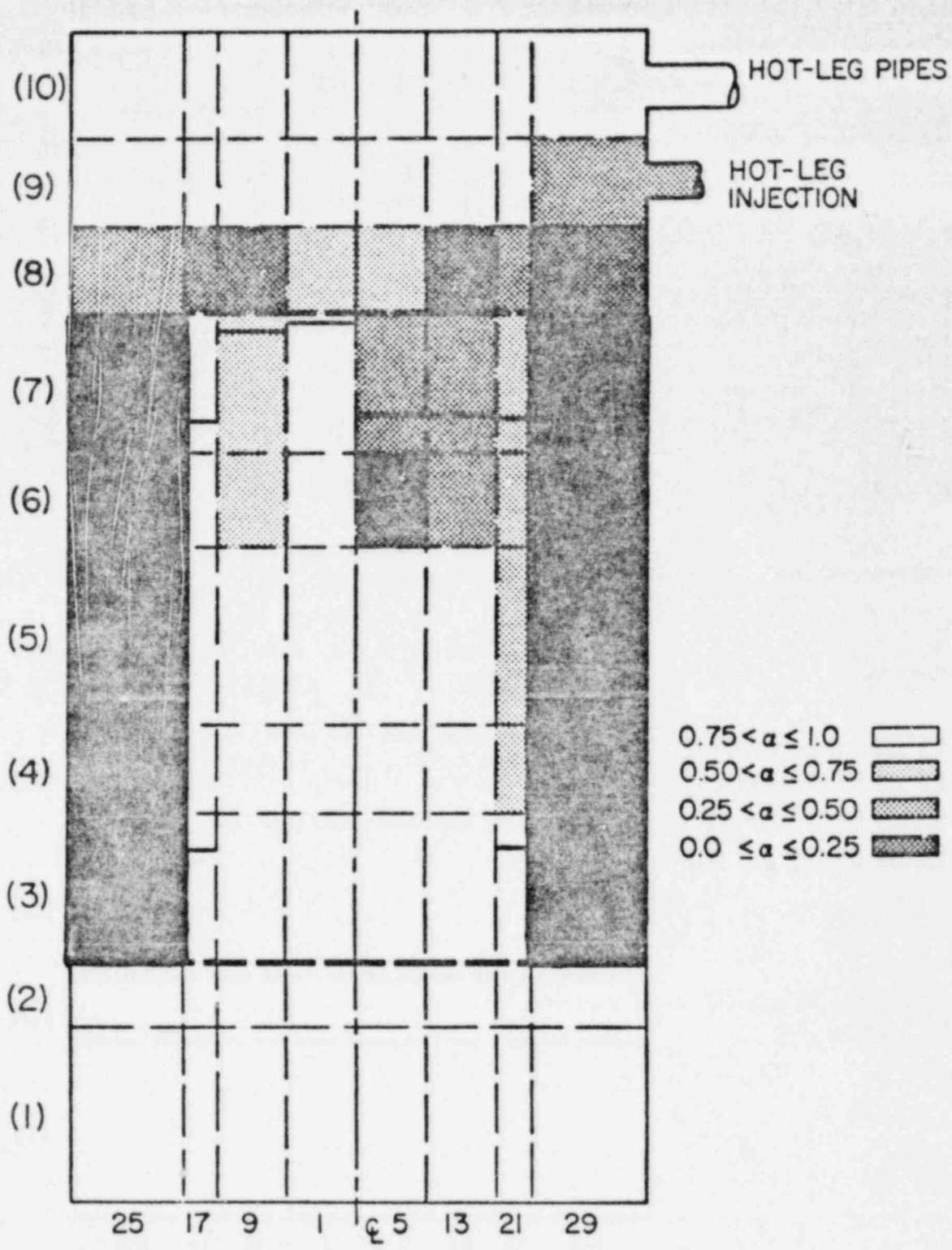


Fig. 18.  
 PKL vapor volume fractions and quench front positions at  $t = 5$  s.

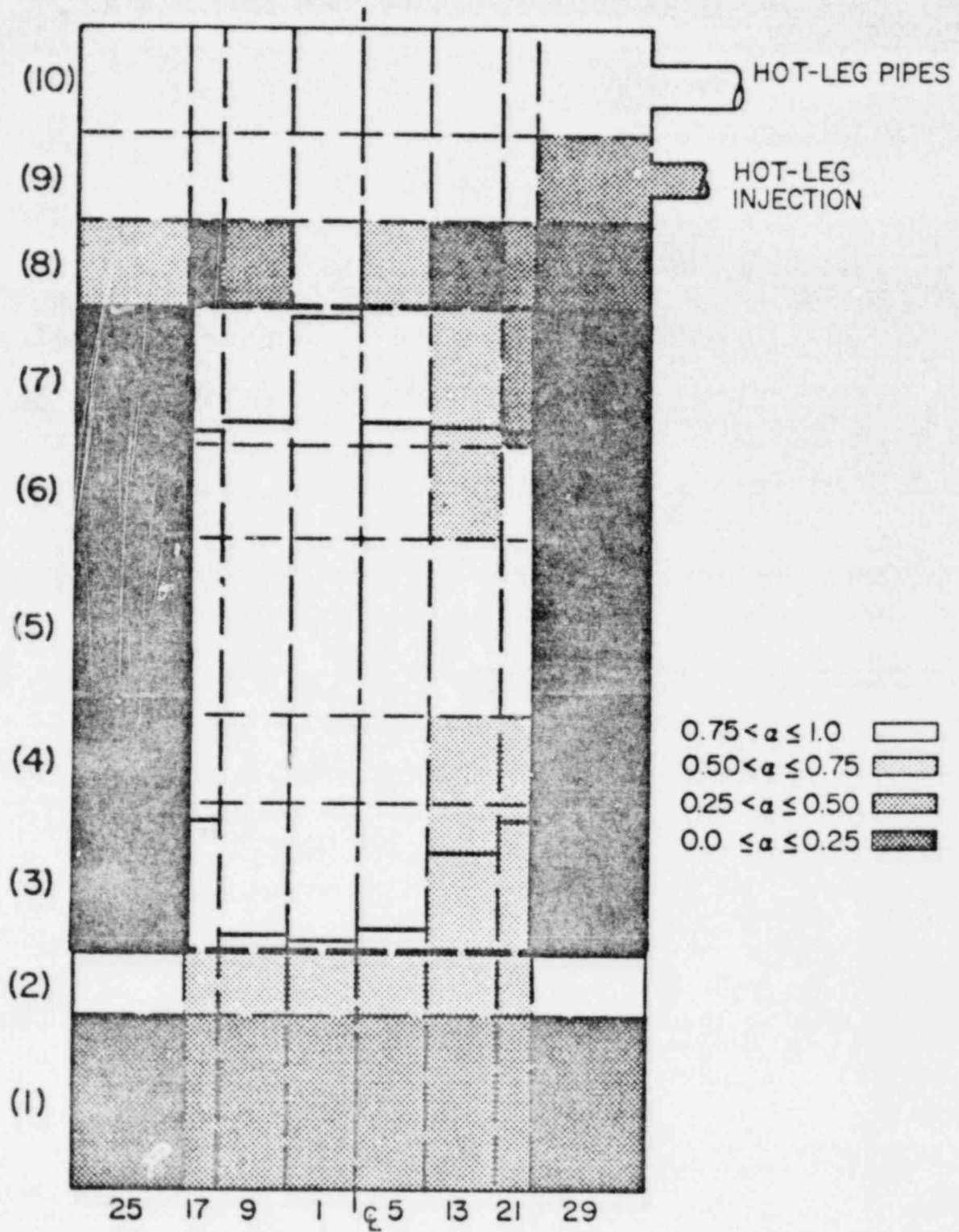


Fig. 19.  
PKL vapor volume fractions and quench front positions at  $t = 10$  s.

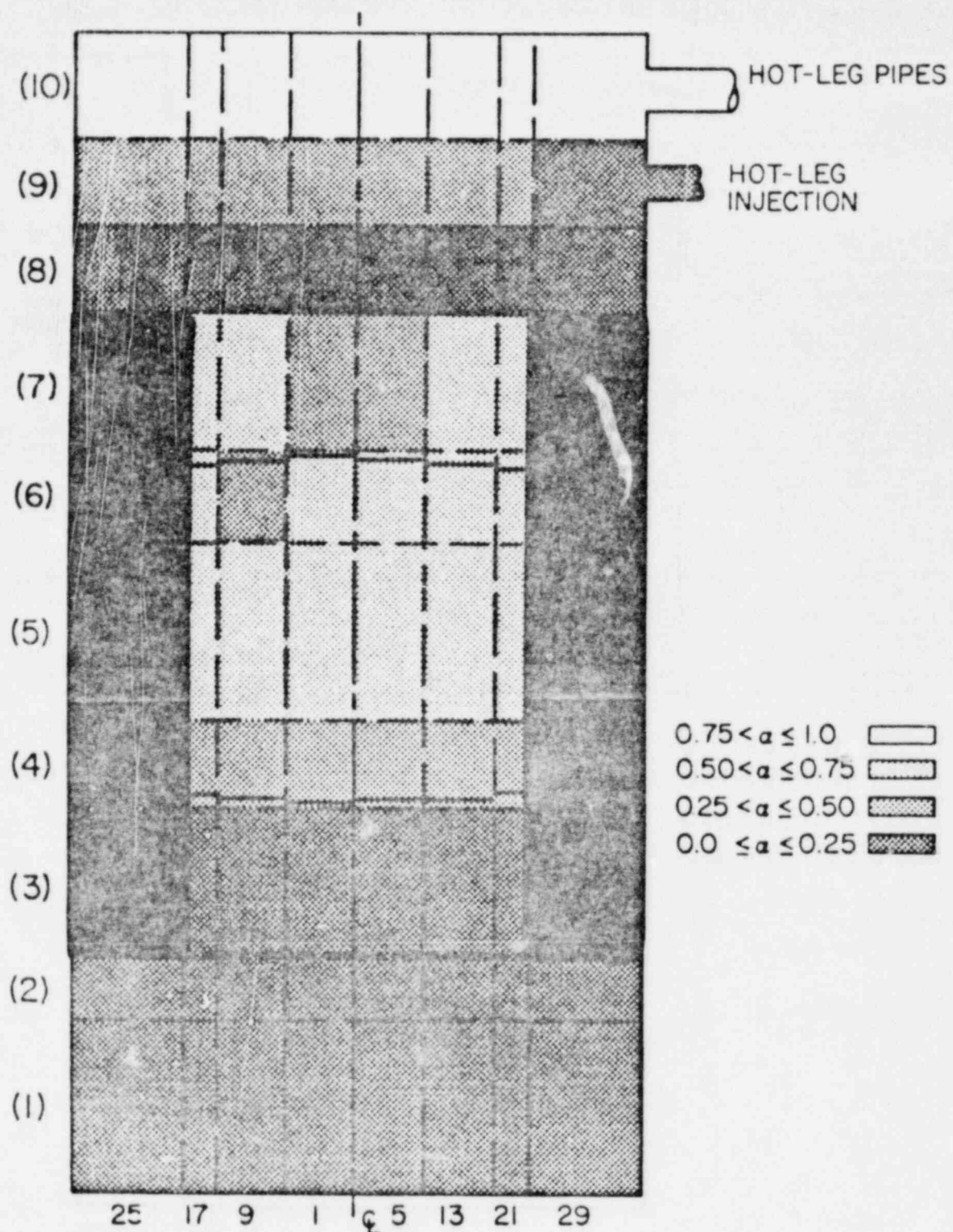


Fig. 20.  
PKL vapor volume fractions and quench front positions at  $t = 25$  s.

phenomenon mentioned previously had been adequately demonstrated. This problem has served to demonstrate some of TRAC's capabilities in preparation for more detailed posttest analyses.

## 2. U.S. PWR TRAC Model and Steady-State Calculation

(P. B. Bleiweis and J. R. Ireland, Q-6)

A typical U.S. four-loop PWR design, which combines features of a variety of different Westinghouse PWR designs,<sup>23-26</sup> was set up during the past quarter. Figure 21 shows a schematic of the loop and vessel arrangement used to model the PWR. Shown in this figure is the loop that contains the pressurizer; another loop, which represents two of the other typical PWR loops (these two loops are modeled separately in the actual TRAC calculation); and a third loop, which represents the broken loop. Also shown in the figure are junction numbers (circled numbers) and component numbers (numbers in squares). There are a total of 42 components and 45 junctions. As can be seen from Fig. 21, each of the three intact cold legs includes a tee connected to a FILL which model both the HPIS and LPIS. These legs also include a tee connected to a valve and an accumulator. There are no ECC systems included in the broken cold leg because it was assumed this system was not operational and would not significantly affect the transient.

Almost all of the dimensions for the pipes and tees in each of the loops were obtained from the RELAP input<sup>27</sup> for the BE/EM study.<sup>25</sup> Figure 22 shows the noding for the three unbroken cold legs from the vessel to the steam generators, including the ECC systems. Most of the cells in the pipes and tees are on the order of 1-2 m long, except where geometric considerations forced the use of smaller cells. The HPIS and LPIS are combined into one injection tee connected to a FILL module on each of the three unbroken cold legs. The actual HPIS and LPIS flow rates, which also were obtained from the BE/EM study, are combined through this tee when these two systems are actuated by trips during the transient. As can be seen from Fig. 22, the accumulators are connected to a valve that is tripped open when the valve pressure on the loop side decreases below  $4.08 \times 10^6$  Pa. The pump characteristics such as speed, head, torque, and dimensions, were obtained from Ref. 25.

Figure 23 gives the dimensions and noding for the hot leg that contains the pressurizer. A tee connects the vessel to the steam generator, and the secondary side of the tee is used to model the long surge line connecting the

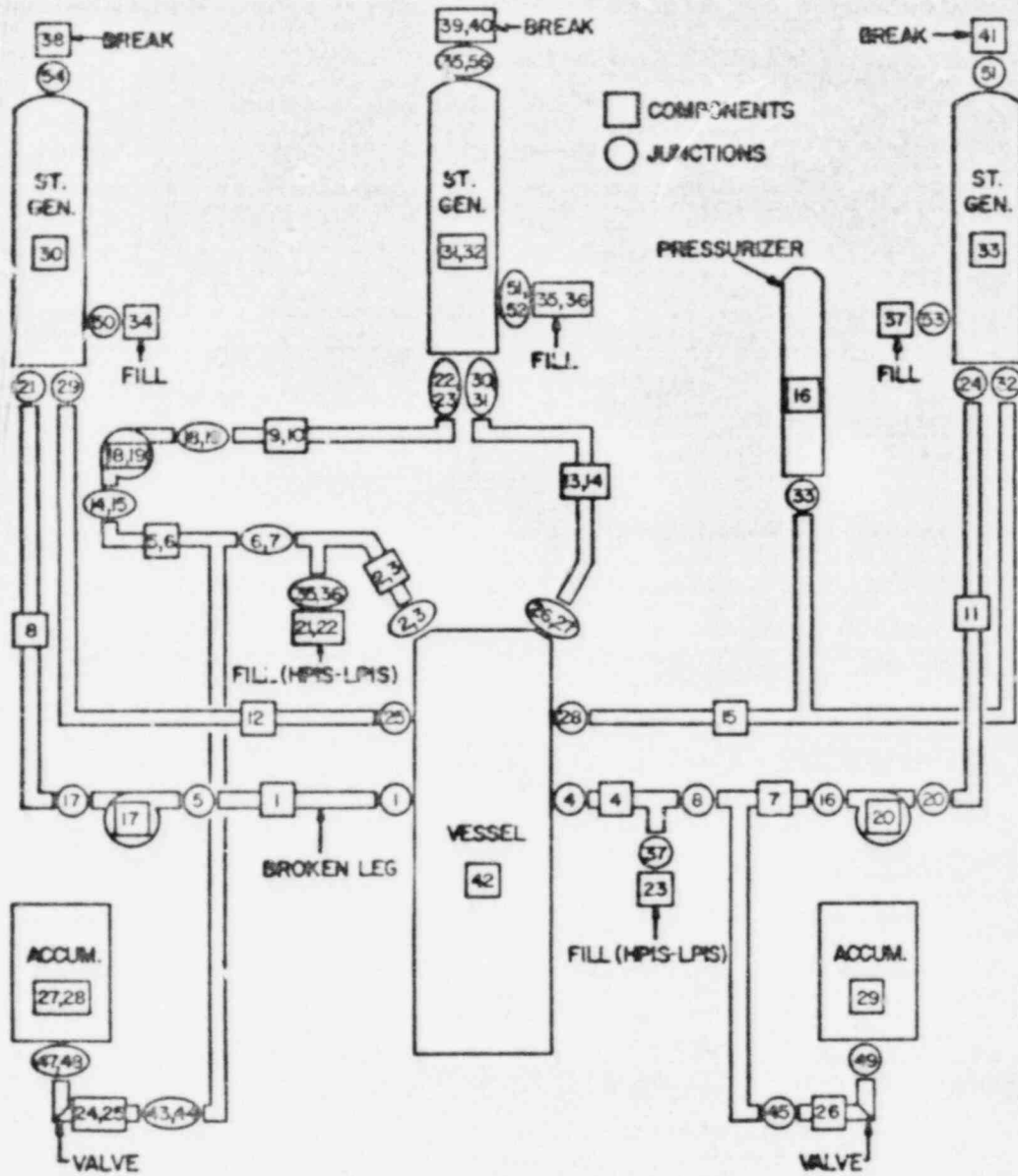


Fig. 21.  
TRAC schematic of a typical PWR.

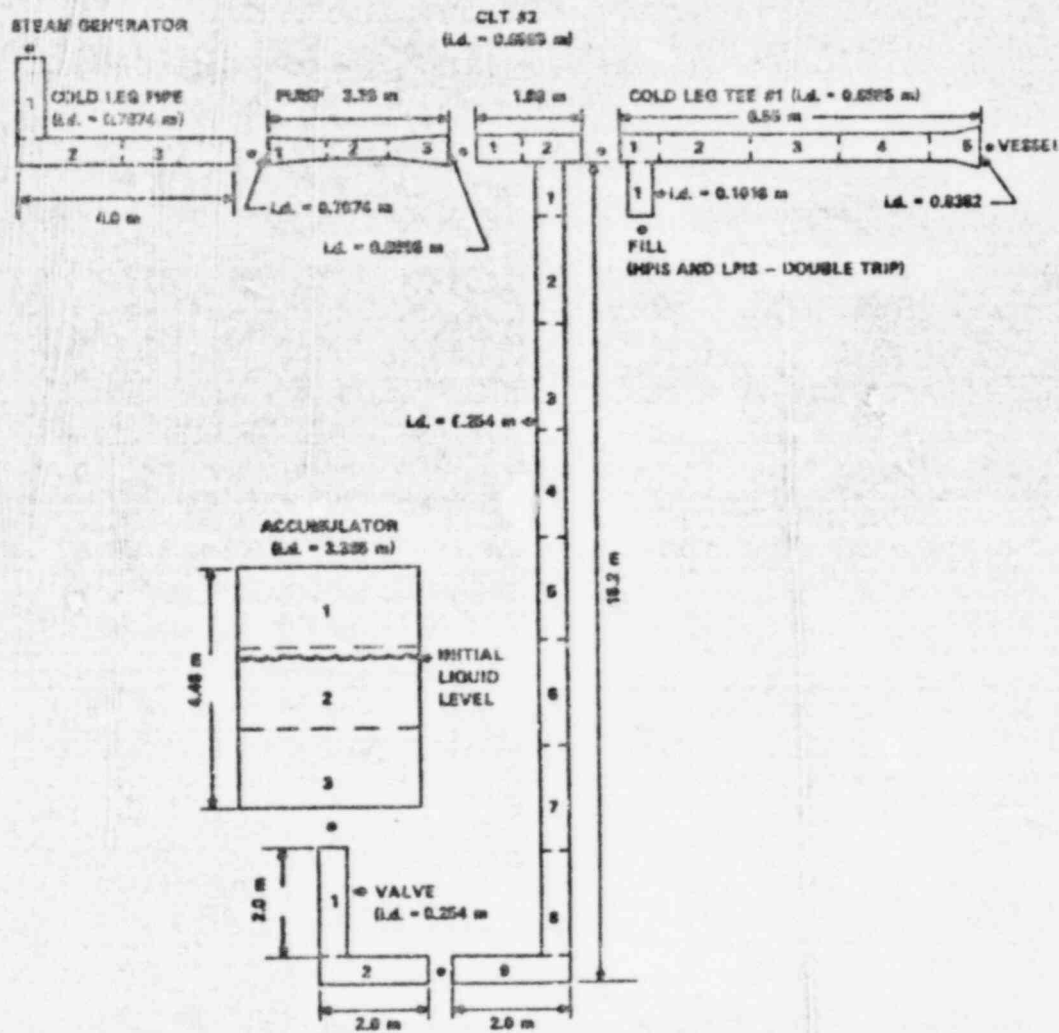


Fig. 22.  
TRAC noding for unbroken cold legs.

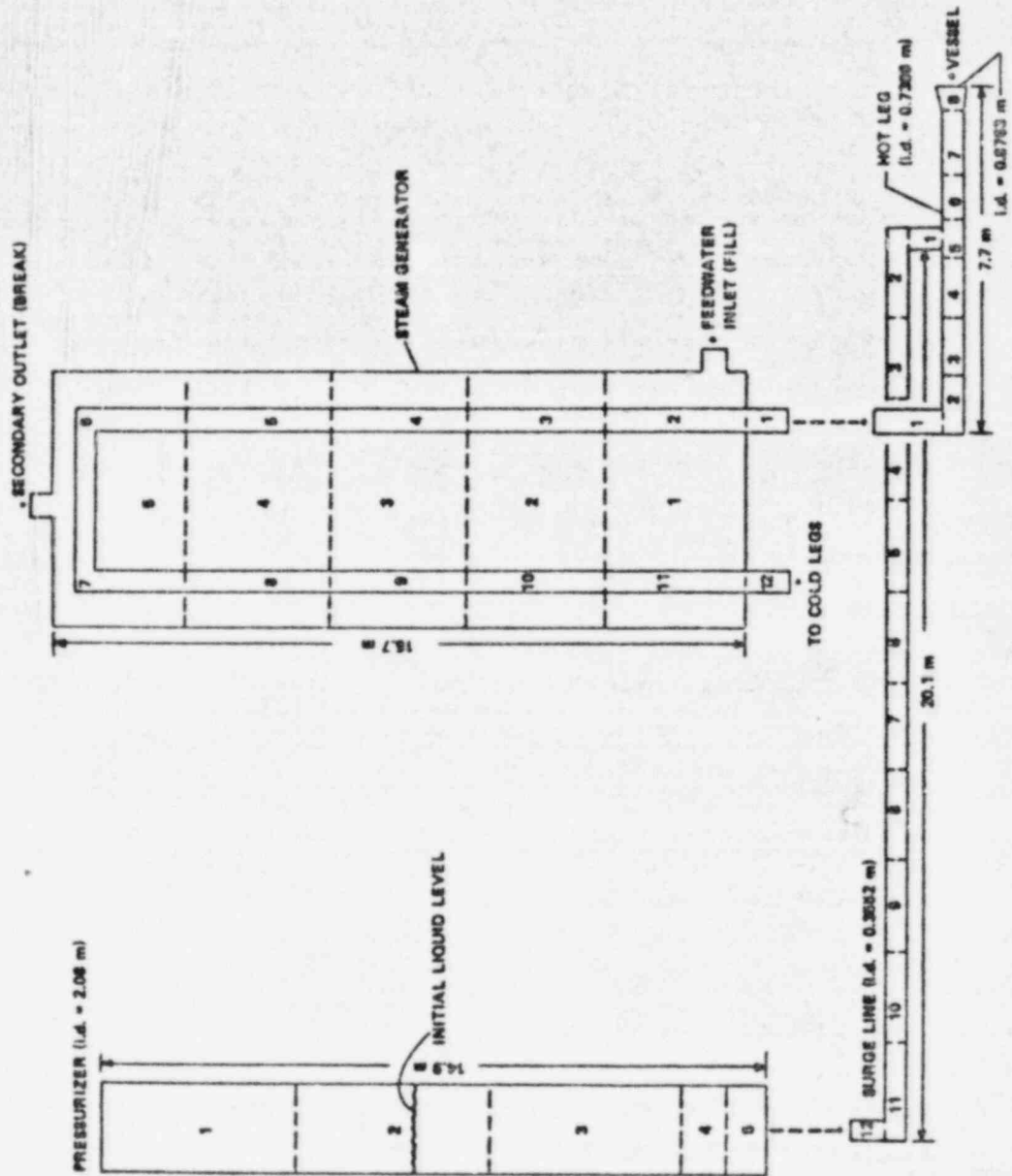


Fig. 23.  
TRAC nodding for pressurizer hot leg.

pressurizer to the hot leg. The only difference between the hot leg containing the pressurizer, shown in the figure, and the other three hot legs is that the tee is replaced with a pipe connecting the vessel to the steam generators.

Figure 24 shows the noding for the broken cold-leg pipe and gives the noding used for the pipe during steady state and the noding that will be used after the break. During the steady-state calculation all the pipes are calculated using the semi-implicit option in TRAC.

Figure 25 presents the noding scheme used for the PWR pressure vessel and its associated internals. As can be seen, there are 8 angular, 5 radial, and 10 axial nodes totalling 400 TRAC cells. This noding distribution was chosen to define the following regions in the vessel: core, upper and lower plena, upper head, barrel-baffle section, and the downcomer. The positions of the axial nodes correspond to major flow restriction locations such as the flow distributor plate, lower core support plate, and upper core support plate. The location of the azimuthal nodes accounts for the eight vessel penetrations (four hot legs and four cold legs), while the radial noding accounts for the three major radial power regions (orifice zones). The radial noding also defines the barrel-baffle region and the downcomer.

The lower plenum extends from the bottom of the first to the top of the second axial level, where the lower core support plate is located. The core axial boundaries extend from the bottom of the third to the top of the seventh axial level, where the upper core support plate is located, while the radial core boundary is located at the core shroud (the outer edge of the third radial region). The barrel-baffle region also extends from the bottom of the third to the top of the seventh axial level, and this region extends from the third to the fourth radial regions between the core shroud and core barrel. A small amount of flow area is available through the core shroud in the radial direction and at the bottom of the second level in the axial direction for the barrel-baffle region to allow for cooling and depressurization. The downcomer extends from the bottom of the first to the top of the ninth axial level and is located in the fifth radial zone between the core barrel and the vessel wall. The upper plenum extends from the top of the upper core support plate in the eighth axial level to the bottom of the upper support structure assembly located in the ninth axial level. The hot and cold legs enter at the

ninth axial level. The hot legs extend into the fourth radial region, while the cold legs penetrate the fifth radial region only and feed directly into the downcomer inlet. Finally, the upper head of the pressure vessel is located in the tenth axial level between the top of the upper support structure assembly and the top of the vessel.

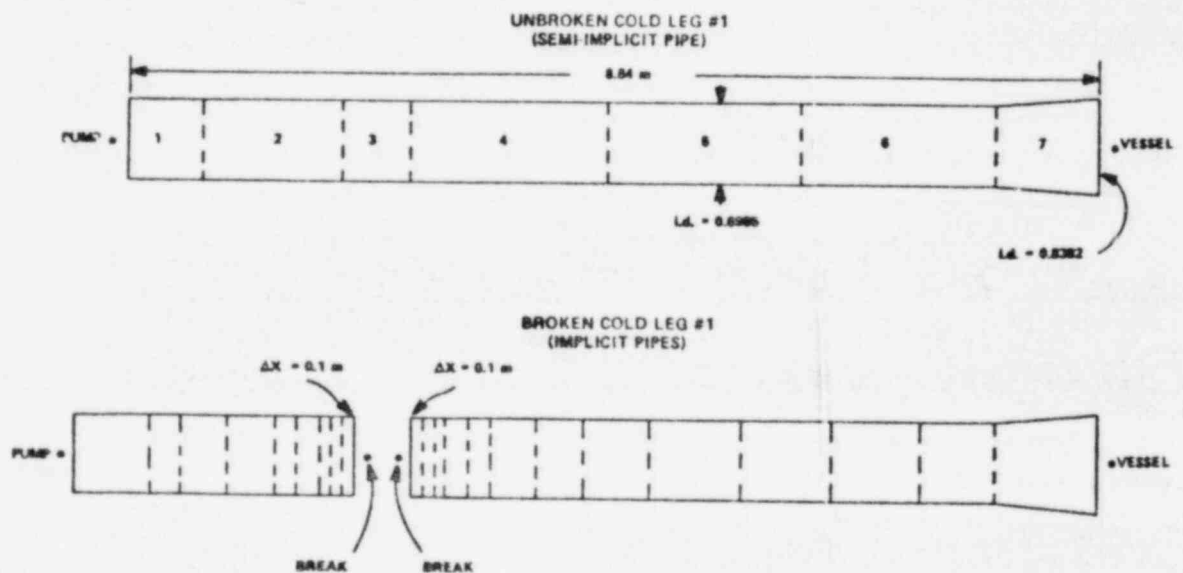


Fig. 24.  
TRAC noding for broken cold leg.

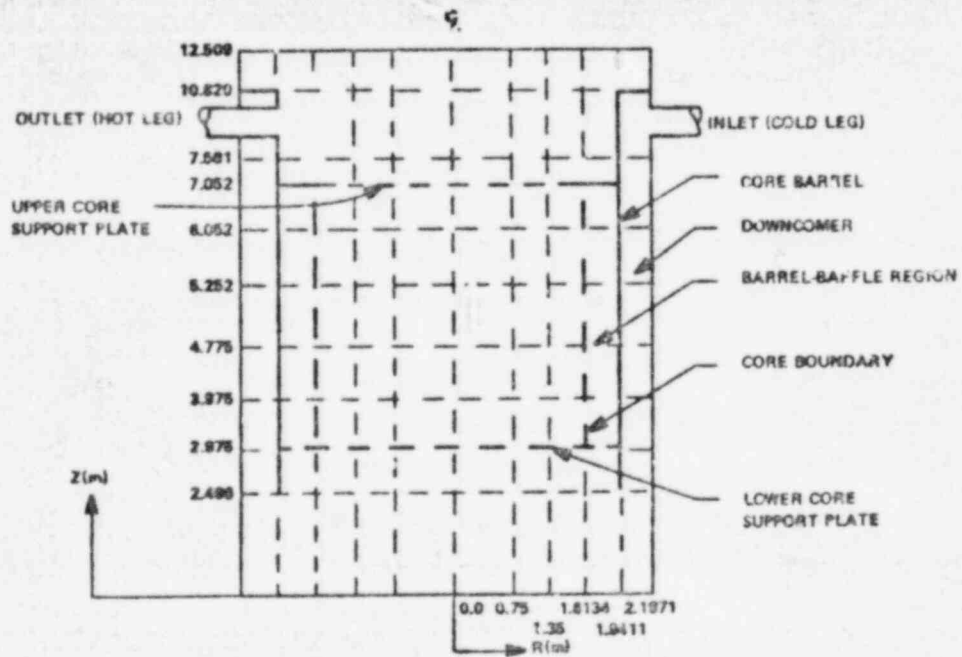
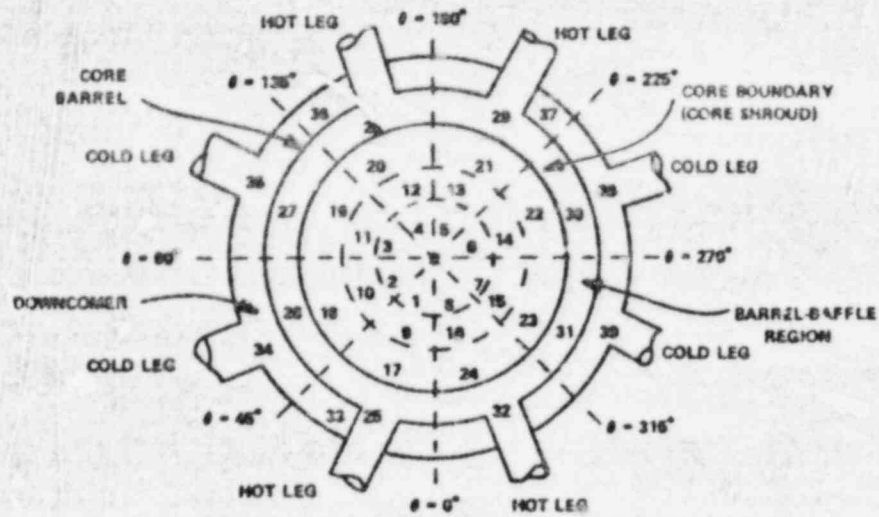


Fig. 25.  
TRAC noding for pressure vessel.

Based on the geometry and noding described above, a steady-state calculation was performed using the generalized steady-state option in TRAC. The calculation was run to 140 s of reactor steady-state time. All of the initial velocities in the input were set to zero. Until the pumps reach full speed, the reactor power is also internally zeroed to prevent boiling in the core. At approximately 17 s, the velocities in the system have almost reached a zero-power steady state and the power is turned on. It thus takes approximately another 120 s before all the temperatures, velocities, and pressures converge to a steady state.

Figures 26 through 31 show some representative steady-state results for velocities, pressures, and temperatures. Figure 26 shows the mixture velocity time histories for the four cold legs at the cells connecting to the vessel. Figure 27 shows the velocities for the four hot legs at the vessel junctions and the pressurizer that is connected to hot leg #4 (HL #4). Note that the

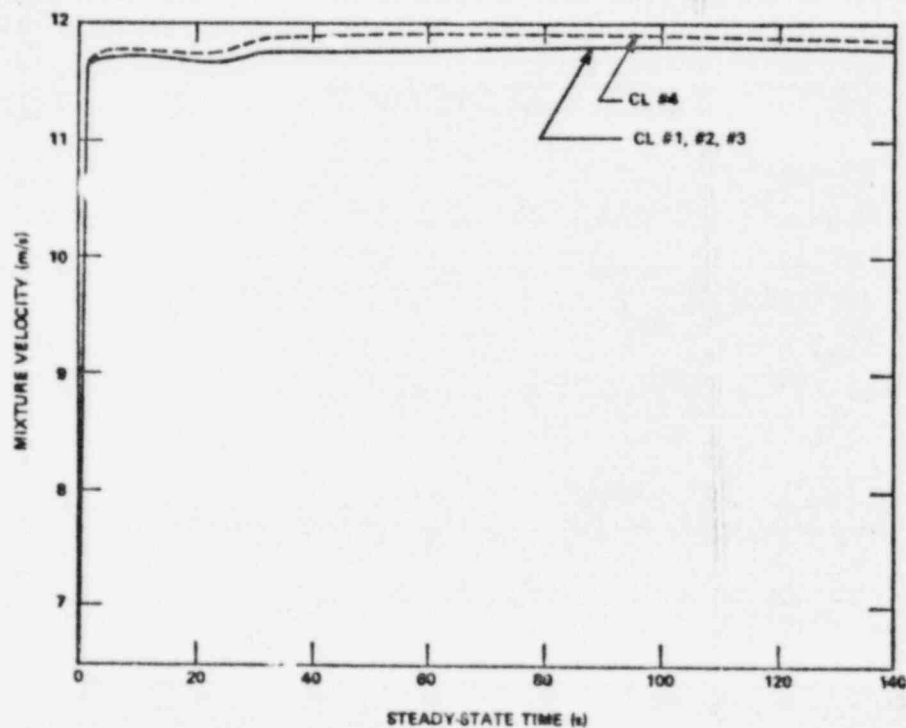


Fig. 26.  
Cold-leg mixture velocities at vessel entrance.

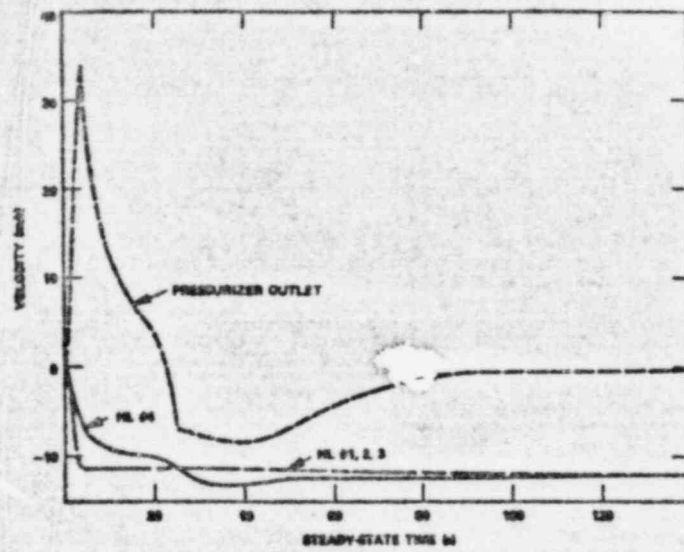


Fig. 27.  
Hot-leg and pressurizer velocities.

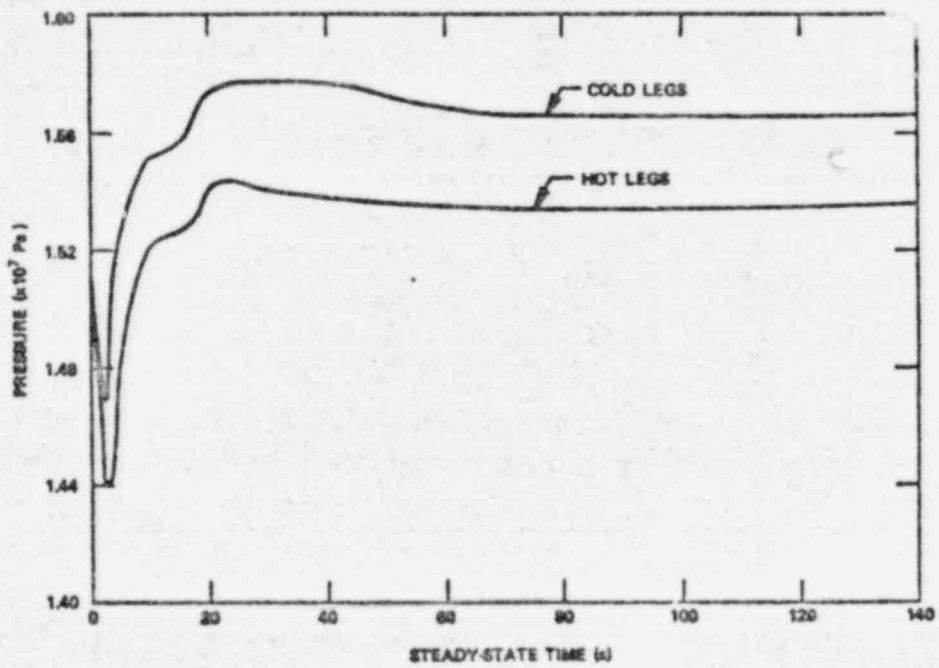


Fig. 28.  
Cold- and hot-leg pressures at vessel.

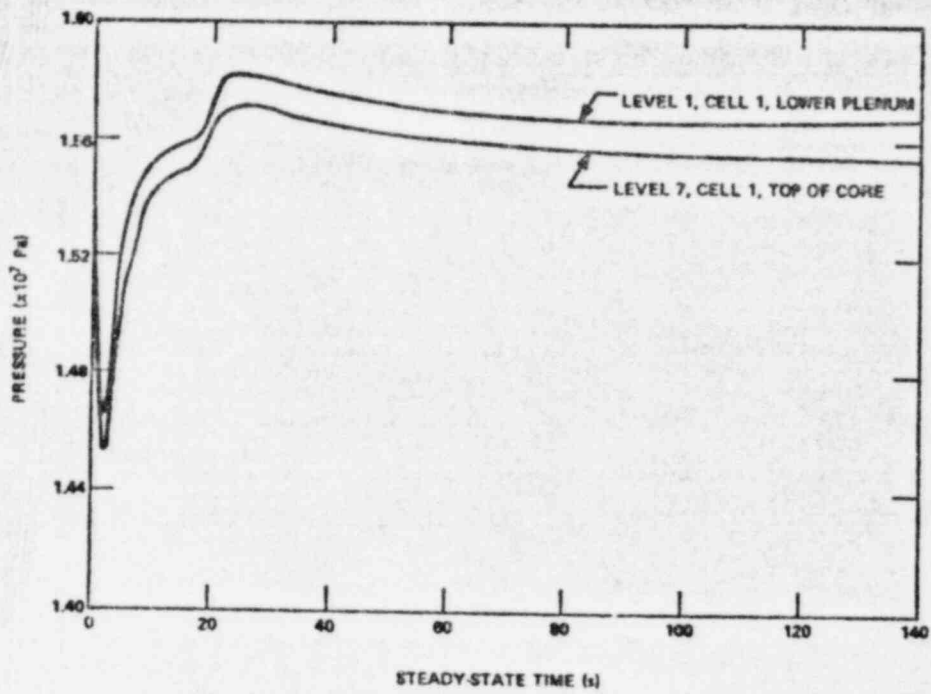


Fig. 29.  
Pressure in vessel.

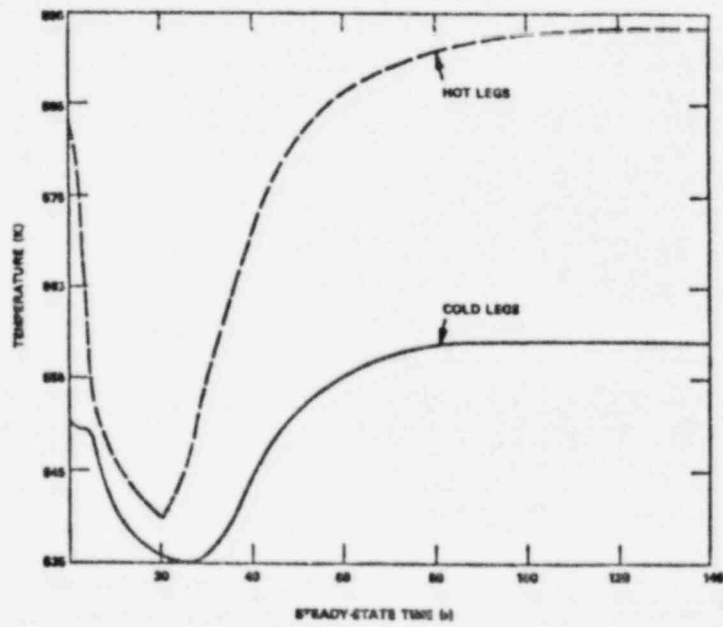


Fig. 30.  
Steady-state cold- and hot-leg temperatures.

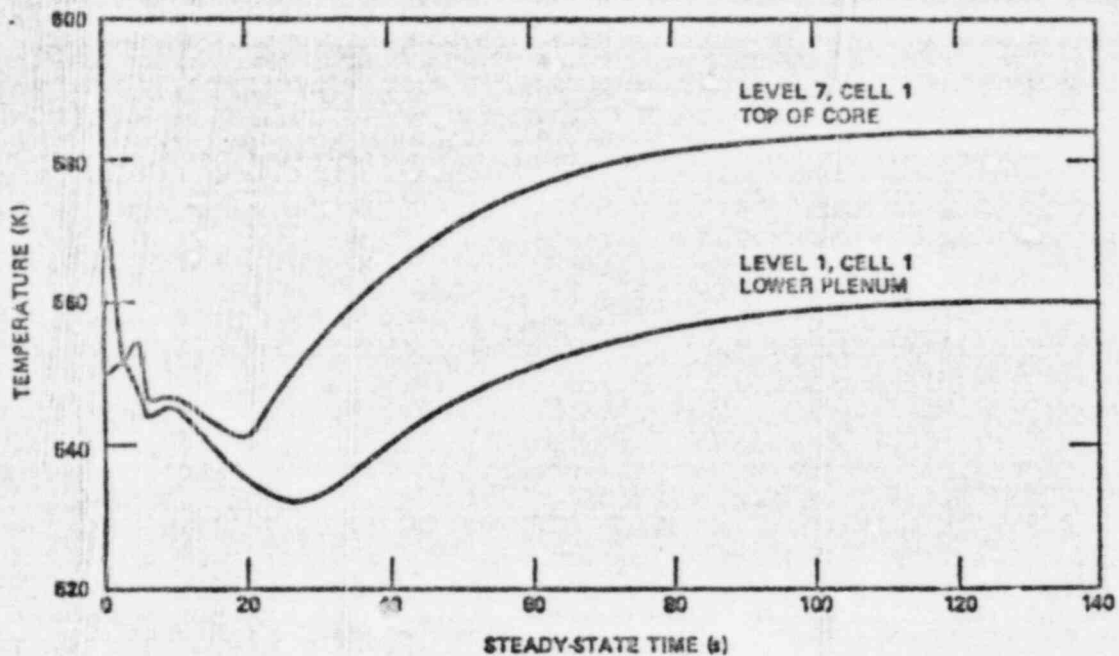


Fig. 31.  
Liquid temperature in vessel.

pressurizer is treated simply as a constant pressure break during the steady-state calculation to prevent it from emptying. Figures 28 and 29 show the steady-state pressure time histories for the hot- and cold-leg cells at the vessel junctions, and for two axial locations in the vessel. (at the same  $r$  and  $\theta$  locations), respectively. Figures 30 and 31 show the average hot- and cold-leg temperatures at the vessel junctions and two vessel locations, respectively.

As can be seen from the velocity histories, the cold-leg velocities essentially converge to a steady state within 60 s. It takes longer for HL #4 because the pressurizer is connected to it. Since the initial condition guesses for the system were only rough estimates, it takes the pressurizer about 100 s to converge to a zero-discharge velocity. During the first 5 s, the pressurizer empties rapidly into HL #4 to make up for the zero initial velocity condition input to the code. After a zero-power velocity is achieved in the system, the pressurizer velocity decreases until a zero-discharge velocity is reached.

From the pressure histories in Figs. 28 and 29, we see that the steady-state pressures take 60-80 s to converge. The cold legs have a higher steady-state pressure than the hot legs due to the pressure drop through the core. The core pressure drop is shown in Fig. 29.

From Figs. 30 and 31, it can be seen that initially the system fluid temperatures decrease, since the power is zero, but after the power is turned on they increase and eventually converge to their steady-state values. The steady-state  $\Delta T$  of about 33 K is the expected design value, and the other steady-state results are quite reasonable.

### 3. Preliminary Noding of the INEL Air-Water Injection Tests

(D. Dobranich, Q-6)

The INEL air-water injection tests will enable a preliminary investigation of some of the important phenomena and flow characteristics in the region above the upper core support plate during the reflood phase of a PWR LOCA. These tests are directly related to the proposed German upper plenum experiments,<sup>2</sup> and posttest analyses of these tests are being performed. Using air in place of steam in the test eliminates condensation. This allows the phenomenon of frothing (or foaming) to be observed exclusively in order to determine its importance as a mechanism for hot-leg carryout. The mechanisms of entrainment and fallback will also be observed.

The test vessel is designed to allow a flow area for one Westinghouse 15 x 15 fuel bundle with sufficient upper plenum space to allow for scaled upper plenum internals. A preliminary TRAC noding scheme for this vessel is shown in Fig. 32. The vessel is represented by 7 axial, 2 radial, and 2 angular segments. A hot leg is connected to the vessel at axial level 5. The counter-current flood plate, spacer, and core support plate are represented by an area restriction in axial level 4. A short section of simulated fuel rods is located in levels 1 and 2. In the experiment, air and water will be injected at the bottom of the vessel. At present, the appropriate air-water flow rates can be achieved by adjusting the initial values of velocity at the first axial level.

Very preliminary TRAC calculations have been performed to check out the noding. These were done with steam-water and are not representative of an actual experiment. Additional calculations will be performed after the first series of tests have been completed.

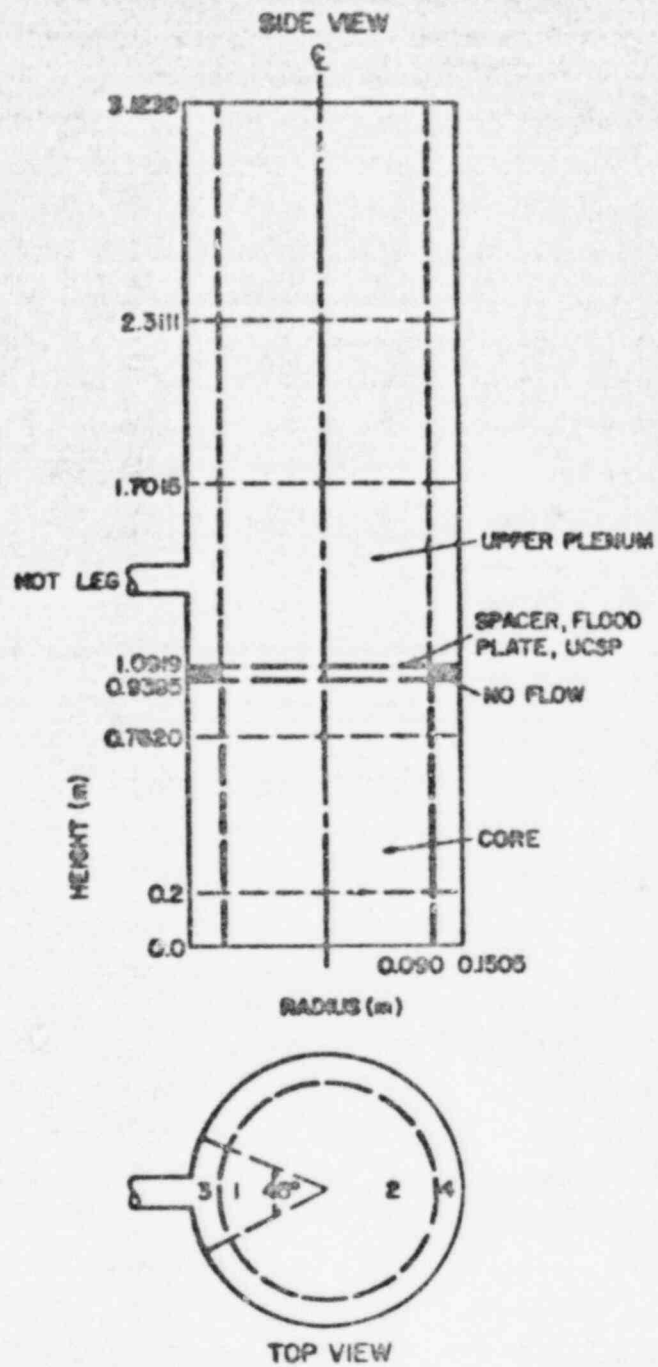


Fig. 32.  
Preliminary TRAC noding for INEL air-water injection tests.

#### 4. TRAC Noding for the Japanese Reflood Experiment

(D. Dobranich and P. B. Bleiweis, Q-6)

The loops of the 2000-rod Japanese cylindrical core reflood experiment have been noded for preliminary TRAC calculations. A preliminary noding scheme for the vessel was reported in the last quarterly report.<sup>2</sup> This noding has since been changed due to new design information and is also described below. Figure 33 is a schematic of this model, which, along with Table IV, references all the major components and their relative locations. As can be seen from the figure, the experiment and TRAC model consist of a vessel with four hot and four cold legs connected to two steam generators. Connected to all four cold legs by tees is a low-pressure injection system (represented by a fill component) and a valve controlling an accumulator. Each accumulator in the model represents one-quarter of the volume of the actual accumulator and the valves are trip-controlled by primary system pressures. A break component is connected to both ends of the broken cold leg while the remaining hot and cold legs remain intact.

Figure 34 is a noding scheme for the 2000-rod, electrically heated cylindrical vessel. The vessel consists of 10 axial segments (corresponding to instrument locations), 4 radial segments (corresponding to different heated core regions and a downcomer), and 8 angular segments (corresponding to the 8 vessel penetrations). The cold legs enter the fourth radial region feeding into the downcomer while the hot legs enter the third radial region passing through the core barrel. The downcomer extends from the second to the eighth axial segment and the core extends from the third to the sixth axial segment.

#### 5. Analysis Support for Japanese Slab Core Tests

(F. H. Harlow and A. A. Ansdn, T-3; and P. B. Bleiweis, Q-6)

The development of the SAM computer code is being carried out in the hydrodynamics group (T-3) at LASL and is described in another section of this report. This code initially will be the main computer tool used to provide design-related assistance and pretest predictions for the proposed Japanese slab core tests. Such design-related questions as downcomer geometry, upper plenum boundary conditions, and flow characteristics will be investigated as soon as the code is finished and when more detailed descriptions of the basic experimental setup are obtained.

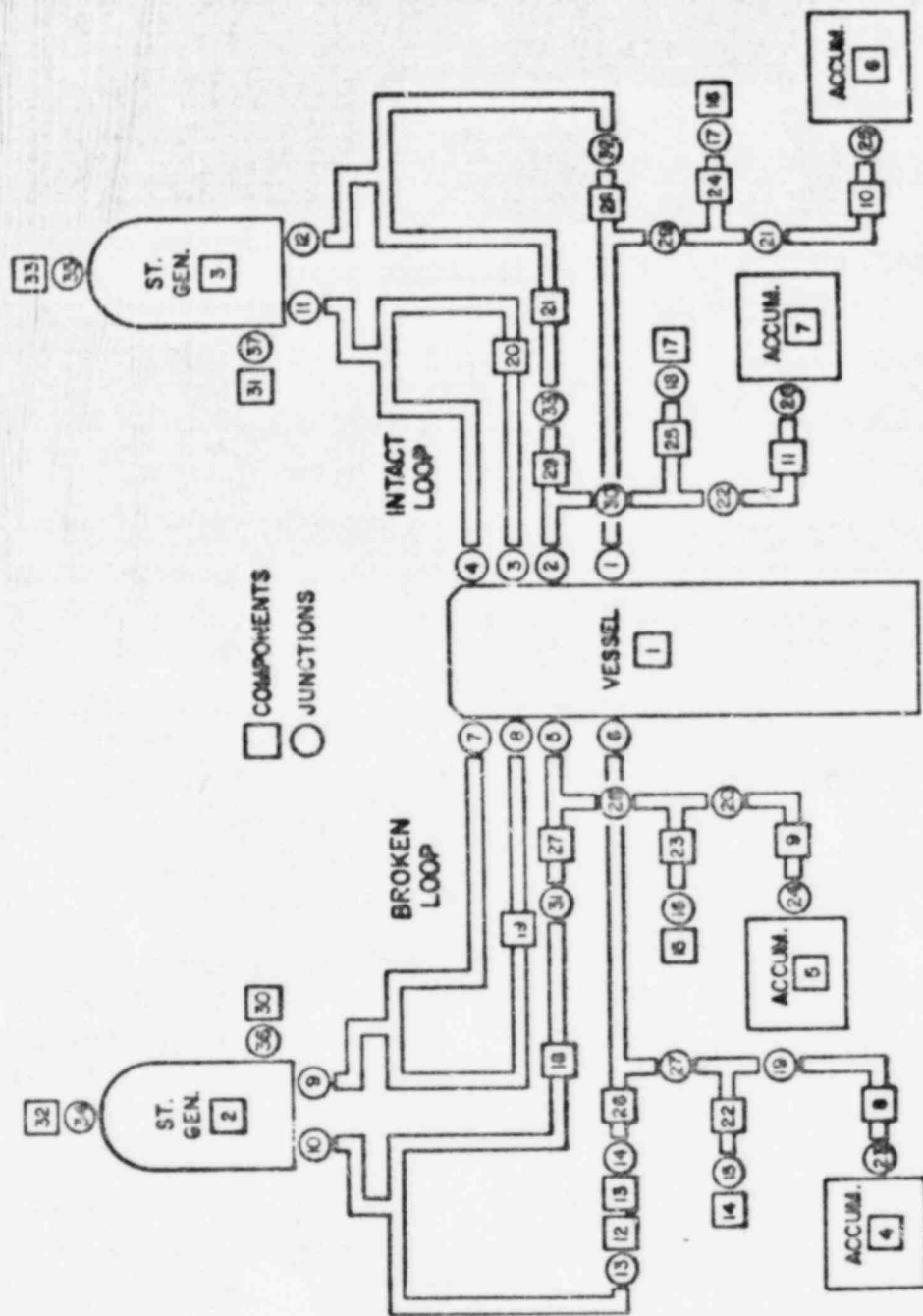


Fig. 33.  
TRAC model for Japanese reflod experiment.

TABLE IV  
 COMPONENT IDENTIFICATION FOR JAPANESE REFLOOD EXPERIMENT

<u>Component No.</u>	<u>Component Type</u>	<u>Comments</u>
1	VESSEL	320 cells
2	SGEN	10 cells primary and 5 cells secondary
3	SGEN	See above
4	ACCUM	1/4 volume
5	ACCUM	1/4 volume
6	ACCUM	1/4 volume
7	ACCUM	1/4 volume
8	VALVE	Pressure trip
9	VALVE	Pressure trip
10	VALVE	Pressure trip
11	VALVE	Pressure trip
12	BREAK	Cold leg
13	BREAK	Cold leg
14	FILL	LPIS
16	FILL	LPIS
17	FILL	LPIS
18	TEE	
19	TEE	
20	TEE	
21	TEE	
22	TEE	
23	TEE	
24	TEE	
25	TEE	
26	TEE	
27	TEE	
28	TEE	
29	TEE	

POSSIBLE CYLINDRICAL CORE NODING

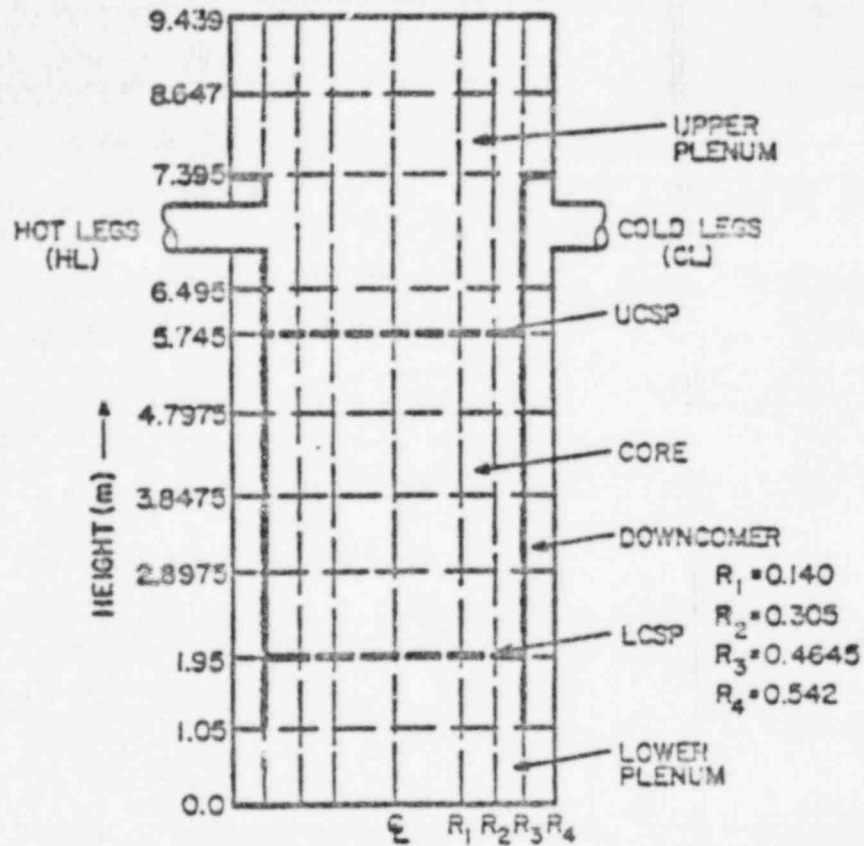
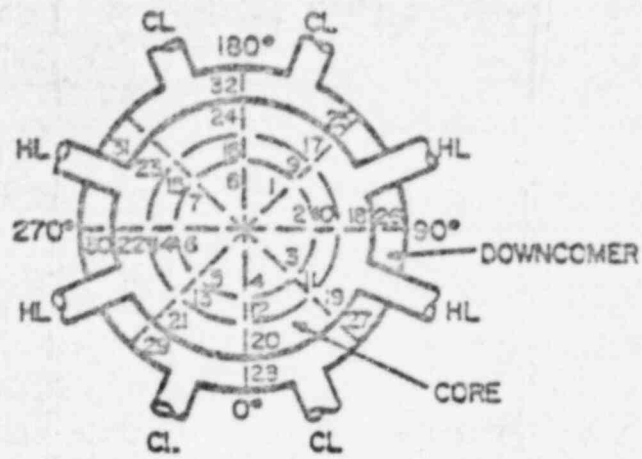


Fig. 34.  
TRAC noding for Japanese vessel.

### C. Thermal-Hydraulic Research for Reactor Safety Analysis

(T. D. Butler, T-3)

The research reported in this section addresses a wide variety of thermal-hydraulic and fluid-structure interaction problems encountered in LWR safety analysis. This quarter we focus on the progress in four areas:

1. Theoretical analysis of critical nozzle flows. This study has shown the dependence of the break flow multiplier used in one-dimensional codes on the ratio of the nozzle length to its diameter. The purpose of this effort is to ascertain a priori the value of the multiplier that is needed for a given nozzle or break geometry.
2. Development of a code to investigate slab core reflood experiments. The SAM computer code is a two-dimensional, two-fluid program that has been written to analyze the proposed Japanese reflood experiments in a slab geometry.
3. Analysis of transient steam-water flows in a PWR downcomer. The K-TIP code was used to calculate a wide range of ramped steam flow experiments for comparison with data from the Creare, Inc. 1/15-scale PWR model. The modeling parameters were the same as those determined in previous steady-state comparisons and were not changed throughout the sequence of runs. We found that the code properly predicted trends over the entire range, but showed a consistent earlier-than-measured time of delivery of the water to the lower plenum.
4. Comparison of two- and three-dimensional calculations of a fluid-structure interaction problem. The core barrel dynamics during blow-down for the HDR reactor vessel were calculated both with the 2-D SOLA-FLX code and the K-FIX (3-D, FLX) code. We found that a simple physical model enabled SOLA-FLX predictions to agree well with the more complex, fully 3-D calculation.

#### 1. The Effect of the Throat-Length-to-Throat-Diameter Ratio in Critical Nozzle Flows

(J. R. Travis, C. W. Hirt, and W. C. Rivard, T-3)

It has been demonstrated<sup>8</sup> that two-dimensional flow effects explain the need for the use of a break flow multiplier in the one-dimensional analysis<sup>28</sup> of the Semiscale Henry nozzle. Recent one- and two-dimensional calculations, when compared with data of the LOFT counterpart nozzle,<sup>29</sup> indicate that only a small, if any, break flow correction is needed. At first,

one might claim a contradiction in that the Semiscale Henry nozzle requires a break flow multiplier to bring the one-dimensional calculations into agreement with the data and the two-dimensional calculations, while the one-dimensional calculations for the LOFT counterpart nozzle do not require such a multiplier. The abrupt entrance to the throat of the LOFT nozzle seems more likely to exhibit two-dimensional effects than the entrance to the Semiscale nozzle throat, which is slowly varying in cross-sectional flow area.

In order to demonstrate the effect of entrance geometry, we ran a two-dimensional calculation of a modified Henry nozzle; i.e., the entrance to the throat was made abrupt by essentially replacing the tapered section with a constant cross section equal to that of the inlet pipe. The mass flow rate and the throat pressure for the abrupt entrance geometry was found to be approximately 2% less than the tapered entrance geometry for the same initial and boundary conditions. Therefore, this change in nozzle entrance geometry into the throat accounts for only a small percentage of the difference between the one- and two-dimensional theories. Subsequent calculations revealed that the largest effect seems to be due to the throat-length to throat-diameter ratio.

In Fig. 35, the break flow multipliers calculated from one- and two-dimensional theories are shown as a function of the throat-length-to-throat-diameter ratio for the general geometric configuration of the LOFT nozzle. Only the throat length is varied to obtain the (L/D) range indicated by the curve. For small throat lengths, such as an orifice plate,  $L/D \ll 1$ , the break flow multiplier appears to approach the value of 0.61. When the throat length is increased,  $L/D \geq 1$ , calculations indicate the break flow multiplier approaches unity. This indicates that as the throat length becomes sufficiently long, say  $L/D \geq 5$ , two-dimensional effects are no longer important and the exit flow can be approximated as being one dimensional.

An additional data point representing the Semiscale Henry nozzle is shown in the figure. The Henry nozzle has a break flow multiplier which is roughly 3% smaller than the LOFT counterpart type nozzle with the same throat L/D ratio. Because of the tapered entrance, the two-dimensional velocity distribution is slightly more pronounced at the throat, therefore reflecting a smaller break flow multiplier.

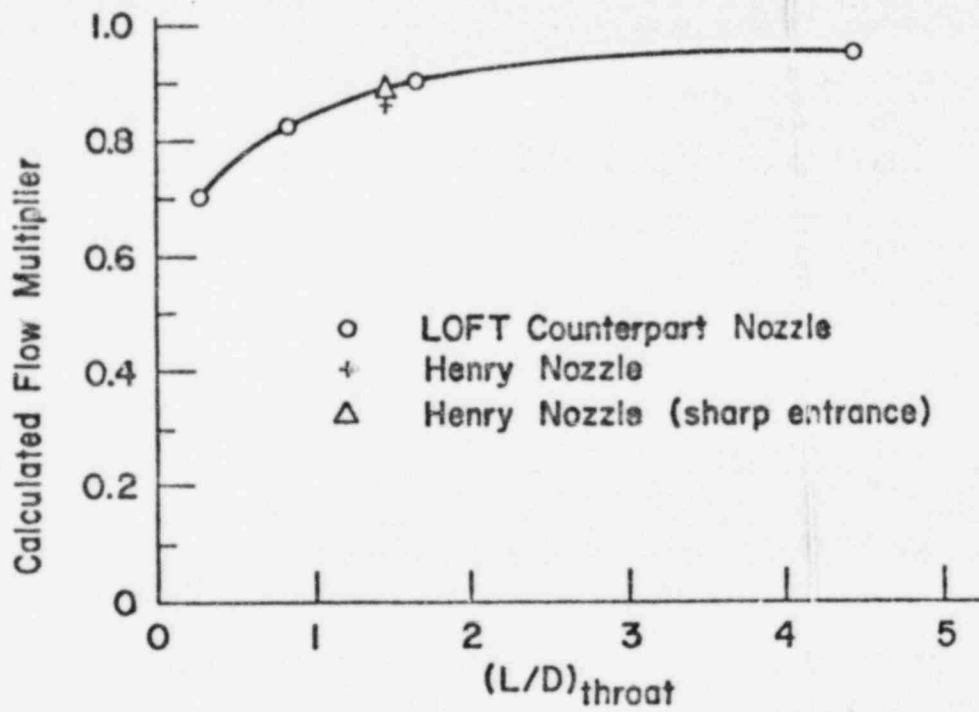
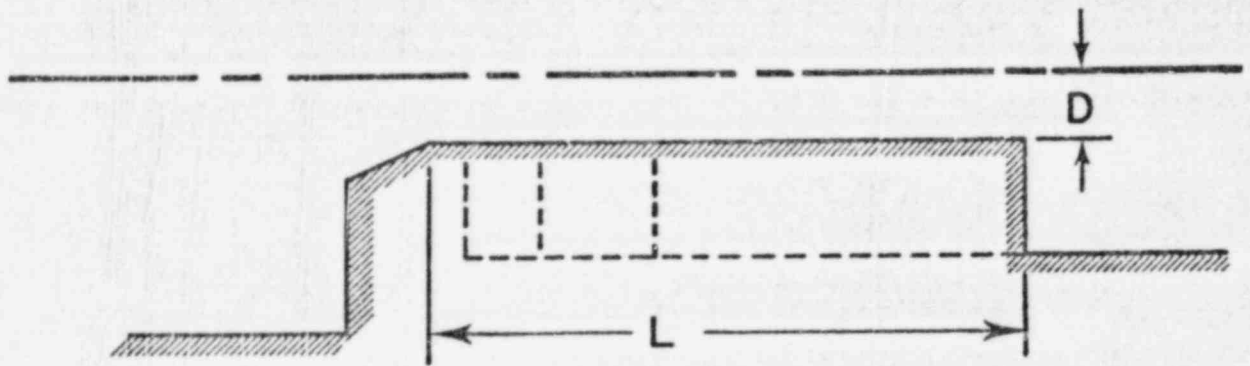


Fig. 35.  
Effect of throat-length-to-throat-diameter ratio on the  
calculated flow multiplier.

The break flow multiplier curve as shown in the figure does not represent a universal function. Sharp and rounded entrance orifice plates are clearly not described by this curve. However, other calculations, which are not reported here, show that for a variety of practical entrance and exit geometries, the corrective discharge multiplier reported in this figure is correct to within a few per cent.

## 2. Slab Vessel Reflood Calculations

(F. H. Harlow and A. A. Amsden, T-3)

The SAM computer program has been written for the numerical analysis of core reflood in a slab configuration. The calculation region can consist of four parts: downcomer, lower plenum, core, and upper plenum. In each there is a specified distribution of volume fraction attributable to structural elements, either positive (up to unity) to denote the presence of constricting structure, or negative to denote the local enlargement of slab width beyond a prescribed nominal dimension. Throughout each part, there is also a prescribed distribution of flow resistance coefficients representing the nonisotropic friction exerted by the structural elements and slab walls, and also representing the nonisotropic resistance of perforated support plates, which are otherwise usually too thin for resolution. Implicit numerical treatment of the support plate resistance allows for the representation of internal rigid walls by means of a very large value for the coefficient. The structural elements are given a specified distribution of initial temperature, which changes in the calculation as a result of a specified distribution of supplied power and the effects of heat flux to the adjacent water, the latter limited by critical heat flux considerations whenever appropriate. The dynamics, heat transfer, and phase transition calculations resemble those of the K-TIP computer program, but the heat transfer calculations are modified in SAM to account more directly for the temperature variations in the structural elements.

Typical initial conditions have the entire vessel filled with steam. As the calculation proceeds, water at a specified inlet temperature travels down the downcomer or is inserted through a hole in the side of the lower plenum, fills the lower plenum, and commences to penetrate into the lower part of the core. At that stage, considerable steam is generated, moves up through the core into the upper plenum carrying some entrained water droplets, and passes

out through a hole in the side of the upper plenum. At the same time, the structural elements in the core will start cooling if the applied power level is low enough, and the water level will then rise through the core and can be followed through the full reflood process.

Major debugging of the computer code has now been completed and calculation examples are being produced with a quick-running coarse scale of resolution, in order to scope out the results obtained with a variety of different initial and inlet conditions within the range of expected experimental conditions. Exchange and mixture functions have been chosen by means of our experience with K-TIP calculations and will incorporate progressively more refined representations of the detailed microscopic physics as these become available through the coordinated research being simultaneously carried on with K-TIP, SAM, K-FIX, and SOLA-DF.

Six SAM calculations have been completed without difficulty as of this writing, each carried far enough in time to demonstrate the various types of partial or total reflood that can be accomplished in each case. No insurmountable difficulties with the SAM program have been encountered, and none are expected, other than those associated with the continuing questions of representing extremely complicated flows by means of macroscopic modeling.

One calculation example is shown in Fig. 36. Included are the volume-fraction-weighted velocity vectors for the water and steam, the volume fraction contours, and contours of water temperature and structure temperature. These plots are given for four stages in the reflood process. At the first stage ( $t = 2.5$  s) water has filled about half of the lower plenum volume, and a study of closely spaced configurations shows that the water wave is sloshing back and forth at this stage. At  $t = 6.0$  s, water is entering the core region and violent boiling has commenced. The structure, which continues to be heated by a specified power input, is above the critical-heat-flux (CHF) limiting temperature over most of the left. Therefore, water enters this region and the cooler right-hand region more easily than in the central parts of the core where heat transfer is greatest. Just before  $t = 6.0$ , the lower left part of the core cooled to below the critical heat flux limitation, resulting in the newly developed hot spot in water temperature visible in the illustration. By  $t = 11.5$  s, the core is nearly half flooded, with the hottest region of the core structure confined to the upper left. At the last

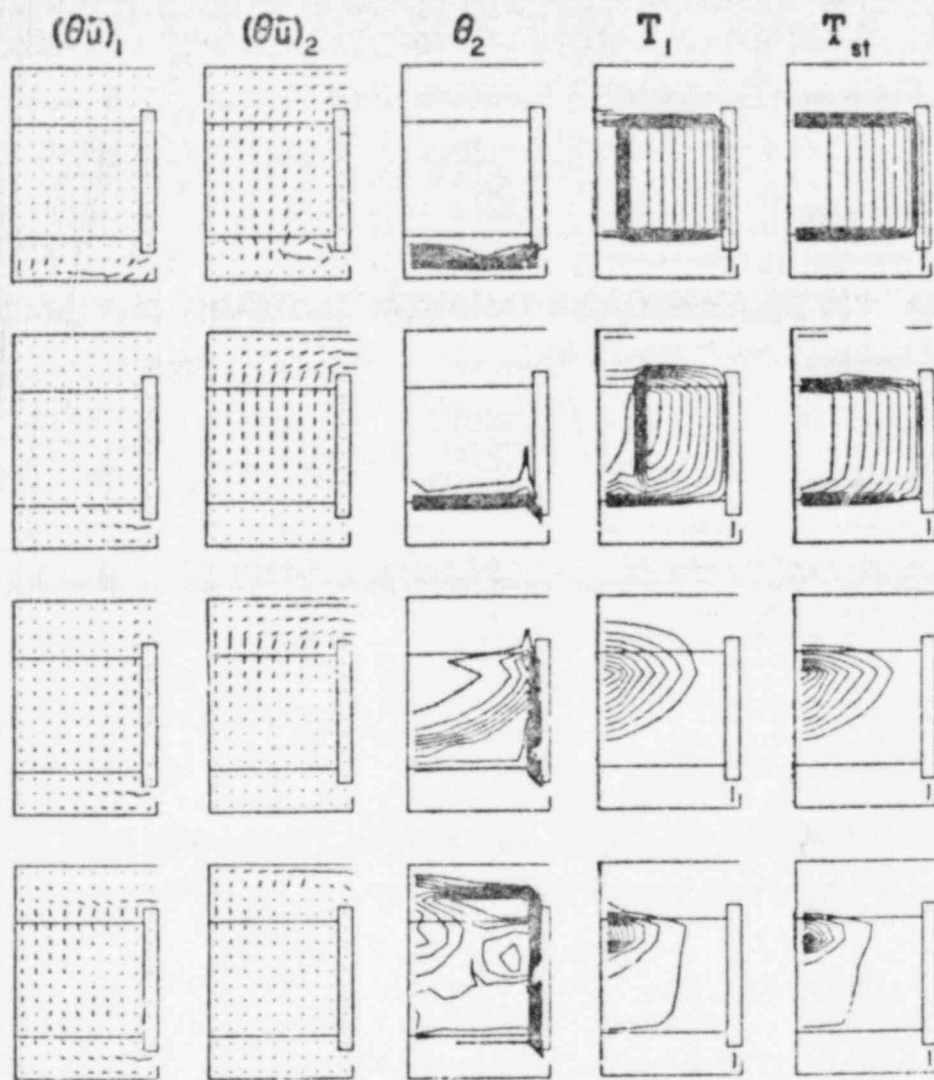


Fig. 36.

Volume-fraction-weighted velocity vectors of the water and steam flow, contours of volume fraction, and contours of water temperature and structure temperature. Top row,  $t = 2.5$  s; second row,  $t = 6.0$  s; third row,  $t = 11.5$  s; bottom row,  $t = 18.0$  s. The maxima for the first column are, respectively, 36.7 cm/s, 42.6 cm/s, 42.0 cm/s, and 43.1 cm/s; for the second column, 33.4 cm/s, 2403.0 cm/s, 1776.5 cm/s, and 742.8 cm/s; for the fourth column, 400.4 K, 400.0 K, 396.0 K, and 374.1 K; and for the fifth column, 505.0 K, 512.4 K, 493.2 K, and 379.5 K.

stage,  $t = 18.0$  s, the core reflood is almost complete and the structure has cooled nearly to the saturation temperature, 373 K in this example.

### 3. Numerical Study of Downcomer Steam-Water Flows

(A. A. Amsden, B. J. Daly, and F. H. Harlow, T-3)

A series of K-TIF calculations was performed to determine the accuracy of the model in predictions of downcomer dynamics for a wide variety of physical conditions. A coarse-finite-difference mesh was used in this study to minimize the computation time. The specific set of modeling parameters is the same as used in most of our previously reported work and was not changed from problem to problem, so that the only variations among the calculations were the initial and boundary conditions specifying each case.

The numerical calculations were designed to simulate specific transient, ramped steam flow experiments performed by Creare, Inc. in a 1/15-scale pressurized water reactor model. The boundary conditions used in this study are illustrated in Fig. 37. The top and bottom boundaries of the computation mesh are rigid, free-slip boundaries, while the left and right boundaries are periodic. The horizontal line through the computation region separates the downcomer from the lower plenum, which is an extension of the downcomer with volume approximately equal to that of the cylindrically symmetric experimental apparatus. Steam is injected into the system throughout the entire lower plenum at the transient ramping rate measured in the experiment. An experimentally measured transient lower plenum pressure is used in the calculations to determine the time-varying steam density and saturation temperature. ECC water is injected into the downcomer through the three intact cold legs (A), and water and steam move through the broken leg (B) at rates appropriate to volume conservation in the system. Because of the coarseness of the calculation mesh, the effect of the hot legs (X) is neglected in this study, except as noted below.

Figure 38 shows a comparison between calculated and experimental filling curves for a 60-gpm water injection rate and four different steam ramp rates. The calculation of the Creare H-1 experiment was performed with the coarse mesh and with a finer mesh, the resolution of which was double that of the coarse mesh in both the horizontal and vertical directions. The finer scale calculation also included obstacle cells to simulate the hot legs. It can be seen from the figure that these changes had little effect on the lower plenum filling rate.

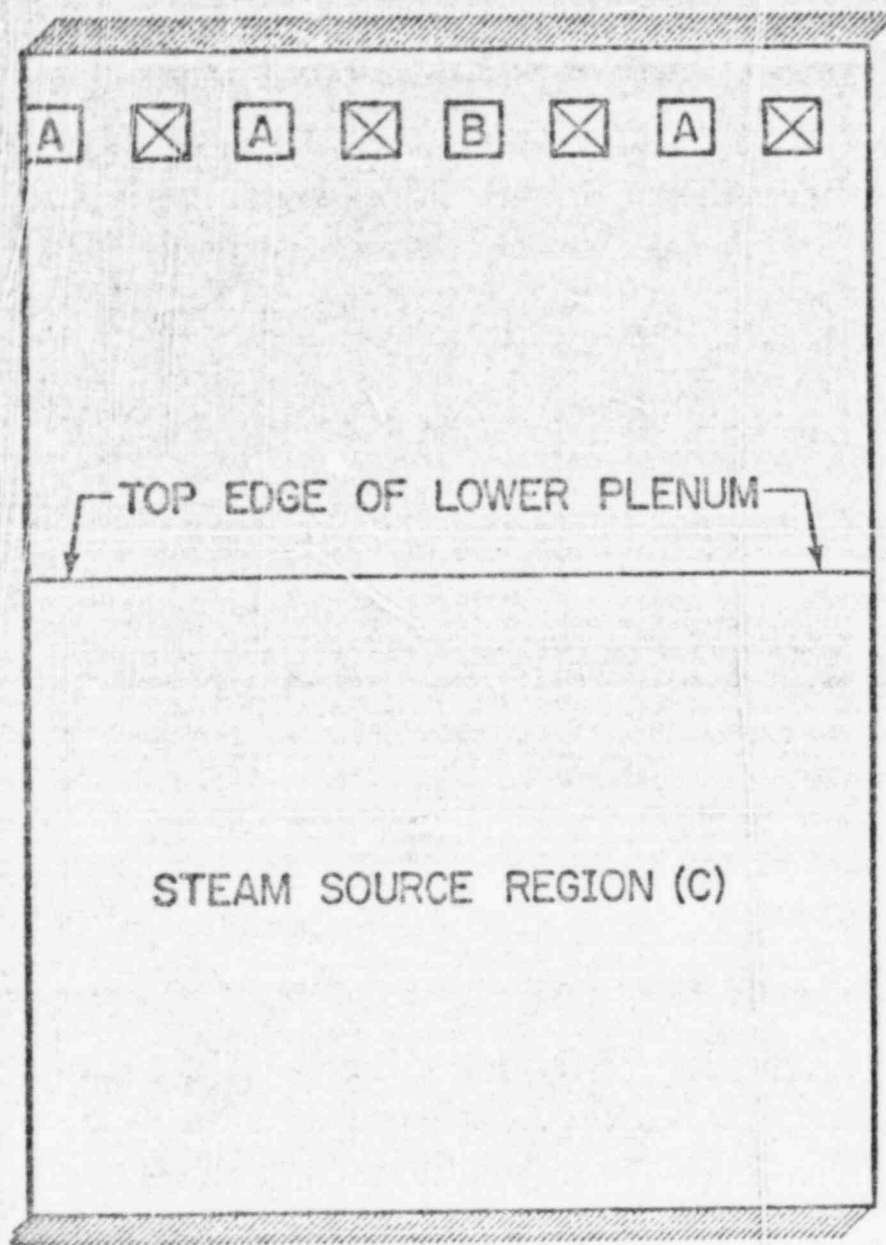


Fig. 37.

K-TIF computation region for unwrapped downcomer studies. The top and bottom boundaries are rigid, free-slip walls. The left and right boundaries are periodic. ECC water is injected into the system through the intact cold legs (A cells), while steam enters through the entire lower plenum region. Both steam and water exit through the broken leg (B cell), but only steam enters the system through this port. The hot-leg obstacles (X) are included only in the fine-resolution calculations.

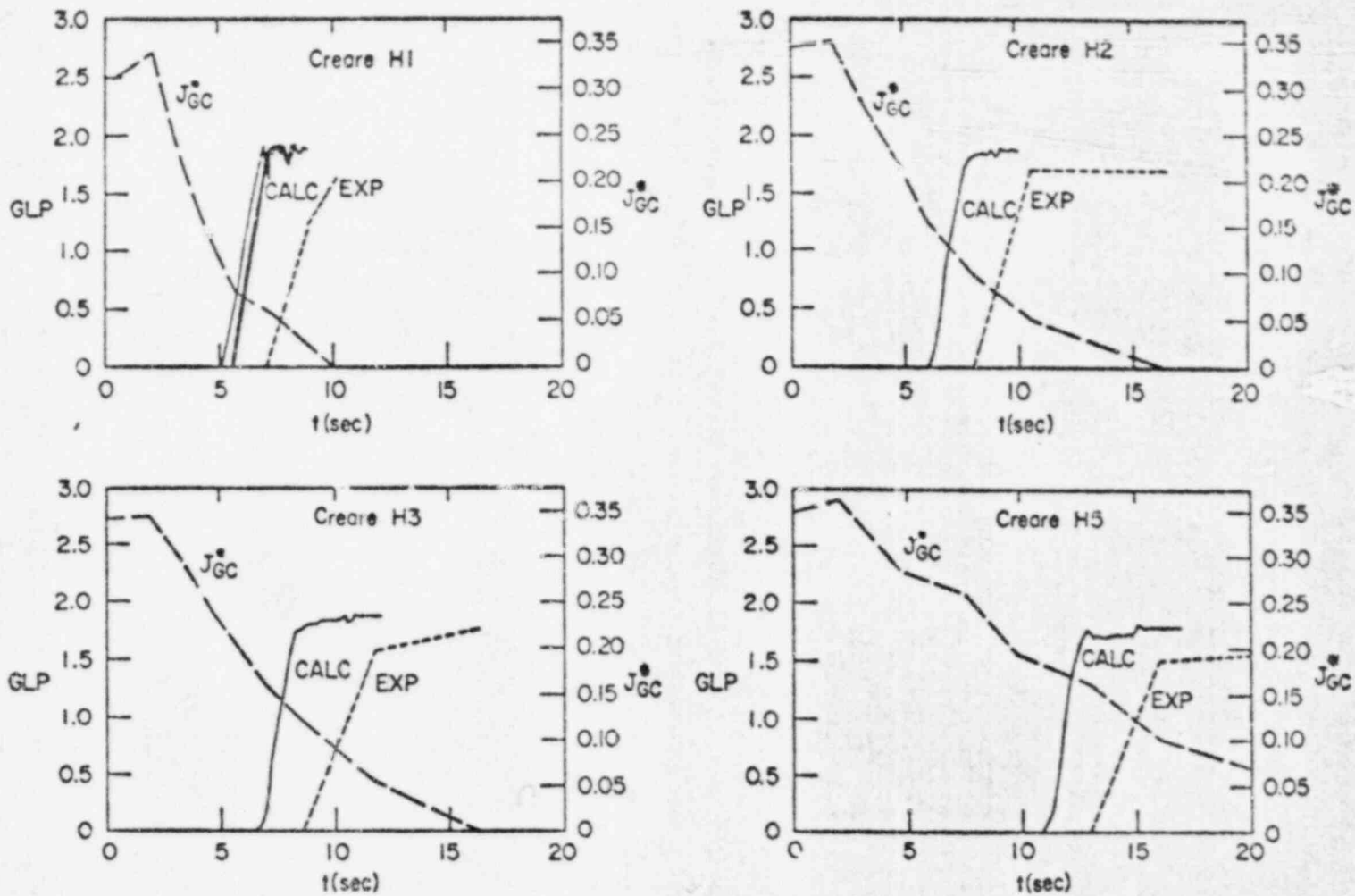


Fig. 38.

Comparison of calculated (solid lines) and experimental (short-dashed lines) water delivery curves for 60-gpm water injection rate and four different steam ramp rates (long-dashed lines). The heavy solid line in the Creare H-1 comparison shows calculated results obtained with a fine-scale mesh.

A comparison of the calculated and experimental filling curves indicates that the calculated delay time for the onset of water delivery is approximately 2 s less than the experimental value, independent of ramp rate. The calculated plenum filling curves are slightly steeper than the experimental curves.

Figure 39 shows similar comparisons of water delivery curves for three different water injection rates and approximately the same steam ramp rate. The three comparisons show similar trends: a shorter delay time for the onset of water delivery and a steeper delivery curve for the calculated results as compared to the experiments. Both of these trends are enhanced slightly with increased water injection rates. The water delivery curve for the 30-gpm water injection rate experiment shows an early onset of delivery associated with oscillatory dumping of water into the lower plenum prior to the main delivery. Oscillatory motions of the water-steam front were also observed in the calculations and, in some cases, these resulted in premature dumping of water into the lower plenum.

A comparison of calculated and experimental water delivery curves for heated wall tests and two different steam ramp rates are shown in Fig. 40. As in the previous comparisons the calculated delay time for the onset of water delivery is less than the experimental delay time. The same trend is evident when the EOC water is heated and the walls are not (results not shown).

#### 4. HDR Core Barrel Dynamics

(J. K. Dienes, W. C. Rivard, L. R. Stein, and M. D. Torrey, T-3)

The three-dimensional version of the K-FIX<sup>30</sup> code has been coupled with the elastic shell code FLX to calculate the core barrel dynamics during blow-down for the HDR reactor vessel. The results of the calculation are used as a standard to assess the adequacy of two-dimensional calculations performed with the SOLA-FLX<sup>31</sup> code. When a simple physical model for depressurization in the lower plenum and core is used in SOLA-FLX, the results are found to agree very well with the K-FIX(3-D, FLX) calculation. Figures 41a through 41d compare the core barrel radial displacements in the r-z plane through the broken pipe at 10, 20, 30, and 40 ms after pipe rupture. Results from two SOLA-FLX calculations are shown to illustrate the increased accuracy obtained when the depressurization model is used, relative to that obtained with constant pressure in the lower plenum and core. A sectional view of the cylindrical HDR

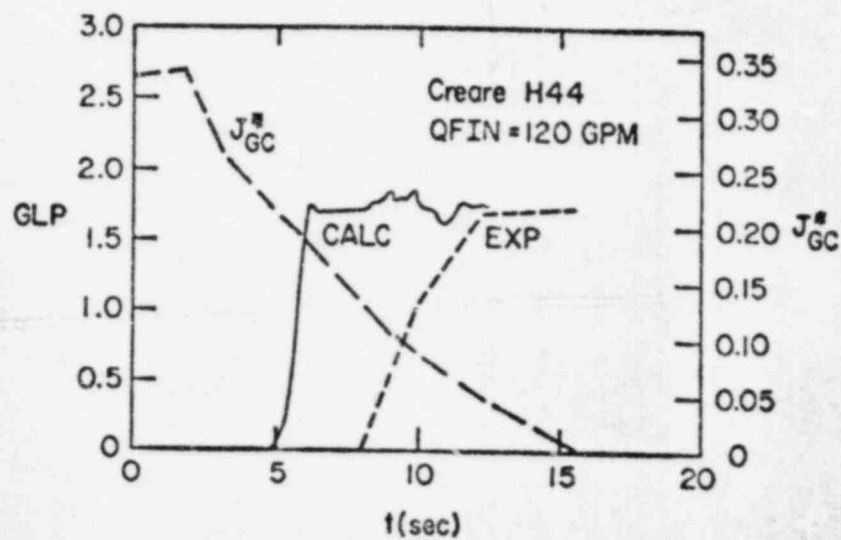
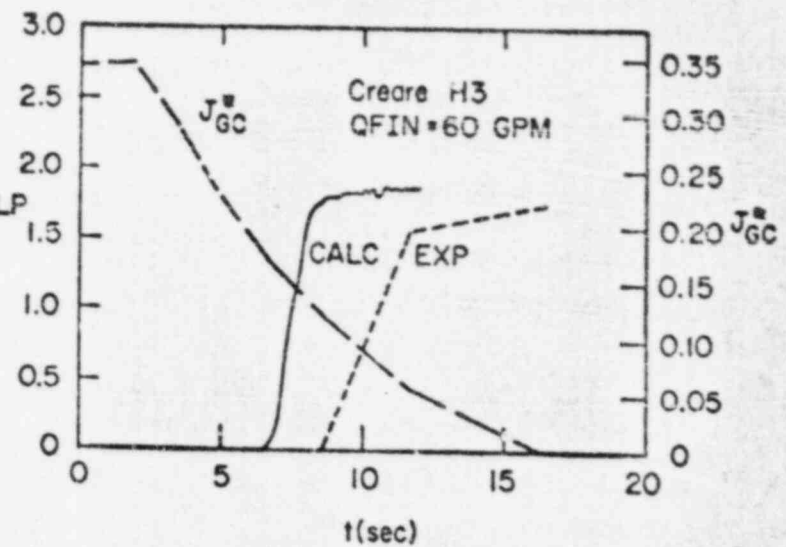
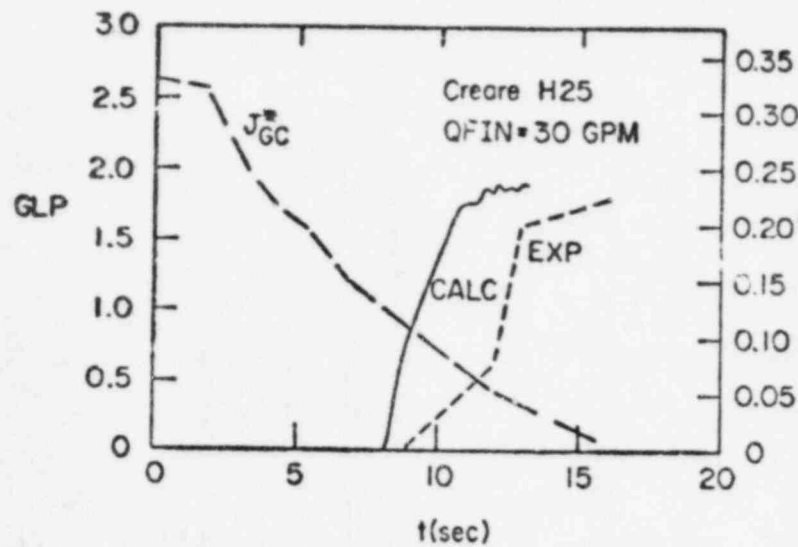


Fig. 39.

Comparison of calculated and experimental water delivery curves for three different EOC injection rates and approximately the same steam ramp rate. The curves are as indicated in Fig. 38.

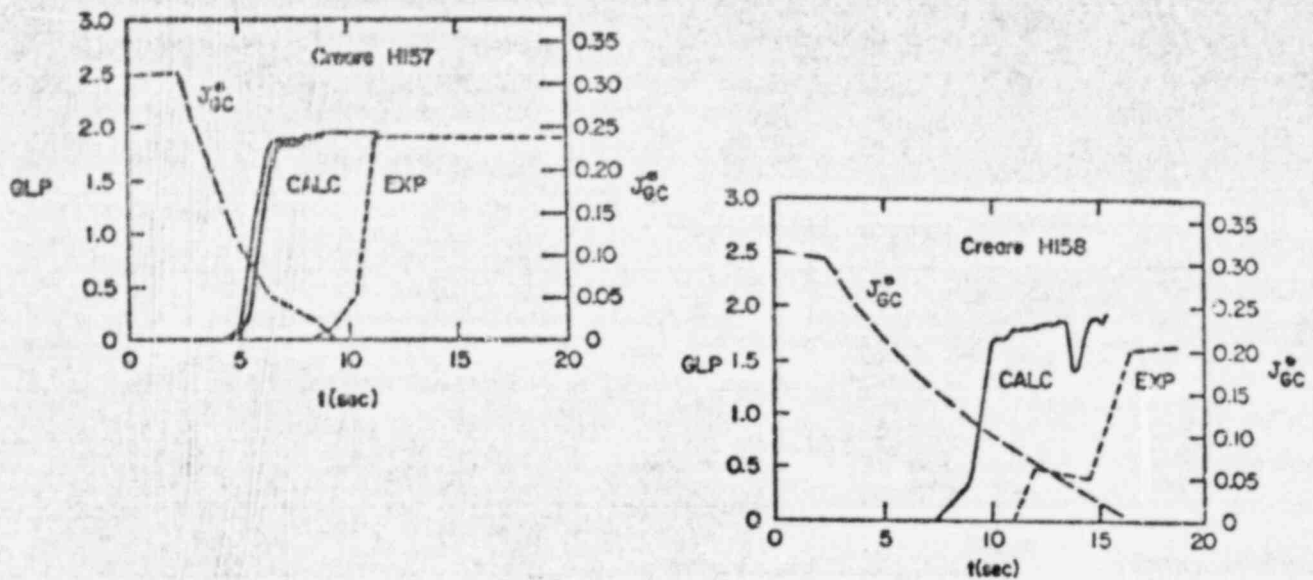


Fig. 40.

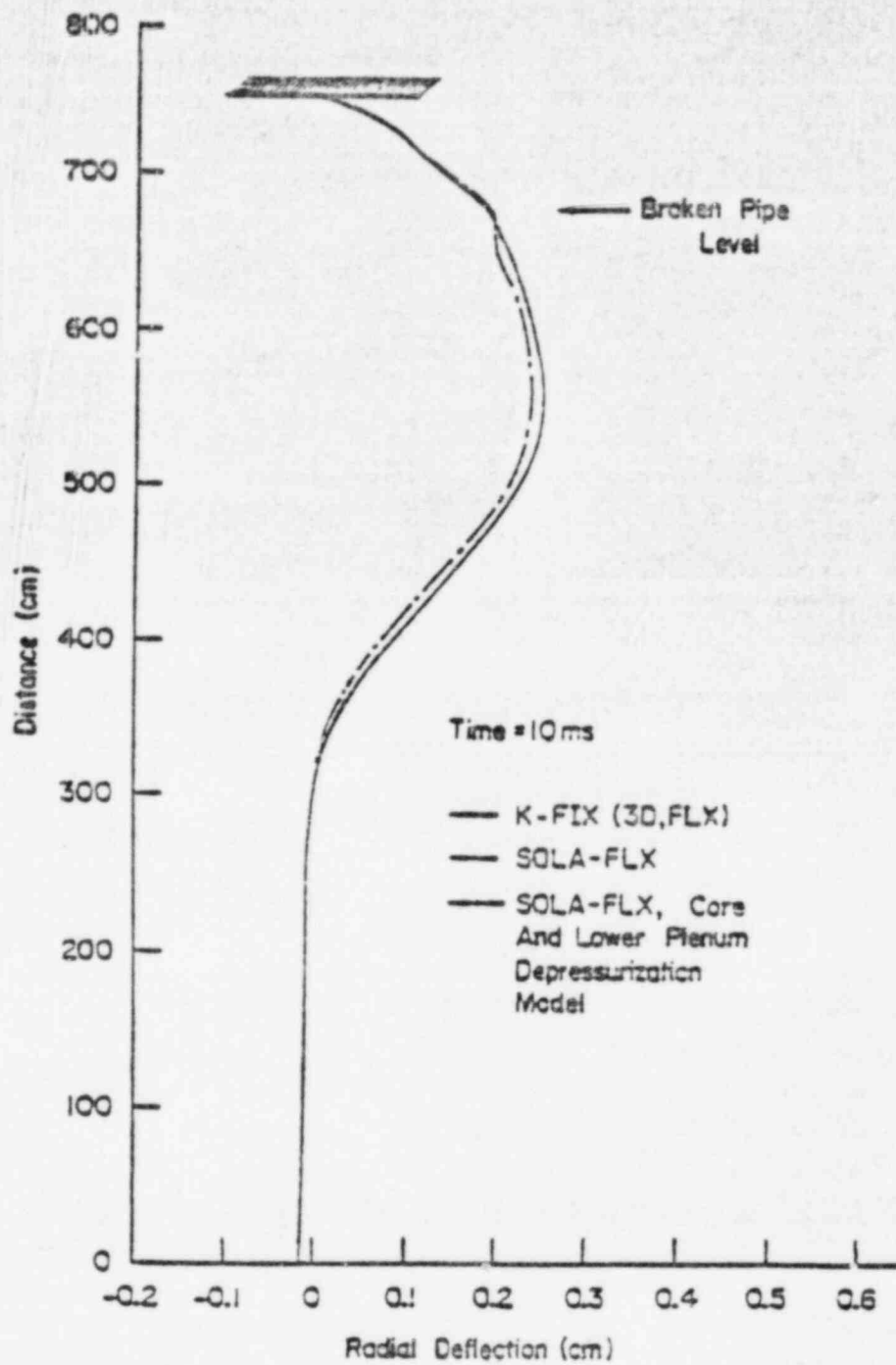
Comparison of calculated and experimental water delivery curves for 60-gpm FCC injection rate, two different steam ramp rates and superheated (350°F) vessel walls. The light solid line in the Creare H157 experiment shows the effect of including a critical heat flux transition in the wall heat transfer model. Otherwise, the curves are as indicated in Fig. 38.

vessel is shown in Fig. 42. The vessel is initially filled with subcooled water at 543 K and pressurized to 11.0 MPa. The pressure in the lower plenum and core decreases during the blowdown, reaching a value of about 9.0 MPa at 40 ms. This depressurization, which affects the pressure differential on the core barrel, is modeled in the SOLA-FLX calculations by monitoring the liquid efflux. At any instant, the pressure in the lower plenum and core is specified as

$$p = p_0 - a^2(m_0 - m)/V ,$$

where  $p$  and  $m$  are the instantaneous pressure and liquid mass,  $V$  is the combined volume of the lower plenum and core,  $a$  is the liquid sound speed, and subscript  $0$  refers to the initial state. The depressurization described by this model agrees very well with the pressure fields calculated with K-FIX(3-D, FLX).

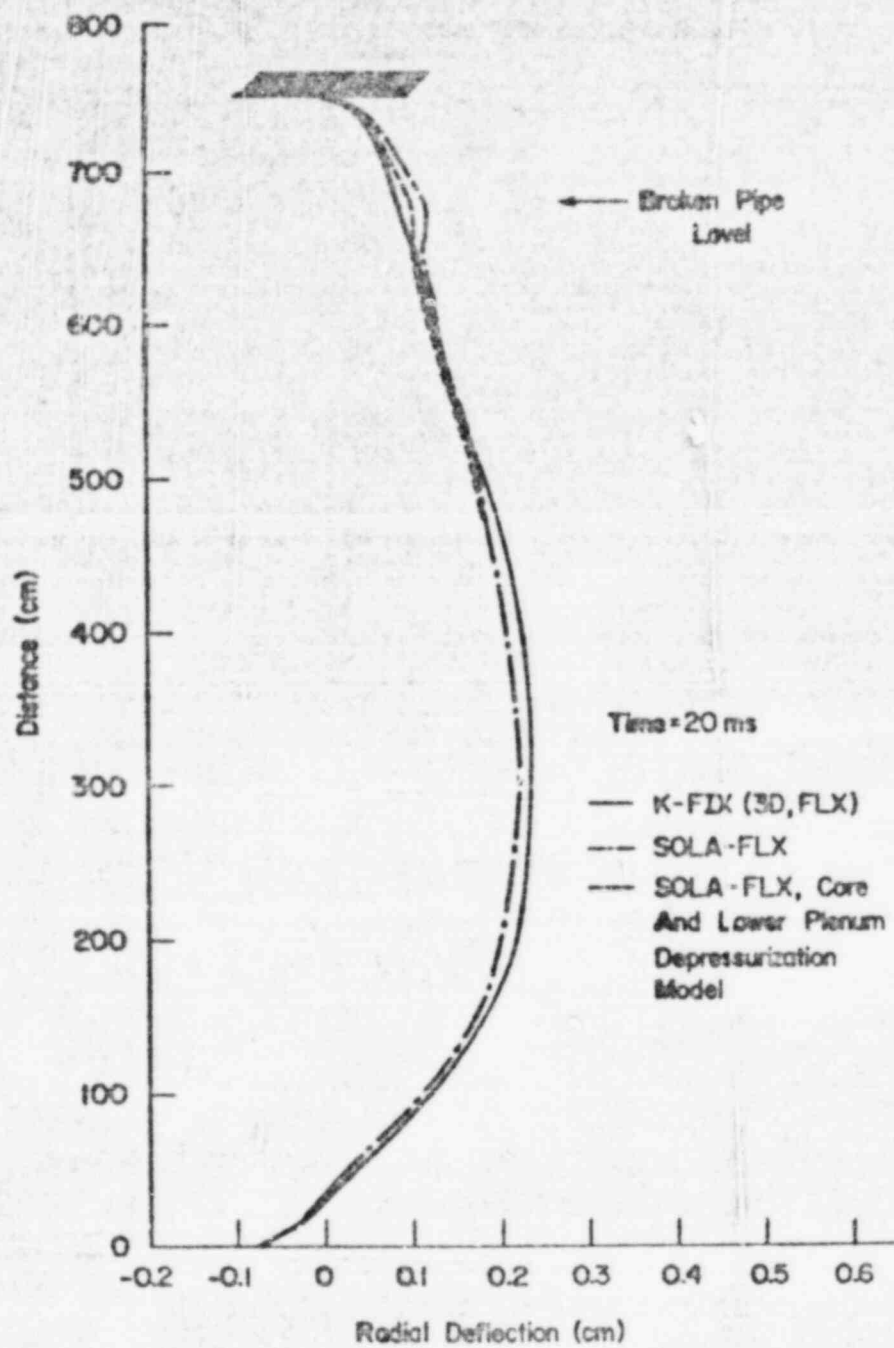
For these calculations, SOLA-FLX used 15 circumferential zones and 26 axial zones to describe the fluid dynamics in 180° of the downcomer annulus.



(a)

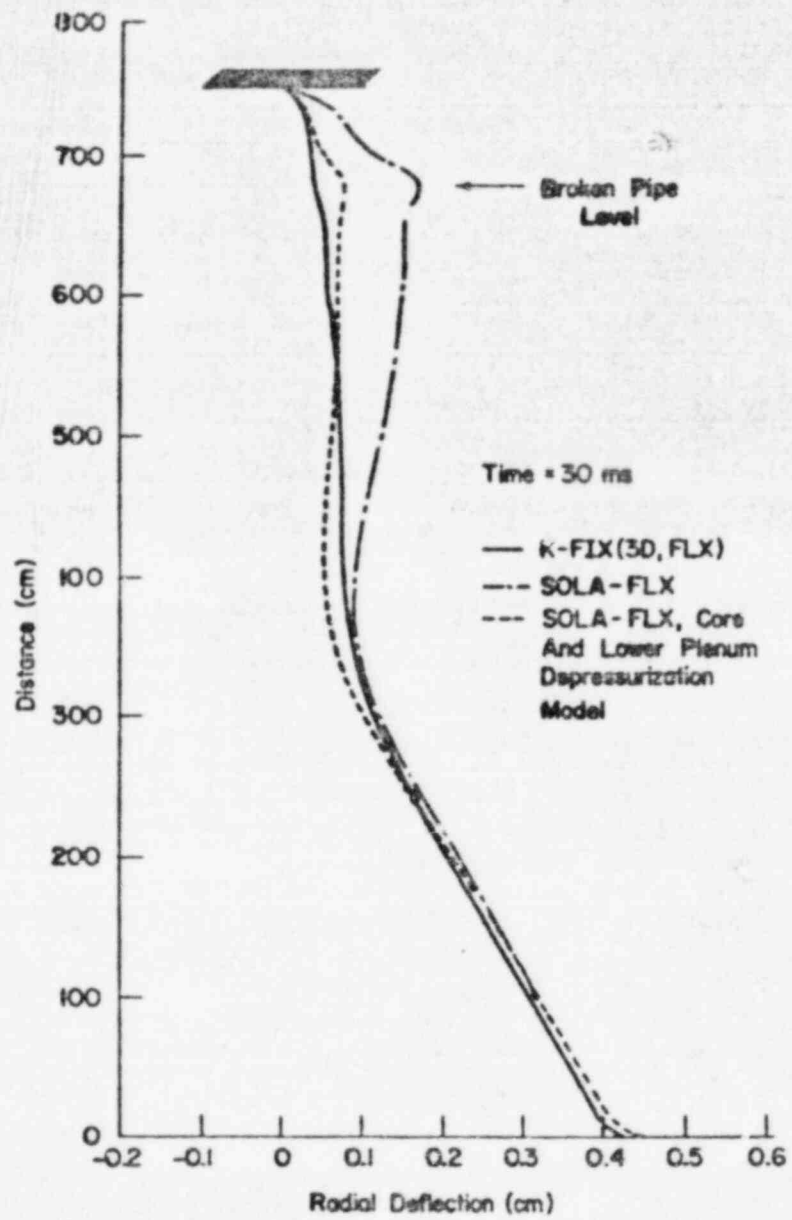
Fig. 41.

Core barrel radial deflection profiles at the circumferential location of the broken pipe at 10, 20, 30, and 40 ms after pipe rupture.



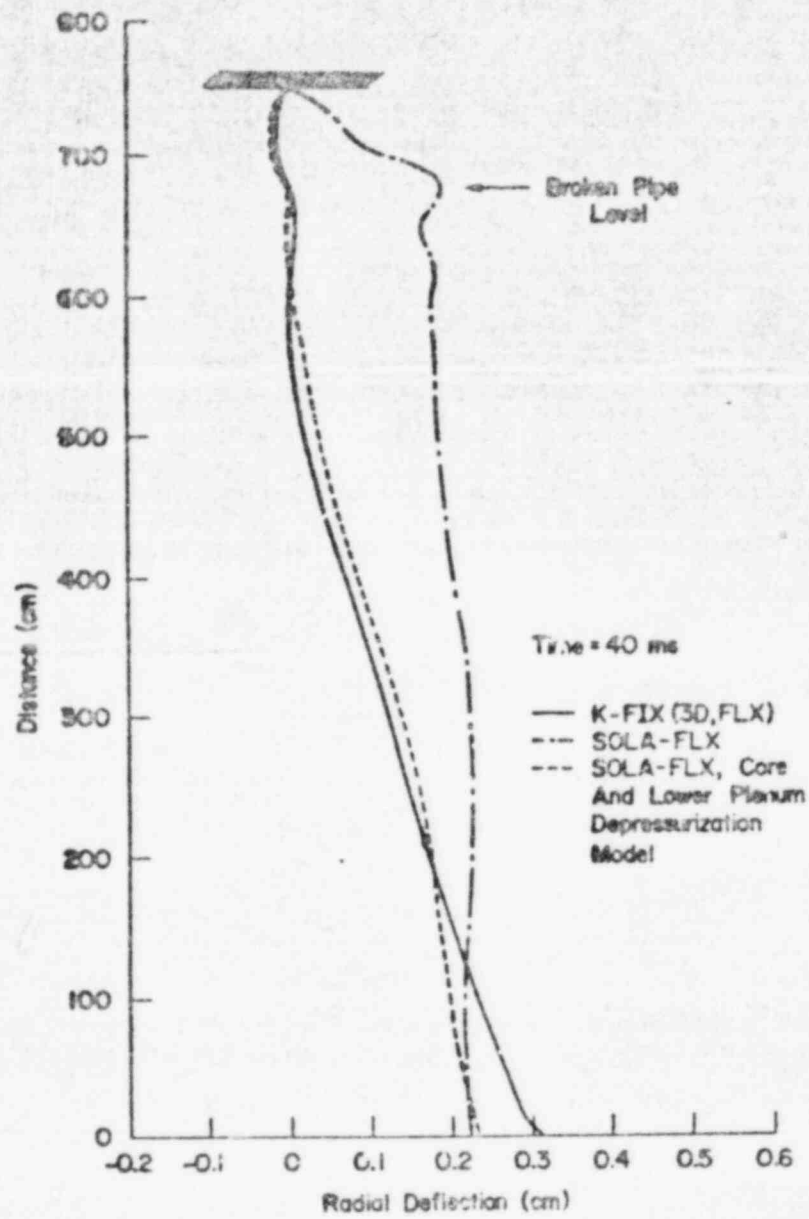
(b)

Fig. 41. (cont).



(c)

Fig. 41. (cont)



(d)

Fig. 41. (cont)

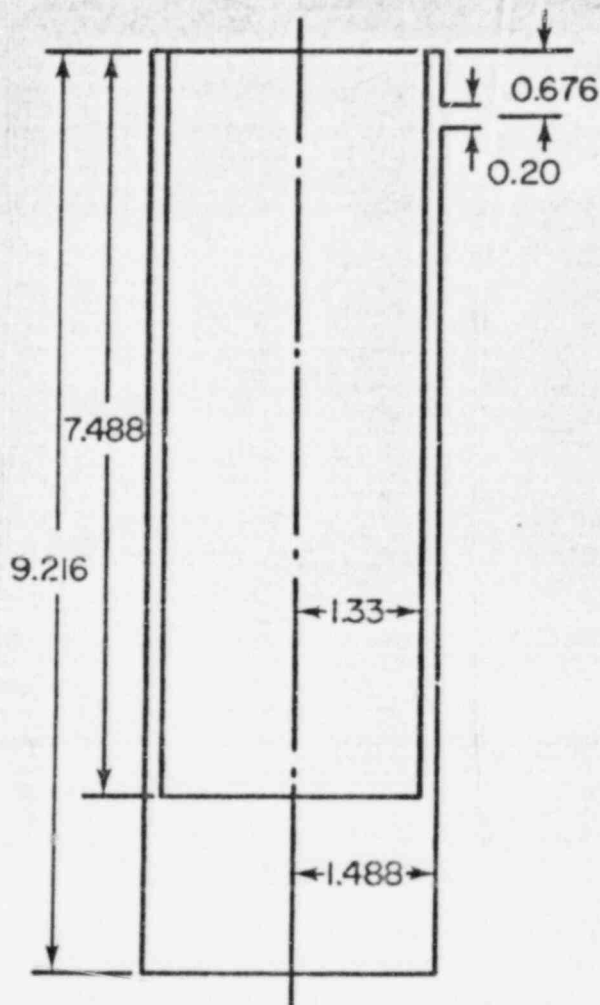


Fig. 42.  
Sectional view of the cylindrical HDR single-loop vessel (dimensions in meters).

Similar noding was used for the structural dynamics. K-FIX(3-D, FLX) used the same circumferential zoning, 32 axial zones (6 zones in the lower plenum), 4 radial zones, and the same noding for the structure. SOLA-FLX required 15 min of CDC-7600 time while K-FIX(3-D, FLX) required 45 min.

The good agreement with the three-dimensional results demonstrates that two-dimensional SOLA-FLX calculations provide an accurate description of the core barrel displacements. The accuracy of the hoop and bending stress calculations, which depend on displacement spatial derivatives to fourth order, is being investigated for various structural nodings and will be discussed in a future progress report.

#### D. LWR Safety Experiments

(H. H. Helnick, Q-8)

The objectives of LASL's LWR safety experimental program are:

1. to provide experimental support for model development activities and
2. to develop advanced safety experimental instrumentation techniques to facilitate the detailed measurements required for advanced code development and verification efforts.

This program is conducted in close coordination with code and model development projects at LASL. It is also coordinated with other experimental programs for which advanced instrumentation is being developed.

Development of the Storz lens video system is proceeding on schedule. All of the video equipment has been procured and tests of simulated upper plenum scenes have been performed. Equipment is being prepared for delivery to the PKL facility (Erlangen, W. Germany) for the performance of preliminary on-site tests. A single video channel will be located to view the upper plenum of PKL. The purpose of this test is to determine the severity of electromagnetic interference in the environment where the equipment will have to be located during the actual tests.

The development of software for computer reconstruction of the video images is approximately 50% complete. Transfer functions of the Storz lens (with barrel distortions) and the vidicon system have been measured. This information will allow the image simulation required for the testing of models during model development.

Progress was made on the entrainment-de-entrainment experiment.<sup>8</sup> Fabrication of the test fixture is now about 75% complete and preliminary tests have been run on the water spray nozzles and air flow system. Hot-film anemometry equipment is operational and is awaiting completion of the experimental vehicle for installation of the sensors.

##### 1. Storz Lens — Video System

(C. R. Mansfield, J. Spalding, and P. F. Bird, Q-8)

The work on developing the Storz lens for droplet velocity measurements is progressing essentially on schedule.

a. Storz Lens Development

The Storz lenses to be used in the proposed large-scale reflood experiments in Germany and Japan are being modified to protect them from the high steam temperature test environment. We are proceeding with two types of protective sheaths. One concept is based on a design proposed by MPR Associates that uses a nitrogen-cooled sheath. The other concept is based on heat pipe technology. The work in this area has progressed to the conceptual design stage.

A short test of the video equipment in the electromagnetic environment of the German PKL experiment is planned for early February 1978. The equipment for this test has been ordered, some of the equipment has arrived, and some is being fabricated.

The prime objective is to run a television camera during an experiment and see if acceptable signals can be recorded on video tape. Electromagnetic shielding cases have been ordered for this test. A secondary objective is to look into the upper plenum with a zoom lens and make preliminary recordings of what is occurring inside the plenum. We plan to look in via a sapphire window and illuminate the volume with a fiber optic bundle.

A stroboscopic flash system to be used in conjunction with the Storz lens video system has been designed and is being fabricated. This system is intended to produce two or three flashes spaced as close in time as one-half millisecond and at a repetition rate of 30 Hz. Illumination of the viewing area will be through fiber optic bundles or direct exposure, depending on accessibility and light-level requirements.

b. Data Reduction Techniques

Techniques are under development to automatically reduce the Storz lens data directly from the video recordings. This work is being done in conjunction with Group M-8 at LASL. A model is being developed to determine the accuracy of the deduced droplet velocities and densities and the range of velocity and droplet density distributions which can yield useful results. We have been making measurements of system modulation transfer functions and noise levels to provide Group M-8 with the data which they need.

A short motion picture was produced in October for the Fifth Light Water Reactor Safety Conference. The movie was intended to demonstrate two points.

1. the obtaining of stereo information from video input and
2. the ability to stroboscopically expose a vidicon and then scan the information in video fashion.

A xenon flashlamp was used to provide stroboscopic exposures. Stereoscopic views were obtained by simultaneous recording of the output of two TV cameras. The video signals were recorded on a 1/2-in., black and white video tape recorder. This was accomplished by alternately recording horizontal lines from each camera at normal video scan rates. The composite recording was converted into a movie using equipment at the Los Alamos Division of EG&G.

### 2. Upper Plenum De-entrainment Experiment

(P. F. Bird, Q-8 and W. L. Kirchner, Q-6)

Design and fabrication of the apparatus for the upper plenum de-entrainment experiment is approximately 75% complete. The test section that simulates the upper internals is in the process of being fabricated. The water injection section is in the design stage, including investigation of appropriate nozzles. Available commercial nozzles present relatively uniform sprays over a surface perpendicular to the central axis of a cone. Within some limits, the droplet size distribution and flow volume can be controlled. Additional control of the flow volume requires changing the number and distribution of the nozzles. At present, an exhaust collection system will not be used since initial information of interest can be obtained by measuring input air and water flows and de-entrained water flow.

### 3. Hot-Film Anemometer

(P. F. Bird, Q-8)

With assistance from the LASL metrology group we have completed calibration of a hot-film anemometer for measuring air flows up to 100 m/s. This calibrated anemometer will be used as a secondary calibration for other anemometers and gas flow measuring equipment.

We have added a linearizer and zero suppressor to our hot-film anemometer equipment. Additional calibration is necessary to use this general-purpose polynomial linearizer and zero suppressor. Initial observation of falling water droplets suggests that the signal due to remnant film drying is relatively small and rather insignificant compared to the total signal from a passing droplet. The relatively larger trailing signal due to the remnant

film drying (and seen in the nonlinearized output from a hot-film anemometer) is characteristic of the quartic nonlinearity of these devices.

With the assistance of LASL electronics groups we have designed and are fabricating a device to take the output signal from a hot-film anemometer (or other devices, which detect the presence of liquid droplets entrained in flowing air), and convert it to read digitally as void fraction. The output can also be stored in a computer-controlled data acquisition system. This technique will be evaluated to determine ranges of conditions over which it can be applied and whether it will have general utility in two-phase flow experiments.

#### 4. Unwrapped Downcomer Experiment

(V. S. Starkovich, Q-8)

Reconfiguration of the unwrapped downcomer apparatus has been completed. The new version was designed to better correspond to the existing SOLA-TIF mesh-cell configuration. In addition, the air flow meters have been calibrated at pressures up to 100 psig, to limit uncertainties in the air-flow data at high pressures and volumetric flow rates.

## XII. LMFER SAFETY RESEARCH

(M. G. Stevenson, Q-DO and J. E. Bourreau, O-7)

The Liquid Metal Fast Breeder Reactor (LMFER) safety research effort at IASL consists of several programs. In the first of these, the SIMMER code is being developed and applied to core disruptive accident (CDA) analysis with support from the Division of Reactor Safety Research (RSR) of NRC. SIMMER is a two-dimensional, coupled neutronics-fluid dynamics code intended for transition phase, core disassembly, and extended fuel motion analysis. The second version of the code, SIMMER-II, has been completed and is now being used in the analysis of CDA problems.

In a separate program funded by the U.S. Department of Energy (DOE), models are being developed for phenomena important to the progression and consequences of CDAs. Some of this work is basic research on phenomena, but in some cases the developed models will be included directly in accident analysis codes and, particularly, in SIMMER. Another part of this DOE program is focused on the application of the accident codes, particularly the SIMMER code, to the study of specific aspects of accident sequences. This program is reported in Sec. III.B.

Experimental investigation, including confirmation of reactor safety analysis methods, is an important part of safety research. Section III.C provides a summary of recent work in a program involving out-of-pile experiments and related analysis in support of SIMMER model development and verification.

Finally, Sec. III.D reports recent work in the IASL LMFER Safety Test Facility (STF) study, a program funded by NRC/RSR.

### A. SIMMER Code Development and Applications

(L. L. Smith, Q-7)

A more implicit phase transition method has been developed for use in SIMMER-II. The model is compatible with the more complex surfaces modeled in SIMMER-II and is related to the conduction heat-transfer-limited model of SIMMER-I.

The analysis of postdisassembly expansion previously performed with SIMMER-I has been repeated with SIMMER-II. The structure of SIMMER-II

precludes identical reproduction of the input quantities and models of SIMMER-I. Nonetheless, a comparable calculation was performed and the system kinetic energy was about a factor of 10 lower than that calculated with SIMMER-I.

#### 1. SIMMER-II Phase Transition Methods

(W. R. Böhl, Q-7)

The simple vaporization-condensation model option used in SIMMER-II is one in which the phase transition rates are limited by heat conduction rates to or from the interface where the phase transition is assumed to occur. The model is similar to the one used in SIMMER-I,<sup>32</sup> although three revisions were made to the SIMMER-I equations. First, modifications were inserted to accept the surface complications introduced by the additional components and the structure surface treatment in SIMMER-II. Second, both the vapor internal energy and component saturation temperatures are now evaluated in a totally implicit fashion, although the liquid and structure temperatures are assumed to remain constant. Third, the vapor heat transfer coefficients are allowed to depend implicitly on the vaporization or condensation rate at a given surface. In addition to these revisions, the resulting model equations are solved in a different manner, as is detailed below.

In this SIMMER-II model, the vaporization-condensation rates are obtained by iteration. Three inner iterations are contained within an overall outer iteration. The first inner iteration solves simultaneously for the new vapor densities, the updated saturation temperatures, and the heat of vaporization assuming that the vapor specific internal energy and the heat transfer coefficients remain unchanged. The second iteration uses the change in the vapor conditions to begin a calculation updating the vapor heat transfer coefficients. The third iteration solves the vapor energy equation to update the vapor internal energy. Following overall convergence, heat and mass transfer rates are evaluated using the final updated values of the vapor temperatures, the component saturation temperatures, the heat of vaporization, and the heat transfer coefficients.

The changes in the vapor conditions in the first inner iteration are obtained by solving the coupled vapor continuity equations and the equation of state. A Newton-Raphson procedure is used with all vapor properties assumed to depend solely on the changing vapor densities and the known average vapor

internal energy. This first inner iteration can thus accommodate both the potentially strong dependence of the vapor densities on the respective saturation temperatures and the nonlinearities associated with the equation-of-state information, e.g., the rapid change in the heat of vaporization near the solid-liquid critical point.

The second inner iteration updates the vapor-side heat transfer coefficients. In the current model these are defined by

$$A_w h_{gw}^{k+1} = \frac{-\Gamma_{gw}^{k+1} \bar{c}_{pg}^{k+1}}{\exp \left[ \frac{-\Gamma_{gw}^{k+1} \bar{c}_{pg}^{k+1}}{A_w h_{gw}^*} \right] - 1}, \quad (40)$$

where

- $A_w$  is the surface area of surface  $w$ ,
- $h_{gw}^*$  is the corrected vapor heat transfer coefficient at surface  $w$ ,
- $h_{gw}$  is the normal vapor heat transfer coefficient at surface  $w$ ,
- $\bar{c}_{pg}$  is the average constant-pressure specific heat of the vapor mixture,
- $\Gamma_{gw}$  is the total mass transfer rate at surface  $w$ , and
- $k$  denotes the outer iteration counter.

Substitution of Eq. (40) into the definition of the phase transition rate allows a Newton-Raphson procedure to be formulated using  $\Gamma_{gw}$  as the iteration parameter. In the conduction-limited model, the definition of the phase transition rate at a surface is

$$\Gamma_{gw}^{k+1} = \sum_{\lambda} \left\{ \frac{1}{h_{lg,\lambda}^{k+1}} \left[ A_w h_w (T_{Sat,\lambda}^{k+1} - T_w) + A_w h_{gw}^{k+1} (T_{Sat,\lambda}^{k+1} - T_g^k) \right] \right\}, \quad (41)$$

where

- $\lambda$  designates all components that can condense or vaporize from a given surface,
- $h_{lg,\lambda}$  is the latent heat of vaporization for component  $\lambda$ ,
- $h_w$  is the liquid or structure heat transfer coefficient for surface  $w$ ,

$T_{\text{Sat},\lambda}$  is the saturation temperature of component  $\lambda$ ,  
 $T_w$  is the temperature of surface  $w$ , and  
 $T_g$  is the vapor temperature.

Here, all parameters other than  $\Gamma_{gw}$  are held constant. The vapor heat transfer coefficient is subsequently augmented during condensation and decreased during vaporization. This characteristic significantly improves the model's stability by automatically adjusting the degree to which the latent heat of vaporization or condensation can be taken from or added to the vapor field.

The third inner iteration solves the vapor energy equation, with the quantities that are directly dependent on the vapor temperature expressed in terms of the change in the vapor temperature. Thus, the vapor temperature and vapor internal energy are expanded as

$$T_g^{k'+1} = T_g^{k'} + \delta T_g^{k'+1}, \quad (42)$$

and

$$e_g^{k'+1} = e_g^{k'} + \bar{c}_{vg}^{k'} \delta T_g^{k'+1}, \quad (43)$$

where

$\bar{c}_{vg}$  is the average constant-volume heat capacity of the vapor mixture and

$k'$  is the inner iteration counter.

Substitution of Eqs. (42) and (43) into the vapor energy equation results in an expression for  $\delta T_g^{k'+1}$  given in terms of a ratio of known quantities. Because the denominator of this ratio is the vapor temperature derivative, this third inner iteration is also essentially a Newton-Raphson procedure. Following convergence of  $T_g^{k'+1}$ , the final value of  $e_g^{k'+1}$  is used as the vapor internal energy for a recalculation of the first inner iteration.

Overall convergence is checked, starting on the second outer iteration and following the first inner iteration. Here, an equation-of-state call is made to determine a final set of consistent vapor properties, e.g.,  $e_g^{k+1}$ ,  $h_{\lambda g,\lambda}^{k+1}$ ,

$\bar{c}_{vg}^{k+1}$ ,  $T_{\text{Sat},\lambda}^{k+1}$ . These properties are then used to:

1. help determine whether overall convergence has been obtained,
2. calculate heat and mass flows if convergence has been achieved, and
3. finish updating values for the second and third inner iterations if the convergence tests fail.

Three outer iteration convergence tests have been established. The vapor temperature must be converged to within one degree; the saturation temperature for each component must be converged to within one degree; and the vapor heat transfer coefficients must be converged to within 0.1%. Generally, fewer than five outer iterations suffice for convergence.

This new iterative solution procedure for the simple vaporization-condensation model does solve several of the SIMMER-I problems involving negative temperatures or instabilities. It can be excessively time consuming in cases where extremely rapid condensation is modeled (due to a required small time step size), or where both cold structure and nearly critical hot sodium exist in the same node (due to a large number of iterations required for convergence). In addition, the current model does not include terms for a vapor component condensing on the droplets of a different material, the suppression of condensation due to fission gas, or actual time-dependent mass transfer limitations on phase transition rates. The multicomponent phase transition model under development will remove these limitations.<sup>2</sup>

## 2. SIMMER-II Postdisassembly Expansion Analysis

(W. R. Bohl, Q-7)

As part of the SIMMER development program, early versions of the code are being applied to key problems related to hypothetical core disruptive accidents (HCDAs). In particular, the SIMMER-I code has been used to calculate the system kinetic energy following postulated energetic disassemblies in the Clinch River Breeder Reactor (CRBR).<sup>33</sup> This previous study examined cases with an average initial core temperature of 4800 K. The study concluded that when all of the interactive transport processes modeled in SIMMER-I are made operative in a "best estimate" fashion, the system kinetic energy at impact with the reactor head is 3 MJ as compared to an isentropic work expansion potential of 100 MJ.

The purpose of the current study was to use this problem as a test case for SIMMER-II, compute a "best estimate" system kinetic energy at head impact

following a postdisassembly core expansion, and compare the results to SIMMER-I. Hence, the same thermophysical property data were used, and identical input was employed for those SIMMER-I model options that are still present in SIMMER-II. However, the current version of SIMMER-II contains most of the exchange process models for heat, mass, and momentum transport explicitly in the code, including a particle size calculation. Thus, the major effort involved in setting up this "best estimate" SIMMER-II case was to ensure a consistent geometric configuration. Compared to SIMMER-I results, the SIMMER-II calculation was considerably less energetic. Indeed, the SIMMER-II system kinetic energy at head impact was reduced by approximately an order of magnitude to ~ 0.3 MJ.

There appear to be two major reasons for this energy reduction. First, the SIMMER-I code was able to maintain pressure in the core region longer despite appreciable transport of fuel vapor into the fission gas plenum. This was due to

1. a slow rate of fuel to steel energy transfer (based on a 2.25 mm particle radius) and
2. a forced local equilibration of fuel vapor with the liquid fuel saturation conditions (resulting from an assumed high liquid-fuel heat transfer coefficient).

With the SIMMER-II code, the initial pressure gradients and vapor velocities result in the prediction of small particles and significant fuel to steel energy transfer. Because the steel temperature is initially 1700 K, the quenching effect on the liquid fuel reduces the propensity of fuel to vaporize, resulting in a pressure reduction. Second, the sodium in the region between the fission gas plenum and the flow guide tubes forms a natural "mixing zone" for the production of sodium vapor resulting from the introduction of core material and steel ablated from the fission gas plenum. The relatively large particle radius employed in the SIMMER-I calculation (0.002 m) allowed the vapor produced to separate from the liquid in the interaction region and accelerate the single-phase sodium in the flow guide tubes and the sodium pool. This, then, allowed additional hot fluid to enter the interaction region and mix with the remaining liquid sodium. In SIMMER-II, the attempted escape of vapor causes particle fragmentation. The hot and cold materials then move together, limiting both the time that liquid sodium is in the interaction region and the amount of hot liquid that interacts with this sodium.

SIMMER-II currently possesses only limited capability to simulate the "best estimate" SIMMER-I phenomena. To increase the fuel vaporization rate, the physical properties for fuel must be changed, e.g., the fuel's thermal conductivity must be increased. This has undesirable side effects: all heat transfer associated with liquid fuel is then augmented. Input does exist for lowering both liquid-liquid heat transfer and the structure heat transfer coefficients, and a case with these changes was attempted. SIMMER-II then predicted that the resulting relative vapor/liquid velocities would produce a high vapor heat transfer coefficient for the vaporization and condensation. Heat transfer from liquid fuel to liquid steel was then augmented using vapor as a transport medium. Again, a quenching effect was observed.

A second method of maintaining the core driving pressure is to tie the two fields together without decreasing the particle radius. This can be done in SIMMER-II by increasing the form drag coefficient,  $C_D$ . Here,  $C_D$  was arbitrarily increased from 1 to 100. To guarantee that liquid fuel to liquid steel heat transfer would not be excessive, the liquid fuel to liquid steel heat transfer multiplier was set to 0.1. This case did maintain core pressure for a longer time. However, mixing of liquid sodium with hot core materials was reduced, and the system kinetic energy at slug impact was still only on the order of 1 MJ. In an attempt to increase such mixing, structure condensation was eliminated. Initial upward core material velocities did increase but the increased velocities caused an increase in the ablation of cold plenum steel into the expanding fuel-steel mixture. As a result, there was little difference in the maximum sodium slug kinetic energy.

It was concluded that it is difficult to simulate the effects predicted by SIMMER-I with SIMMER-II, given the SIMMER-II input allowed in the current format. However, this conclusion should not be interpreted as denoting the absolute impossibility of achieving greater liquid kinetic energies at slug impact with SIMMER-II. For example, sodium vaporization can be increased by moving the liquid sodium interface from the top of the fission gas plenum to the core blanket interface. In an HCCA, sodium could indeed be closer to the core if a blockage existed before the disassembly event. In a case simulating this configuration, the system kinetic energy at slug impact increased to 9 MJ. To limit the quenching phenomenon caused by liquid fuel to liquid steel

heat transfer, one can assume that the disassembly event takes place under transition phase conditions, where the predisassembly liquid steel temperature is above the fuel melting point. Using the previous case but increasing the steel temperature to 3300 K gave an increased kinetic energy at slug impact to ~ 20 MJ.

In conclusion, the more complex treatment in SIMMER-II does not seem to change the basic conclusions drawn from the SIMMER-I study<sup>33</sup> in that a large reduction in the maximum system kinetic energy can result from a mechanistic treatment of the predisasassembly core expansion following an energetic core disassembly event. Indeed, considerable insensitivity to model assumptions and especially to material properties seems to be present as long as there is not a significant change in the role of the above-core structure upon the character of the pressure source that acts on the bulk sodium. The details of the expansion do change in SIMMER-II. There are two principal effects observed in cases done to date. First, the dynamic calculation of the liquid droplet radius in SIMMER-II tends to increase heat transfer in a situation where a hot liquid is premixed with a cold liquid and to decrease heat transfer if the liquids are initially separated. Second, the current models of SIMMER-II more completely integrate all the fluid dynamics and heat transfer phenomena, thereby decreasing the flexibility for the user to change one phenomenon while holding everything else constant. This latter characteristic is advantageous from the standpoint of more correctly simulating the true nature of the event under study, but it tends to make the calculated results less transparent to the user's interpretation.

### 3. Application of Probabilistic Methods to Work-Energy Partition Calculations with SIMMER-II

(R. D. Burns, III and L. B. Luck, O-7)

The impact of uncertainties in input values for work-energy partition calculations was studied as a part of the SIMMER verification effort. The statistical procedure for SIMMER sensitivity analysis was used.<sup>8,34</sup> Distributions of results were calculated based on the statistical variations of uncertain input values, and sensitivity analyses were performed. A few node version (3 radial and 12 axial nodes) of the work-energy partition problem<sup>33</sup> was used to gain experience with both the statistical procedure and the problem itself and to provide a basis for designing the analysis of the larger, more detailed version (20 radial and 38 axial nodes) of the problem.

As the first step in the analysis, input uncertainties were specified, including initial conditions, exchange coefficients, equation-of-state parameters, and SIMMER-II convergence parameters. A total of 20 independent parameter variations were used. A realistic description of the uncertainty ranges for these parameters was not attempted. This has been postponed until the analysis of the larger problem. Therefore, most input values were taken to vary within 10% of their reference values, and all probability distributions were assumed to be uniform. The 10% ranges were modified for some parameters when the analysis led to nonphysical initial conditions.

The impact of input parameter uncertainties was measured by observing variations in key output quantities. Some of these are time-varying quantities while others are time-integrated or end-point quantities. These include vessel head impulse; component mass and energy; structure, liquid, and vapor-field volume fractions; and other SIMMER-II output quantities.

Ten SIMMER-II calculations were performed using different values of each uncertain input parameter. The input sets were independently and randomly selected, thus making it possible to calculate average values and standard deviations of output quantities.

The sensitivity analyses were based on calculations of partial ranked correlation coefficients (PRCCs). The significance of PRCCs is explained as follows: if an input value monotonically affects a particular output value, the input and output values will rise and fall correspondingly from run to run. For strongly correlated relations, the maximum value of the output quantity should occur in the SIMMER-II calculation using the maximum (or minimum, for inverse relationships) value for the correlated input parameter. The next largest output value should occur in the calculation with the next highest input value, and so on throughout the rest of the sequence of 10 runs.

To quantify the degree of correlation, each input and output sequence is transformed by replacing the lowest value in the sequence with 1, the next highest with 2, and so on. Then for strong correlations, the sequences of numbers 1 through 10 should correspond exactly (or inversely). Usually, however, more than one input variation will affect an output value, and the transformed output value sequence will not correspond exactly to any input

sequence. It should, however, be similar to one or more input sequences. The PRCC is therefore used as a quantitative measure of the degree of correspondence between sequences.

The PRCC is calculated using the transformed sequences of numbers 1 through 10:

$$\text{PRCC} = 1 - \frac{\sum_{i=1}^n (x_i - y_i)^2}{n(n^2 - 1)}, \quad (44)$$

where

- $n$  = number of calculations (i.e.,  $n = 10$ ),
- $x_i$  = transformed value of input parameter value for  $i^{\text{th}}$  calculation,
- $y_i$  = transformed value of output quantity value for  $i^{\text{th}}$  calculation.

The absolute value of the PRCC is always less than or equal to one. Values close to one indicate direct correlation, close to minus one indicate inverse correlation, and close to zero indicate no correlation. By comparing each output sequence with each input sequence in this manner, output variations can be explained in terms of specific input uncertainties. (In addition, the PRCC can be used to cross-correlate two output values.)

All calculations were for 250 ms of accident time. Vessel head impact occurs after 150 ms and peaks at 200 ms. The results of the calculations and the analysis follow.

1. Variations in the calculated mass of sodium vapor are large during the transient and appear to show that the strength of fuel-coolant interaction (FCI) is considerable in some cases. The initial sodium vapor mass is 4 kg. The maximum observed mass occurs at 100 ms and is 184 kg, indicating a possibly strong FCI preceding vessel head impact. This is apparent from the strong correlation (PRCC = 0.92) between rise in core pressure and sodium vapor mass at 100 ms. In three of the 10 runs, however, the sodium mass does not exceed 26 kg, indicating no strong FCI in these cases.

Figure 43 summarizes the calculations of sodium vapor mass for 10 SIMMER-II calculations. The maximum curve in Fig. 43 represents the maximum of the 10 calculated values at each point in time.

Based on PRCC calculations, the variation in initial core liquid fuel temperature appears to be responsible for the wide variation in

sodium vapor mass generation due to FCI. The standard deviation in fuel temperature is 6% of the mean, whereas the standard deviation in sodium vapor mass is 85%, indicating that the strength of FCI is both nonlinear and sensitive.

2. The liquid field kinetic energy shows wide variation and is strongly cross-correlated with the sodium vapor mass generation (PROC = 0.90). This indicates a strong relation to the strength of the FCIs. Initially zero for all runs, the maximum observed liquid field kinetic energy was 200 MJ, which corresponds to the highest observed value for sodium vapor mass and core pressure at 100 ms. In 3 of the 10 calculations, this value remains below 20 MJ.
3. As shown in Fig. 44, the vessel head impulse is five times greater in the maximum than in the minimum of 10 calculated values. At 250 ms the standard deviation is 44% of the  $1.4 \times 10^5$  N-s average impulse. The impulse is defined as the area-weighted integral of pressure in the upper row of SIMMER cells.

The variation in the magnitude of the impulse after 150 ms is most closely related to the uncertainty in the fuel heat of vaporization (PROC = - 0.7). There is no correlation of impulse magnitude and the FCI-related quantities: sodium vapor mass, total liquid field kinetic energy, and core pressure increase. The inverse correlation with fuel heat of vaporization implies that lower values for the heat of vaporization lead to greater impulse.

4. Little deviation is observed in the calculations of the following output quantities: liquid fuel temperature, total system energy, and the field volume fractions.

The average computation time for the calculations was 240 s on the CDC 7600. The maximum and minimum for 10 runs were 262 and 152, respectively. This variation in time is not clearly related to any specific input parameter variation.

In conclusion, the above examples demonstrate the use of statistical techniques in the analysis of accident phenomena using SIMMER. A more careful study in which input parameter uncertainty ranges are carefully specified and in which a finer nodal structure is used is under way. The results of that study will be used, in part, to plan experiments related to sensitive and uncertain aspects of the SIMMER modeling for this problem area.

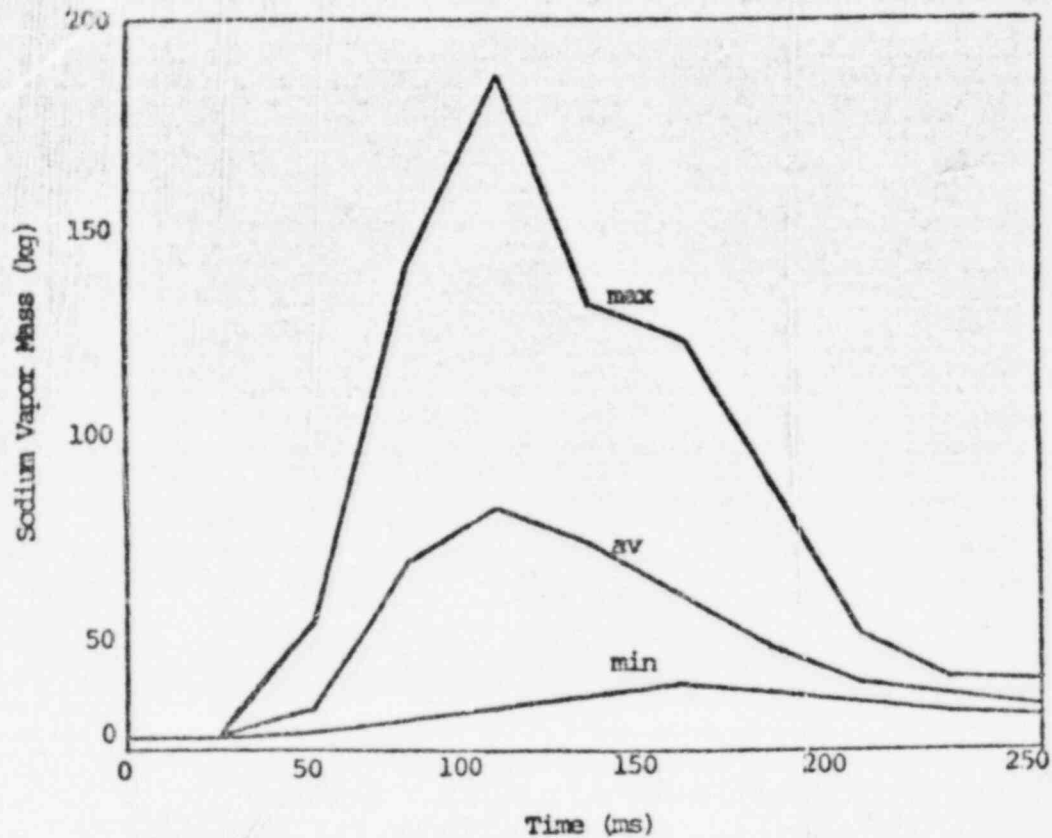


Fig. 43.  
Sodium vapor mass — maximum, minimum, and average for 10 SIMMER-II calculations.

B. Modeling of Phenomena and Studies on the Limits and Control of CDA Energetics

(C. R. Bell, 0-7)

The SIMMER-I analysis<sup>33</sup> of the postdisassembly core expansion and system kinetic energy development identified several important phenomena which appear to contribute to the low system kinetic energy calculated at the time of sodium pool impact with the reactor vessel head. Some of these phenomena are

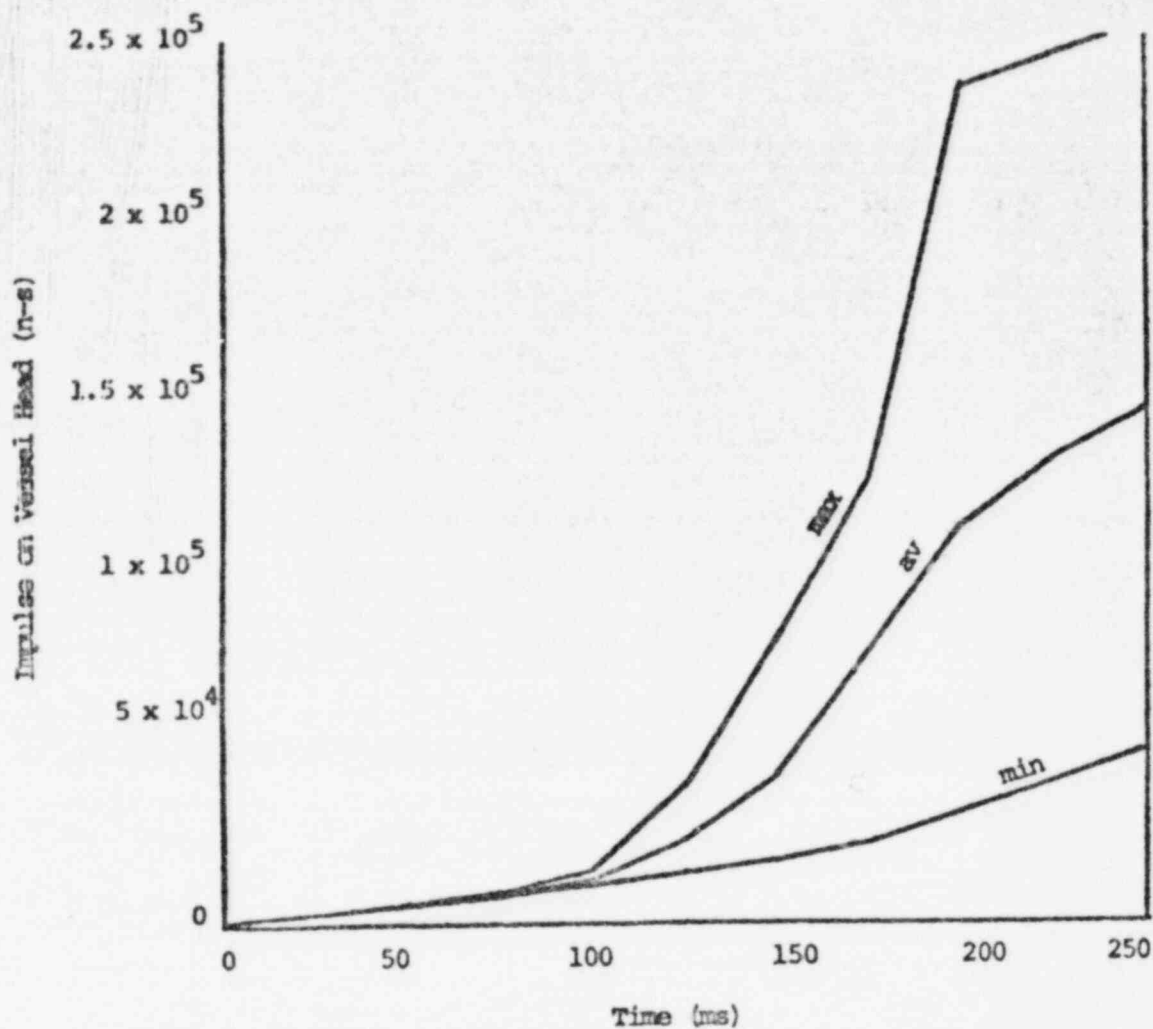


Fig. 44.  
Impulse on vessel head -- maximum, minimum, and average for 10 SIMMER-II calculations.

being investigated with a simplified one-dimensional representation of the reactor geometry. A study of the character of the nonuniform expansion phenomenon has been performed and is presented below. The ability of SIMMER to correctly predict this behavior is assessed and found to be highly acceptable.

The postdisassembly core expansion analysis referred to above and other applications of SIMMER-I, such as the long-term meltdown of a subassembly<sup>35</sup>

indicate that condensation and vaporization in complex environments may play a substantial role in the results. The multicomponent condensation model<sup>35</sup> recently developed and implemented in SIMMER-II is intended to provide a more realistic treatment of the process in these environments. Initial results from the verification experiments<sup>35</sup> for this model have been obtained and analyzed. The comparison of these results with the model indicates good agreement between experiment and model if material properties are evaluated at the appropriate position in the vapor stream.

#### 1. Evaluation of Nonuniform Expansion Phenomenon in the Postdisassembly Core Expansion

(C. R. Bell, P. J. Blewett, and G. P. DeVault, Q-7)

The nonuniform expansion phenomenon has been identified<sup>33</sup> as playing an important role in the reduction of the severity of the postdisassembly core expansion as calculated by SIMMER-I for an assumed highly energetic core disruptive accident. The SIMMER-I code<sup>32</sup> calculates the kinetic energy acquired by the fluids in the reactor system before the sodium pool impacts the reactor vessel head as a measure of the potential damage to the primary system. The object of this study is to determine the accuracy with which the total kinetic energy of the expanding core-sodium slug system is calculated by SIMMER-I. Our approach is to compare the SIMMER-I results with those of a vastly different code, WONDY<sup>36</sup> when the two codes are forced to treat this expansion problem in a consistent manner.

SIMMER-I is a complex multicomponent, multifield Eulerian code while WONDY is a single-phase, one-dimensional Lagrangian code. Figures 45 and 46 give the geometric models and detailed initial conditions for the standard cases for SIMMER-I and WONDY, respectively. In Fig. 46 it is seen that the entire sodium slug is replaced merely by the boundary condition,

$$\ddot{x}_{61} = P_{60}/M_S, \quad (47)$$

where  $P_{60}$  is the zone-centered pressure in the 60th zone,  $M_S$  is the sodium slug mass per unit area and  $\ddot{x}_{61}$  is the acceleration of the core-slug interface. The slug and core masses are identical in both treatments. The zoning used in the two cases is very different due to the different numerical methods used by SIMMER-I and WONDY.

A second major difference between the two codes is in the thermodynamic treatment of the flashing, two-phase fuel-steel material in the core region.

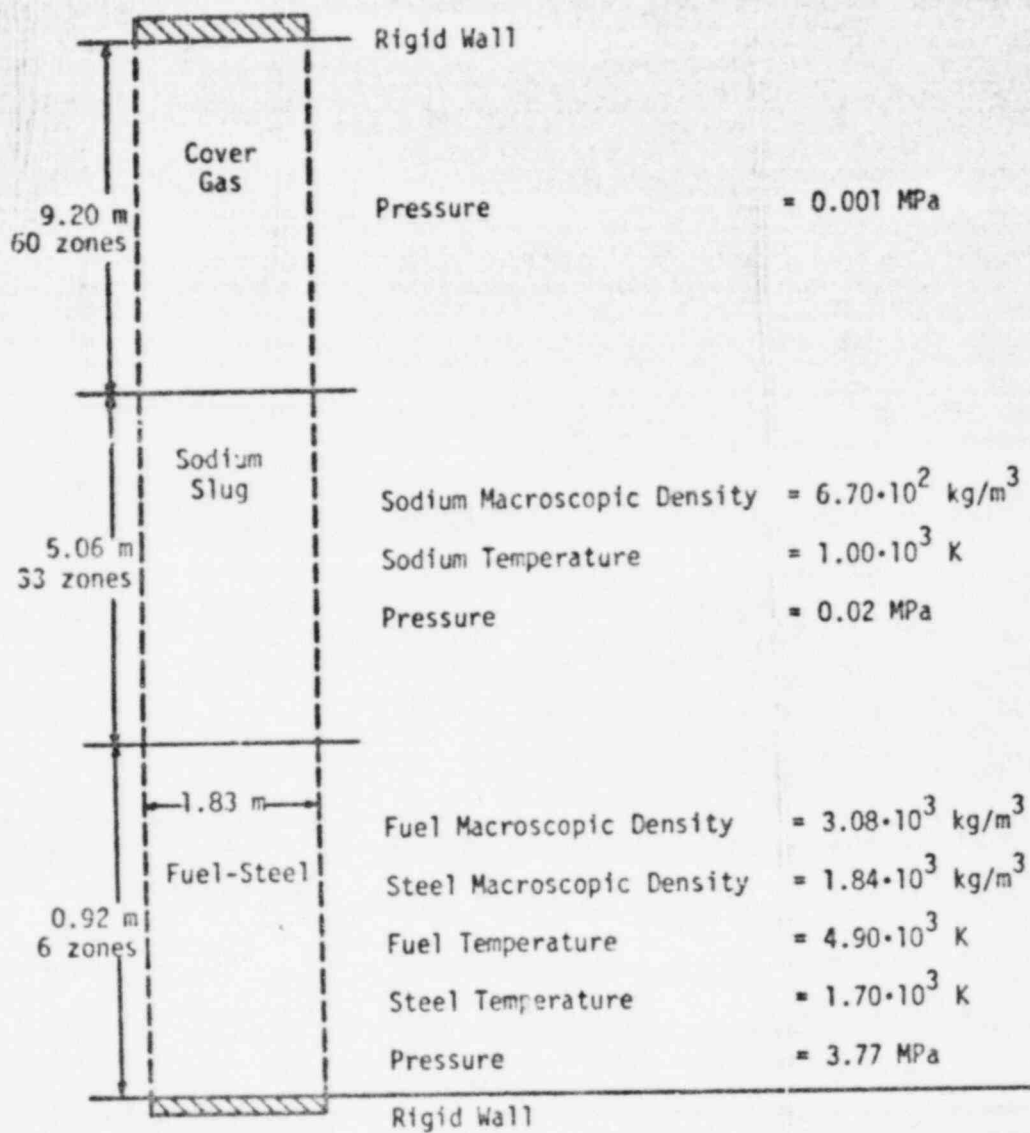


Fig. 45.  
Geometric model and initial conditions for the standard case SIMMER-I calculation.

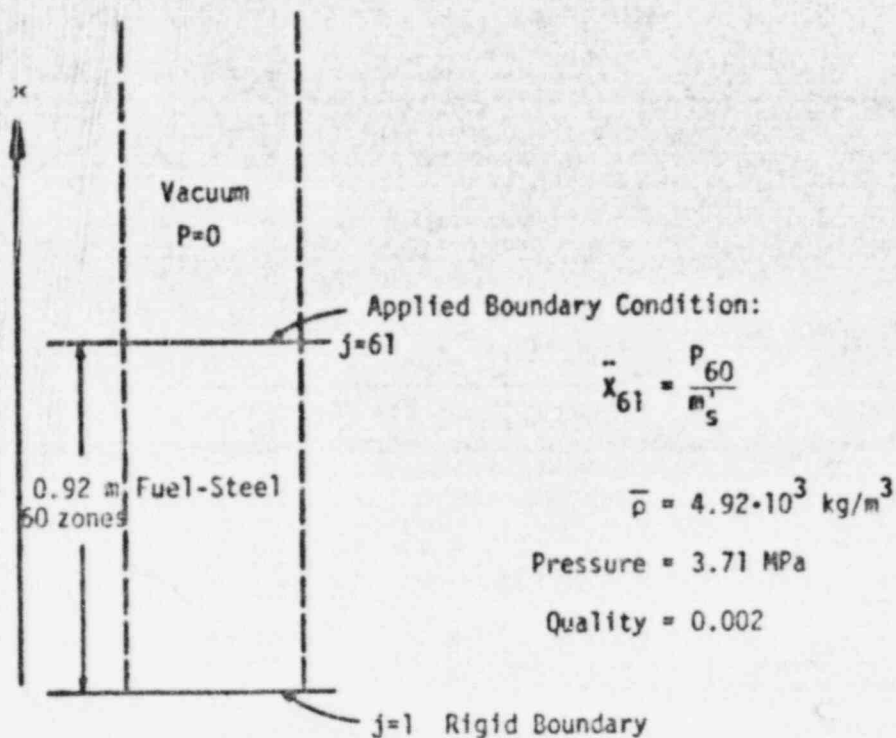


Fig. 46.  
Geometric model and initial conditions for the standard case WONDY calculation.

Because WONDY treats a single-phase system only, a new equation of state was required for the overall two-phase mixture. The equation of state was represented as a pressure versus density table. To determine this equation of state, the following assumptions were made.

1. The liquid fuel and liquid steel are incompressible and the latter is only a noninteractive mass added to the former.
2. The specific heat,  $c$ , and the heat of vaporization,  $h_{fg}$ , of the fuel are constant.
3. The specific volume of the liquid fuel may be ignored, compared to the specific volume of the fuel vapor.

4. The vapor component is an ideal gas.

Let  $x$  be the quality (vapor mass fraction) and  $T$  be the saturation temperature of the two-phase fuel-steel system. From initial values,  $T_1$  and  $x$ , to final values,  $T_2$  and  $x + \Delta x$ , the change in the specific entropy,  $\Delta s$ , of the mixture by assumptions 1 and 2, is

$$\Delta s = h_{lg} \left[ \frac{x+\Delta x}{T_2} - \frac{x}{T_1} \right] + c \ln \frac{T_2}{T_1}. \quad (48)$$

If this process takes place reversibly within an adiabatic enclosure (let  $T_1 = T$  and  $T_2 = T + \Delta T$ ), Eq. (48) becomes

$$\frac{dx}{dT} - \frac{x}{T} = - \frac{c}{h_{lg}}, \quad (49)$$

or

$$\frac{x}{T} = \frac{x_1}{T_1} + \frac{c}{h_{lg}} \ln \frac{T_1}{T}, \quad (50)$$

where  $x_1$  is initial quality. Hence,  $x$  is determined by  $T$ . By assumptions 3 and 4, Eq. (48) also implies the Clausius-Clapeyron equation. Therefore, the pressure,  $p$ , and the vapor density,  $\rho_g$ , are determined as functions of  $T$ . Then  $p$  as a function of two-phase mixture density,  $\bar{\rho}$ , is obtained by combining Eq. (50), the perfect gas law, the Clausius-Clapeyron equation, and the following equation,

$$\frac{1}{\bar{\rho}} = v = x v_g + (1-x)v_l. \quad (51)$$

Figure 47 shows this dependence over the range of interest and it is noticed that the curvature is opposite to that of a single-phase material, i.e., the sound speed decreases with density.

In contrast to the WONDY model, SIMMER-I calculates the macroscopic densities of the gas and liquid components separately by the use of the respective continuity and momentum equations and the mass exchange between phases. For these calculations the phase transition model in SIMMER-I is purposely

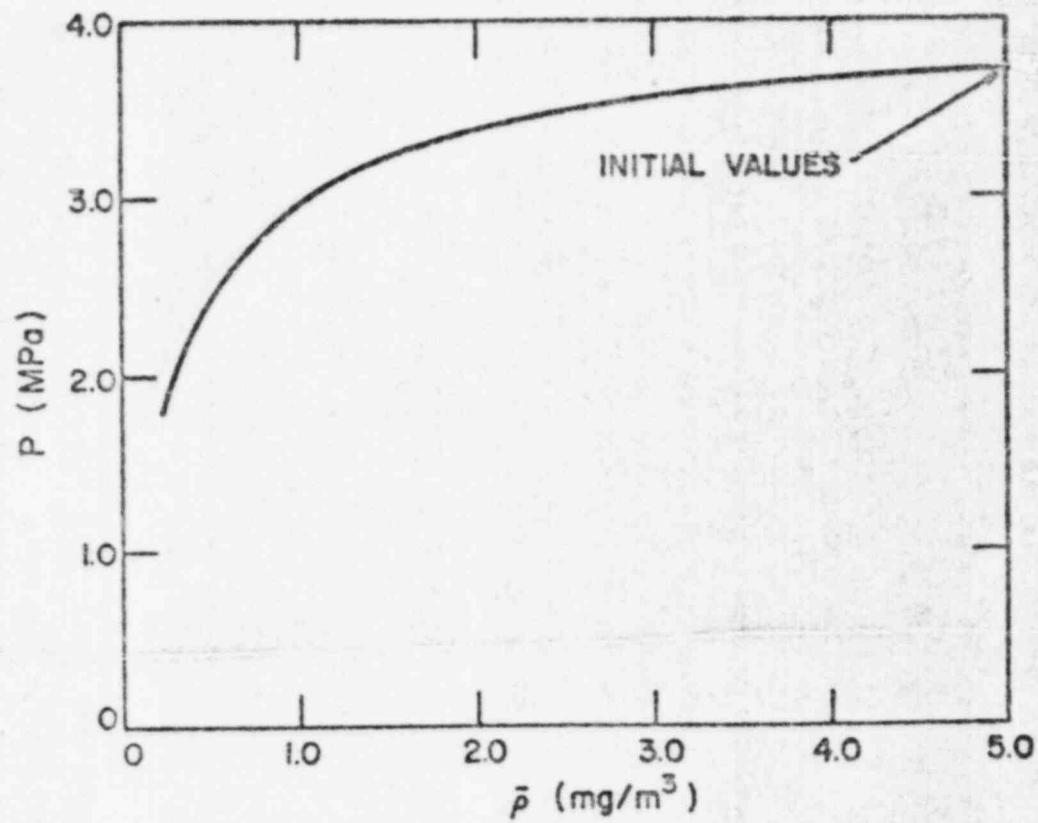


Fig. 47.  
Dependence of pressure on density of the fuel-steel mixture for WONDY calculations.

adjusted so that the vapor and liquid components are continually in saturated equilibrium. The relation between temperature and pressure along the saturation curve has the same analytic form as the solution to the Clausius-Clapeyron equation under assumptions 3 and 4 but the constants in the equation differ markedly. Also, the heat of vaporization is treated as a function of temperature. Finally, the dissipative processes of heat transfer and inter-field drag are eliminated in the SIMMER-I calculations by using zero values for the heat exchange coefficients and by eliminating slip between the fluid phases.

The early dynamics of the WONDY calculation are simple. At  $t = 0$ , a rarefaction fan begins to form with one boundary moving toward the rigid wall with the ambient sound speed,  $c_0$ , of the fuel and steel mixture. The other boundary is the core-slug interface as it accelerates in the opposite direction. The WONDY treatment can be checked in the case of an ideal gas as the expanding medium because this problem has an analytic solution.<sup>37</sup> Figure 48 compares a WONDY calculation with the analytic solution. The normalizing time,  $\tau$ , is interpreted as the time required to accelerate the sodium slug mass,  $M_S$ , by the initial pressure,  $p_0$ , to the sonic velocity,  $c_0$ , of the gas at the initial conditions. In Fig. 48,  $\tau$  is less than the transit time of the rarefaction wave to reach the rigid wall, hence the rigid wall does not influence the motion of the slug. Upon reflection of the wave at the rigid wall, another rarefaction is formed and the flow becomes more complicated. Figure 48 indicates that WONDY's accuracy for this problem is within 0.5%. For the fuel-steel mixture, similar behavior occurs in the WONDY calculations and we can have considerable confidence in its predictions. In the SIMMER-I calculations, a rarefaction wave travels into the core while simultaneously a pressure wave travels into the sodium slug, accelerating it progressively toward the head.

Our primary interest in this study is to compare the kinetic energy of the total fuel-steel, sodium slug system when the slug has been displaced 8.02 m. For a cylinder of radius 0.913 m, this would represent a displacement of 21.0 m<sup>3</sup> which is approximately the cover gas volume in CBR. Figure 49 shows the results of 8 SIMMER-I calculations and 13 WONDY calculations in which the slug mass,  $M_S$ , is varied over a wide range. The core mass is fixed at 11 900 kg, which equals the combined inventories of fuel and steel in the active core of CBR. The slug mass was chosen as the parameter to vary for comparison of the

two methods since in the postdisassembly core expansion analyses, this mass or inertial constraint controls the magnitude of the nonuniform expansion effect.

The two extreme points in Fig. 49 represent different times to slug impact with the vessel head. For the maximum slug mass, WONDY predicts a time to impact of 350 ms. For the minimum slug mass, WONDY predicts the slug impact at 20 ms. For all practical purposes, the minimum WONDY value represents a free expansion of the fuel-steel system. For small values of  $M_g$ , the Lagrangian zone adjacent to the core-slug interface becomes progressively larger; thus, more Lagrangian zones were added. For the three lower values of  $M_g$ , 720 zones were used. As  $M_g$  increases, the time scale of the problem is increased to the point that all transients in the core are damped out over the majority of the expansion. In this limit, the expansion tends to produce a constant force on the slug. Therefore, the analysis reduces to a constant acceleration problem in which the kinetic energy at slug impact is independent of  $M_g$  and approaches the isentropic limit of a completely uniform expansion.

The SIMMER-I results show the same general dependency of system kinetic energy on slug mass as calculated with WONDY. In fact, the agreement is

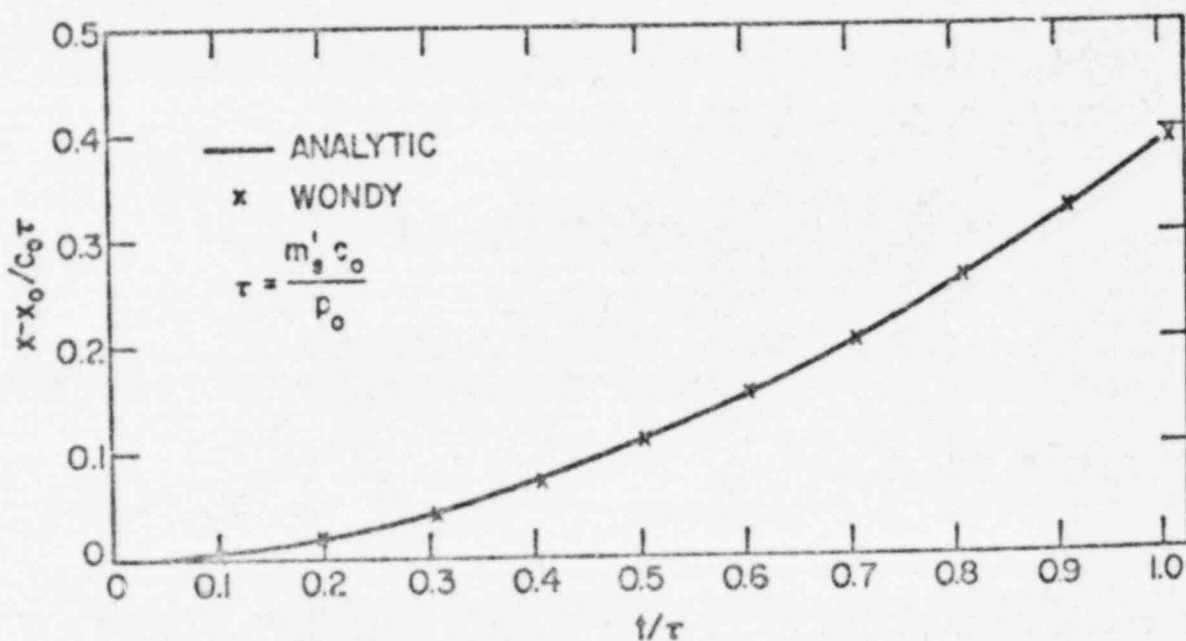


Fig. 48.  
Slug displacement as a function of time for an ideal gas,  
 $\alpha = 1.06$ .

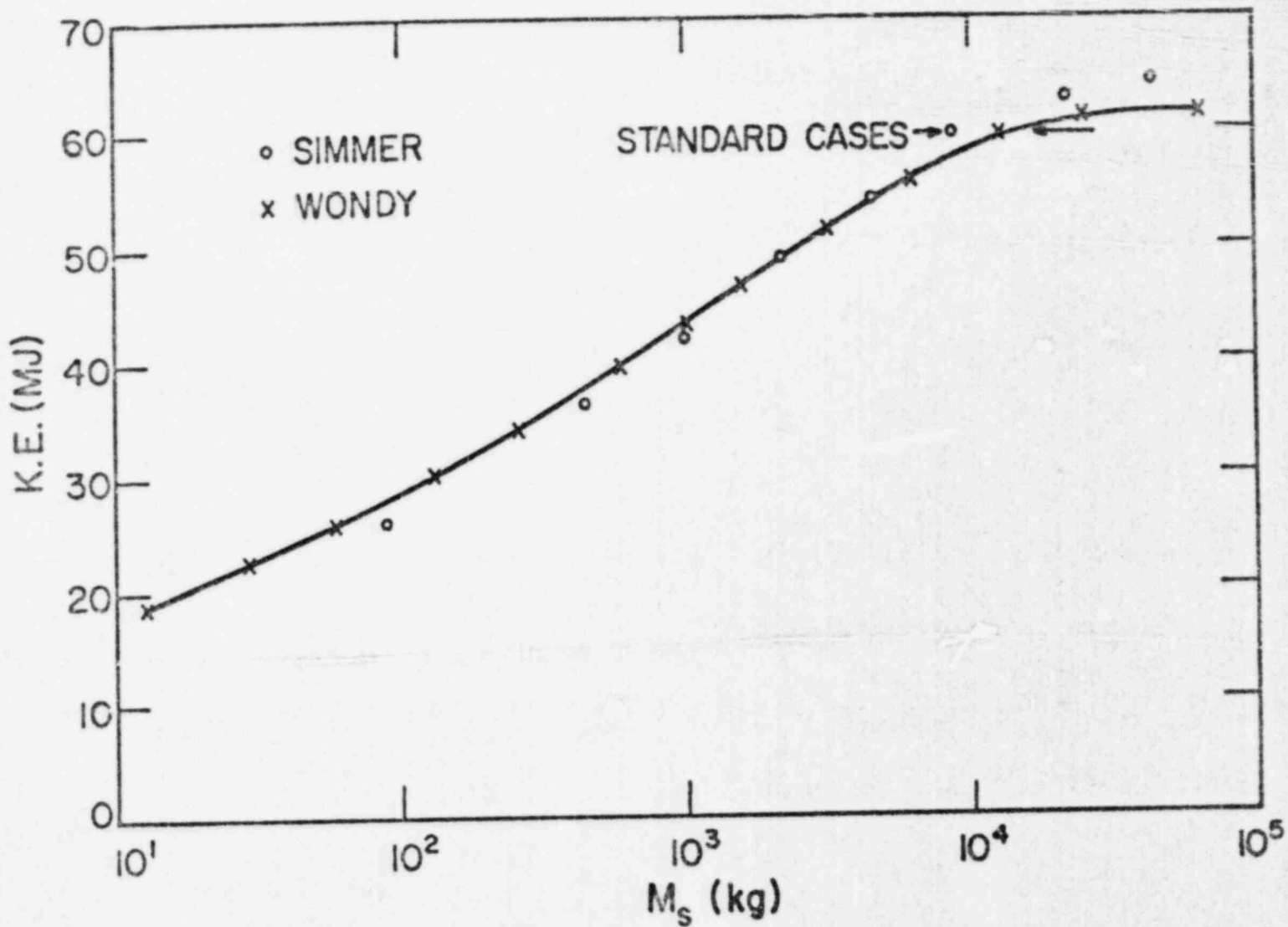


Fig. 49.  
Kinetic energy of the system at slug impact as a function of slug mass.

remarkably good between the two very different calculations. In the high mass limit SIDMER-I predicts a slightly higher kinetic energy. This can be attributed to the different constants used in the relationship between the saturation temperature and pressure and the nonconstant heat of vaporization used in SIDMER.

We conclude from this study that the treatment of the nonuniform expansion phenomenon by SIDMER-I is essentially correct from a purely fluid dynamics standpoint. It not only predicts the behavior appropriately in the slug mass range of interest but also approaches the isentropic work potential in the mild expansion (high slug mass) limit as it should. This also leads us to believe that the basic phase transition representation is correct.

Further work in this area will consider the relaxation of some of the constraints employed in this study. These will include the effects of slip and nonequilibrium vaporization and condensation.

## 2. Analysis of Multicomponent Condensation Experiments

(A. J. Suo-Anttila, Q-7)

The purpose of the initial series of multicomponent condensation experiments<sup>35</sup> performed with a steam-air system was to check out both the experimental apparatus and the theoretical multicomponent phase transition model.<sup>35</sup> A steam-air system was chosen as the simulant system because the materials are nontoxic, the thermophysical properties of these components are readily available, and the air acts as a noncondensable gas.

The experiments were conducted by filling the bottom of the condensation apparatus with water, which was subsequently boiled with a 2 kW heater. The vapors were heated in the superheat section to 408 K. Air was injected into the boiler section at various flow rates so that variable free stream noncondensable concentrations were generated. A copper sphere (0.025 m diam) was suddenly immersed into the test section. The superheated steam condensed on the sphere and caused a transient rise in sphere temperature. The temperature rise of the copper sphere was recorded by a strip chart recorder via a thermocouple imbedded in the center of the sphere.

The theoretical predictions of the copper sphere temperature were made with the multicomponent phase transition model<sup>35</sup> now available in SIDMER-II. The model was modified to account for the presence of a condensed liquid film and a natural convection boundary layer. The condensed liquid film was

included by using a standard Nusselt film formula applicable to spheres,<sup>38</sup> i.e.,

$$Nu = \frac{hD}{k_l} = 0.785 \left[ \frac{g \rho_l^2 h_{fg} D^3}{\mu_l k_l (T_i - T_w)} \right]^{1/4}, \quad (52)$$

where  $h$ ,  $k_l$ ,  $D$ ,  $g$ ,  $\rho_l$ ,  $h_{fg}$ ,  $\mu_l$ ,  $T_i$ , and  $T_w$  are the liquid film heat transfer coefficient, liquid film thermal conductivity, sphere diameter, gravitational acceleration, liquid density, latent heat of vaporization, liquid viscosity, vapor-liquid interface (surface) temperature, and the sphere surface temperature, respectively. The surface temperature of both the sphere and the liquid film were calculated implicitly during the course of the time-dependent calculation. The natural convection boundary layer was modeled by using a standard correlation available in the literature.<sup>39</sup>

$$Nu = \frac{h_v D}{k_v} = 2 + 0.55 \left[ \frac{g \rho_v (\rho_\infty - \rho_i) D^3}{\mu_v^2 Pr} \right]^{1/4}, \quad (53)$$

where the subscript  $v$  implies vapor phase. The driving force,  $\rho_\infty - \rho_i$ , is the vapor density difference between the vapor-free stream and the surface (vapor-liquid interface). Proper evaluation of the vapor phase properties is crucial in obtaining reasonable agreement with experiment because significant concentration gradients of the two species (water and air) exist in the boundary layer.

The results of the experiments and the analyses are shown in Figs. 50 and 51. Figure 50 shows experimental measurements and theoretical predictions for the temperature rise of the copper sphere with variable amounts of air present. Excellent agreement can be seen for the case having 1.8% air concentration. The experimental data for the "no-air" case fall slightly below the theoretical prediction. This is probably caused by trace quantities of air in the apparatus during the experiment. If a trace quantity of 1 ppm is assumed, the experiment and prediction agree. The case of 10% air had somewhat poorer agreement, probably due to variations in the vapor-liquid interface temperature over the surface of the sphere. A deviation should be expected at low mass transfer rates because the Nusselt number correlations for the liquid

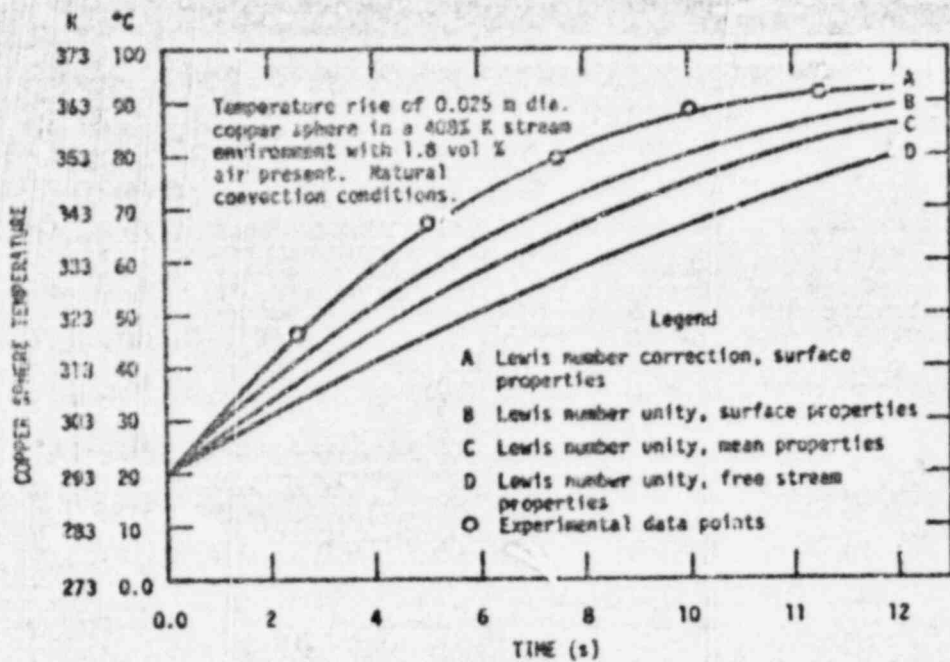


Fig. 50.

Temperature rise of a 0.025 m diam copper sphere in a 408 K steam environment with variable amounts of air present under natural convection conditions.

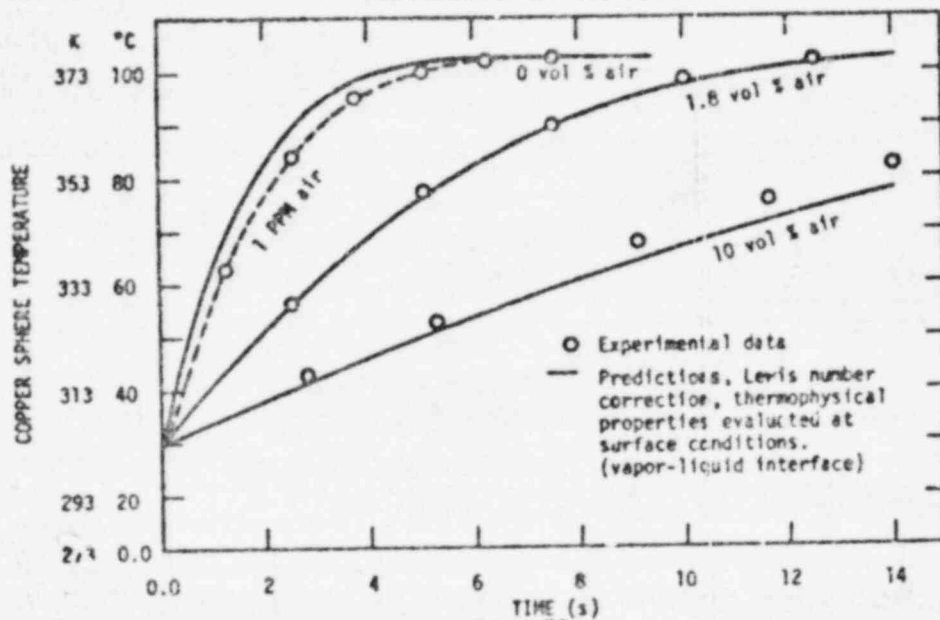


Fig. 51.

Variation in the predictions with respect to thermophysical property evaluation.

film and the vapor boundary layer are based upon average temperatures over the surface. Further, the accuracy of these correlations was not reported in the literature.

Figure 51 shows the effect of thermophysical property evaluation upon the predicted results. All of the curves in Fig. 51 correspond to the 1.8% air case in Fig. 50. Curve A represents the prediction using the thermophysical properties of the vapor-liquid interface (surface) and has been corrected for the mass diffusivity of the water-air mixture, i.e., no assumption has been made about the Lewis ( $Le$ ) number, the ratio of the mass diffusivity to the thermal diffusivity. If the mixture mass diffusivity is taken into account (i.e.,  $Le = 1$ ), curve B is the result. The assumption of a Lewis number of unity is essential in simplifying the calculations when more than two components are involved. Curves C and D are the predictions one would obtain using the mean-boundary layer and free-stream properties, respectively.

Future experiments will include forced convection and vapor systems with greater variations in properties, such as  $He-H_2O$  and  $CO_2-H_2$ . These experiments should help to resolve the question of thermophysical property variations and will also provide for different flow conditions.

Our conclusion on this first set of experiments and analyses is that the multicomponent phase transition model adequately predicts the behavior of a binary vapor system provided that adequate thermophysical property data and heat transfer correlations are available.

### C. SIMMER Model Development and Verification Experiments

(J. H. Scott, Q-7 and H. H. Helmick, Q-8)

Two activities related to SIMMER verification were completed this quarter. Diagnostics development for and statistical analysis of the interfield drag (air-particle) experiments were completed. Also, preliminary tests for the flow coastdown simulation were performed. The tests led to definition of new experiment needs related to this class of experiments.

#### 1. Interfacial Area and Drag Experiment

(P. E. Rexroth, Q-7 and V. S. Starkov, Q-8)

In current SIMMER modeling, momentum coupling between liquid and vapor is included through drag force terms. The interfacial area and drag experiment is intended to evaluate the vapor droplet drag correlation for a variety

of component and flow properties. The previous quarterly report<sup>2</sup> included a brief description of the experimental apparatus and procedure. The slugging motion that occurred when nitrogen gas was passed through a column of glass beads was described. It was noted that the SIMMER analysis of the experiment yielded this same general slugging behavior, as well as similar values for maximum slugging height and period.

To facilitate correlation between the calculations and experiments, more quantitative data are required from the experiment such as the void fraction in the column as a function of time and location. Among the methods we have considered to obtain these data are:

1. flash x radiography with subsequent optical densitometry on the resulting images,
2. measurement of electrical conductance or capacitance across the tube, which can be related to the amount of material at the measured location, and
3. gamma densitometry.

We have chosen gamma densitometry as the best short-range option. For gamma densitometry, the experimental column is located between a series of gamma-emitting sources and sodium iodide detectors spaced along the length of the tube. The magnitude of the signal reaching the detectors can be related to the amount of material between the source and detector. Based on the successful performance of a single gamma probe, several sources and detectors will be obtained so that data can be taken simultaneously at several axial locations. The signals from the detectors will be digitized and processed by computer.

A two-channel analog-to-digital converter system using two Hewlett-Packard 5416A converters, a Digital Equipment Corporation PDP 8/I, and appropriate interfacing electronics is operational. Additionally, more powerful and much more flexible data acquisition and control equipment is either delivered or is in transit. Simultaneous pulse counting from two gamma densitometer channels is operational. The system is being expanded to handle 12 simultaneous counting channels.

The experimental program was extended this quarter to include an initial evaluation of the equipment in the gas-liquid flow system. An experiment was performed in which colored water replaced the beads of the previous runs. The

behavior resulting from several different gas flow rates was observed and recorded on color movie film. At very low vapor flow velocities ( $\sim 0.1$  m/s), a turbulent bubbly flow was observed, displaying little or no apparent periodicity. At higher flow rates, some slugging was observed, but high levels of turbulence masked the periodicity.

When the multiprobe gamma densitometer is available, data from the system will be analyzed using autocorrelation techniques in an attempt to identify any periodicity that might exist. We have begun SIMMER calculations to simulate the behavior of a gas-liquid system.

## 2. Statistical Analysis of the Interfield Area and Drag Experiment

(R. D. Burns, III and P. E. Ruxroth, O-7)

Previously reported results<sup>2</sup> of analysis of the interfield area and drag experiment indicated that the behavior of the fluidized bead bed as calculated with SIMMER-I closely resembled experimental observations. These results enhanced the confidence in the SIMMER-I treatment of interfield drag. The results reported here provide a statistical analysis of the experiment and an understanding of the calculational sensitivities.

Uncertainty in the selection of values of input parameters in the SIMMER-I calculations suggests the need to establish corresponding uncertainty or error bounds in calculated values for rise height and period of the rise and collapse cycle. This provides a basis for comparison with experiments. Quantification of the input uncertainty is shown in Table V.

Random selections of input values from the ranges specified in Table V were made according to the Latin Hypercube Sampling/Partial Ranked Correlation Coefficient (LHS/PROC) procedure for SIMMER-I sensitivity analysis. Twelve SIMMER-I calculations were performed for each of five rise and collapse cycles. Statistical and sensitivity analyses were based on the results of these calculations. The stack of glass beads was initially at rest.

Considerable variation among the 12 calculations was observed in the results for rise height. Figure 52 shows the average, maximum, and minimum values of rise height in each of five successive cycles. The range of uncertainty in rise height calculations is about 0.3 m (about 15%).

PROC correlations of the variations in rise height with each of the 10 input variations described in Table V show there are 3 input uncertainties dominating the results. A vapor density uncertainty of  $\pm 5\%$  correlates with

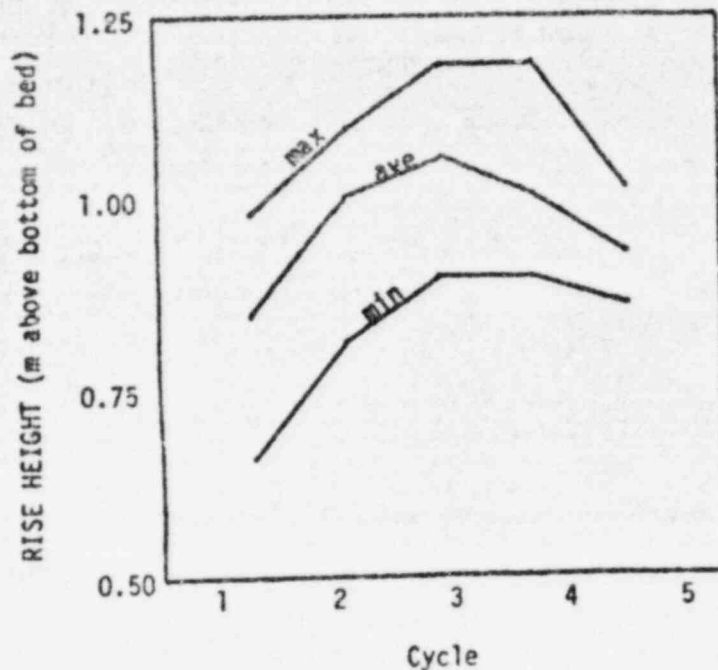


Fig. 52.  
Fluidized bed rise height — maximum, minimum, and average  
of 12 SIMMER-I calculations.

the rise height variation in cycles 1, 3, and 5 (PRCC = +0.7).<sup>\*</sup> Initial void fraction uncertainty correlates in cycle 2 (PRCC = -0.7) and initial stack height uncertainty in cycle 4 (PRCC = -0.8). No other input parameter correlation exceeded 0.55 for the absolute value of the PRCC during any cycle. Thus, it appears that the uncertainties in each of these three parameters contributes strongly to the rise height variation.

Figure 53 indicates about a 10% variation in the time to reach maximum height in the rise and collapse cycle. As with the rise height variations, three input uncertainties appear to dominate. Vapor density uncertainty correlates in cycles 3 and 4 (PRCC = +0.7), glass bead radius uncertainty correlates in cycles 1 and 5 (PRCC = -0.7), and vapor velocity uncertainty correlates in cycle 2 (PRCC = +0.7). These three input uncertainties each appear to contribute to the variations in rise/collapse period.

The internal SIMMER-I drag model is contained in the momentum exchange coefficient,  $K_g$ . This model involves several of the terms in the input

<sup>\*</sup> PRCC near 1 indicates direct relationship, near -1 indicates inverse relationship, and near 0 indicates no relationship.

uncertainty list in Table V. To determine the combined effect of the input uncertainties on the uncertainty in  $K_g$  and then to correlate drag uncertainty with the rise height and cycle period variations, the following analysis was performed.

The form of the momentum exchange is

$$K_g = \frac{3\rho_g \alpha_l}{2\alpha_g r_p} \left( 3\nu_g + \frac{1}{4} r_p C_D |v_g - v_l| \right) (v_g - v_l), \quad (54)$$

where

$v_g - v_l$  = relative vapor-bead velocity,

$\rho_g$  = microscopic vapor density,

$\alpha_l$  = bead volume fraction =  $(1 - \alpha_g)$ ,

$\alpha_g$  = vapor volume fraction

$r_p$  = glass bead radius,

$C_D$  = form drag coefficient, and

$\nu_g$  = vapor kinematic viscosity.

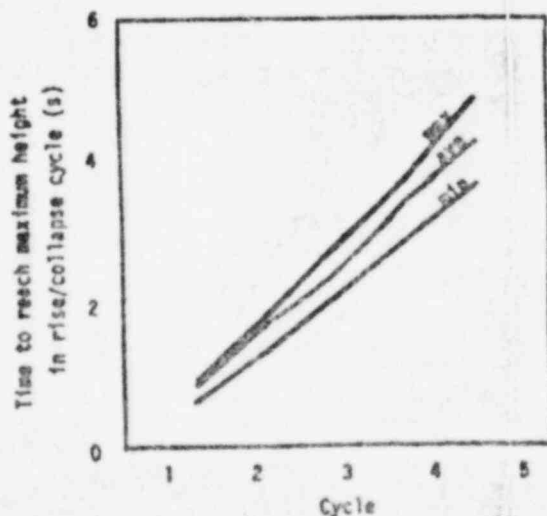


Fig. 53.

Fluidized bed rise/collapse cycle time -- maximum, minimum, and average of 12 SIMONE-I calculations.

TABLE V  
INPUT UNCERTAINTY FOR  
THE INTERFIELD AREA AND DRAG EXPERIMENT

<u>Input Parameter Description</u>	<u>Range</u>
(1) Vapor microscopic density ( $\text{kg}/\text{m}^3$ )	$975 \pm 5\%$
(2) Glass bead, microscopic density ( $\text{kg}/\text{m}^3$ )	$2350 \pm 15\%$
(3) Vapor specific heat ( $\text{J}/\text{kg}\text{-K}$ )	$718 \pm 5\%$
(4) Ratio of specific heats ( $\gamma = c_v/c_p$ )	$1.4 \pm 1\%$
(5) Vapor viscosity ( $\mu\text{P}$ )	$1.5 \times 10^{-5} \pm 10\%$
(6) Initial vapor-volume fraction	0.3 - 0.4
(7) Glass bead radius (m)	$0.0015 \pm 13\%$
(8) Vapor velocity (m/s)	$4.4 \pm 10\%a$
(9) Initial stack height (m)	$0.16 \pm 10\%$
(10) Form drag coefficient, $C_D$	$0.44 \pm 10\%$

<sup>a</sup>A recent check of the flow meter calibration indicates the nominal value may actually be considerably lower.

A drag-related coefficient dependent only on input parameters was derived from equation (54) by dropping dynamic quantities or assigning initial values.

This reduced drag correlation was then defined by

$$\text{Drag coefficient} = \frac{\rho_a a_l}{\alpha_{go}^2 r_p^2} (3v_g + \frac{1}{4} r_p C_D v_{go}) v_{go}$$

- $v_{go}$  = initial vapor inlet velocity,  
 $a_{lo}$  = initial bead volume fraction, and  
 $\alpha_{go}$  = initial void fraction.

This drag coefficient varied 30% from maximum to minimum in the 12 calculations.

PRCC calculations between the above drag coefficient and rise height and cycle period show very strong correlation. The PRCC of drag and height is above +0.7 for all five cycles and above +0.8 for four of the cycles. The drag/period PRCC is about +0.8 for four of five cycles. The positive values of the PRCC values indicate that increased drag leads to higher rise heights and longer rise and collapse cycle periods.

Experiments performed with a variety of vapor velocities and initial stack heights indicate that increasing either of these two parameters results in increasing the rise height and the rise and collapse cycle period. The direction of the vapor velocity dependencies is consistent with the analytical results. It is opposite for the stack height dependencies, which may be caused by the stack height variations in the SIMMER-I calculations being small (+ 0.002 m) compared to the height of the Eulerian SIMMER cell (0.04 m). Initial stack heights that are not even multiples of 0.04 m result in the spatial homogenization of the unfilled cell at the top of the stack. Hence, slight decreases in stack height should decrease the density in the uppermost cell of the stack, permitting it to be pushed to a higher rise height. This is consistent with the analytical results and implies that variations in stack height should be made consistent with the cell structure of SIMMER for the best calculational results.

### 3. Multicomponent Condensation Experiment

(W. M. Hughes, Q-8 and A. J. Suo-Anttila, Q-7)

Multicomponent condensation experiments (MCE) have been conducted. Analysis of the initial experiments has indicated good agreement for two-component, two-phase conditions. Subsequent experiments with three-components and three-phases are under analysis at this time. Components that have been used

include water, toluene, synthetic air, nitrogen, and helium. Modifications have been instituted recently to ensure better calibration of component flow rates, improved homogeneity of components, and better defined flow regime in the condensation region. Modifications that are presently being contemplated include a reworking of the apparatus to have better defined initial conditions.

A schematic of the MCE apparatus is given in Fig. 54. The entire system is wrapped with heat tapes, insulated, and instrumented with thermocouples. The three volumes are made of nickel-coated steel and the source chambers are stainless steel. Vapor and gas sources are found in the lower portion of the figure. Component flow rates are determined from a calibrated flow meter in the gas input line and by metering current/voltage input for boiling the liquids in the vapor source chambers. The components are mixed and heated additionally in the mixing volume.

An experiment is usually initiated by inserting a chilled body into the condensation volume. A thermocouple is located at the center of the condensation body and is the prime diagnostic device in these experiments. The body can be viewed through ports to determine such parameters as the condensation film uniformity and the time of phase change. It appears that analysis of motion pictures of the condensation process may be a useful diagnostic technique. Some experiments use a glass sleeve to provide conditions where the condensation rate is dominated by forced convection flow rather than being limited by diffusion flow.

A planned reconfiguration should allow analysis of data into the millisecond regime. Data taken under multicomponent multiphase fast-time scale conditions will begin to approach some of the complexity of a SIMMER calculation of an IMPER accident.

#### 4. Flow Coastdown Simulation Experiments

(H. M. Forehand, Q-7 and J. F. Davis, Q-8)

The flow coastdown simulation (FCS) experiments are a vehicle to test the overall capabilities and models of the SIMMER code and to provide guidance for future model and methods development and experiment definition. For the tests described herein, water (coolant), shrink fit tubing (clad), and zinc (fuel) were used. In the test vehicle for the FCS experiments, described in Fig. 55, zinc (simulant fuel) was heated by radio frequency induction with a coupling

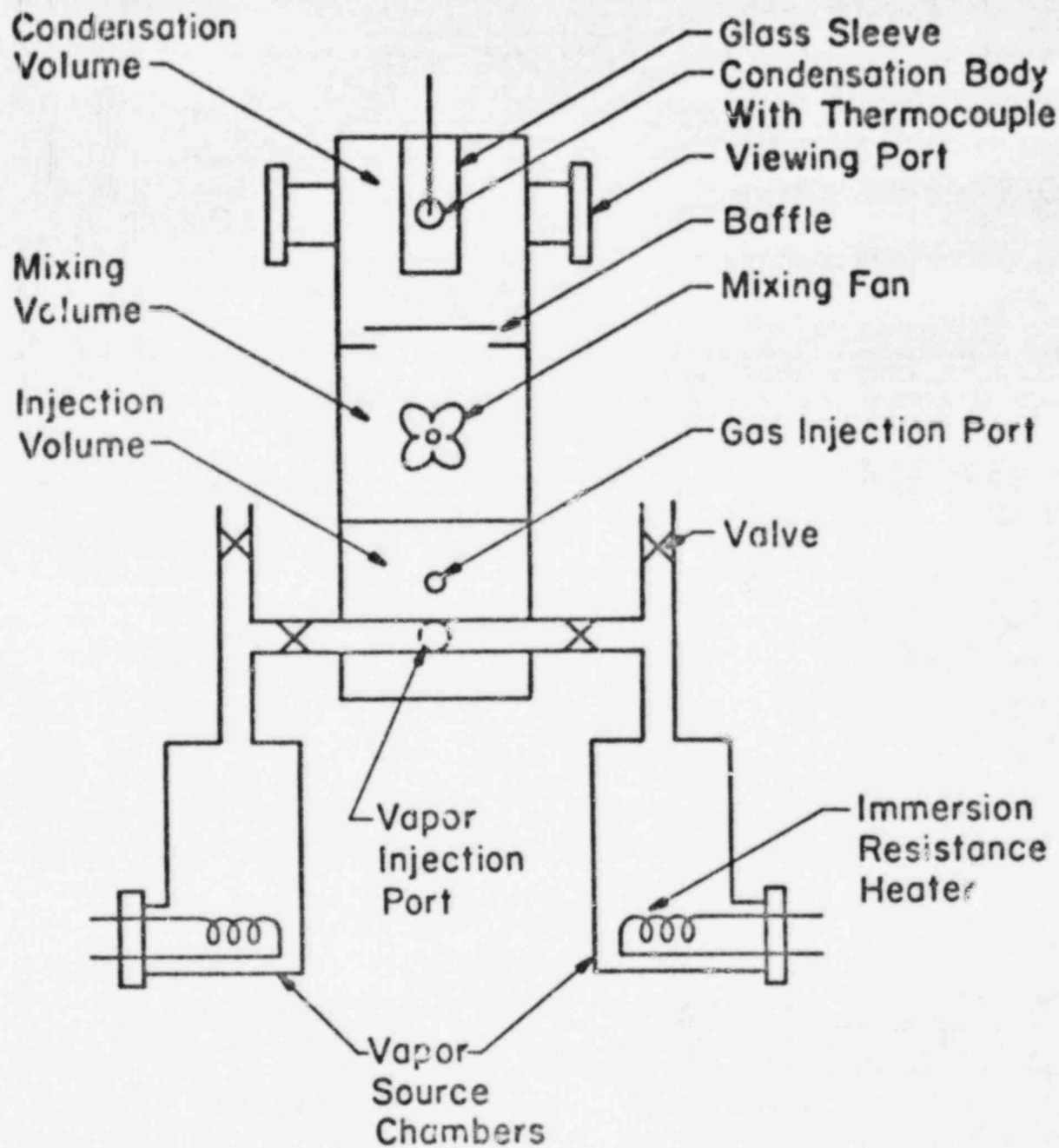


Fig. 54.  
Schematic of multicomponent condensation experiment apparatus.

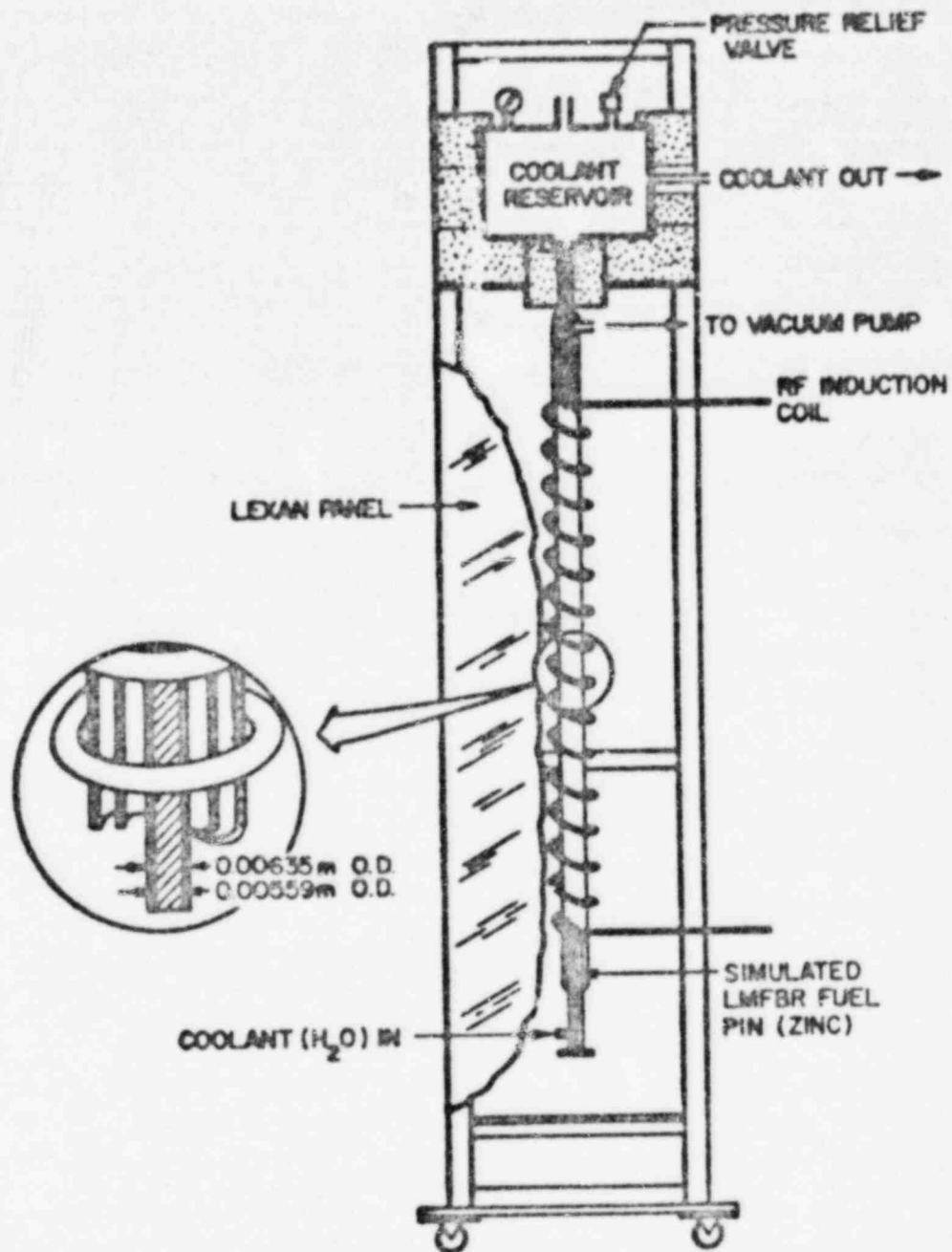


Fig. 55.  
Flow coastdown simulation experiment.

efficiency of 30-40%. Two preliminary experiments were performed and data were recorded by means of slow-motion photography. The first experiment was conducted with a furnace power of 8.9 kW and no water (simulant coolant) flow and was terminated at the time of massive coolant voiding. A summary of events for case 1 is presented in Table VI. The second experiment was conducted with a furnace power of 18 kW and a constant coolant flow of 0.0014 t/s and was terminated after substantial zinc relocation. A summary of events for case 2 is presented in Table VII. The shrinkable tubing (simulant cladding) unexpectedly failed to melt and relocate. The tubing maintained its geometry with the exception of ruptures which provided a leak flow path for the molten zinc. These ruptures were the result of the thermal decomposition of the tubing.

These first exploratory PCS experiments have demonstrated the necessity for the following design revisions:

1. the replacement of the shrinkable tubing with a simulant cladding which will pass through a molten (liquid) phase,
2. the incorporation of a bypass loop to allow flow reversal,
3. the replacement of Pyrex glass tubing with high-service temperature glass tubing, and
4. the replacement of the induction heating coil with a maximum viewing field coil.

When the major features of a loss-of-flow accident (LOFA) sequence can be reproduced in the PCS experiments, SIMMER will be used to perform pre- and posttest analyses, and calculational/experimental comparisons will be made.

#### D. Safety Test Facilities Study

(M. G. Stevenson, Q-DO)

##### 1. Endoscope Diagnostic System Evaluations

(A. E. Evans, Q-14)

Preparations are under way to increase the size of the test hole in PARKA and place therein a 127-pin assembly of fast test reactor (FTR) size fully enriched  $UO_2$  fuel pins. Conversion will involve removal of 18 additional

TABLE VI  
SUMMARY OF EVENTS FOR CASE 1

<u>Time (s)</u>	<u>Event</u>
0	Power-up to 8.9 kW Small bubble formation on bare zinc surface
25-30	Small bubble escape from bare zinc surface
45-55	Small bubble formation on cladding surface
70-80	Vigorous nucleate boiling from bare zinc surface
100	Massive coolant voiding
110	Power off

PARVA fuel rods, installation of a new 110 mm o.d. x 89 mm i.d. rotating steel test hole liner with remote actuator, fabrication of 127-hole aluminum grid plates, and construction of a system to permit remote withdrawal of up to 6 pins or groups of pins during operation. Fabrication of the rotary test hole

TABLE VII  
SUMMARY OF EVENTS FOR CASE 2

<u>Time (s)</u>	<u>Event</u>
0	Power-up to 18 kW and coolant flow at 0.0014 l/s Small bubble formation on bare zinc surface
10-22	Small bubble escape from bare zinc surface Small bubble formation on cladding surface
30-40	Vigorous nucleate boiling from bare zinc surface
50-60	Massive coolant voiding
140-200	Zinc relocation begins

liner and of the aluminum grid plates has been completed. Uranium oxide fuel pellets with which to fabricate the 90 additional fuel pins needed for the new test assembly are being fabricated by Group OMB-6. Tubing for the pins cladding is being obtained from Hanford Engineering Development Laboratory (HEDL). Delivery of completed fuel pins is expected in February 1978.

In anticipation of higher radiation levels and an increased workload associated with planned 127-pin assembly tests, the radiation shielding surrounding PARKA has been increased. The reactor has been wrapped with 12.7 mm of lead on the sides and 50 mm of lead on top to reduce personnel exposure during changes to the core or test assembly. In addition, 40 m of concrete block has been erected against the wall between PARKA and the shielded instrumentation room to reduce background in the instrumentation room. A 0.8 m thick concrete block wall now separates PARKA from the area where the Godiva assembly is used. This will reduce activation of PARKA by Godiva bursts and permit freer scheduling of setup, maintenance, and operation of these two reactors. A photograph of PARKA with its new shielding is shown in Fig. 56. A plan view of the facility is given in Fig. 57.

Stilbene detectors previously described<sup>2</sup> were used with the VASL 4-channel hodoscope facility at PARKA to study hodoscope imaging of 1- and 37-pin PTR fuel bundles. To recapitulate briefly, these detectors have the property of pulse-shape discrimination between neutrons and gamma rays so that a pulse-risetime analyzer can be used to distinguish between and to count simultaneously neutron- and gamma-ray induced events. Two detectors were used: one detector had a pulse-height discriminator setting for gamma-ray events with  $E_\gamma > 0.33$  MeV and neutron events such that  $E_n > 1.3$  MeV; the other detector counted all gamma-ray events with  $E_\gamma > 0.66$  MeV and neutrons with  $E_n > 2.2$  MeV.

Results from neutron scanning of a single pin in PARKA are shown in Fig. 58, together with background scans of the empty PARKA test section. As would be expected, the higher discriminator setting resulted in a better signal-to-background (S/B) ratio,  $\sim 0.75:1$  for  $E_n > 2.2$  MeV as contrasted to about  $0.5:1$  for  $E_n > 1.3$  MeV. The S/B result for the lower discriminator setting is only slightly better than the S/B ratio previously obtained with Hornyak buttons ( $E_n \geq 1$  MeV).<sup>8</sup> However, the new detectors are a factor of five more efficient than the Hornyak buttons, so that statistically better data can now be taken with less reactor operating time and power.

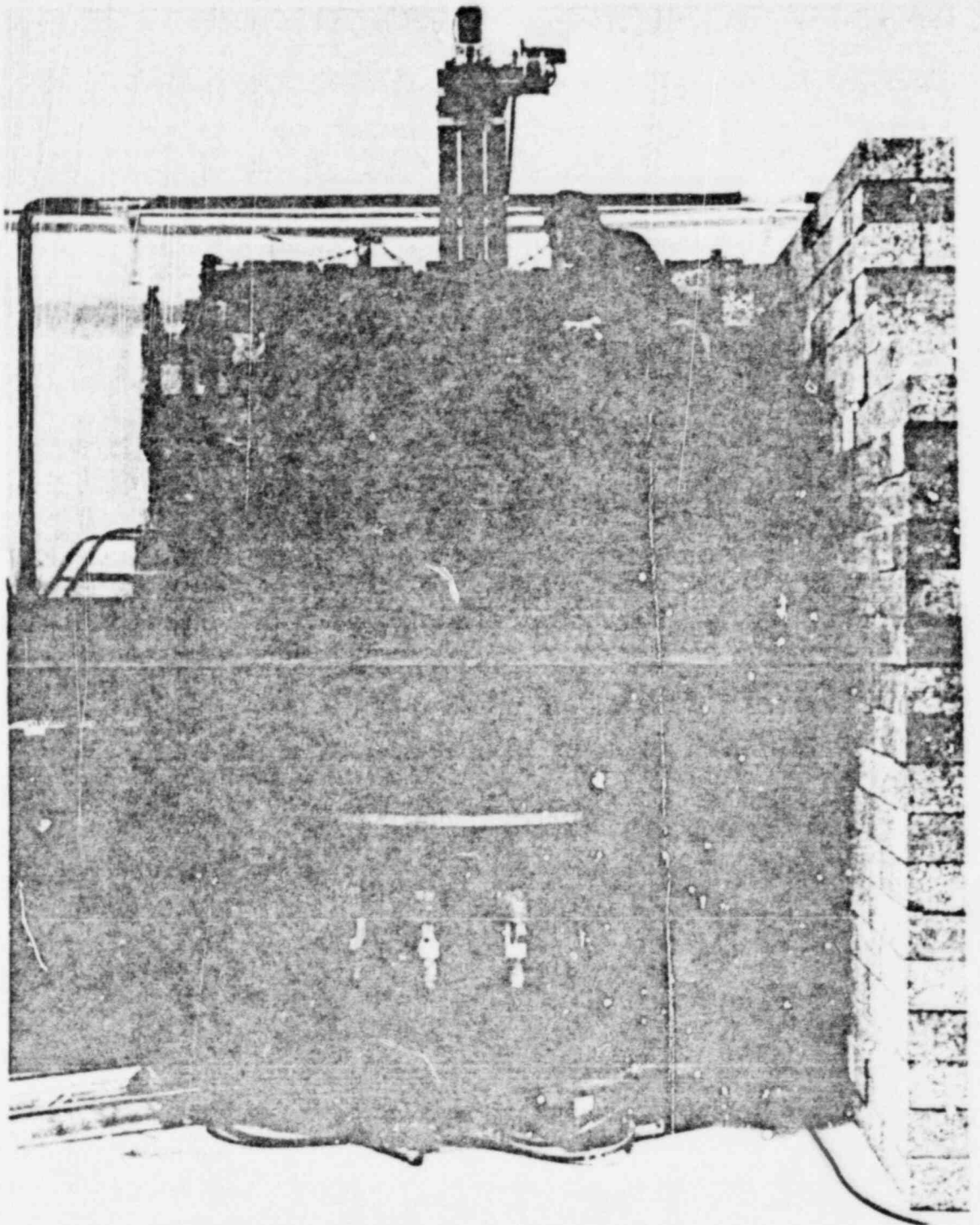


Fig. 56.  
Photograph of the PARKA facility showing increased shielding.

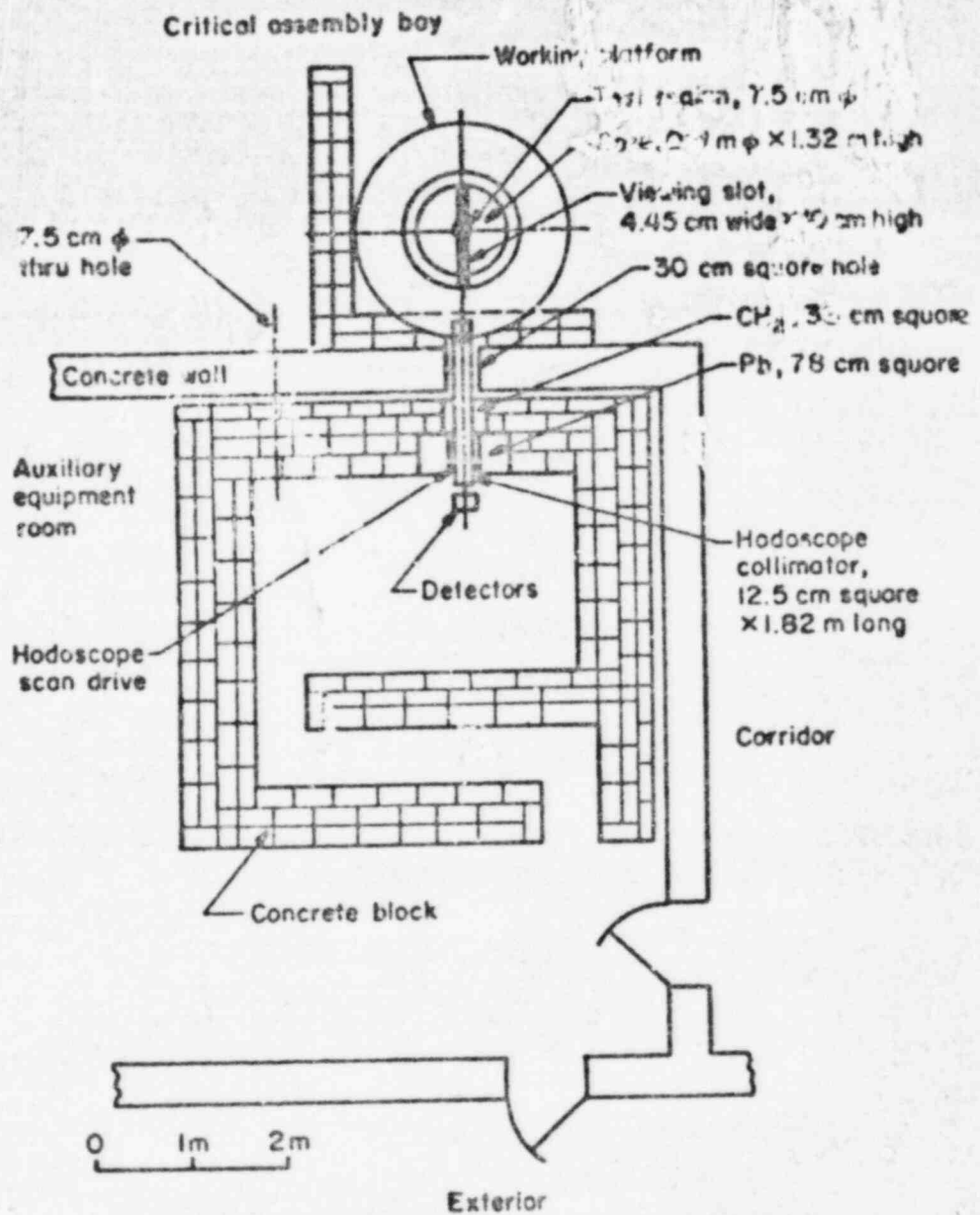


Fig. 57.  
Plan view of the PARKA facility as used for hodoscope evaluation.

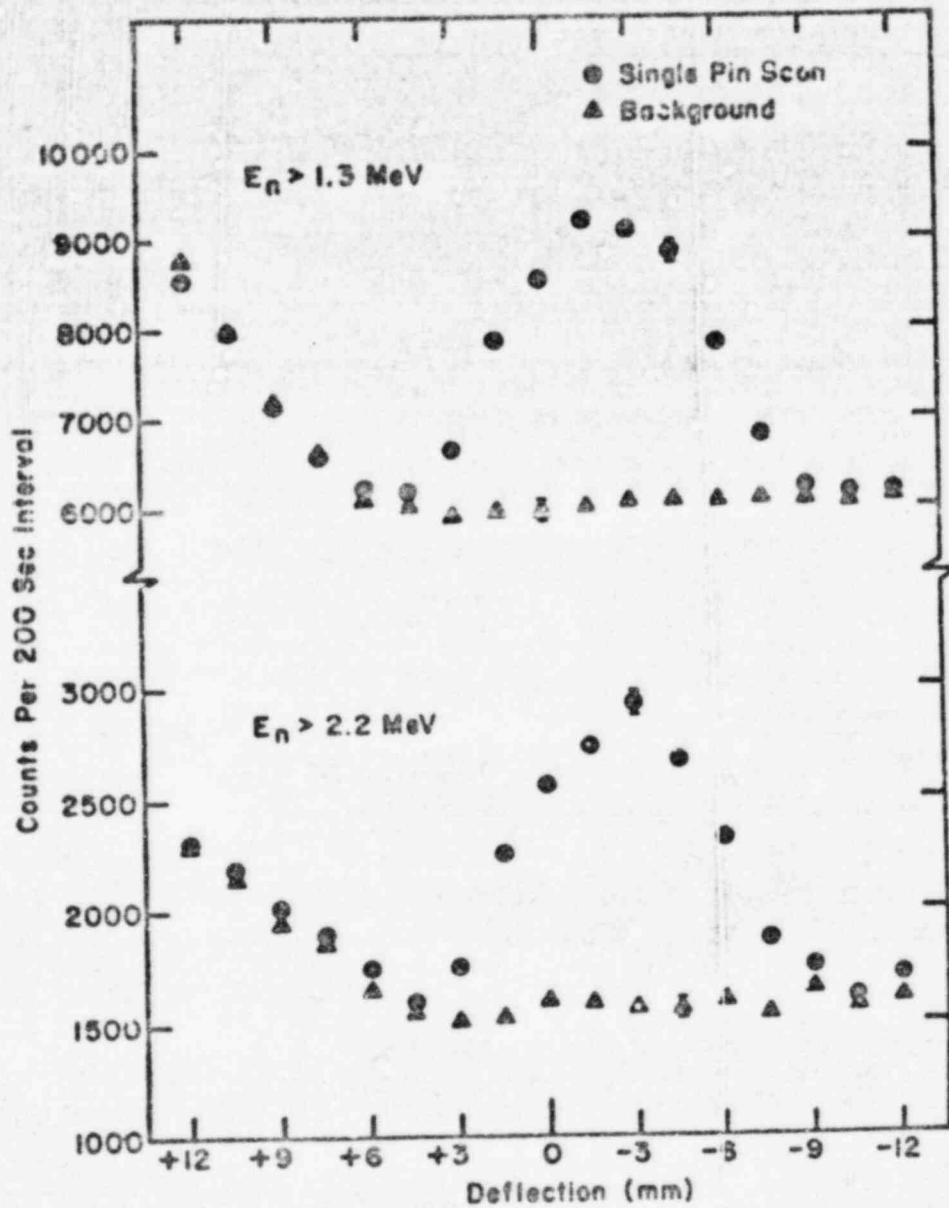


Fig. 58.

Neutron hodoscope scans of a single simulated FFTF pin in PARKA. The asymmetry in the background radiation is believed to be caused by scattering from temporary shielding between the hodoscope and the reactor.

Single-pin gamma scans, shown in Fig. 59, resulted in S/B ratios of the order of 1:1, somewhat better than the S/B ratios obtained for neutrons. This is contrary to our experience for larger sized test bundles.<sup>2,40,41</sup>

We also scanned a 37-pin test bundle across the flats with both the full bundle and with the center pin missing. Neutron and gamma-ray results appear in Fig. 60. The data shown are raw counts, which reflect a counting rate increase with time for the gamma-ray and lower energy neutron scans due to buildup of fission and activation products. Both scans were taken from left to right and the 36-pin scan followed the 37-pin scan. We have subsequently found that most of the counting-rate increase problem can be eliminated by running the reactor at the power level of the experimental run for 1 h before starting to take data. One may also, if desired, measure this time-dependent buildup and correct for it. This effect is, of course, not important to the performance of multichannel hodoscopes, with which all data are taken simultaneously, provided that power distribution and history are uniform across the test region.

The time-related buildup for the  $E_n > 1.3$  MeV scan probably results from incomplete separation of neutron and gamma-ray counts due to slight overlap of pulse-risetime distributions as measured by the pulse-shape analyzer.<sup>2</sup> One might also expect contamination of the gamma-ray scan data by neutrons which are captured or inelastically scattered in the vicinity of the detectors, which then indirectly "see" these neutrons as gamma-ray events. To test for intermixing of gamma-ray and neutron-induced counts in the detectors, 37-, 36-, 1-, and 0-pin scans were repeated with 200-mm-long Lucite plugs inserted into the reactor end of the hodoscope collimator holes. The effect of the Lucite plugs on gamma-ray and neutron counting rates is shown in Table VIII. Crude estimates indicated attenuations should have been  $\sim 3$  for reactor gamma radiation and 2-3 orders of magnitude for fast neutrons. Most of the neutrons counted for the 0-pin, Lucite-plugged case are room background rather than neutrons coming down the collimator, which explains the apparent lower attenuation of these neutrons by the Lucite plugs.

It is noted in Table VIII that the absolute neutron counting loss due to the withdrawal of one pin from the 37-pin bundle was less than half of the net count (less background) from a single pin in the test section. For gamma radiation, the situation is much worse, the counting loss due to withdrawal of one pin from a 37-pin bundle being less than one-fourth of the net count from

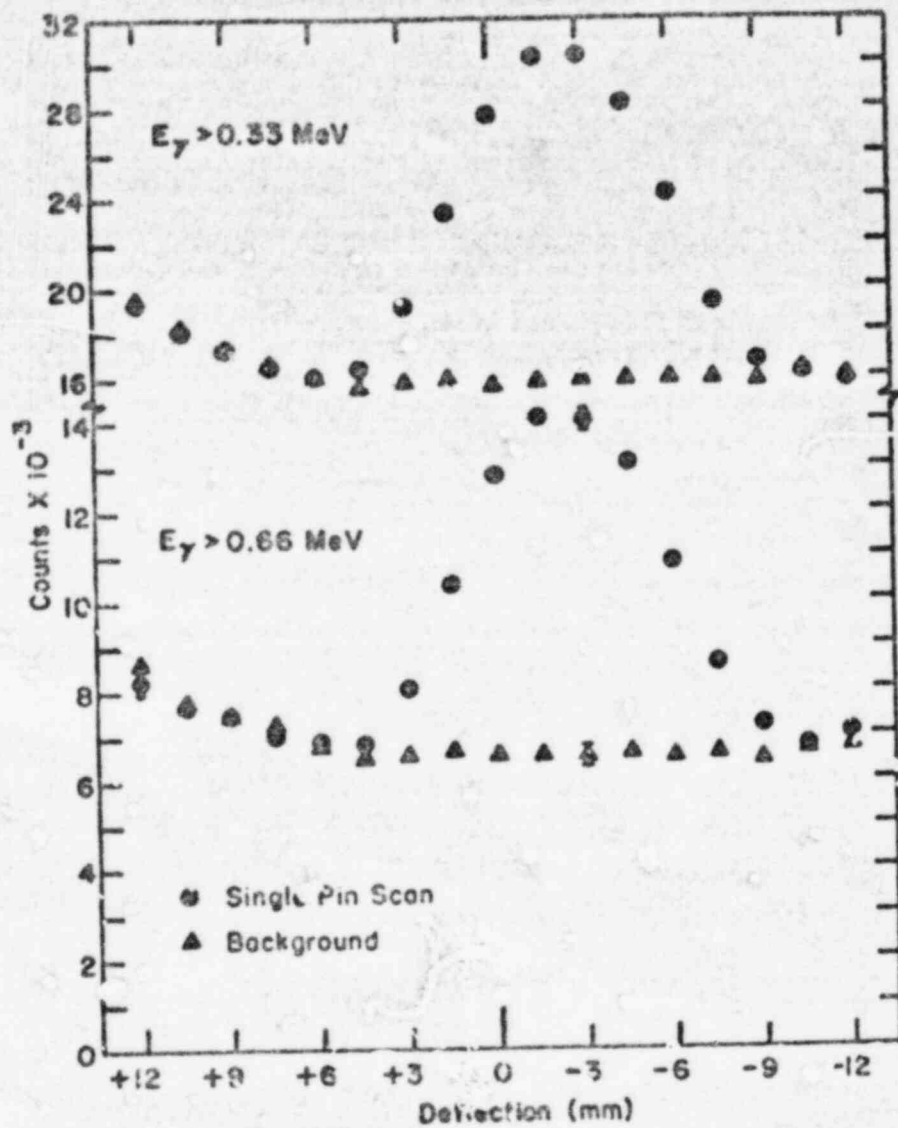


Fig. 99.  
Results of gamma-ray scan of a single simulated FFTP pin in PARKA.

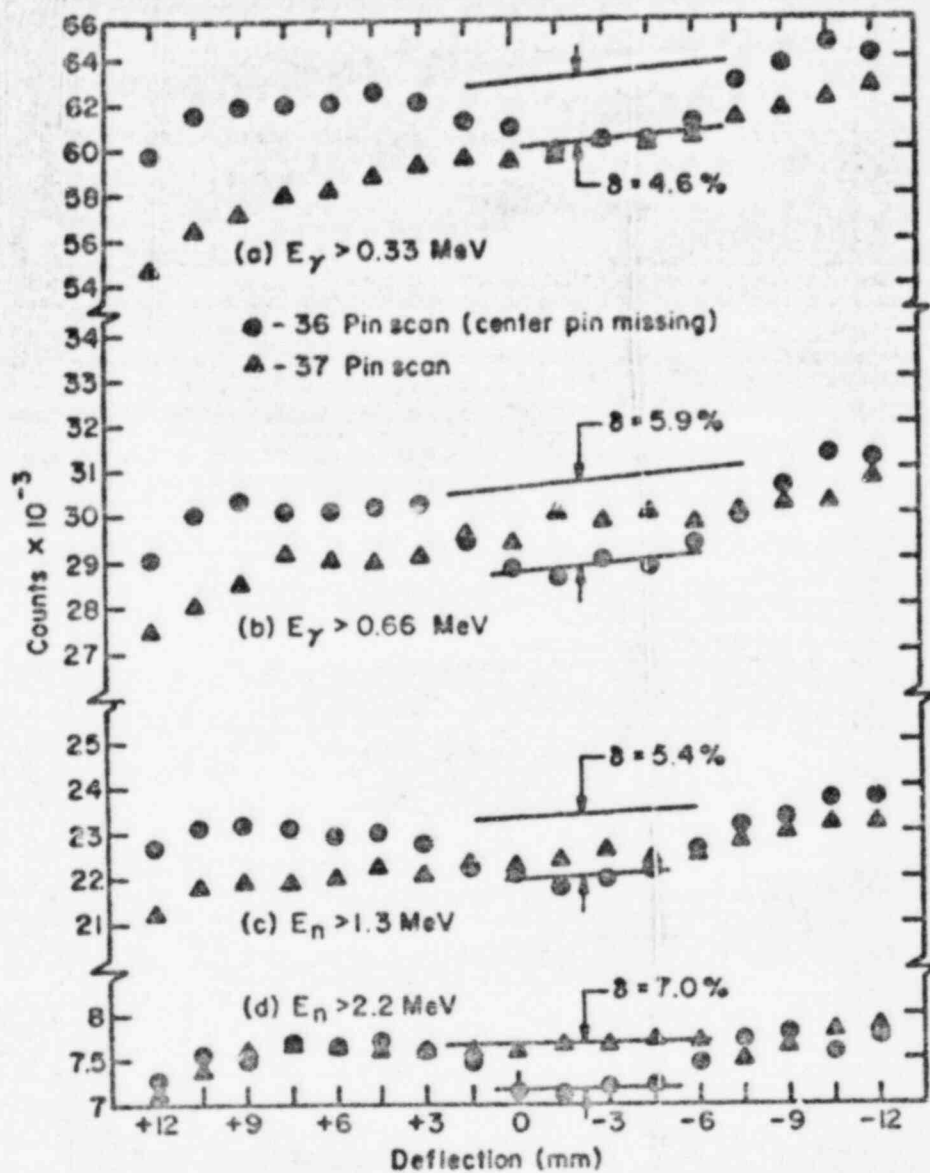


Fig. 60.

Results of neutron and gamma scans of a 37-pin assembly intact and with the center pin missing. Direction of scan was across flats of the hexagon. These data, which were taken during a 3-h run that commenced immediately after reaching operating reactor power, are uncorrected for buildup of fission and activation products.

TABLE VIII

SUMMARY OF ON-CENTER HODOSCOPE COUNTING RATES FOR 37-, 36-, 1-,  
AND 0-PIN SCANS, WITH AND WITHOUT 200 mm LUCITE PLUGS IN COLLIMATOR

	Count Rate (counts/s)	Count Rate (counts/s)	Count Rate Ratio
37-pin, $E_n > 2.2$ MeV	7720	450	17
$E_n > 1.3$	23400	1300	18
$E_Y > 0.66$	30700	10600	2.9
$E_Y > 0.33$	63400	19300	3.3
36-pin, $E_n > 2.2$ MeV	7180	400	18
$E_n > 1.3$	22050	1250	18
$E_Y > 0.66$	28900	10000	2.9
$E_Y > 0.33$	60400	18200	3.3
1-pin, $E_n > 2.2$ MeV	2800	175	16
$E_n > 1.3$	9100	600	15
$E_Y > 0.66$	14000	5400	2.6
$E_Y > 0.33$	30400	10000	3.0
0-pin, $E_n > 2.2$ MeV	1600	110	14.5
$E_n > 1.3$	6000	450	13.3
$E_Y > 0.66$	6500	3200	2.0
$E_Y > 0.33$	16000	6200	2.6

a single pin in the test section. This raises questions concerning the linearity of response of the hodoscope and the sensitivity of the hodoscope calibration to the position of a perturbation in fuel density within the test bundle.

Position sensitivity of response was tested in a 37-pin bundle by scanning the bundle with the center pin withdrawn and then scanning with a front pin (nearest the collimator) and with a back pin withdrawn. The results are shown in Fig. 61. A general reduction in sensitivity from front to back of 20-30% is noted for fast-neutron scans and 35-50% for gamma scans.

Linearity of response was tested by scanning while withdrawing from 1-4 pins in line from the bundle. The results are shown in Fig. 62 for neutrons and Fig. 63 for gamma rays. The neutron scans are consistent with linearity within the counting statistics, which are shown. The gamma scans show a slight (5-10%) increase in sensitivity per gram of the last fuel pin removed over the first two pins.

In summary, the experiments show that the hodoscope can easily detect pellet-sized voids in a 37-pin array of FFTF fuel pins but that quantitative measurements will require a point-by-point calibration of the hodoscope sensitivity within the array. It is also evident that quantitative measurements of fuel motion for a bundle this size and larger must be tomographic; i.e., one cannot accurately measure fuel motion without knowing the depth at which the motion occurred. Given tomographic capability, depth and linearity corrections in an assembly of this size do not appear unmanageable. It remains to be seen whether this conclusion will hold for larger assemblies.

Data from previously taken gamma scans of a single-pin and of 36- and 37-pin bundles<sup>2</sup> have been reduced and plotted at the LASL Central Computing Facility using a program written by D. M. Peterson, Q-8 and H. M. Forehand, Q-7. Data reduction involved correction for buildup of fission- and activation-product activity during the scans, normalization for integrated reactor power, and calculation of statistical errors. In the future, it will be possible to provide for "hands off" reduction and plotting of all hodoscope scanning data from cassette tapes generated by the data-acquisition equipment.

Results of gamma scans taken with 13 mm diam x 13 mm long NaI(Tl) crystals and NE102 plastic scintillators are shown in Figs. 64 through 67. These

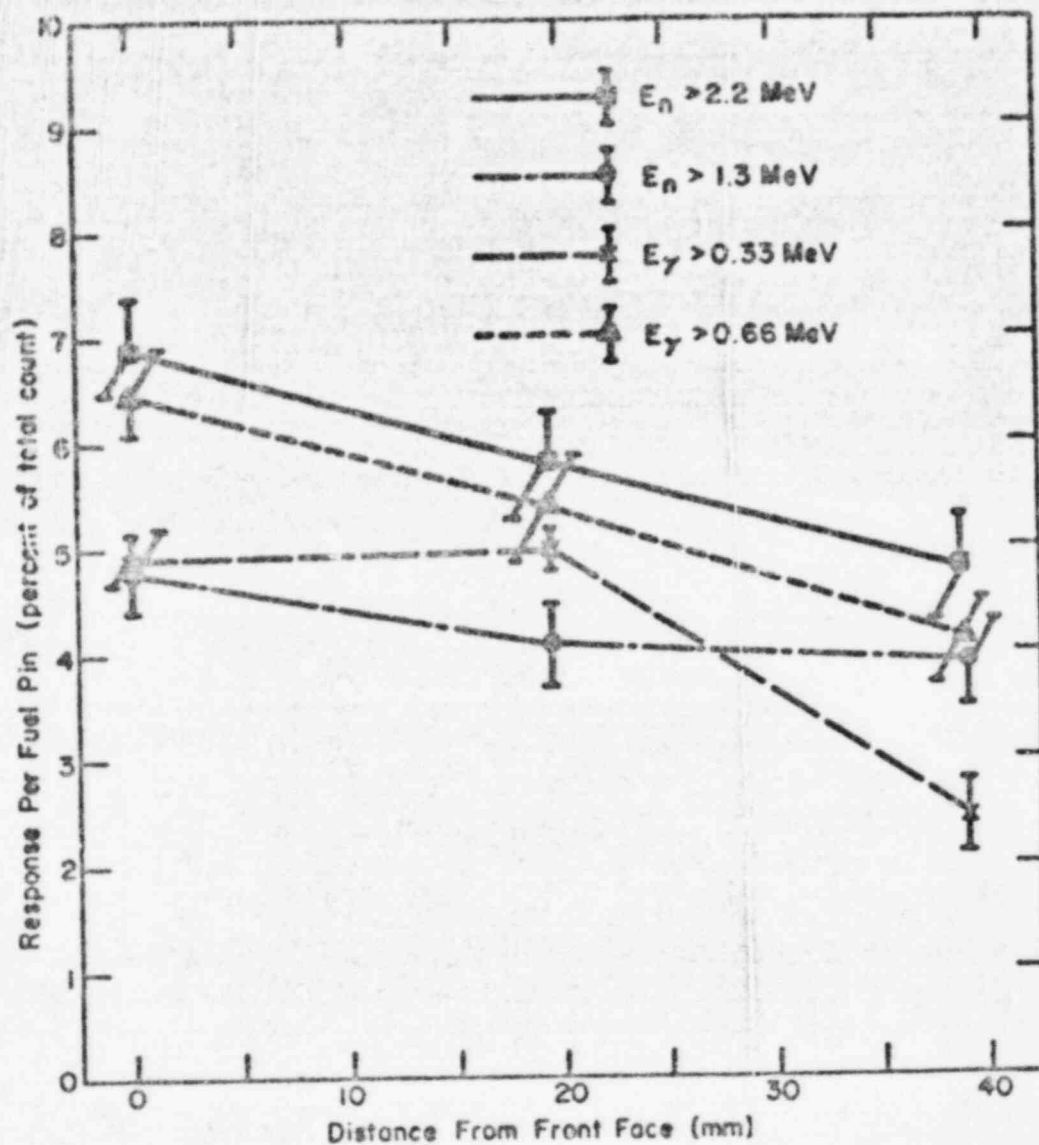


Fig. 61.  
Sensitivity of the hodoscope to removal of fuel as a function of position of the void in the test bundle. The center (20 mm) points have been corrected for a known 15% power-distribution depression in the center of the test bundle. Indicated errors are from counting statistics only.

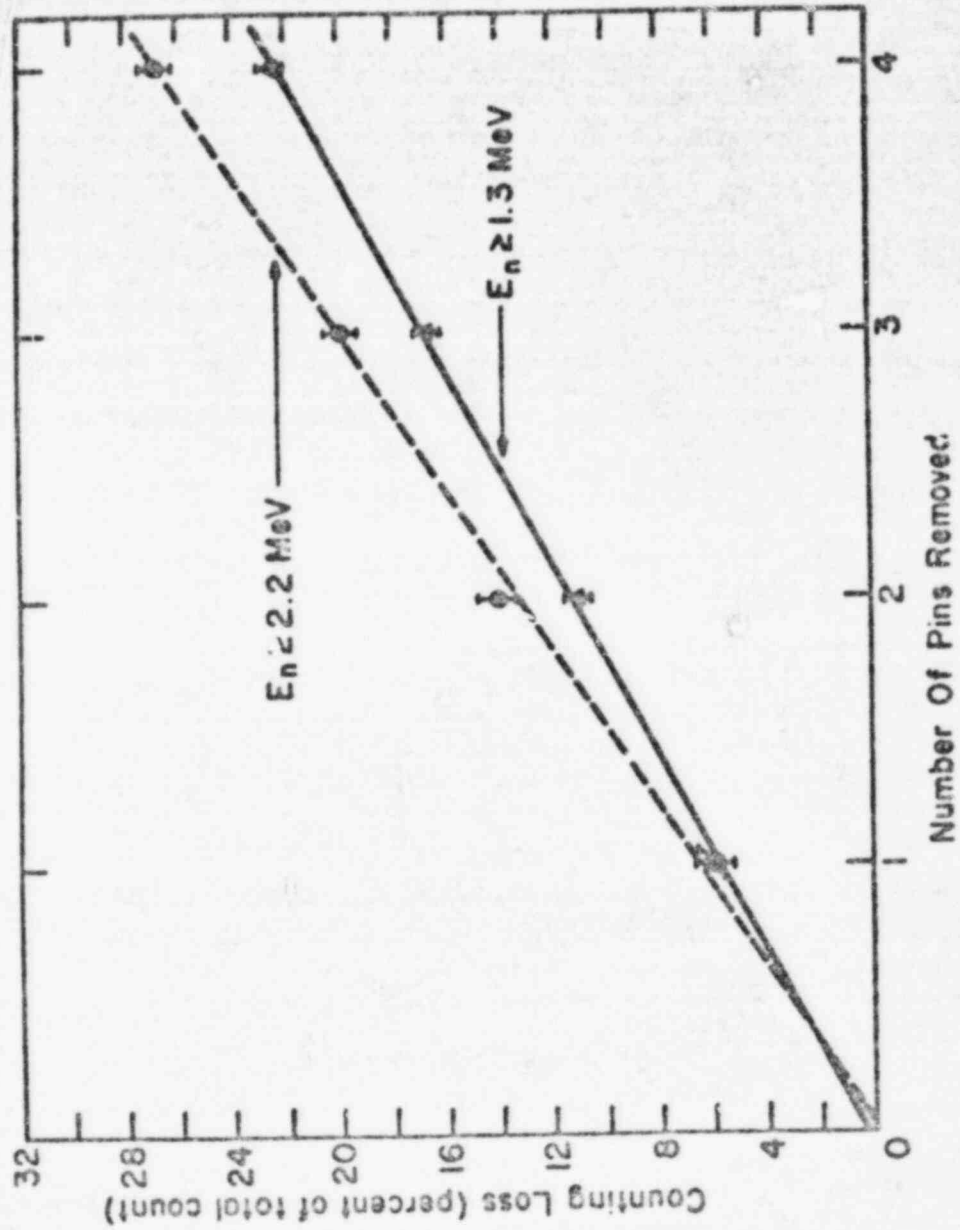


Fig. 62.  
Results of linearity test for neutrons. Errors are statistical only.

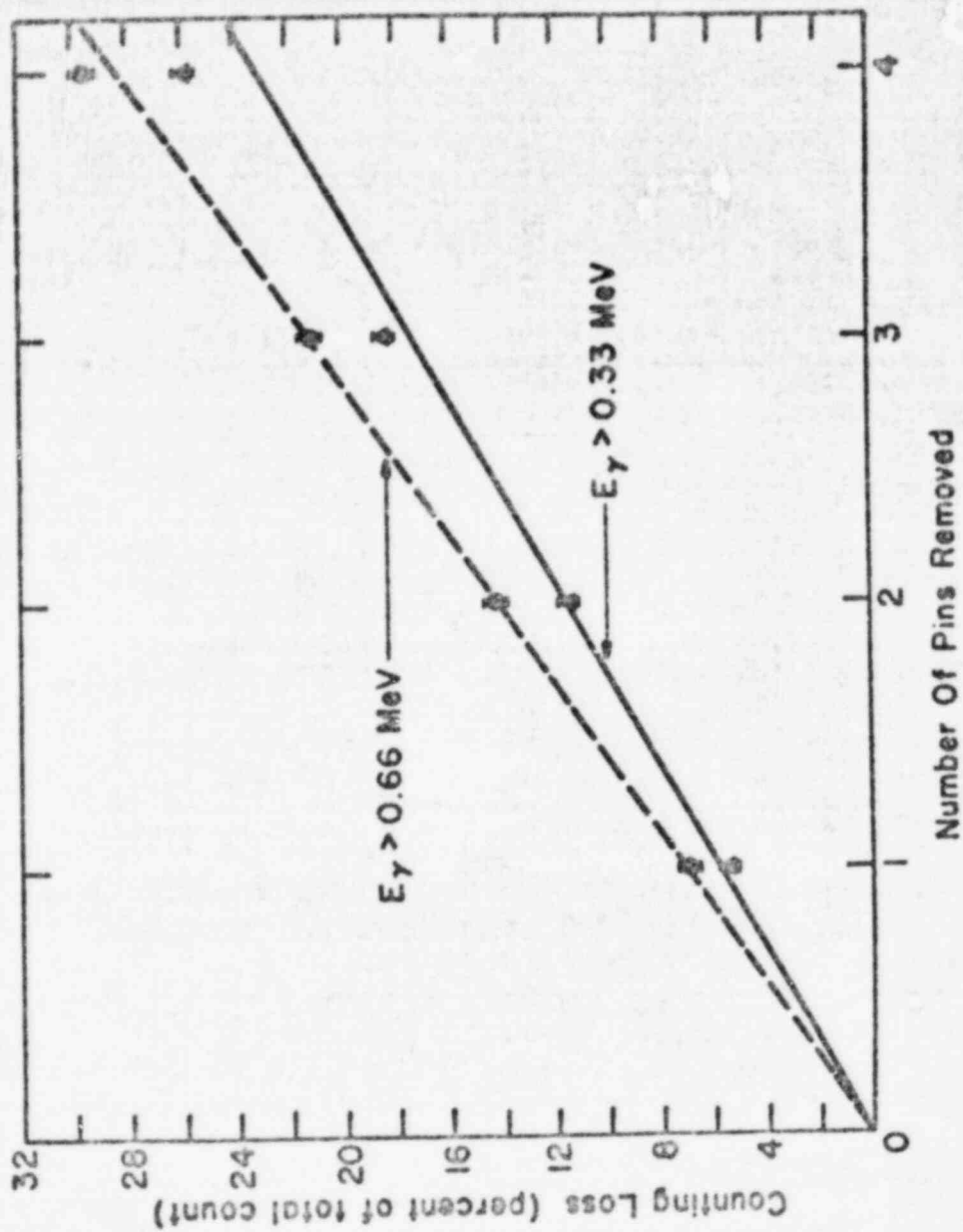


Fig. 63.  
Results of linearity test for gamma rays.

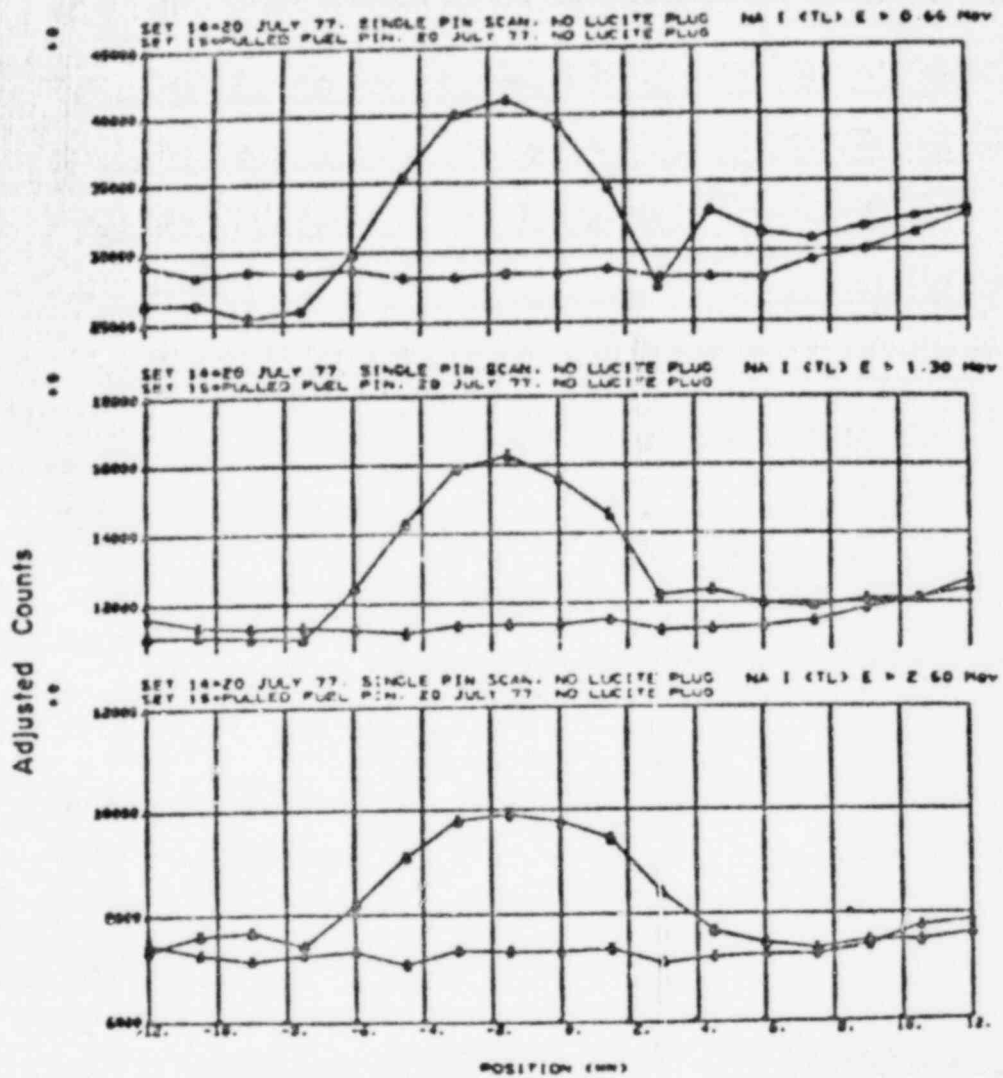


Fig. 64.  
 Results of single-pin and background gamma scans with a NaI(Tl) detector  
 with various energy discriminator settings.

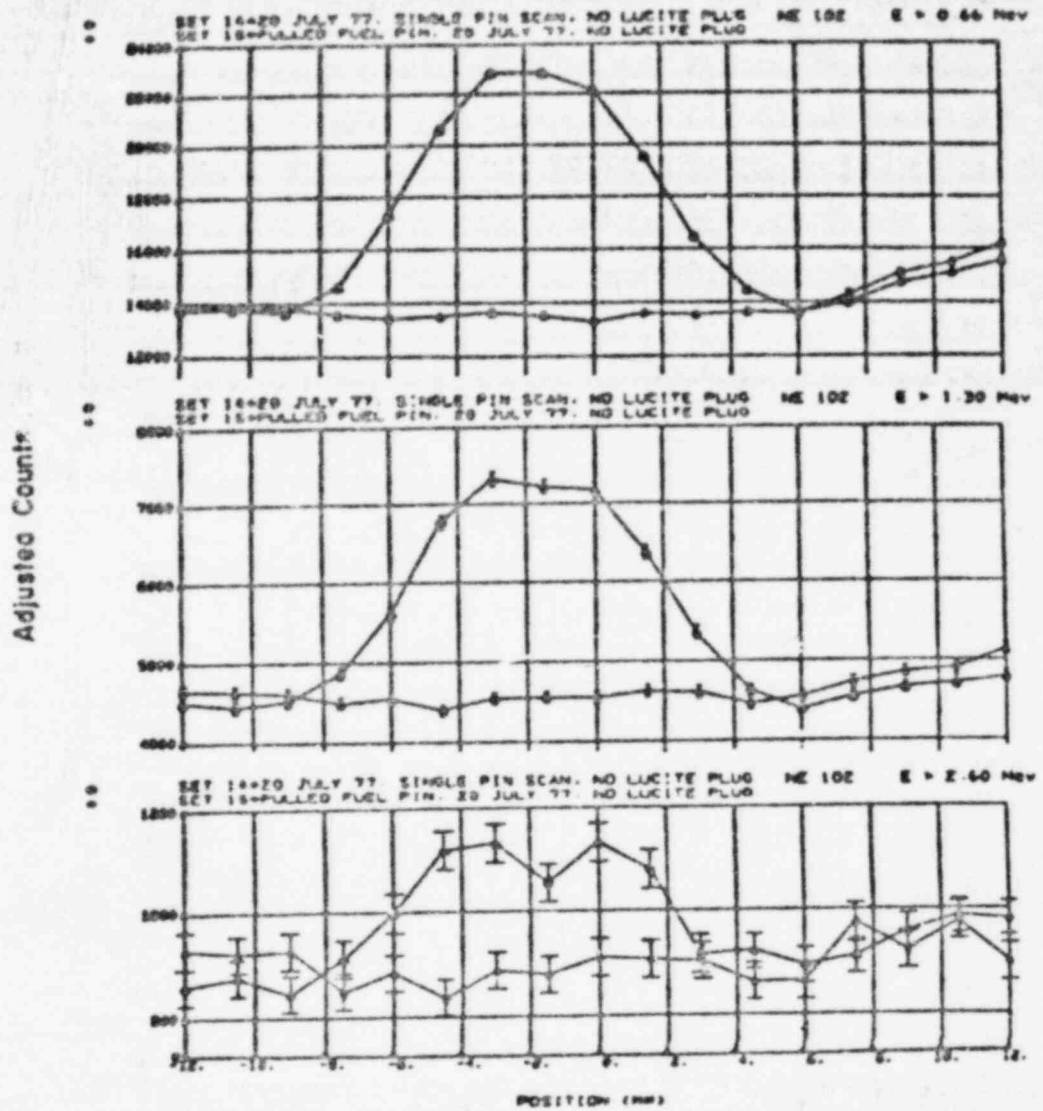


Fig. 65.  
Results of single-pin and background gamma scans with an NE102 plastic scintillator.

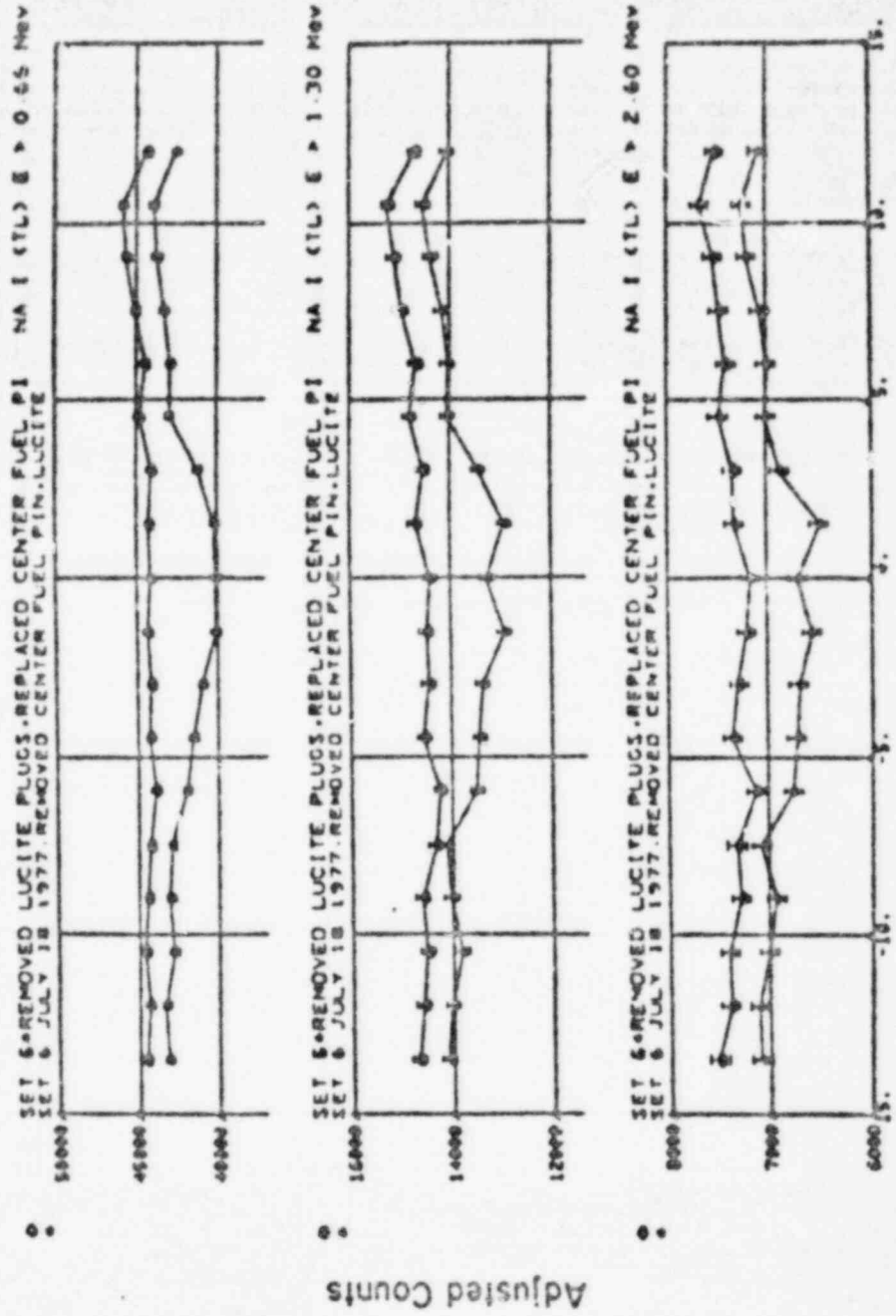


Fig. 66.  
 Results of 37- and 36-pin gamma scans with a NaI(Tl) detector.

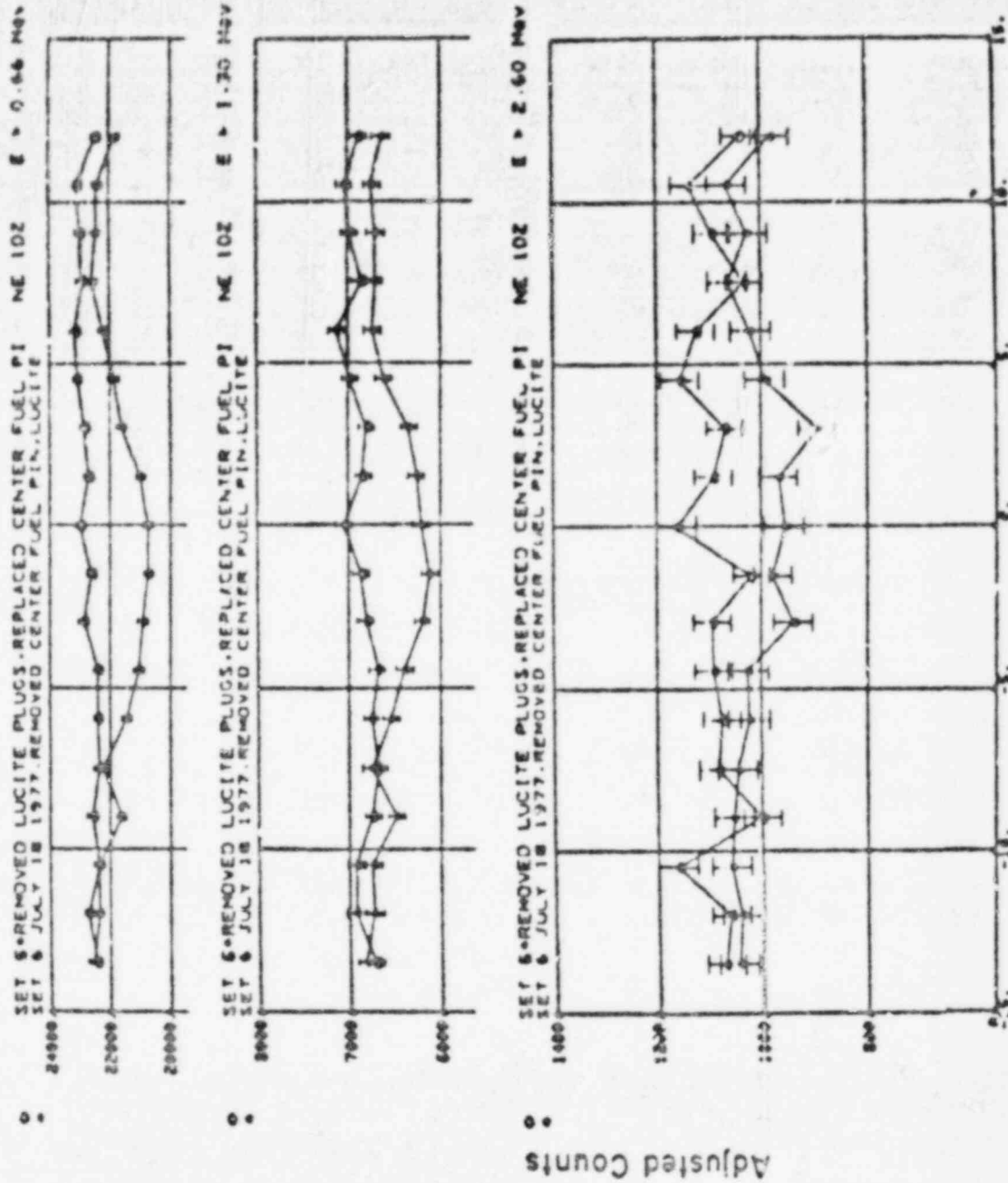


Fig. 67. Results of 37- and 36-p/n gamma scans with a NE102 plastic scintillator.

results are similar to those obtained from the gamma scans made with the stilbene detectors. The figures are superpositions of unretouched computer printouts.

## 2. Flash X-Ray Monitoring of Reactor Fuel Motion

(W. E. Stein, P-DOR)

The potential capability of flash x-ray monitoring of fuel motion in Fast Reactor Safety Test Facilities is being evaluated with the facilities and equipment available at IASL. X-ray radiographs of various safety experiment fuel configurations are being made with film as well as an electro-optical imaging system. These radiographs are taken with pulsed, 30 MeV bremsstrahlung filtered through steel of various thicknesses (50-100 mm), which is used to simulate the experiment containment vessels. Film radiographs are used to ascertain the amount and quality of information contained in the transmitted x rays and, thereby, to establish the expected spatial resolution and mass density sensitivity of this diagnostic technique.

To satisfy all of the goals of the desired system, particularly the repetition rate requirement of up to  $10^3$  pictures per second (1 ms time resolution), it is clear that an imaging system other than direct recording on film will be required. It appears that it would be very difficult, if not impossible, to attain sufficiently rapid shutter speed and frame motion of the film to prevent fogging of the film by radiation from either the reactor or previous and subsequent x-ray flashes. Therefore, an electro-optical imaging system is being evaluated concurrently with film.

The present electro-optical imaging system consists of a fluorescent screen and a gatable image intensifier coupled to a vidicon (TV camera). The fluorescent screen is used to convert the x-ray radiograph to a visible picture which is viewed via a mirror by the image intensifier-vidicon combination. Results obtained with this state-of-the-art imaging system are being used not only to demonstrate the presently attainable spatial and temporal resolutions but also to establish the x-ray source intensity which will be necessary for satisfactory mass density sensitivity.

X rays produced by PHENIX, a 30 MeV electron accelerator with a 0.2- $\mu$ s pulse duration, were used to radiograph arrays of PTR-size fuel pins using enriched  $UO_2$  pellets instead of mixed oxide. The fuel pin array under study was positioned equidistantly between the x-ray source and the film or

fluorescent screen. The overall source-to-detector distance was 6 m. To test the mass sensitivity of this technique, the central pin in each array contained an intentional 25.4-mm-long void.

Film radiographs taken perpendicularly to the flats of the hexagonal arrays clearly show the central void for up to 169 pins surrounded by a steel cylinder with radial thickness of 38 mm. Examples of densitometer traces taken perpendicularly to the array axis and through the region of the voided central pin are shown in Figs. 68 and 69. Also shown in Fig. 68 is the calculated x-ray transmission for the same trace through the 37-pin array and steel cylinder. Analysis of these film density variations indicates that the information contained in the transmitted x rays is sufficient to provide about 1 mm spatial resolution and a mass density sensitivity of about  $1 \text{ g/cm}^2$  and about  $2 \text{ g/cm}^2$  for the 37- and 169-pin arrays, respectively. This is about 6% sensitivity in each case.

Similar results for the electro-optical imaging system are shown in Fig. 70 for the 37-pin array. It is clear that the results, although encouraging, are, at present, inferior to those obtained with film. The present imaging system is not capable of extracting all of the information contained in the transmitted x rays. The corresponding estimates for the present imaging system are about 2 mm spatial resolution and about  $3 \text{ g/cm}^2$  areal density resolution for the 37-pin array.

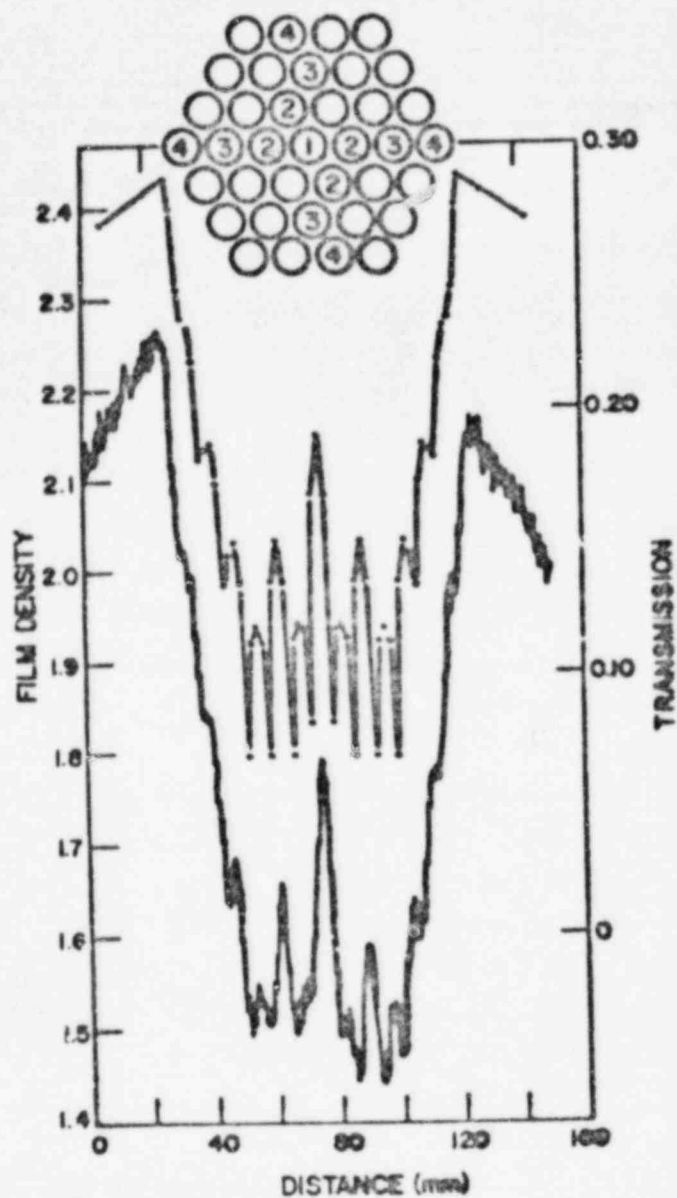


Fig. 68.  
Density of film radiograph and calculated x-ray transmission for a 37-pin array viewed perpendicularly to the hexagonal flats and surrounded by a steel cylinder with 25.4 mm radial thickness. The densitometer data and transmission calculations are for a trace taken perpendicularly to the array axis and through the void in the central pin. The intensity of the x-ray flash was 34 R at 1 m.

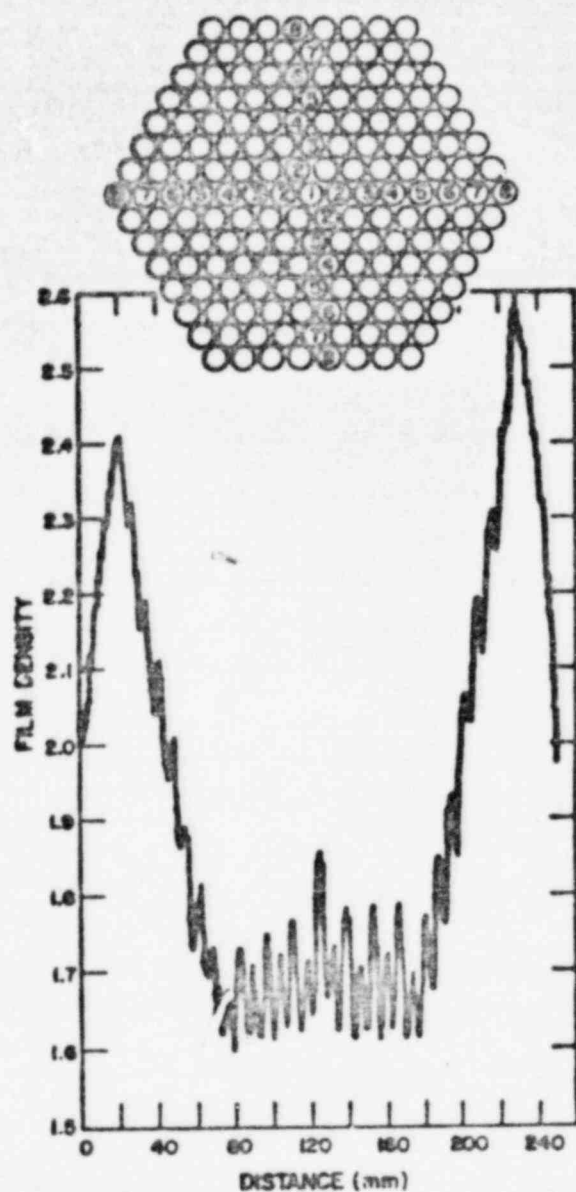


Fig. 69.  
 Density of film radiograph for a 169-pin array viewed perpendicularly to the hexagonal flats and surrounded by a steel cylinder with 38 mm radial thickness. The densitometer data were taken perpendicularly to the array axis and through the void in the central pin. The intensity of the x-ray flash was 80 R at 1 m.

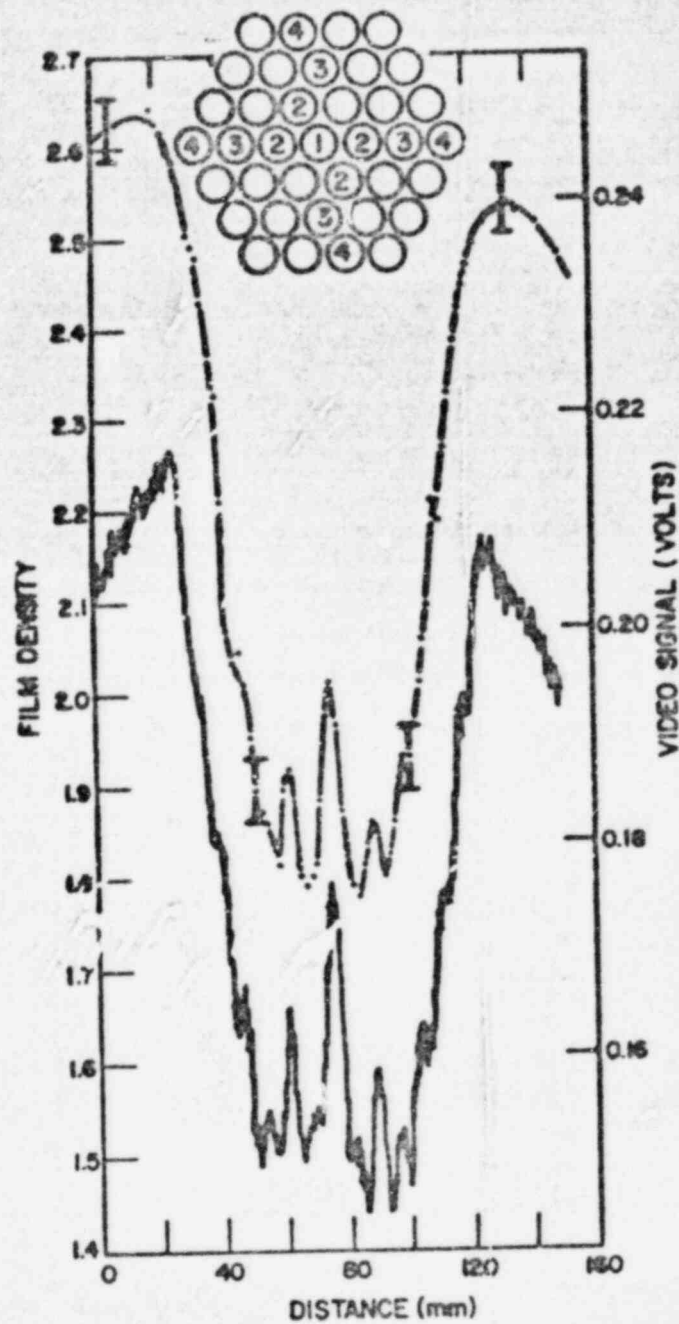


Fig. 70.  
 Density of film radiograph and measured video signal for a 37-pin array viewed perpendicularly to the hexagonal flats and surrounded by a steel cylinder with 25.4 mm radial thickness. The densitometer data and the video signal are for a track taken perpendicularly to the array axis and through the void in the central pin. The intensity of the x-ray flash was 34 R at 1 m.

#### IV. HTGR SAFETY RESEARCH

(M. G. Stevenson and J. F. Jackson, O-DO)

Under the sponsorship of the NRC/RSR, IASL is conducting a program of research in High-Temperature Gas-Cooled Reactor safety technology in the following task areas.

- Fission Product Release and Transport
- Structural Evaluation
- Phenomena Modeling, Systems Analysis, and Accident Delineation

The progress reported in this section is arranged according to these task areas.

##### A. Fission Product Release and Transport

(C. E. Apperson, Jr., O-13)

IASL activities in the fission product transport task include the development of computer codes to be used for calculating fission product transport in various parts of the reactor and both theoretical and experimental studies to define transport mechanisms and supply data for calculations.

During this quarter one technical paper<sup>42</sup> and one technical note<sup>43</sup> were published. Analytical work concentrated on optimizing the direct search algorithm in QUTL/QUIC, modifying the evaluation of burst release in SUVIUS, and preparing a preprocessor for SUVIUS. The cesium desorption kinetics studies reported last quarter were repeated and the initial results were verified. A work plan for the fuel particle heatup experiment was submitted to NRC. Several modifications are being made to upgrade the operational capability of the equipment used in this experiment.

##### 1. Fission Product Release Experiments

(R. G. Behrens and M. A. David, OMB-3)

Studies of cesium desorption kinetics from H-451 graphite using a vacuum ultra-microbalance were continued during this reporting period. Work involved repeating the two experiments (Experiments 2 and 3) performed during the previous quarter in order to confirm their validity. The experiments involved studying cesium desorption from graphite using samples prepared in two different ways:

1. doping the graphite with CsOH solution and then placing the sample under vacuum for one week at room temperature and
2. doping the graphite with CsOH solution and then heating the sample at 1373 K for 2 h in a closed tantalum crucible to aid in decomposition of the CsOH to adsorbed cesium metal and to evenly distribute the cesium throughout the graphite.

A summary of experimental conditions is given in Table IX.

The two experiments performed during this quarter (Experiments 6 and 7) confirmed the mass-loss behavior observed for the two previous experiments. Figure 71 shows the time dependence of the desorption flux at temperatures

TABLE IX  
SUMMARY OF EXPERIMENTAL CONDITIONS FOR DESORPTION MEASUREMENTS  
ON H-451 GRAPHITE

Expt. No.	Graphite Mass (mg)	Projected Graphite Surface Area (cm <sup>2</sup> )	Comments
2 <sup>a</sup>	107.9	1.2	Not preheated.
3 <sup>b</sup>	121.7	1.2	Preheated at 1373 K for 2 h in closed Ta crucible.
6	117.8	1.3	Not preheated.
7	96.5	1.2	Preheated at 1373 K for 2 h in closed Ta crucible.
Blank #1	113.2	1.4	Not preheated.
Blank #2	141.3	1.5	Preheated at 1373 K for 2 h in closed Ta crucible.

<sup>a</sup>Neutron activation of graphite after experiment showed cesium concentration of 0.84 mg Cs/g C.

<sup>b</sup>Neutron activation of graphite after experiment showed cesium concentration of 9.6 mg Cs/g C.

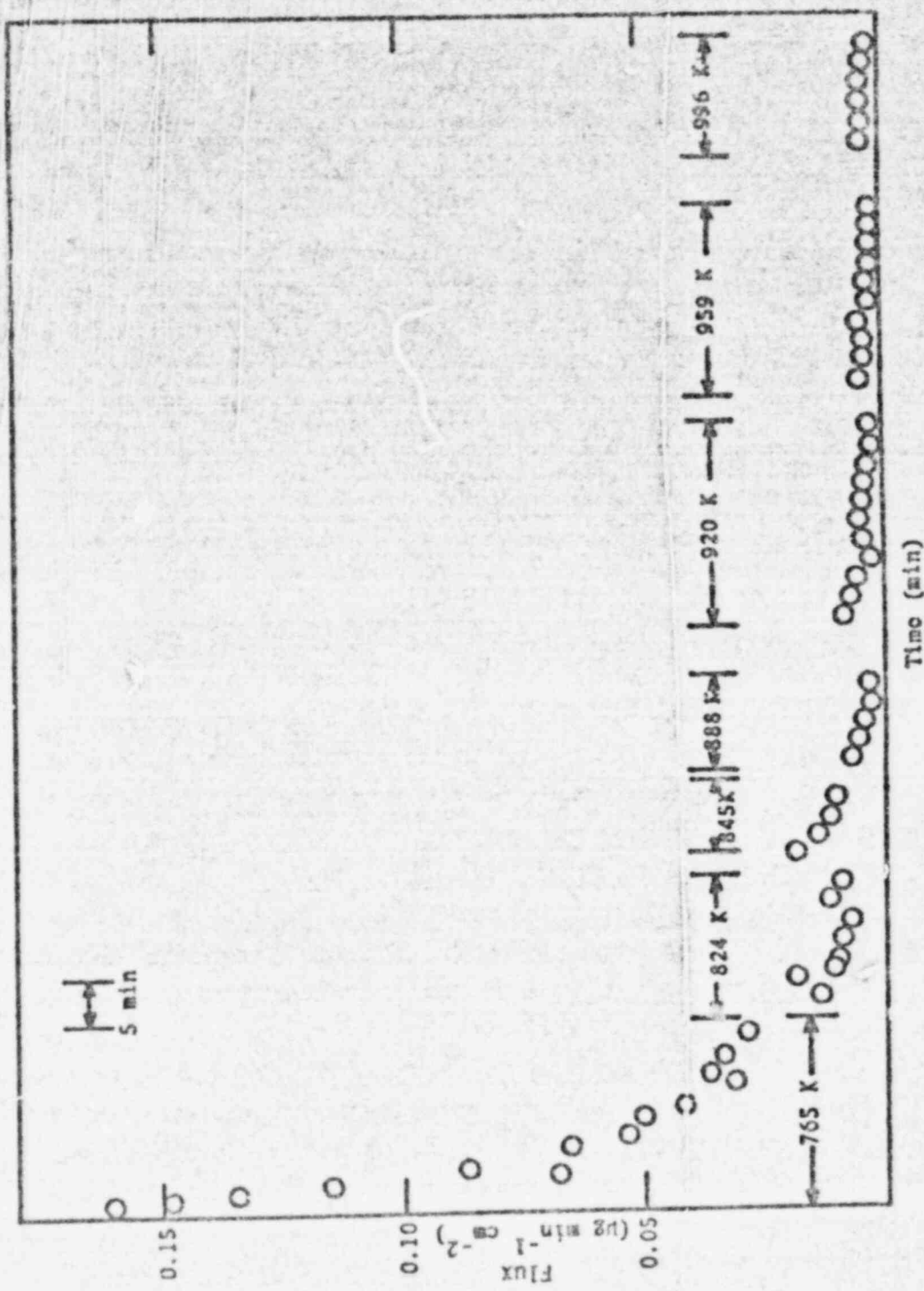


Fig. 7L. Time dependence of desorption flux from cesium-doped H-451 graphite at constant temperatures between 765-996 K for Experiment 6.

between 765 and 996 K for Experiment 6. The cesium-doped graphite used in this experiment was not preheated to 1373 K. Figure 72 shows a similar plot of data obtained in Experiment 3 in which the cesium-doped graphite was preheated to 1373 K prior to investigation with the microbalance.

Mass-loss measurements were also performed using blank graphite samples. Blank No. 1 consisted of graphite doped with water and was not preheated to 1373 K. Blank No. 2 was doped with water and was preheated to 1373 K in a closed tantalum crucible for 2 h (see Table IX). Results of the blank experiments show desorption fluxes similar to those found for the cesium-doped samples. This implies that mass losses observed with the cesium-doped samples may not be due to cesium desorption alone but may include desorption of water and other gases.

It is interesting to note that desorption fluxes of the nonpreheated cesium-doped graphite and blank graphite samples measured in this work are similar to cesium desorption rates measured by Aronson using CsI and CsNO<sub>3</sub>-doped samples.<sup>44</sup> Since we measure total mass loss and Aronson measured mass loss of cesium only, our measured desorption rates should be higher than those derived from Aronson's reported mass-loss results. The reason for this discrepancy between the two types of experiments is not clear. It seems that the desorption behavior of CsOH in the presence of water is considerably more complex than originally thought. It is clear that information concerning the vapor composition of species desorbing from the graphite surface is needed in order to better understand the results of our experiments with CsOH-doped graphite.

## 2. Fuel Failure and Fission Gas Release Experiments

(J. L. Lunsford, OMB-8)

Several modifications are being undertaken to upgrade the operational capability of the equipment used in the fuel particle heat-up experiments. In the past, operator attendance was desirable for several reasons. First, temperature measurements for the experiment were made with a disappearing filament pyrometer which requires manual operation. Second, range selection on the vibrating capacitor electrometer was carried out by "riding" the range selection switch in order to obtain that scale which gave maximum sensitivity. In order to obtain more accurate data during the longer runs required by the loss-of-forced-coolant (LOFC) accident histories, an automatic two-color recording pyrometer will be added to the high-temperature furnace. Also, a

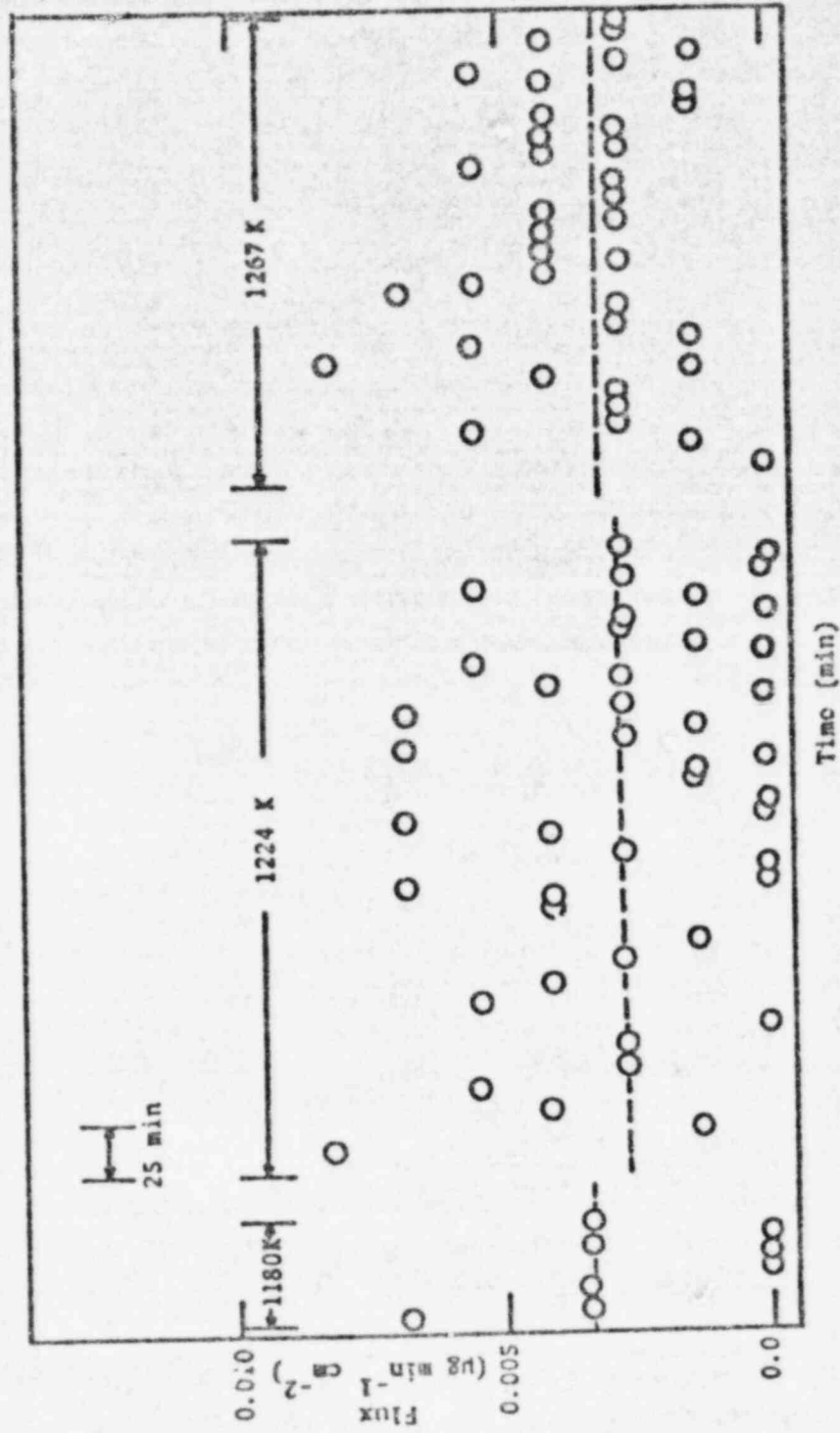


Fig. 72. Time dependence of desorption flux from cesium-doped H-451 graphite at constant temperatures between 1180-1267 K for Experiment 3.

Logarithmic converter will be placed between the electrometer and the strip chart recorder so that the electrometer can be left on the highest scale deemed reasonable. Because two data records will now be produced, a two-pen strip chart recorder will be substituted for the single-pen unit presently used. (Although temperature profiles could be estimated during unattended operation by calibrating the temperature against the programmed power profile, it was decided that better data would result if continuous temperature measurements were available.)

The high-temperature furnace recently experienced serious overheating on one of the power feed flanges. The cause of the thermal excursion is unknown. However, to guard against a repetition of such a problem and to permit diagnostics in the event that the difficulty occurs again, the temperature of the four return-water cooling circuits from the furnace to the furnace controller will be instrumented with indicating digital meters equipped with analog output capabilities. In addition, these meters will drive digital controllers wired into a high-alarm, manual-reset mode, which will remove the 35 kVA furnace from the line in the event of overheating. This should protect the furnace and increase confidence in scheduling long-time unattended operation.

### 3. Fission Product Transport Calculations

(J. L. Linsford, CB-8)

#### a. Fission Product Kinetics

Output capabilities for the kinetics side of the scoping code QUIL/QUIC have been completed. Printed output is extensive and includes reaction coordinates, reaction rates; species, and equilibrium constants. Plotted output includes a plot of the species distributions and a plot of the reaction rates in the system. Reaction potentials are also plotted when they are included in the input.

The system solver in QUIL employs a two-dimensional direct-search technique. The two search variables are  $E$ , a scaling factor which is applied to the calculated correction to the current approximation to the final solution, and  $p$ , the Levenberg-Marquardt parameter.<sup>45</sup> In a typical problem, several thousand calculations of  $\phi$  (the sum of the squares of the errors) are required by the direct-search strategy in QUIL. In general, the amount of computing required to apply the two parameters differs markedly. Application of the Levenberg-Marquardt parameter requires that the linearized set of equations be

solved once for each trial value of  $\phi$ . To speed up execution for QUIL, the two-dimensional direct search was rewritten in such a way that the search proceeds along cross sections of constant  $p$ . Although the search remains two-dimensional, a new solution vector is required less frequently. It is estimated that this change will speed up execution times for QUIL by a factor of two.

#### b. Gaseous Fission Product Release

(C. E. Apperson, Jr., Q-13)

The SUVIUS code has been modified to more accurately model the release of fission gases at the instant of fuel particle failure. Initially, precursor behavior was approximated. This resulted in slightly underestimating the burst component of fission gas release. Use is now made of the exponential operators developed for the main solution routines in SUVIUS. These operators have been discussed in previous quarterlies.

The release fraction of the fuel particles is a function of temperature. For calculational purposes, it is convenient to specify the average release fraction of a core region in terms of an effective temperature. Unfortunately, this temperature does not necessarily correspond to the volume-weighted region average temperature. To improve the accuracy of the activity estimates calculated by SUVIUS, a preprocessor code has been developed, which performs a detailed volume-weighted average of the failed and intact release fractions. These results can be translated directly into the proper effective temperature for use in SUVIUS. Using these improvements, future emphasis will be placed on resolving the differences noted last quarter in the results predicted by SUVIUS and the General Atomic Company (GAC) code.

#### B. Structural Evaluation

(C. A. Anderson, Q-13)

The data obtained from all of the seismic model tests conducted at the White Sands Missile Range (WSMR) during FY 1977 have been reduced. Results, reported as maximum strains produced in the various models, are presented and discussed for both true and distorted models. The current status of the three codes, NONGAP-C, INGEN, and MOVIE.IASL, which have been used for Prestressed Concrete Reactor Vessel (PCRV) analysis, is discussed. An elastic-plastic concrete constitutive model that differs from the variable modulus model now

being used in NONSAP-C is discussed; this model is proposed for implementation in NONSAP-C to provide better correlation with experimental data from PCRV models. Results from a reliability assessment of a single-cavity PCRV are summarized.

#### 1. Seismic Program

(R. C. Dove and J. G. Bennett, Q-13)

The data obtained from all of the vibration tests which were conducted at WSMR during FY 1977 have been reduced. The dimensions, material properties, and instrumentation of the systems that were tested and the characteristics of the test facility at WSMR were given in a previous report;<sup>36</sup> therefore, only the test results are presented here.

The first series of tests involved the use of sinusoidal excitation to investigate the effect of selected parameter variations on system response. The results of tests conducted on the prototype system are shown in Figs. 73 and 74. Figure 73 shows how the maximum strain (a convenient measure of block response) is affected by the clearance gap between the blocks. Comparison of results presented in Fig. 73 to results obtained from the analytical model, FYSMOD (see Fig. 16, p. 24 of Ref. 46) shows that both experiment and theory predict the same trend for the effect of clearance gap on system response.

Figure 74 shows how the system response is affected by variation in the exciting frequency. The analytical model, FYSMOD, was not used to make this kind of study (constant acceleration at various frequencies) so no comparison with theory is available in this case.

The second series of tests involved the use of simulated earthquake excitation to investigate the feasibility of using a scale model to predict system response. As given in a previous report<sup>36</sup> it was found that there is some variation in the response of either prototype or model system when either is subjected to several supposedly identical tests.

The reason for this lack of repeatability was judged to be the uncontrollable difference in the starting conditions between otherwise identical tests. For example, consider the four-block prototype system subjected to a simulated earthquake. Although the gap can be carefully set before each test (for example, equal gaps between each block), small variations in static coefficient of friction among the four blocks may cause small, but important, relative motion between the blocks before the first major pulse, which causes impact, occurs.

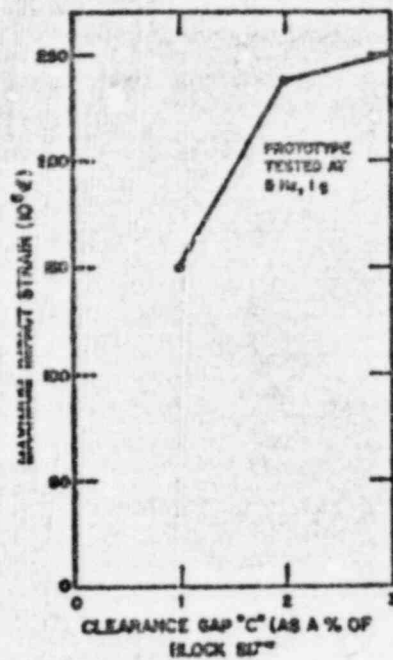


Fig. 73.

Effect of clearance gap on the four-block prototype system response.

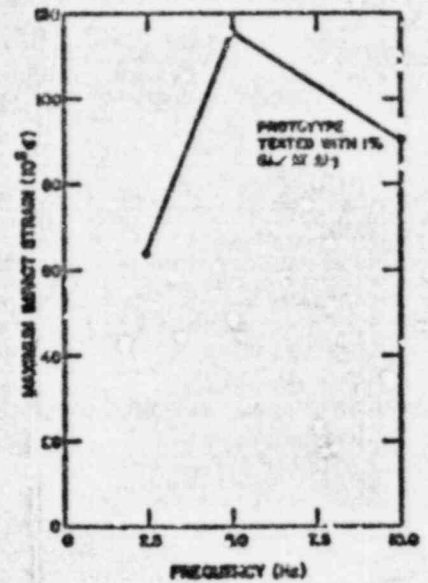


Fig. 74.

Effect of excitation frequency on the four-block prototype system response.

To test this hypothesis, several tests were conducted on the four-block prototype system in which starting conditions were deliberately varied. In each test the system was driven at 5 Hz to  $\pm 1$  g. The total gap remained the same for each test (3%); however, the initial positions of the blocks were varied. The results of two of the tests are shown in Figs. 75 and 76. Clearly, the initial position has a great effect on the impact sequence. These harmonic motion tests were run for a large number of cycles, and it was observed that the response motion never becomes periodic, i.e., there is no response condition that can be described as "steady-state, periodic" even with steady-state periodic excitation.

For these reasons, we anticipated that when either the prototype or the model system was excited several times by identical earthquake signals, the responses would vary for each test. This was found to be the case, and as a result, model predictions are compared to prototype results, using average and maximum values of impact-induced strains rather than by comparison of a single pulse as was done in the previous tests which involved only a single impact of two blocks (see Figs. 70 and 71 of Ref. 36).

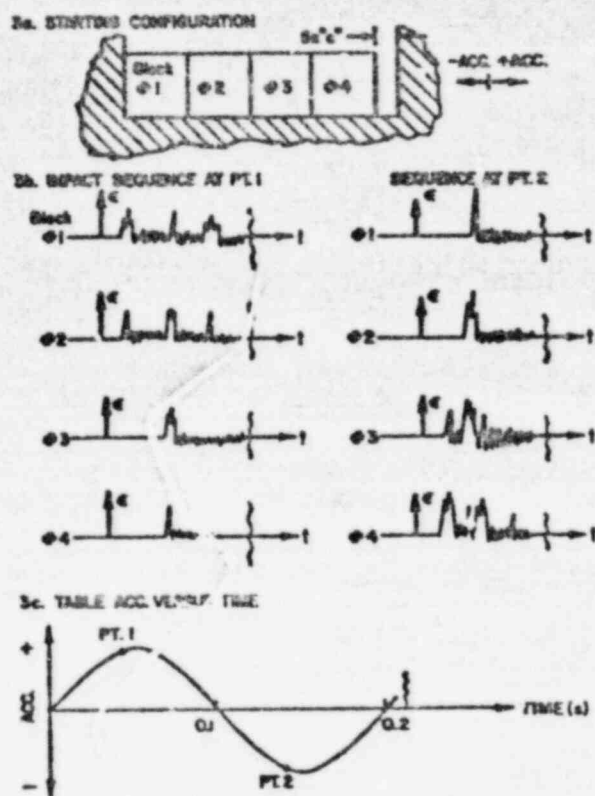


Fig. 75.  
Effect of the initial configuration -- gap at right end.

The four-block prototype system was subjected to five earthquake tests. The exciting function (i.e., the simulated earthquake) was the same for each test within the limits of the ability of the servo-hydraulic system to reproduce the control signal. The initial clearance gap between blocks and the starting position of the blocks were identical for each test within the limits of setup error. Table X shows the maximum strains produced in the prototype system for each of the five tests, together with the average value.

The four-block plastic model system was also subjected to five earthquake tests, which were as nearly identical as was possible. For these model tests the acceleration-time history used as the exciting function was, of course, properly time scaled. The maximum strains produced in the model system for each of the five tests, together with the average value, are also shown in Table

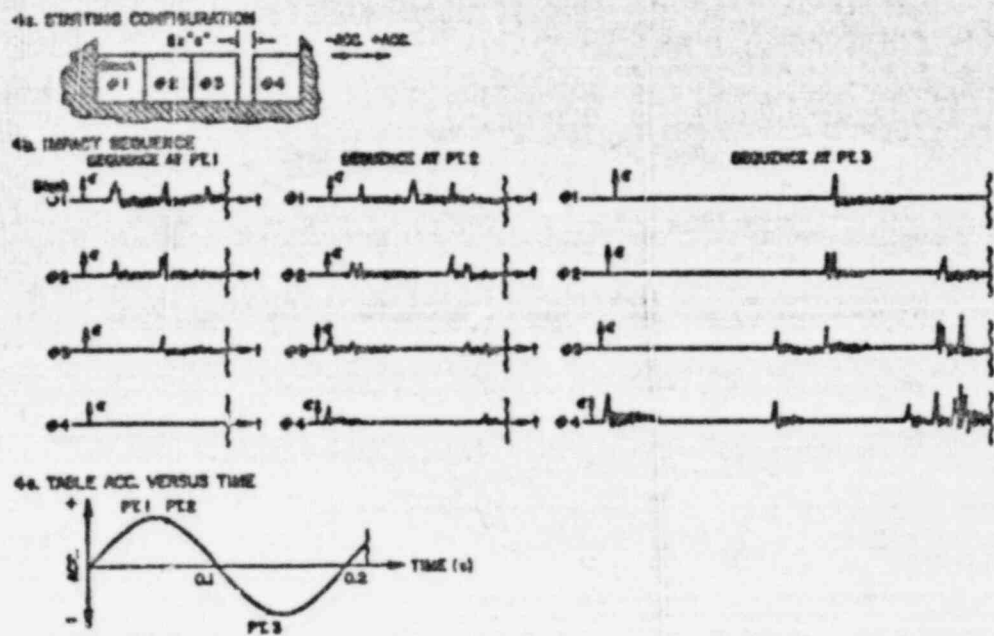


Fig. 76.  
Effect of the initial configuration — gap between blocks 3 and 4.

X. These data indicate that the model predicts amplitude of response (as measured by strain produced) reasonably well but that there is more variation in results for "identical" model tests than there is for "identical" prototype tests. We believe the reason for this is the fact that static frictional effects are more difficult to control in the model system than in the prototype system.

It should be remembered that, as pointed out in a previous report (see Figs. 74 and 77 of Ref. 36), the model does not predict exactly the sequence or pulse shapes of block impacts that occur over the earthquake time-history. However, no two tests of the prototype itself produce exactly the same sequence of pulse shapes of block impacts.

TABLE X  
 MAXIMUM STRAIN PRODUCED IN FOUR-BLOCK SYSTEMS DURING  
 SIMULATED EARTHQUAKE TESTS

Test No.	Max. Strain in Prototype $\times 10^6$	Max. Strain in Plastic Model $\times 10^6$	Max. Strain in Distorted Model $\times 10^6$
1	212	212	265
2	191	187	223
3	191	170	254
4	201	254	244
5	223	191	254
Average of 5 Tests	204	201	248
Deviation from Ave.	-6.4% to +9.3%	-15.4% to + 25.4%	-1. . to +6.8%
Error in Prediction of Average Maximum		-1.4%	+21%

The third series of tests involved the testing, again using simulated earthquake excitation, of a graphite model. This model was made of the same material as was the prototype, A-378 graphite, but was the same size as the plastic model. This model was known, from theoretical considerations, to be a distorted model in that all friction forces are improperly scaled (too small) as compared to inertial and contact forces. The question to be investigated in this study was: "What is the effect on system response of this distortion of frictional forces?" This question had been investigated analytically by using FYSMOD to study the effect of variation in the coefficient of friction,  $\mu_k$ , and the modulus-to-weight ratio,  $\frac{Eh^2}{W}$ , of the core blocks (see Figs. 17 and 19 of Ref. 46 and the discussion of distorted models on pp. 32-35 of Ref. 47). As a result of this investigation, it was expected that use of a distorted model would result in a prediction of strains (or accelerations) that were larger than would actually be produced in a prototype. However, with earthquake excitation the actual magnitude of the effect of the distortion cannot be conveniently determined from the analysis.

This distorted model was subjected to five identical earthquake tests. The acceleration-time history used as the exciting function was, of course, properly accelerated and time scaled. The maximum strains produced in the distorted model system for each of the five tests, together with the average value are also shown in Table XII. The measured strain and, hence, the predicted strain, since strain is scaled by a factor of unity, is larger than the strain measured in the prototype test. This finding confirms the distorted model theory previously discussed.

Funds are available for additional test work at WSMR, and several additional tests are being planned. These include studies of the effect of coefficient of friction and excitation amplitude.

## 2. Code Development for Analysis of PCRVs

(P. D. Smith, W. A. Cook, and C. A. Anderson, Q-13)

### a. Status of NONSAP-C, INGEN, and MOVIE.IASL

The three codes, INGEN, NONSAP-C, and MOVIE.IASL, used for PCRV structural analysis require the use of large core memory (LCM) in the CDC-7600 computer. Until an industry-standard compiler was made available at LASL in October 1977, all three codes had to have nonstandard FORTRAN coding to have access to LCM. Both INGEN and NONSAP-C have been recoded to run with the standard language. MOVIE.IASL is heavily tied to the nonstandard LTSS version of FORTRAN; it would be a major effort to reproduce an exportable version of this code. Discussed below is the current status of the three codes.

1. Preprocessing: The user's manual<sup>48</sup> for INGEN has been sent to press. Routines have been added to INGEN to process the 3-D mesh data and write files that can be accessed directly by MOVIE.IASL. One can now generate a mesh and obtain a plot of the mesh immediately.
2. Structural Analysis: The original NONSAP code has been modified to include an orthotropic, variable modulus reinforced concrete model with thermal strains and cracking, a creep model with thermal strains and time- or temperature-dependent material properties, a 3-D membrane element with either a linear, orthotropic material, or a von Mises elastic-plastic material, gravity loads, pressure loads, and boundary conditions in cylindrical coordinates. These added features are working well, but the code is still inadequate for use as a PCRV safety analysis tool.

The reinforced concrete model does not yet satisfactorily reproduce observed load-deflection behavior during postcracking stages of failure. Suggestions for modifications will be discussed in Sec. 2.b below. In addition, a three-node prestressing element is needed, and a

crack formation model needs to be added to the creep material model. Execution times can be reduced significantly by recoding matrix assembly routines to take advantage of the random access file manipulations that are newly available with the FORTRAN EXTENDED compiler. Some of the above modifications are small jobs and some are major; they will all add to the value of the NONSAP-C code.

3. Postprocessing: NONSAP-C generates nodal displacements in a form that can be used directly by MOVIE.LASL for deformed mesh plots. For stress and strain contour plots, MOVIE.LASL requires stress and strain data at node points. The incremental solution scheme used by the NONSAP/ADINA family of codes for nonlinear analysis permits calculation of stresses only at interior integration points. To modify NONSAP-C to calculate nodal strains and stresses directly would require the use of 42 additional words of storage for each integration point in the mesh. Such an additional storage requirement would result in prohibitive increases in execution times. A postprocessing routine is being written for NONSAP-C that will extrapolate stresses and strains from interior integration points to the nodal points of the mesh. These nodal values will then be put into a data file to be accessed by MOVIE.LASL.

A flow chart that illustrates the interaction of the three PCRV analysis codes is shown in Fig. 77. The dashed lines represent the link-up capability that is currently being developed.

#### b. Concrete Constitutive Relations

As was mentioned previously, the reinforced concrete strength model, which has been implemented in the NONSAP-C code, does not yet satisfactorily reproduce the postcracking load-deflection behavior observed in experiments on PCRV models. Figure 78 illustrates the load-deflection behavior of PV-27, one of a series of PCRV models tested under internal pressure at the Structural Research Laboratory of the University of Illinois,<sup>49</sup> that was computed by NONSAP-C and observed experimentally. Far more ductility appears in the experimental curve than in the calculated one.

Ductile behavior of metals has been explained as the motion of dislocations present in the metal, and mathematical theories of plasticity have been developed to explain the plastic behavior of all types of structural elements under complicated stress states. A plastic constitutive relation for concrete under general three-dimensional stress states has been proposed recently by Chen and Chen<sup>50</sup> in which the concrete is assumed to be a continuous, isotropic, and linearly elastic-plastic strain-hardening-fracture material. In this theory, an initial discontinuity surface, subsequent loading surfaces, and a failure surface for concrete are defined, and elastic-plastic stress-strain incremental relationships are derived using the classical theory of

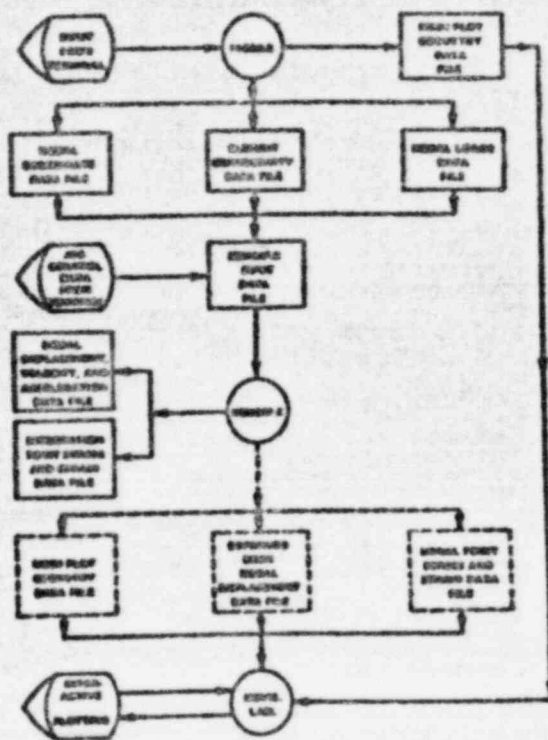


Fig. 77.  
Flow chart illustrating the coupling between the PCRV analysis codes INGEN, NONSAP-C, and MOVIE.IASL.

plasticity. Figure 79 illustrates the failure and initial discontinuity surfaces in principal stress space for this type of material. The failure surface is presumed to be dependent on the first stress invariant,  $I_1$ , (the pressure) and the second invariant of the deviatoric stress tensor,  $J_2$ , of the form

$$\frac{\kappa^2}{3} J_2 - \frac{\kappa^2}{36} I_1^2 \pm \frac{1}{12} I_1^2 + \frac{1}{3} A_\mu I_1 = \tau_\mu^2 \quad (55)$$

where  $A_\mu$  and  $\tau_\mu$  are material constants that can be determined from the concrete tensile and compressive strengths and where  $\kappa^2 = 3$  provides a good fit to multiaxial failure data. This form of failure surface has been proposed previously by Saigy.<sup>51</sup>

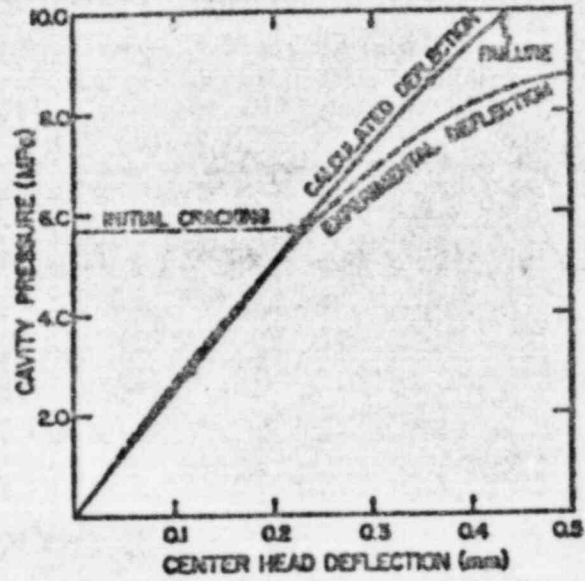


Fig. 78.  
Experimental and computed head load-deflection behavior of PV-27.

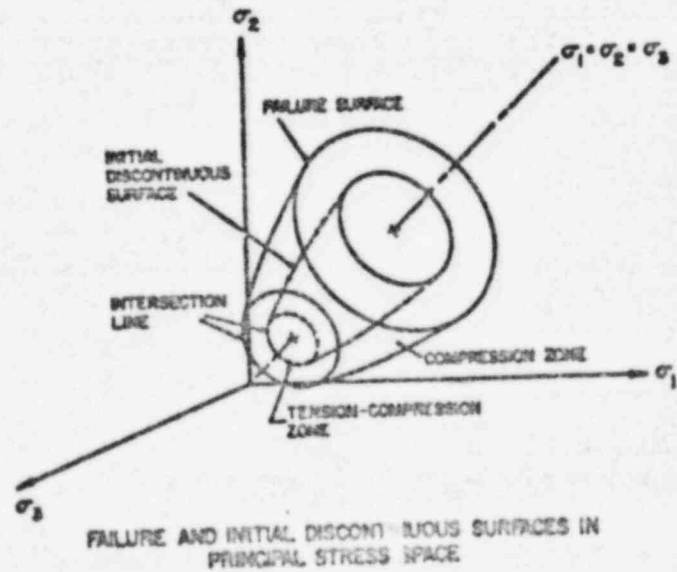


Fig. 79.  
Failure and initial discontinuity surfaces in principal stress space.<sup>50</sup>

A new material model representative of the Chen and Chen elastic-plastic concrete model is being coded and inserted into NONSAP-C. The material model will be tested against the experimental observations on PV-26<sup>49</sup> and compared also with the calculated results using the variable modulus material model. PV-26 is an axisymmetric model that will allow us to save substantially on computer time.

### 3. Reliability Assessment of a Prestressed Concrete Reactor Vessel

(C. A. Anderson and P. D. Smith, Q-13)

The random nature of the strength properties of certain materials of construction is well known and, in certain cases, is well documented. For example, Fig. 80 illustrates the variability of the uniaxial compressive strength of 102 concrete cylinders cast from different batches with fixed mix proportions.<sup>52</sup> Except for the tail portions, the density function for this set of data was found to be nearly normal with a standard deviation of about 10% of the mean compressive strength. Considering that the tensile strength of concrete is likely to be even more variable than the compressive strength,

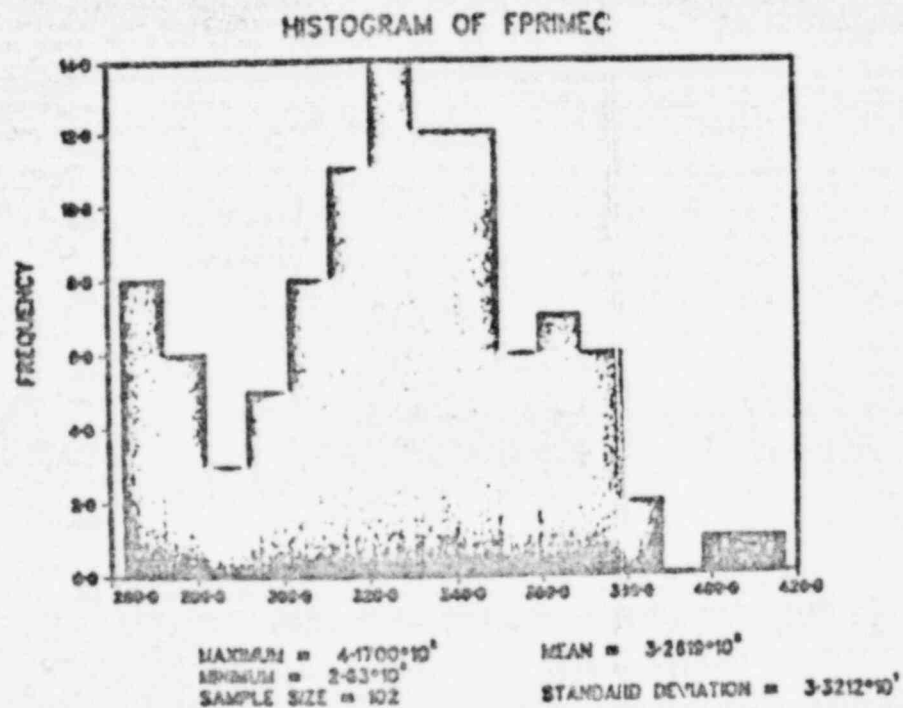


Fig. 80.  
Histograms for concrete compressive strengths.<sup>52</sup>

incorporation of the random nature of concrete strength parameters in assessments of the adequacy of prestressed concrete reactor vessels is essential.

The purpose of this work is to outline a procedure for establishing the probability density function  $f_R(x)$  of the resistance  $R$  of a structure whenever  $R$  depends nonlinearly on a large number of randomly distributed strength parameters. The procedure uses Latin hypercube stratified sampling<sup>34</sup> of the strength parameters to establish the density function  $f_R(x)$  with a smaller number of samples than is required in the Monte Carlo method. The method is particularly efficient (in terms of a decrease in number of necessary computer runs) for establishing trends from large finite element analyses of complex structures. Once the probability density  $f_R(x)$  for the strength of the structure has been determined and the probability distribution function for the loading  $F_S(x)$  has been determined, the reliability  $L$  can be calculated from the expression

$$L = \int_0^{\infty} F_S(x) f_R(x) dx, \quad (56)$$

which represents, for each and every possible value of the resistance, the probability that the applied force does not exceed it. If the strength  $R$  and the load  $S$  are both normally distributed random variables with means  $\mu_R$  and  $\mu_S$  and standard deviations  $\Sigma_R$  and  $\Sigma_S$ , then the random variable  $Z = R - S$  also follows a normal distribution with a mean  $\mu_R - \mu_S$  and a standard deviation  $\Sigma_R^2 + \Sigma_S^2$  and,

$$L = 1 - \Phi \left( \frac{\mu_R - \mu_S}{\sqrt{\Sigma_R^2 + \Sigma_S^2}} \right), \quad (57)$$

where  $\Phi$  denotes the standard normal distribution function.

The reliability aspect of the strength and the behavior of prestressed concrete reactor vessels is complicated by the inherent three-dimensional geometry of these structures and by the ill-defined behavior of concrete in states of triaxial stress. For illustrative purposes, a reliability analysis has been carried out for an idealized model of a prestressed concrete reactor

vessel under internal pressure loading that is geometrically uncomplicated yet maintains the triaxial stress feature that strongly influences the ultimate strength of concrete. The failure condition attributed to Saaxy,<sup>51</sup> discussed previously, was employed to represent failure of concrete under a triaxial stress state.

Figure 81 illustrates the concrete reactor vessel that was used in the reliability assessment. The reactor vessel is a thick-walled cylinder of length  $L$  with inner and outer radii  $a$  and  $b$ , respectively. The concrete vessel is encased in a thin-walled shell of steel of uniform thickness  $h$ . An initial axial compressive prestress of amount  $q_a$  is applied to the concrete vessel; the prestress  $q_a$  was treated as a random variable.

Figure 82 is a cross-sectional view of the cylinder model when it has reached the failure condition. At this stress condition the hoop strain in the steel liner will be assumed to have reached its ultimate value  $\epsilon_g$ . An interface between the failed region of concrete and an outer elastic core is positioned at  $r = c$ . The state of stress in the elastic region is given

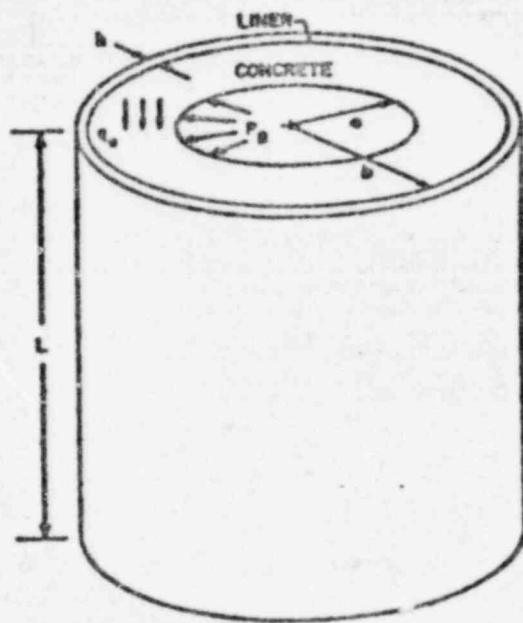


Fig. 81.  
Prestressed concrete cylinder model.

directly in terms of an unknown interface pressure and the radial pressure at the interface between concrete and liner, which depends on the value of  $\epsilon_g$ . In the failed region the stresses satisfy the failure condition, Eq. (55), where coefficients are now random variables since they depend on the tensile and compressive strengths  $\sigma_t$  and  $\sigma_c$ . By requiring that the elastic stress-state at  $r = c^+$  also satisfy the failure condition, a single nonlinear equation for the value of  $c$  was obtained and solved numerically. Finally, the burst pressure  $p_B$  was obtained by numerically integrating the equilibrium equation in the failed region  $a \leq r \leq c$  (see Ref. 53 for details).

The probability density function of the burst pressure  $p_B$  was then estimated by using stratified sampling of what were assumed to be random variables; concrete strengths  $\sigma_c$  and  $\sigma_t$ , liner ultimate strain  $\epsilon_g$ , and axial prestress  $q_a$ . The concrete properties were assumed to be normally distributed, whereas both prestress and liner ultimate strain were taken to be uniformly distributed random variables. The ratio of  $c$  to inner radius of the reactor vessel was taken to be 4.

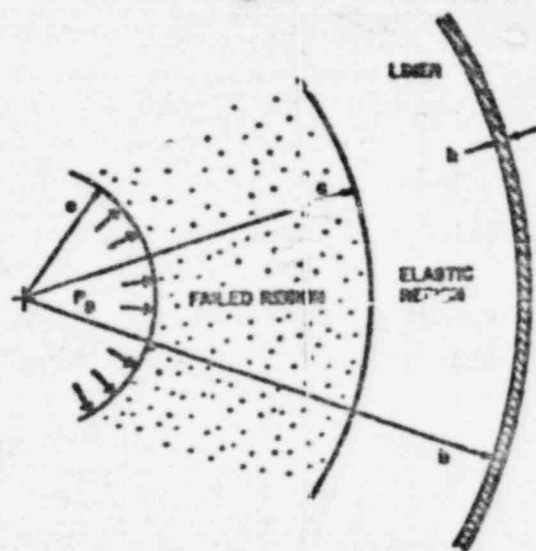


Fig. 82.  
Prestressed concrete cylinder at failure.

Data were taken from successive computer runs using the sampled input values. The distribution function for the burst pressure  $p_B$  is shown on a normal probability plot in Fig. 83 for a sample size of 100. The distribution of  $p_B$  is again close to being normal as indicated in Fig. 83; Table XI summarizes the parameters of the distribution as well as the parameters of the distribution of the input variables.

C. Phenomena Modeling, Systems Analysis, and Accident Delineation

(P. A. Secker, 0-6)

This task is primarily concerned with the development, verification, and application of Gas-Cooled Reactor (GCR) consolidated plant simulation computer programs. The Composite HGR Analysis Program (CHAP) consists of a model-independent systems analysis program which has steady-state, transient, and frequency response capabilities. This model-independent portion of the code has

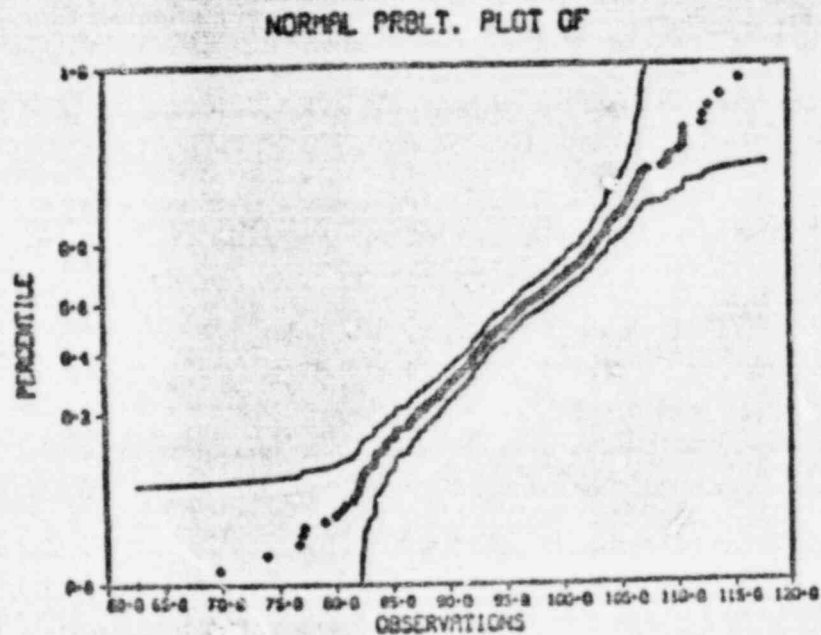


Fig. 83.  
Normal probability plot for failure pressure of the prestressed concrete cylinder.

TABLE XI  
INPUT AND OUTPUT DATA FOR THE PRESTRESSED CONCRETE CYLINDER

<u>Variable</u>	<u>Density Function</u>	<u>Mean</u>	<u>Standard Deviation</u>
$q_a$	Uniform 13.8 to 20.7 MPa (2000-3000 psi)		
$s$	Uniform 0.00025-0.00035		
$t$	Normal	3.45 MPa (500 psi)	0.69 MPa (100 psi)
$c$	Normal	34.5 MPa (5000 psi)	3.45 MPa (500 psi)
$P_B$	Normal	42.3 MPa (6140 psi)	3.24 MPa (470 psi)

been renamed LASAN (Los Alamos Systems Analysis Code). The model-dependent portion of CHAP consists of linked modules, each representing a component or subsystem of the overall HTGR plant model and having a standardized modular structure. The program organization facilitates modification of component models, modification of solution algorithms, and addition of new solution techniques. Overlay and nonoverlay versions of the code have been developed. The initial version of CHAP models the 3000 MW(t) HTGR. CHAP-2 is currently under development and models the Fort St. Vrain (FSV) HTGR.

During the past quarter a frequency response calculation capability was added to the LASAN package, a new treatment of implicit algebraic loops was incorporated, and the numerical integration algorithm was further modified. An improved lower plenum module was developed for CHAP-2, reverse helium flow heat transfer was added to all primary loop modules, a general one-dimensional tube and shell heat exchanger subroutine was developed for FSV emergency cooling problems, and a module for calculating fuel particle failure and nuclide release during accident transients was developed. Rapid depressurization accidents using the FSV model were studied during this period.

## 1. Relative Hazard Indexing

(P. G. Bailey, Q-6 and B. W. Washburn, Q-13)

A relative hazard index for normal and accident plant transients has been included in the CHAP code. The hazard index is defined as the ratio of the accumulated thyroid and whole-body dose calculated just outside of the fuel particles (both intact and failed BISO and TRISO particles) to the dose released from equilibrium fission products at 100 per cent power, assuming all fuel particles have failed. Such an index provides a consistent relative measure of the ultimate severity of all operational and accident transients performed with the code.

Twenty-five nuclides have been identified from previous radiological consequence evaluations as being major contributors to short-term health hazard effects for both light water and gas-cooled reactors.<sup>54,55</sup> Simplified formation and decay chain equations are used to describe the concentration of each nuclide both inside and outside the fuel particles as a function of operating history, reactor power, fuel temperature, and time.<sup>56,57</sup> The decay chain equations include decay branching ratios and accumulative or direct fission product yields and are simplified by eliminating extraneous short-lived nuclides from the chain. All nuclides used in the decay chain analyses are listed in Table XII.

Core-averaged per cent particle failures and fractional release rates of the 10 GAC nuclide groups for both intact and failed BISO and TRISO particles are calculated from failure rate data in a manner similar to that used in the LARC code.<sup>58-60</sup> The particle release rates, nuclide concentrations, and relative hazard index are calculated in CHAP in a new module called HAZARD. The hazard index is calculated external to the fuel particles, i.e., no attempt has been made to include fission product transport or external release mechanisms. The relative hazard index is calculated using dose conversion factors for both the thyroid organ and whole body, assuming a representative breathing rate.<sup>61,62</sup>

## 2. LASAN Numerical Integration Technique

(R. B. Lazarus, C-3 and P. A. Secker, Q-6)

The implicit optimum integrating factor (IOIF) numerical integration method for the approximate solution of a set of stable, nonlinear, constrained, first-order differential equations was investigated and adapted for use in the LASAN code.<sup>55</sup> The IOIF method is applied to an N-component state

TABLE XII  
NUCLIDES INCLUDED IN HAZARD DECAY CHAINS

Br83	Tel131M
Kr83M	I131
Kr85M	Tel132
Kr85	I132
Br87	I133
Kr87	Xel133
Kc88	I135
Sr89	Xel135
Sr90	Cs136
Zr95	Cs137
Nb95	Bal40
Ru103	La141
Ru106	Ce141
I129	Ce144

vector  $y(t)$ , which is given at time  $t = 0$  and whose first time derivative is given by a rate vector,  $\underline{f}(y, t)$ . In the present application, the state vector is subject to the implicit constraint equation,

$$y_i^{\min}(y(t), t) \leq y_i(t) \leq y_i^{\max}(y(t), t), \quad i=1, 2, \dots, N. \quad (58)$$

Furthermore, the components of the rate vector may depend on a number of "switch" variables,  $f_i = f_i(y, t; s_1, s_2, \dots)$ , which themselves may depend on the history of the solution. Thus,  $\underline{f}$  may be discontinuous, and  $\underline{f}$  is not, in general, a point function.

The IOIF method determines an increasing sequence of times  $0 = t_0 < t_1 < \dots < t_k, \dots$ , and estimates  $y(t_k)$  by solving, for  $k = 1, 2, \dots$ , the implicit matrix equation

$$y^k = y^{k-1} + (t_k - t_{k-1}) \left[ B \underline{f}^{k-1} + (I-B) \underline{f}^k \right], \quad (59)$$

subject to the constraints of Eq. (58). Here  $B$  is a diagonal matrix,  $\underline{f}^k$ , and

stands for  $f(\underline{y}^k, t_k)$ , and  $\underline{y}^k$  is our estimate for the true solution  $\underline{y}(t_k)$ .

The general goal of this effort was to develop an algorithm which gives acceptably accurate estimates of the true solution with minimal computational cost. There are, of course, many packaged programs for integrating sets of simultaneous ordinary differential equations, where the rate vector is given by subroutines supplied by the user. Most of them, however, assume that the rate vector is a smooth function of its arguments (except perhaps for isolated, integrable singularities), which is not the case in CHAP applications. Furthermore, in the CHAP code the dimensionality of the system may be increased at any time without warning (i.e., the model may introduce additional state variables during the course of the solution).

On the other hand, it is expected that most of the state variables will have simple derivatives depending on relatively few of the other variables and having almost linear dependencies. Thus, the Jacobian of the system will be sparse, and most of its elements will be almost constant. The integration method exploits these nice properties.

The first major problem was the automatic and efficient determination of that time sequence  $(t_1, t_2, \dots)$  for which Eq. (59) yields numbers  $\underline{y}^k$ , which are satisfactory estimates of the true solution  $\underline{y}(t_k)$ , while at the same time minimizing computational cost. The trick is in the proper choice of the diagonal matrix B. For a linear, uncoupled, unconstrained system, where  $f_i$  has the form

$$f_i(\underline{y}, t) = A_i + B_i t + \alpha_i y_i \quad (50)$$

and where  $A_i$ ,  $B_i$ , and  $\alpha_i$  are constants (i.e., for a system with a constant, diagonal Jacobian and linear explicit time dependence), the choice

$$B_{ii} = \frac{e^{-\alpha_i \Delta t} + (1 - \alpha_i \Delta t)e^{-\alpha_i \Delta t}}{\alpha_i \Delta t (1 - e^{-\alpha_i \Delta t})}, \quad i = 1, N \quad (61)$$

where  $\Delta t = t_k - t_{k-1}$ , for the diagonal element of the B matrix in Eq. (59) causes the IOIF method to track the exact solution:  $y_k = y(t_k)$ . Accordingly, Eq. (61) is used in LASAN as written, but for the coupled, nonlinear

equations expected in practice, various possibilities were investigated for computing the time constants  $\alpha_i$ . A choice which seems satisfactory and is presently in use is as follows. Define a "decay rate"

$$A_i = - \frac{\sum_{j=1}^N J_{ij} f_j^{k-1}}{f_i^{k-1}} \quad i=1, N \quad (62)$$

where  $J_{ij}$  is an approximation to the Jacobian element  $\frac{\partial f_i}{\partial y_j}$  at time  $t_{k-1}$ . Then we use  $\alpha_i = -A_i$  when  $A_i$  is positive but use  $\alpha_i = 0$  (which is to say, use  $B_{ii} = 1/2$ ) when  $A_i$  is not positive. This choice guarantees  $0 < B_{ii} \leq 1/2$ , which makes Eq. (59) asymptotically stable.

The second major problem was the numerical solution of the implicit Eq. (59). These two major problems are related; that is, evidence acquired in the course of the numerical solution of Eq. (59) can be used to guide the choice of the next element of the time sequence. Equation (59) is solved by a modified Newton-Raphson method. To use the standard method, we write Eq. (59) in the form  $\underline{Q} = \underline{Q}(\underline{y}^k)$ , where

$$\underline{Q}(\underline{y}) = \underline{y} - \underline{y}^{k-1} - \Delta t \left[ B \underline{f}^{k-1} + (I-B) \underline{f}(\underline{y}, t_k) \right] \quad (63)$$

We then take an initial guess  $\underline{y}^0$  and iterate

$$\underline{y}^{n+1} = \underline{y}^n - H^{-1} \underline{Q}(\underline{y}^n), \quad (64)$$

where  $H$  is the Jacobian of  $\underline{Q}(\underline{y}^n)$ . We do not actually do precisely this, because it would take too much computer time to get  $H$  at each iteration and because it would take both too much time and too much memory space to solve directly Eq. (64) by fully implicit matrix inversion. Instead, we get an approximate solution of Eq. (64) by a method of decomposition and iteration.

We replace  $H$  by

$$M = I - \Delta t (I-B)J, \quad (65)$$

where  $J$  is the complete approximate Jacobian matrix whose elements are those used in Eq. (62). A significant effort was devoted to finding a good way to

keep  $J$  adequately close to the true Jacobian while minimizing computational work. The  $M$  matrix is then written as

$$M = M_1 + M_2, \quad (66)$$

and we solve the linear equation

$$M\underline{d} = \underline{q} \quad (67)$$

by iterating

$$\underline{d}^{\text{new}} = M_1^{-1}(\underline{q} - M_2 \underline{d}^{\text{old}}) \quad (68)$$

For this iteration to converge rapidly, all the eigenvalues of  $M_1^{-1}M_2$  must be clustered about zero. To minimize storage space and/or computing time on the other hand,  $M_1$  must be so structured as to be easily triangularized. This can always be accomplished by taking  $\Delta t$  small enough but, of course, economy in the large requires a big time step. What must be done is to identify submatrices within  $M$  which are responsible for  $M$ 's largest eigenvalues; those submatrices are then incorporated, and  $M_1$  is treated as a block-diagonal matrix with rows and columns permuted.

In the general case, "to identify submatrices within  $M$  which are responsible for  $M$ 's largest eigenvalues" is a problem without practical solution. It appears, however, that a great deal can be done in real, physical cases, even if we do not ask the user to identify strongly coupled feedback loops. Furthermore, the penalty for failure, in some particularly nasty case, will merely be increased computing cost rather than an inaccurate solution.

Initially, (and every so often) the matrix  $M$  is analyzed as follows. We choose a likely maximum for  $\Delta t$  and an acceptable convergence rate  $r$ . We scan the nonzero off-diagonal elements of  $J$  to find those for which  $\Delta t^2 |J_{ij} J_{ji}| > r^2 |M_{ii} M_{jj}|$ , and put the associated four elements of  $M$  into  $M_1$ , listing  $(i,j)$  as a "pair." When this has been done, we scan the list of pairs for any which are not disjoint [e.g.,  $(3,7)$ ,  $(3,11)$ , and  $(7,14)$ ]. All the  $i$ 's and  $j$ 's for nondisjoint pairs are then thrown into a single  $n$ -tuple [in the example above, we would get the quadruple  $(3,7,11,14)$ ], and we put the associated elements of  $M$  into  $M_1$  (i.e., all  $M_{ij}$  for which  $i$  and  $j$  are both

in the  $n$ -tuple). However, we have preselected a maximum value for the  $n$  of the  $n$ -tuple (presently 9), and, if the logic described above leads to a large  $n$ -tuple, then we reduce  $\Delta t$  and try again. Thus, we end up with an  $M_1$  matrix, which is a permutation of a block-diagonal matrix (one  $n$  by  $n$  block, a number of 2 by 2 blocks, and the rest truly diagonal), plus a maximum allowable time step.

To account for the fact that the Jacobian is changing in time, we repeat this analysis whenever the linear system solver iteration does not converge satisfactorily within a reasonable number of iterations (currently 7), whenever the dimensionality of the system is increased, and whenever the derived value of  $\Delta t$  is actually observed to be restricting excessively the natural time step, which is deduced from the Newton-Raphson convergence, as follows.

Taking  $\underline{y}^{k-1}$  (the old state vector) as a natural first guess for  $\underline{y}^k$  (the new state vector), we observe that the first iterate would be the correct answer if

1. our approximate Jacobian were the correct Jacobian and
2. the correct Jacobian were constant.

An appropriate norm, then, of the difference between the first iterate and the second iterate tells us whether our step is too big, too small, or just about right.

Identification of the "appropriate norm" has been a significant difficulty, because of our desire to demand as little information as possible from the user of the model code. We therefore track "important" variations in the state variables and ignore "unimportant" variations to prevent "unimportant" variations from holding down the time step size. It is customary to pass this value judgment back to the user by asking him to specify what absolute and relative errors he is willing to accept for each state variable. While such a feature is no doubt desirable as an option, we have been successful in providing a basis by which the code can itself deduce the appropriate norm.

The method, as described, has been extensively tested during this quarter. We began by studying linear unconstrained systems whose Jacobian matrix coefficients were randomly selected using a random number generator. Figure 84 plots the analytic time solution of a tenth-order problem with all initial conditions set to 1.0. The IOIF method was applied to this problem with a

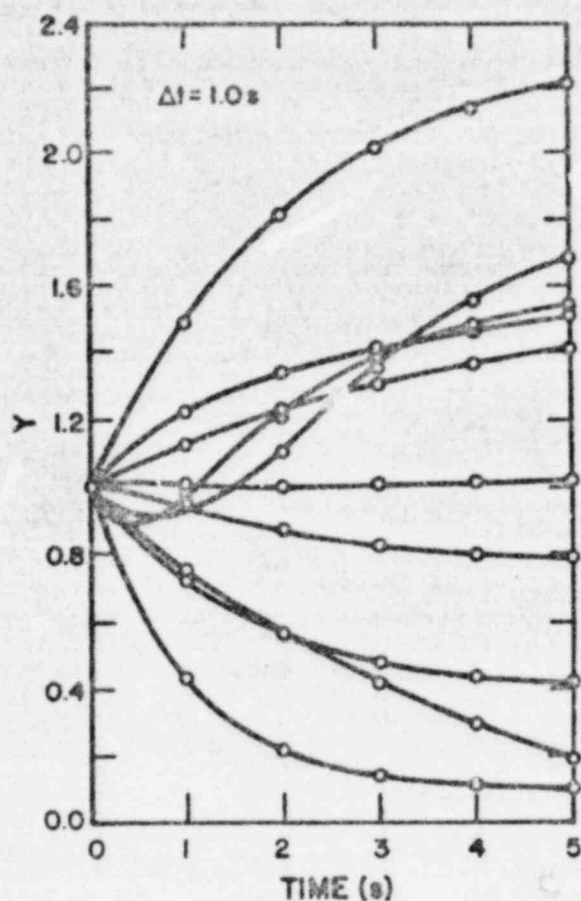


Fig. 84.

IOIF solutions for a tenth-order linear system.

fixed time step of  $\Delta t = 1.0$  s, and the solution points are plotted on the analytic curves. Note that even for variables whose solutions reverse trend, the method accurately predicts the result while jumping over the "structure." This is not desirable, usually, but demonstrates the accuracy and speed of the method.

Many randomly created nonlinear systems were investigated with hard limit constraints imposed. We studied systems with orders as high as 100 and compared solution running times and accuracy with results obtained using the most widely used "canned" integration packages in use at LASL. In these cases our method was superior in all respects. The method was then applied to a variety of CHAP problems using the current FSV (CHAP-2) modules and the CHAP-1 modules. Figure 85 is a plot of prompt neutron power in the FSV reactor resulting from a 1.0 dollar step in reactivity with separate fuel and moderator

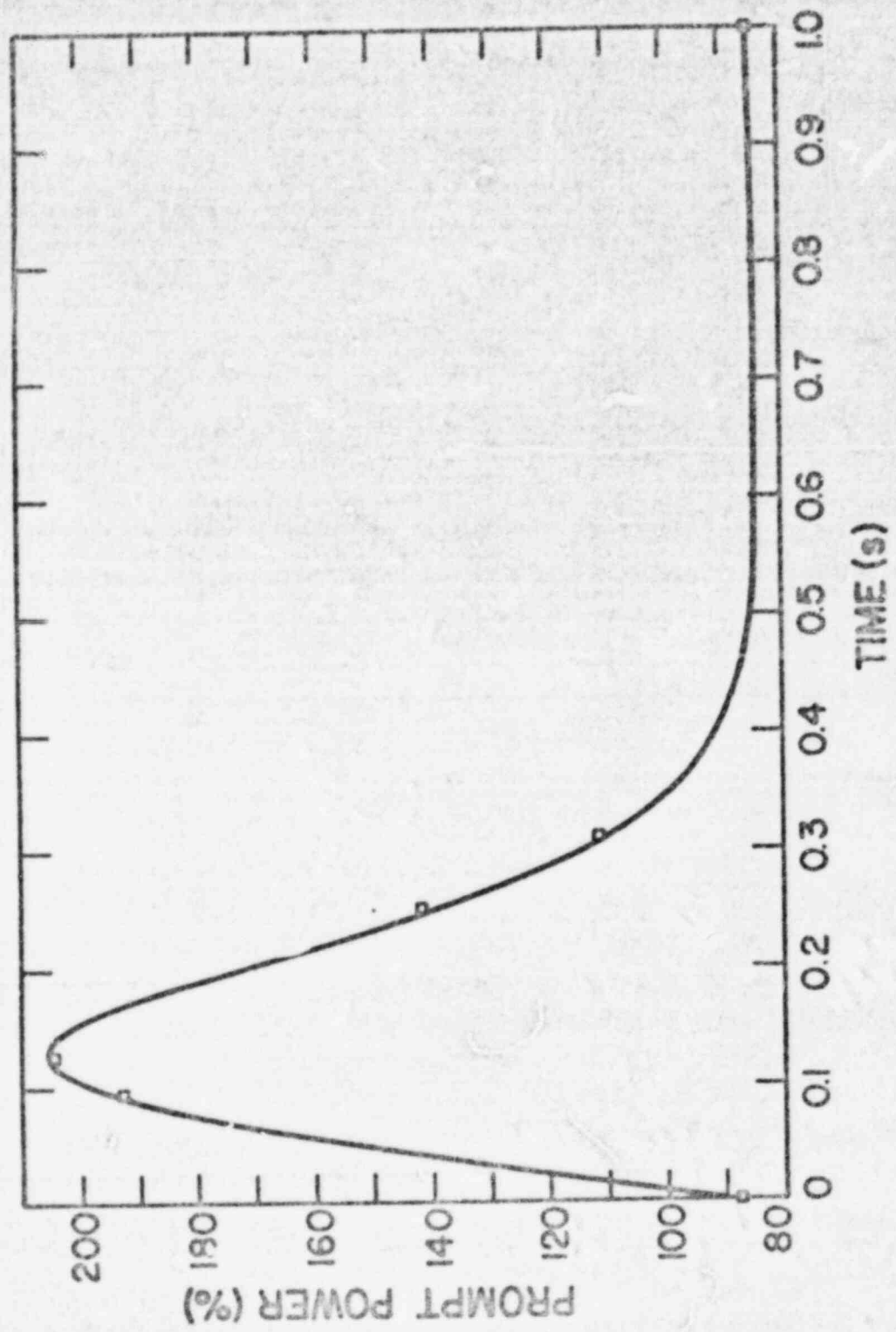


Fig. 85.  
Prompt power for a one dollar reactivity insertion using IOIF.

feedback reactivity. The IOTF method predicted peak power for the transient within 0.5% using only two solution time points. One second of the solution was obtained using only five solution increments.

A rapid depressurization of the PCRV corresponding to loss of helium inventory in the reactor cavity was studied. A 645 cm<sup>2</sup> break was postulated in the PCRV upper plenum of the F8V reactor. During this depressurization accident, protective plant control options were exercised. When the power-to-flow ratio increased above 1.4, the reactor was scrammed. All control rods were driven fully into the reactor core. Figure 86 shows the helium inventory and system pressure as a function of time. The power-to-flow-ratio is plotted in Fig. 87. The transient was carried out for 1 h of transient time but took only 1.2 min. of CDC-7600 machine time using the IOTF method.

### 3. LASAN Frequency Response Capability

(P. A. Secker, Q-6 and M. L. Stein, C-3)

We have added a frequency response solution capability to the LASAN code. The algorithms used for this analysis are similar to those contained in the LASL-developed TAF (Transient and Frequency) code.<sup>63</sup> The LASAN code is capable of obtaining transfer functions of specified CHAP model response variables with respect to specified model input variables by linearizing the nonlinear state variable derivative equations.

The coupled first-order ordinary differential equations (ODEs) in CHAP are described mathematically as

$$\frac{d}{dt} \underline{y}(t) = \underline{f}(\underline{y}, \underline{x}, t) \quad (69)$$

where  $\underline{y}$  is the vector of time-dependent state variables in the model,  $t$  is the independent variable time,  $\underline{x}$  is a vector of  $M$  time-dependent forcing functions, and  $\underline{f}$  is the state variable derivative vector. When the nonlinear ODEs are linearized about some steady-state operating condition, where

$$\frac{d}{dt} \underline{y}(t_0) = \underline{f}(\underline{y}_0, \underline{x}_0, t_0) = \underline{0} \quad , \quad (70)$$

the resulting linear approximations to the nonlinear expressions provide information on the dynamics of the system in a region about the steady-state input  $\underline{x}_0$ . The size of the region over which the linearized model is valid

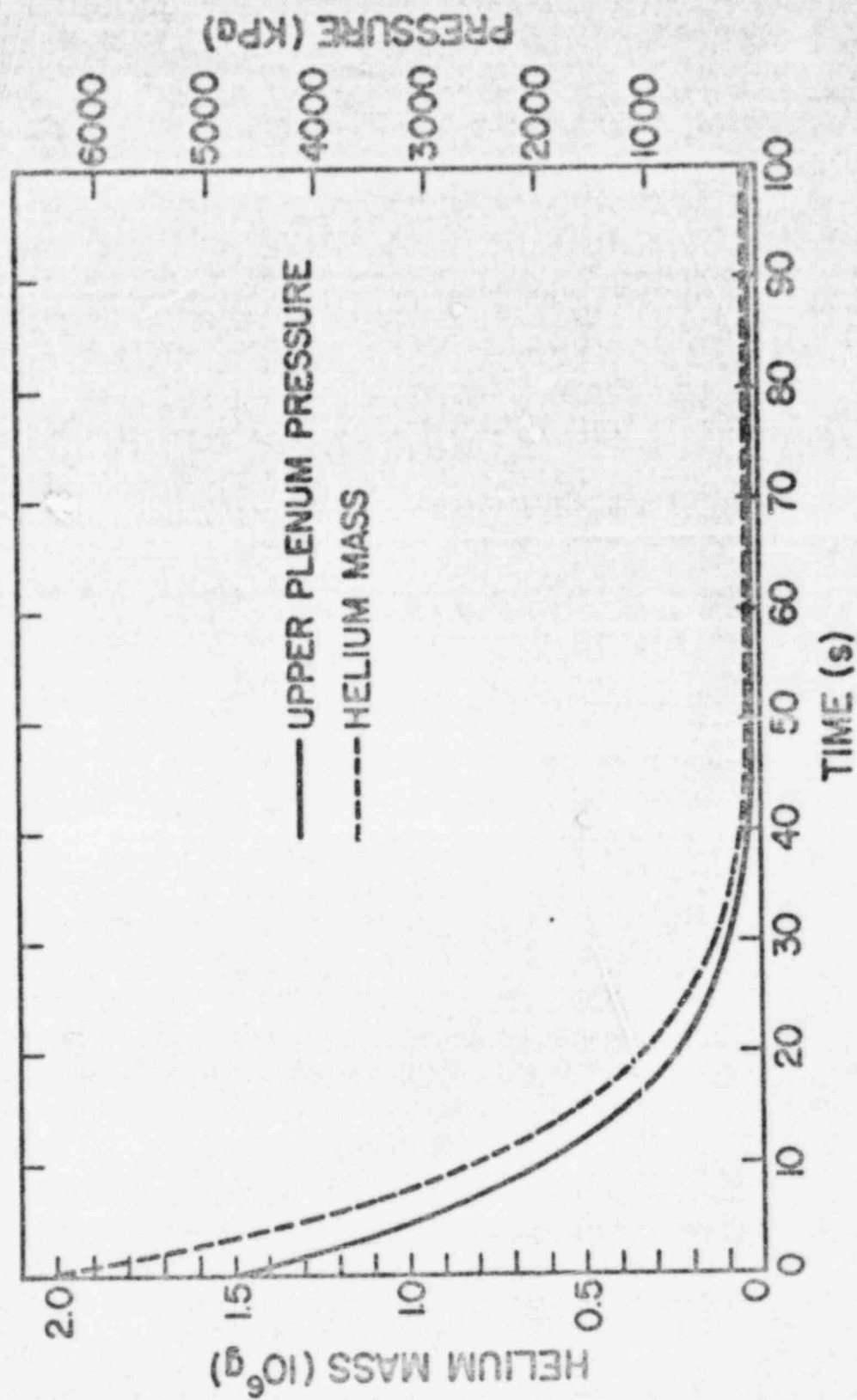


Fig. 86.  
Rapid depressurization accident.

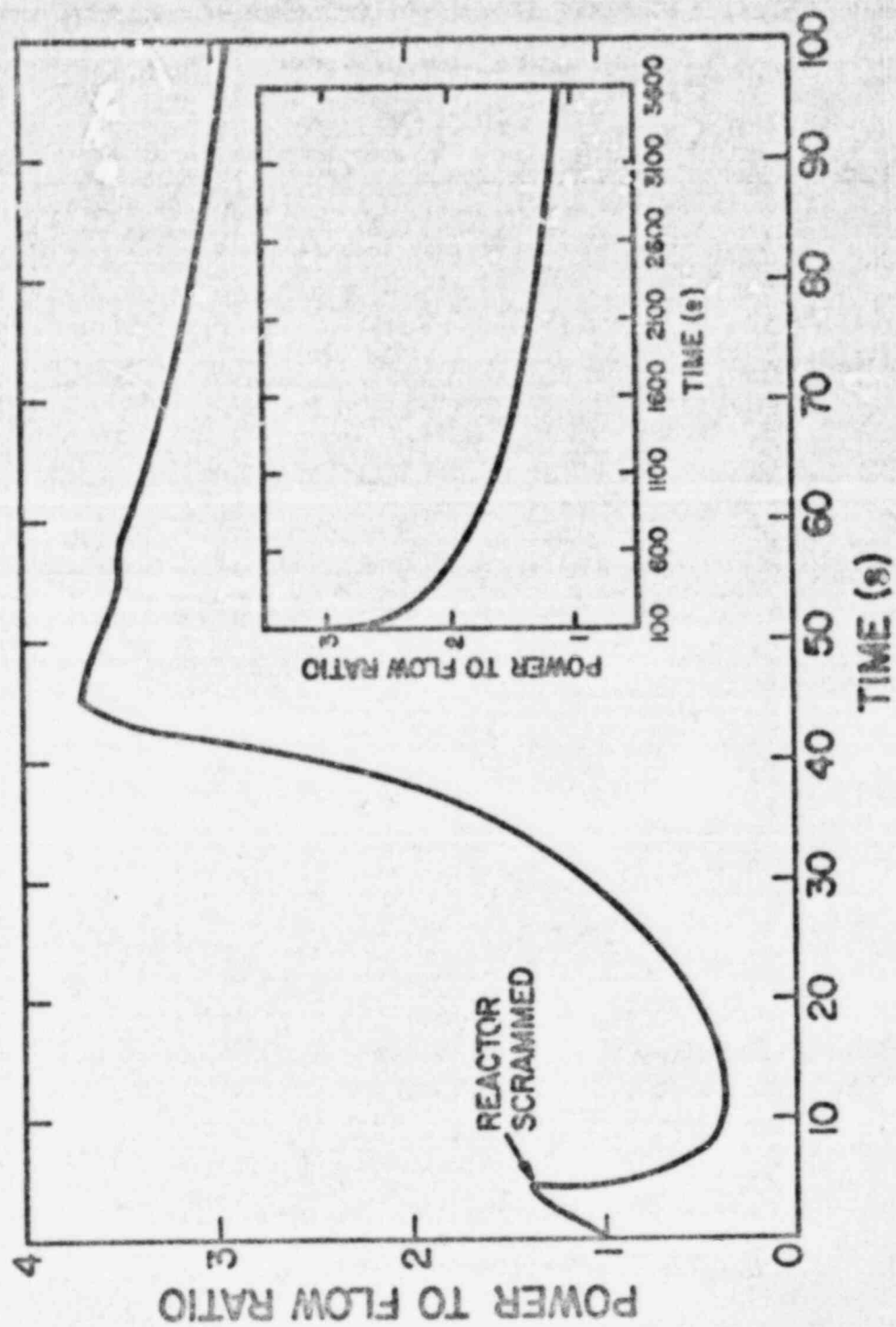


Fig. 87.  
Power-to-flow ratio for a rapid PCW depressurization.

varies with the degree of nonlinearity of the system and the magnitude of the input disturbance. In matrix notation the linearized equations in LASFN are

$$\frac{d}{dt} \delta \underline{Y} = \left[ \frac{\partial f}{\partial \underline{Y}} \right]_{\underline{X}_0} \delta \underline{Y} + \left[ \frac{\partial f}{\partial \underline{X}} \right]_{\underline{X}_0} \delta \underline{X}, \quad (71)$$

where  $\left[ \frac{\partial f}{\partial \underline{Y}} \right]$  is the N by N Jacobian matrix and  $\left[ \frac{\partial f}{\partial \underline{X}} \right]$  is the N by M input matrix.

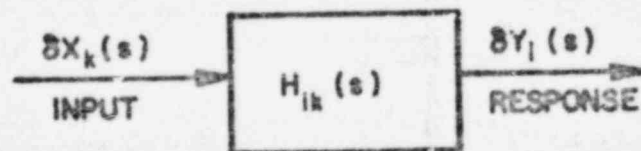
The frequency response of the linearized ODEs is obtained by Laplace transformation of Eq. (71) and calculation of the transfer functions of  $\delta Y_i(s)/\delta X_k(s)$ . The Laplace transform of Eq. (71) is

$$s \begin{bmatrix} \mathbf{I} \end{bmatrix} \delta \underline{Y}(s) = \left[ \frac{\partial f}{\partial \underline{Y}} \right] \delta \underline{Y}(s) + \left[ \frac{\partial f}{\partial \underline{X}} \right] \delta \underline{X}(s) \quad (72)$$

where  $[\mathbf{I}]$  is the diagonal identity matrix,  $s$  is the Laplace independent variable,  $\delta \underline{Y}(s)$  is the Laplace transform of the  $\delta \underline{y}(t)$  vector, and  $\underline{X}(s)$  is the Laplace transform of the  $\delta \underline{x}(t)$  vector. Upon rearranging terms in Eq. (72), the following linear matrix equation is obtained.

$$\left[ s \begin{bmatrix} \mathbf{I} \end{bmatrix} - \left[ \frac{\partial f}{\partial \underline{Y}} \right] \right] \delta \underline{Y}(s) = \left[ \frac{\partial f}{\partial \underline{X}} \right] \delta \underline{X}(s). \quad (73)$$

If all  $\delta X_k(s) = 1$ , ( $k = 1, M$ ) in Eq. (73), then the individual solutions  $\delta Y_i(s)$  in the  $\underline{Y}(s)$  vector are called the transfer functions of  $\delta Y_i(s)/\delta X_k(s)$ , representing the variation of the state variable  $y_i$  with respect to the variation of the input  $x_k$ . The block diagram below illustrates the transfer function process.



where  $H_{ik}(s)$  is the transfer function  $\delta Y_i(s)/\delta X_k(s)$ .

The dynamic response of the variable  $\delta y_1(t)$  with the transfer function  $H_{1k}(s)$  can be conveniently studied when the input  $\delta x_k(t)$  is a sinusoid with frequency  $\omega$  and unit maximum amplitude, i.e.,

$$\delta x_k(t) = \sin \omega_0 t. \quad (74)$$

The output response of a linear system, subjected to a sinusoidal input, is also a sine wave of the same frequency but modified in amplitude and shifted in phase. The frequency response function of a linear system is defined as the magnitude and phase angle of the system transfer function obtained from Eq. (73). In general, both the magnitude and phase angle of the frequency response function are nonlinear functions of the sinusoidal frequency,  $\omega_0$ .

The complex algebraic relationships giving the frequency response function are programmed in LASAN in subroutine PROCSP. The frequency response function for specified inputs and outputs are computed at selected numerical values of  $\omega_0$ . It is customary to plot  $20 \log |H_{1k}(i\omega_0)|$ , which is the definition of a decibel unit, vs frequency  $\omega_0$  on a semilog graph. The value of the magnitude in decibels is plotted on the linear ordinate while the value of  $\omega_0$  in radians/s is plotted on the logarithmic abscissa. The phase angle in degrees of the frequency response function is also plotted linearly on the same graph. The combined semilog plot of  $20 \log |H_{1k}(i\omega_0)|$  and the phase angle  $\theta$  vs  $\omega_0$  is called a Bode plot. Output listings and Bode plots are generated with the LASAN code.

When the input forcing functions are introduced externally to the model, the frequency responses are called "closed loop" frequency responses and represent all the feedback dynamics. If the selected input forcing function is a state variable of the system, the frequency responses computed are called "open loop" frequency responses because all of the feedback dynamics are not present. Both "open loop" and "closed loop" frequency responses can be obtained with LASAN making it a very powerful tool for control system design and sensitivity analysis.

Figures 88 and 89 show selected Bode plots obtained from LASAN using the PSV model of the CMAP-2 code. Figure 88 is a Bode plot of the "closed loop" frequency response of prompt neutron power with respect to power demand. Figure 89 is an open loop frequency response of prompt neutron power with respect to central control rod motion.

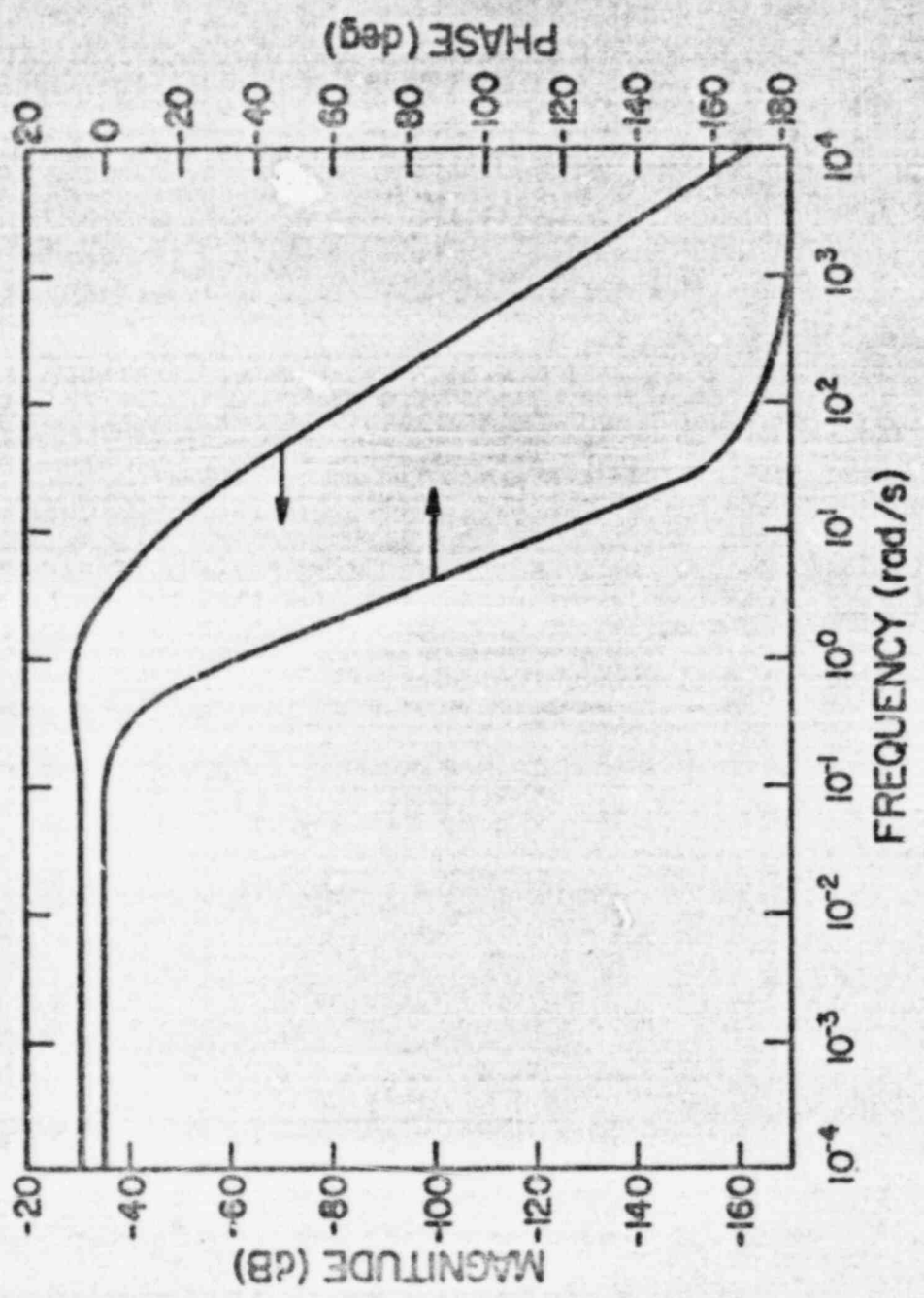


Fig. 88. Closed loop frequency response of present power vs power demand.

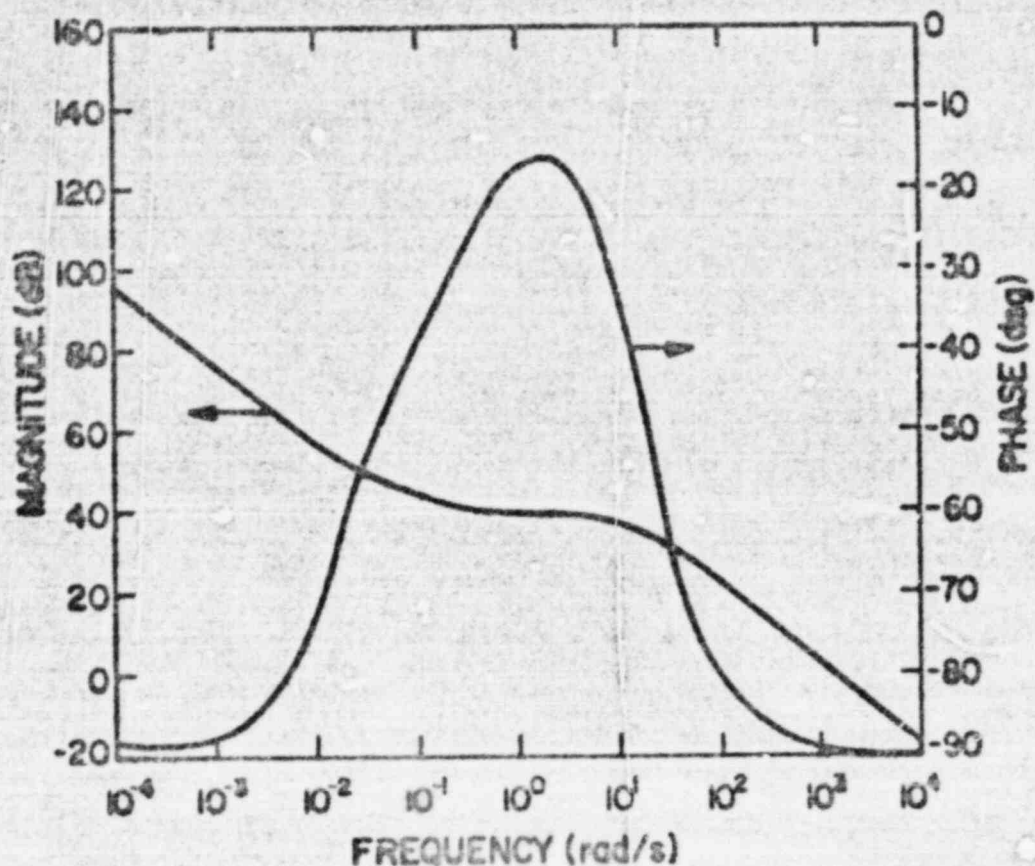


Fig. 89.  
Open loop frequency response prompt power vs rod reactivity.

#### 4. Fort St. Vrain Modeling

(P. A. Secker and G. J. E. Willcutt, Q-6 and T. J. Merson, WX-4)

Fort St. Vrain modeling for CHAP was continued during this quarter. Major model refinements were made to the steam generator/reheater modules, the core and side reflector modules, and the primary loop helium plena modules.

##### a. Steam Generator/Reheater Modeling

A new generic helium-to-water shell and tube heat exchanger subroutine package was developed for CHAP. This subroutine package, named *TLSHL*, is called by both the main steam generator module and the steam reheater module in CHAP-2. The coding for this model allows the user a great deal of

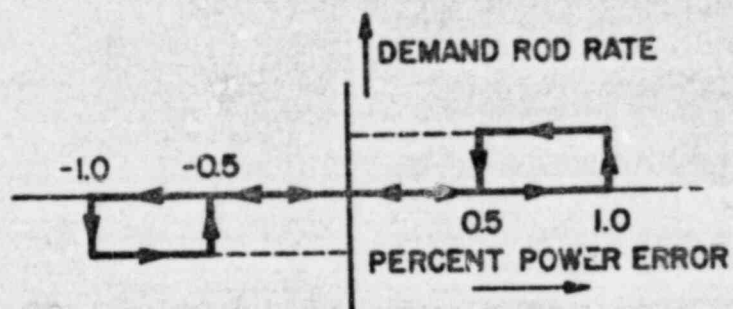


Fig. 90.  
Control rod rate logic diagram.

flexibility in defining the heat exchanger descriptions. The model tracks the saturated liquid and saturated vapor boundary positions during a transient as these positions pass from one modeled region to another. This capability is required for FSV because floodout and dryout can be expected in both the steam generator and reheater during normal and cooldown operation. Thus, the model can be used for startup, shutdown, and emergency cooling scenarios.

The model allows the user to input a variable number of axial heat exchanger nodes. For example, in the FSV steam generator there are five distinct regions with different geometric parameters; the lead-in tubes, the economizer, evaporator, and superheater active heat transfer sections, and the lead-out tubes. The user may elect to treat conservation of momentum in the water across regions either dynamically or quasistatically. The model detects, from input data specifications, whether the geometry is once-through or U-tube and treats the problem appropriately. Heat transfer on the helium side (shell side) is treated quasistatically and accounts for reverse helium flow on the shell side. When the dynamic conservation of momentum option is selected for tube side dynamics, local flow reversal problems can be calculated. Thus, the model is suitable for dynamic flow stability studies.

#### b. Modifications to Core and Reflector Models

Heat transfer from solid material to the helium is by convection in all components of the CHAP-2 model. Further, this heat transfer process is treated quasistatically. When rapid depressurization of the PCRV cavity occurs due to breaks in the upper reactor core plenum (normally at a higher pressure than the lower reactor core plenum), the pressure in the upper plenum rapidly decreases. This causes a helium flow reversal condition in the core and side reflector. The heat transfer equations were thus modified in these components to account for flow reversal.

#### c. Improved Lower Plenum Module

The geometry of the FSV lower plenum and side reflector are different from the 3000 MW(t) HTGR. A peripheral annulus formed by the core barrel and the PCRV exists in FSV through which helium passes upward to the upper plenum from the circulator cavity below the reactor. No such annulus exists for the lower plenum module in CHAP-1. This additional pressure drop and convective heat transfer path has been modeled for FSV both in the lower plenum model and the reflector model. However, new equations were only required for the lower plenum because reverse flow was already allowed in the reflector model.

#### d. Plenum Dynamics

Inertia effects in conservation of mass and energy relationships have been added to the helium plenum modules. These effects are very important for depressurization studies and account for reverse flow mechanisms in the core and side reflector studies. Within small-diameter channels between plenum, conservation of momentum, energy, and mass for the helium are treated quasi-statically.

#### e. Modifications to Kinetics Module

Control rod, shim rod, and scram rod reactivity effects were added to the point reactor kinetics module. The hysteresis-with-deadband control rod rate logic, shown in Fig. 90, was incorporated into the module. Inertia and damping effects of the control rod motor drives were also added. Control rod position, withdrawal prohibit, and scram logic, based on core power-to-flow logic were incorporated in the code. A zero-power neutron source level description was also added to the point kinetics model.

## V. GCFR CORE DISRUPTIVE TEST PROGRAM

(D. L. Hanson, Q-8)

The basic assembly module of the Gas-Cooled Fast Reactor (GCFR) core is a subassembly comprising 264 fuel rods, 6 corner support rods, 1 central rod (instrumented), and their surrounding duct. The duct is a right hexagonal cylinder. The purposes of this out-of-pile experimental program are to demonstrate the behavior of one of these GCFR core modules in the event of loss-of-core (LOC) coolant flow or pressure and subsequent shutdown of reactor power to the level resulting from decay heat alone. The LOFA will be simulated in the Duct Melting and Fall-away Test (DMFT) and the loss of pressure accident will be simulated in the Depressurized Accident Condition (DAC) test. These experiments require the development of an electrically heated fuel rod simulator capable of delivering 2 kW of power while operating at surface temperatures exceeding 1650 K, and the development of a fixture that will permit operation of an ensemble of 450 such rods (1 core module thermally guarded by segments of the 6 surrounding modules) at helium pressures up to 9.1 MPa. This Guarded Core Module (GCM) fixture will be the largest in a sequence of four test fixtures developed in the course of this program. The others are:

1. Ten-inch, single rod fixture,
2. One-meter, seven-rod fixture, and
3. Full-length subgroup (37-rod) fixture.

The GCM fixture will be used first for the DMFT and subsequently for the DAC tests.

### A. Program Planning

(D. L. Hanson, Q-8)

Meetings were held at IASL on November 10 and 11, 1977, between GAC and IASL for the purposes of outlining a test plan for the first Full-Length Subgroup (FLS) sequence and reviewing the GCM fixture conceptual design.

Two types of FLS tests are planned: one in which cladding is held at a steady maximum temperature and one in which power is prescribed at the time-dependent decay heat level. In both types of tests, the testing period

will be bounded by periods of controlled transient startup and shutdown to minimize thermal shock and ratcheting effects. In the controlled power test sequence, cladding temperature will be limited to a maximum of 1075 K in all but the final test, which will proceed for 300 s or until evidence of significant failure appears. Helium pressures of 0.1 MPa and 9.1 MPa will be used in both types of tests.

As presently envisioned in the conceptual design, the GCM fixture has outgrown the available test cell (due to vertical height limitations). Also, horizontal assembly and subsequent transport of this fixture now appear impractical (partly due to an estimated mass of 5 Mg). Accordingly, a high bay annex to Test Cell 1, Bldg. 16, TA-46, wherein both testing and vertical assembly can be performed, is now planned.

## B. Analysis

(A. J. Giger, Q-13; D. L. Hanson, Q-8; and J. C. Miller, E-2)

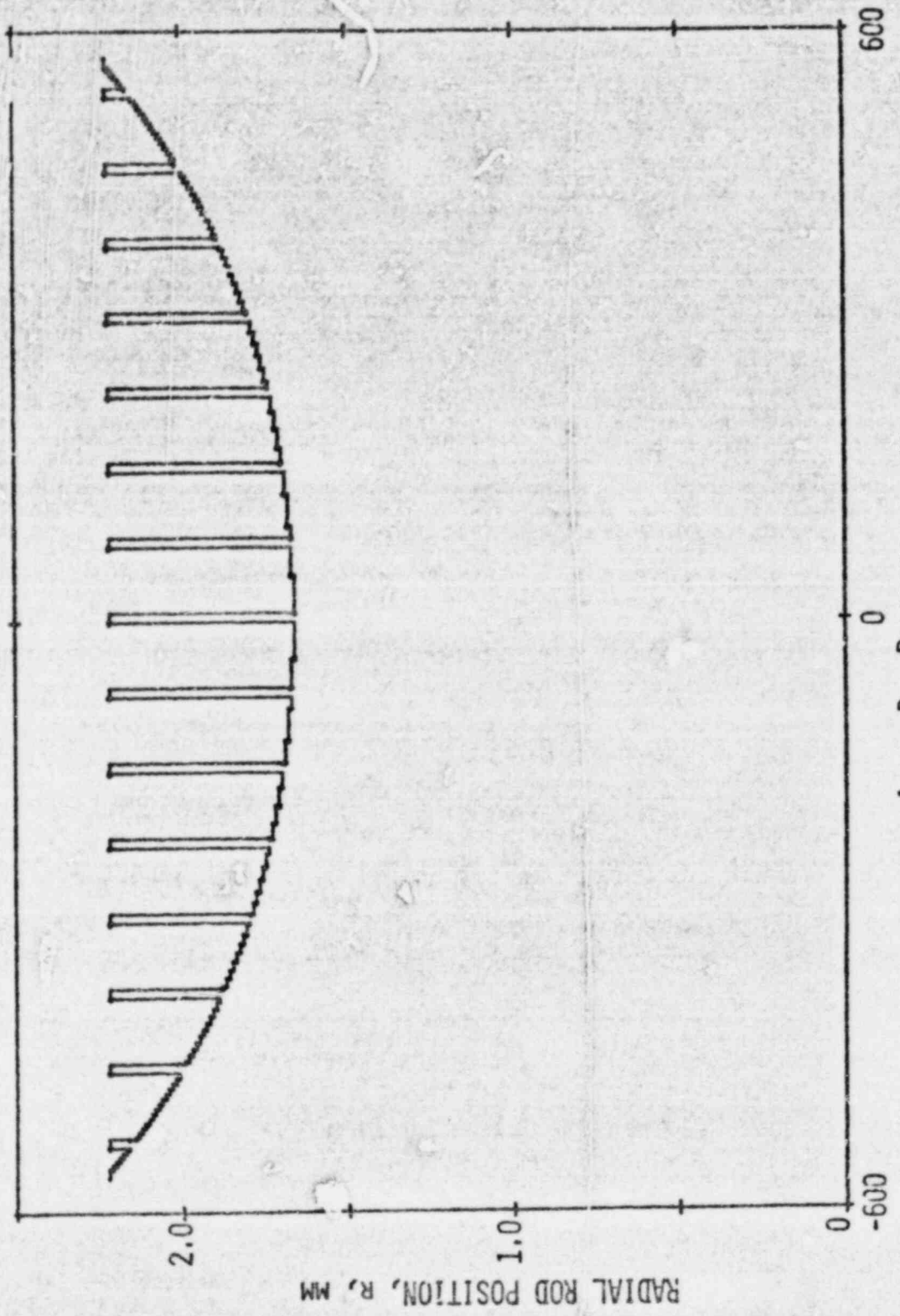
### 1. Heater Rod Grinder

The maximum positional resolutions of the Heater Rod Grinder are 10  $\mu\text{m}$  in the radial (r) direction and 25.4  $\mu\text{m}$  in the axial (z) direction. Since cutting motion is possible in only one of these directions at any time, the continuous profile of the ideal heater rod must be approximated by a sequence of contiguous circular cylindrical segments. It is possible, however, to ensure that the power generated in each of these segments is identical with that generated in the corresponding axial segment of the ideal rod. A computer program that performs this analysis for each successive radial (10  $\mu\text{m}$ ) step has been created and used to generate a discrete step core rod profile specification with the maximum resolution possible from the LASL machine.

A second computer program was created to add equally spaced rod-centering lands along the length of the rod, and a third program utilizes the tabulated results of the first two while controlling the grinder during actual core rod production. The resulting rod profile is plotted in Fig. 91.

### 2. Guarded Core Module (GCM)

An analytical model of test fixture and test assembly insulation was prepared and is operating. The model simulates, from the guard heater outer wall (Fig. 92) outward: a multiple-layer molybdenum foil radiation shield, a fiber or granular layer mounted to the guard heaters, a large gap containing



AXIAL ROD POSITION, Z, MM

Fig. 91.  
Core heater rod profile.

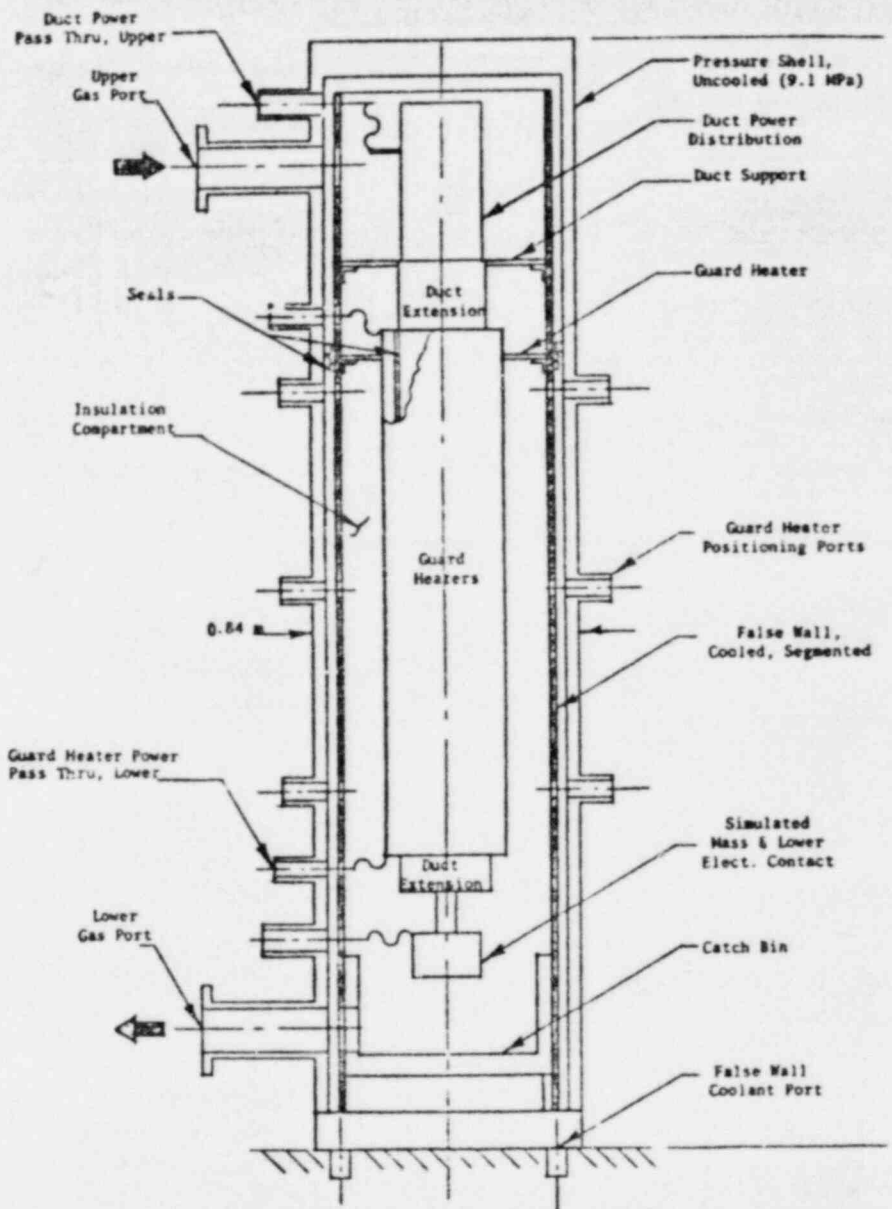


Fig. 92.  
GM conceptual schematic.

stagnant helium, a fiber or granular layer mounted on the false wall, a small helium gap, and the false wall itself. Radiation and convection are assumed with convection suppressed.

Preliminary results using two alumina fiber layers produced the loss rates shown in Fig. 93.

### C. Design

(A. J. Giger, Q-13 and B. C. Cone, SD-2)

#### 1. Full-length Subgroup (FLS)

Design work was completed and drawings produced and issued for a "tail end" heat exchanger to cool effluent helium from the 37-rod fixture to a temperature manageable by a back-pressure control valve.

#### 2. Guarded Core Module (GCM)

A full-scale layout of the test assembly and fixture was completed. Planning for the DMFT is based on operation at 9.1 MPa. The concept being considered uses an interior, segmented, and water-cooled false wall as shown in Fig. 92.

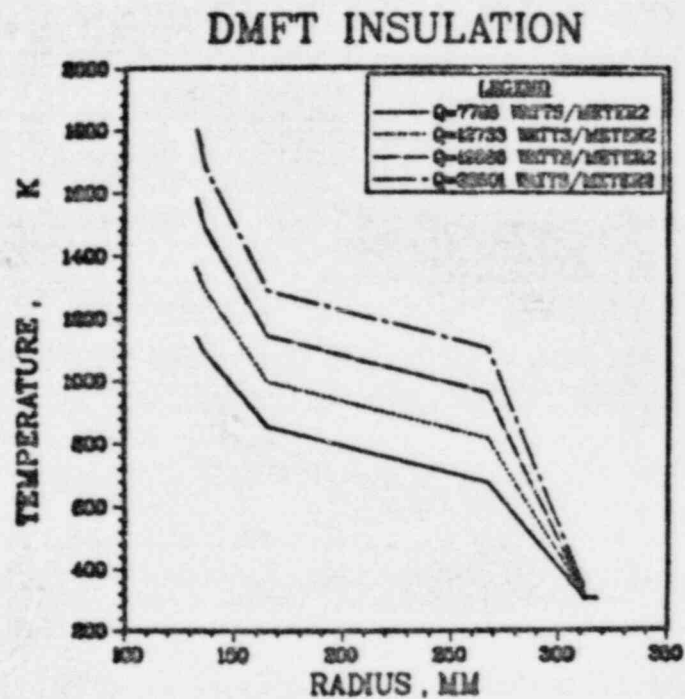


Fig. 93.  
Heat loss from DMFT insulation.

#### D. Procurement and Fabrication

(A. J. Giger, C-13 and B. Cone, SD-2)

##### EIS

With few exceptions, delivery was completed on all parts required to assemble the 37-rod test fixture and its first test assembly. Notably lacking were the contoured polyethylene blanket heater rods. Difficult fabrication required the vendor to investigate new tooling, and this delayed delivery beyond December 31, 1977. Use of the heater rod profile grinder to produce this part is being investigated.

Figures 94-95 show components received for the fixture and test assembly. Figure 94 shows the lower electrical assembly adjacent to the tube bundle. Figure 95 shows the sequence of parts to be located above the tube bundle. The pressure vessel, tube bundle assembly, and simulated duct (circular) are shown in Fig. 96.

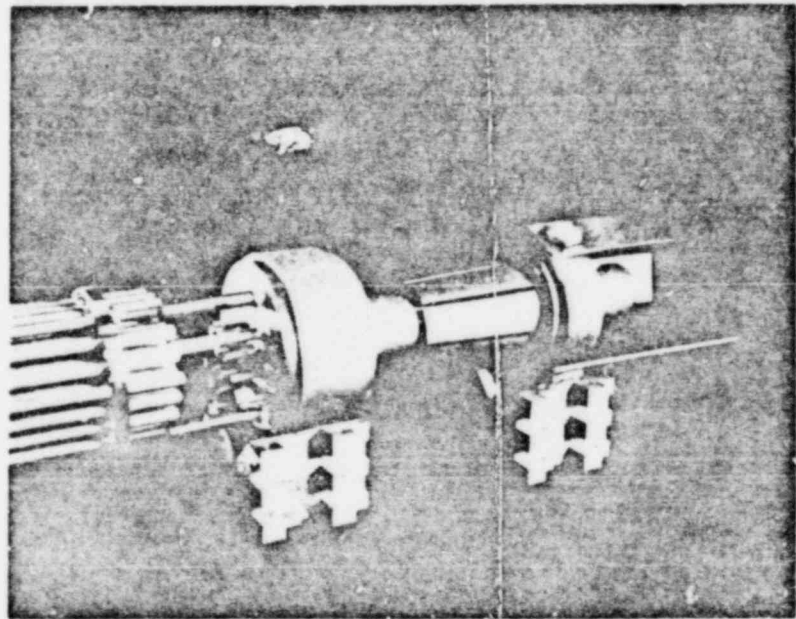


Fig. 94.  
EIS lower electrical assembly adjacent to the tube bundle.

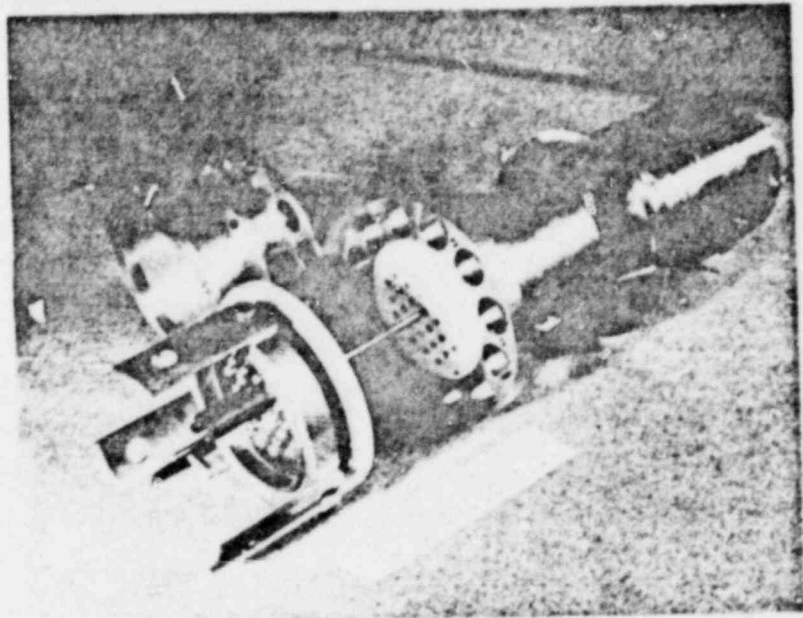


Fig. 95.  
FIS parts above the tube bundle.

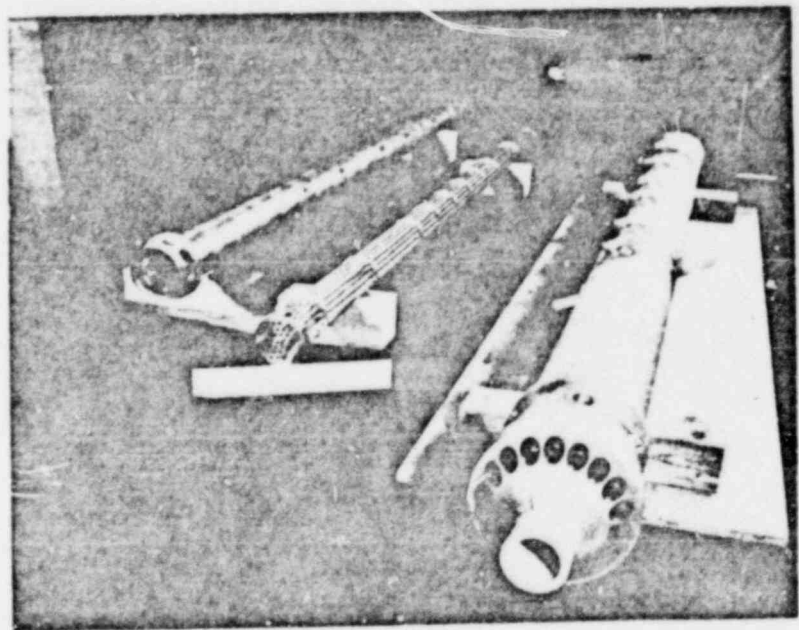


Fig. 96.  
FIS pressure vessel, tube bundle assembly, and duct.

fabrication is approximately 50% complete on the effluent helium heat exchanger.

Two hexagonal ducts and ten hexagonal grid spacers for subsequent 37-rod tests were received from vendors.

#### E. Assembly, Installation, and Checkout

(A. J. Giger, O-13; D. L. Hanson, O-8; W. G. Hanson, E-4; and J. C. Miller, E-2)

##### 1. Heater Rod Grinder

The IASL-designed Heater Rod Grinder is now fully assembled and operational (Fig. 97). A full complement of graphite core rods for the first PDS test assembly has been profiled. The quality of these rods is quite acceptable at this stage, but further improvements appear possible. The necessary modifications to effect these improvements will have to await the development of improved product inspection techniques, however.

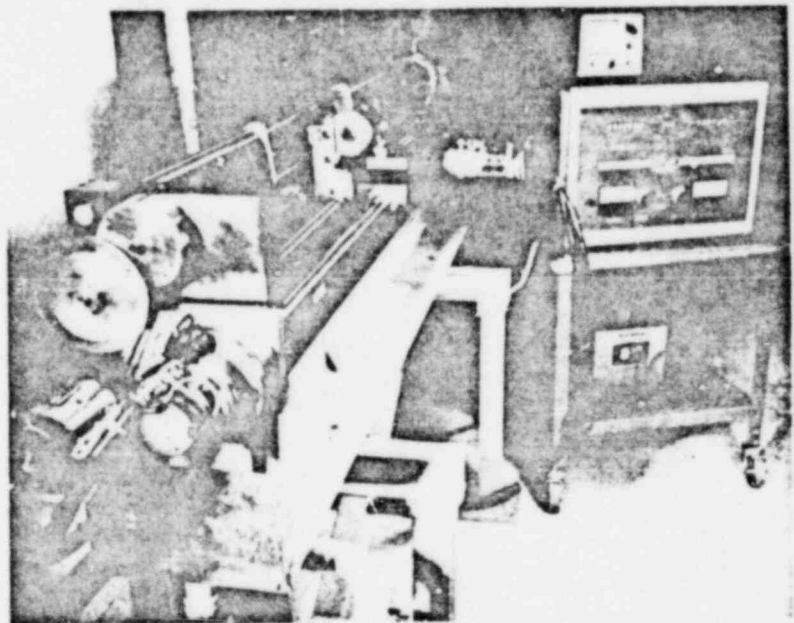


Fig. 97.  
Fully assembled Heater Rod Grinder.

## 2. FLS

Assembly of the first FLS was started (circular duct). The tube bundle was put together as follows. First, the free center tube, which had not been brazed into the support plate with the other 33 tubes, was subassembled to the grid spacers. Chromel-Alumel thermocouples were then attached by spot-welding as in Fig. 98. The subassembly was then slipped onto the other 33 tubes using a vibrating platform to overcome static friction. The balance of the 12 thermocouples on the tube bundle were then applied (Ref. GA 771028 301 GCFR for positions). The tube bundle at this stage is shown in Fig. 99. Figure 100 shows the GA-requested blanking segments spot-welded to the first spacer within the lower axial blanket (ninth position from the top).

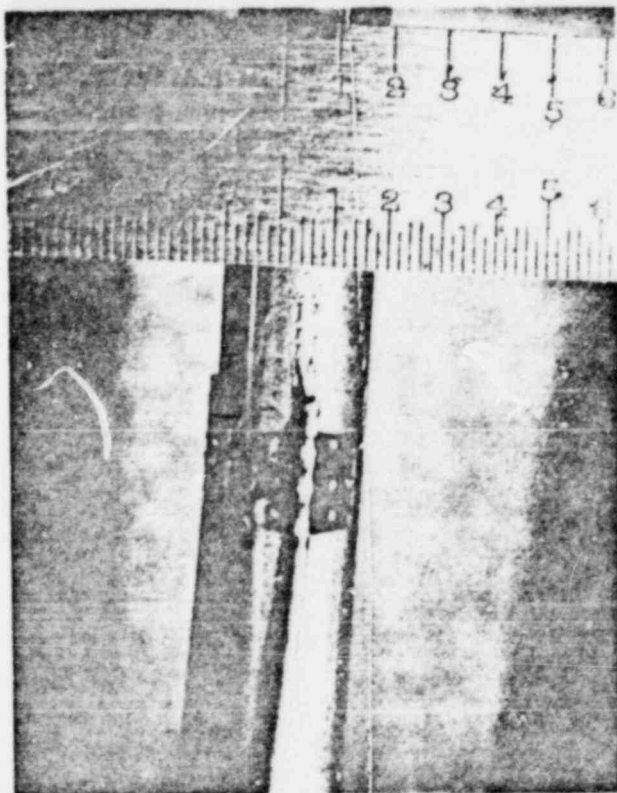


Fig. 98.  
Cladding surface temperature thermocouple installation.

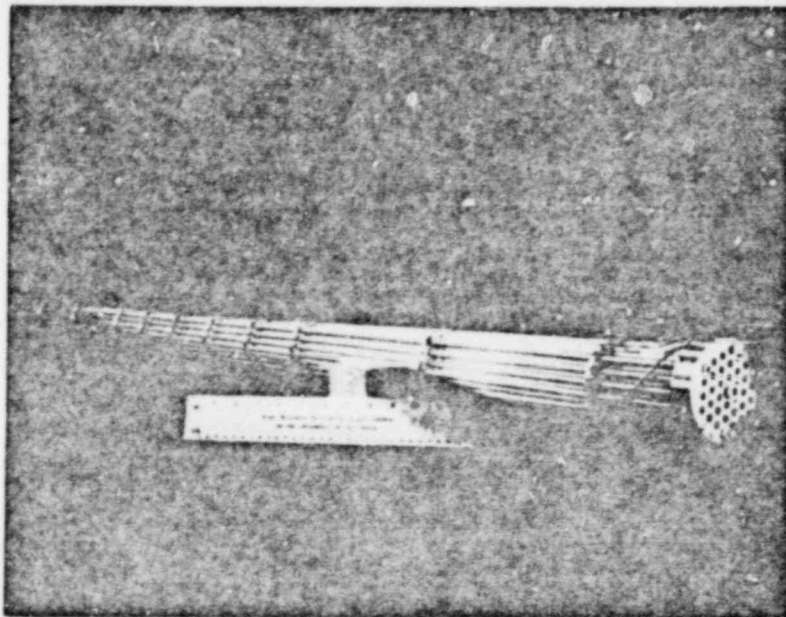


Fig. 99.  
Assembled clanking tube bundle.

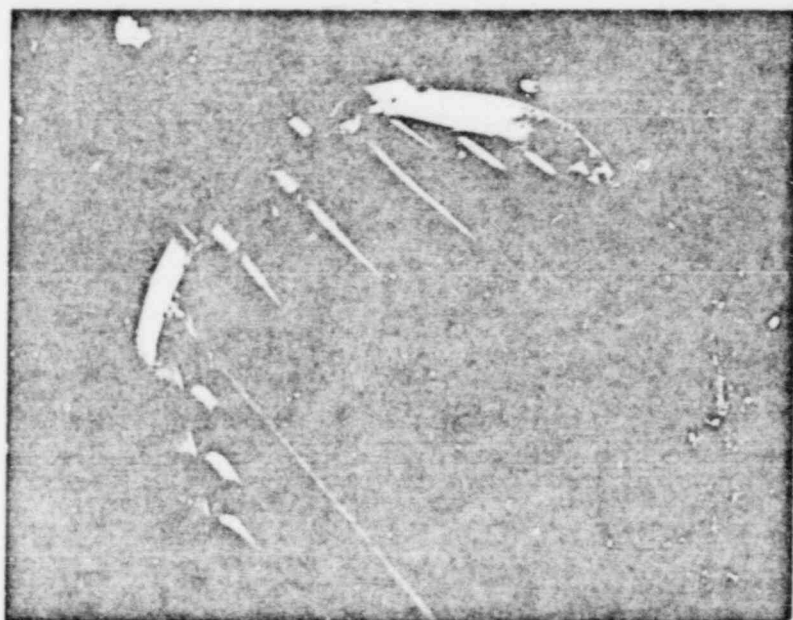


Fig. 100.  
Blanking segments installation at Spacer Grid No. 9.

F. Testing

No tests were performed in either of the two operational test fixtures during this reporting period because of emphasis placed on acquiring heater rod production capability, FLS fixture fabrication, and GJM fixture conceptual design.

## VI. CONTAINMENT SYSTEMS EVALUATION AND STUDIES

(R. G. Gido, O-6)

The following sections summarize the progress from three FY 1977 projects in the reactor containment area funded by the Division of Systems Safety (DSS) of NRC. Work for the first project entitled, "Containment Evaluation," is given in Secs. A and B below. Progress in the second project titled, "Containment Subcompartment Analysis," is presented in Sec. C. Progress in the third project titled, "Main Steam Line Break Analysis," is presented in Sec.

Fiscal year 1977 program task results were transmitted to NRC in the following series of draft reports.

1. Release of COMPARE-Mod 1 code with the capability of performing ice-condenser subcompartment analyses.<sup>64</sup>
2. Comparison of CONTEMP-LT<sup>65</sup> calculations with Marviken, LOFT, and Battelle-Frankfurt tests.
3. Comparisons of COMPARE/RELAP3 subcompartment calculations with Battelle-Frankfurt C-series tests results.<sup>66</sup>
4. Analysis of the Tagami containment tests.<sup>67</sup>
5. Analysis of deposition and entrainment in two-phase flow.<sup>68</sup>
6. Analysis of condensation heat transfer within reactor containments.<sup>69</sup>
7. Containment subcompartment sensitivity study.<sup>70</sup>
8. One-dimensional calculation of flow branching using the method of characteristics.<sup>71</sup>
9. Review of subcompartment analysis codes.<sup>72</sup>

### A. COMPARE-Mod 2

The purpose of this task is to incorporate advanced procedures developed in FY 1977, make comparisons of calculated and test results, make comparisons of COMPARE-Mod 2 calculated results with those from COMPARE-Mod 1,<sup>64</sup> and develop user-convenience features.

#### 1. Method of Characteristics

(R. G. Gido, O-6)

One of the advanced features to be made available in Mod 2 is the ability

to analyze one-dimensional compressible flow using the method of characteristics or wave-diagram analysis method.<sup>73,74</sup> This feature will provide a better accounting for compressibility effects and eliminate some of the detailed nodalization currently utilized to represent this phenomenon. The basic ability to perform such analyses is available. However, emphasis is currently being placed on the capability to model constant, but different, area vents that are stacked in series. In particular, the storage arrangement of the core variables is being modified to be more efficient. In addition, the capability to include an orifice at the stacking point is required to model the Battelle-Frankfurt Comparative Analysis Standard Problem (CASP).

## 2. User-Convenience Development

(G. J. E. Willcutt, O-6)

A user-convenience option has been developed to permit user input time steps that can change for different time intervals during a run. The user selects the end time for each time interval, the time step to be used in the time interval, a print frequency for volume and junction information, and a print frequency for heat sink information. This feature has been incorporated into both COMPARE-Mod 1 and COMPARE-Mod 2.

A plot package has been developed and tested in COMPARE-Mod 1 on the LASL computer system. This package permits both standard plots selected through input and user-specified plots of any variable vs any other variable selected by programming modifications in one subroutine. Standard plots include volume pressures, volume temperatures, junction mass flow rates, and pressure differences between volumes as a function of time. Up to five curves can be specified per plot and either linear or log time scale can be used. Minimum and maximum times for plotting are also specified in the input data. Thus, a plot can begin in the middle of a run and finish before the end of the run. Provision is made for skipping time steps between plotted points to permit storage savings for cases with large numbers of time steps. For each standard plot the user can specify minimum and maximum ordinate values, or these values can be determined from the data extreme values by the program. The user-specified plot package presently permits a single curve per plot of any variable vs any other. It is being modified to permit plotting up to five curves per plot. This package will next be made operational on the NRC system using the CalComp package.

### 3. Tee Representation Capability

(R. W. Meier, WX-4)

The tee representation for the branching of one-dimensional vents analyzed by the method of characteristics<sup>8</sup> has been incorporated into the COMPARE-Mod 2 code and verified by comparison with experimental test results.

Verification of the branch flow model was achieved by comparison of steady-state calculated results with air flow experiments through a tee with three flow junctions of equal diameters of 31.75 mm pipes.<sup>75</sup> The tee flow model geometry and initial conditions are shown schematically in Fig. 101. Air properties were input at 294.4 K and atmospheric pressure. Under the conditions shown in Fig. 101, the air flowed from Volume 1 through Volume 4 and into Volumes 2 and 3 at equal rates. For purposes of comparison with experimental data, a nondimensional loss coefficient,  $C_L$ , was calculated using total pressures:

$$C_L = \frac{P_{P1} + \frac{1}{2} \rho_{A1} u_{P1}^2 - \left( P_{P2} + \frac{1}{2} \rho_{A2} u_{A2}^2 \right)}{\frac{1}{2} \rho_{A1} u_{P1}^2} \quad (75)$$

where

- p = junction pressure;
- u = junction velocity, and
- $\rho$  = junction density.

Subscripts are defined as follows:

- A = old time value at junction end point,
- P = new time value at junction end point,
- 1 = junction 1, and
- 2 = junction 2.

The results of the model calculations are shown in Fig. 102. The loss coefficients,  $K_1$ , (velocity head multipliers) were varied until agreement was achieved with experimental data. In this limited investigation, all three loss coefficients were kept equal but, generally, they would not have to be equal. Good agreement was obtained with experimental data when loss coefficients of 0.3 were used. With the loss coefficients maintained at 0.3, the pressure in Volume 1 was both increased and decreased to obtain different flow rates. These points are also shown in Fig. 102 and agree well with published experimental data.

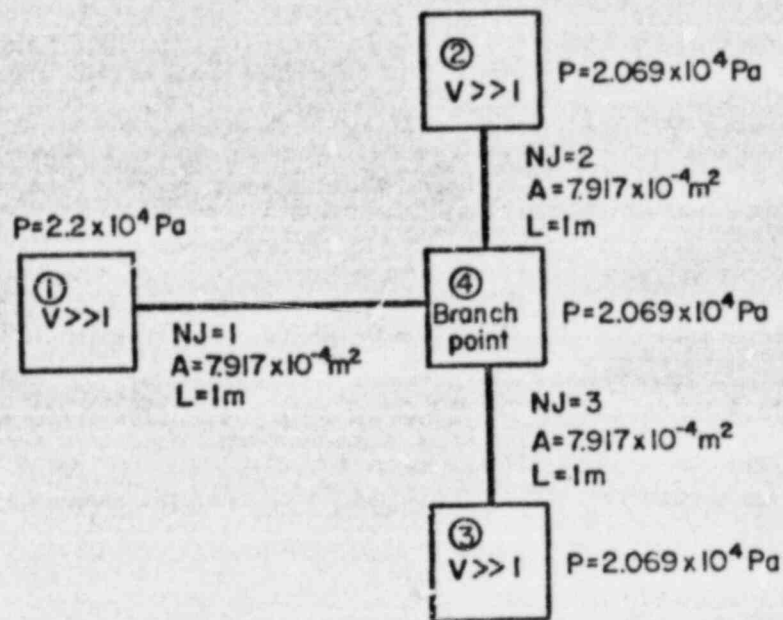


Fig. 101.  
Volume and junction geometry and initial conditions used in tee flow calculation.

Figure 103 shows the effect of variation of the Junction 3 area on the nondimensional total pressure drop coefficient,  $C_L$ . The loss coefficients were maintained at 0.3 for the four calculated points. The results are in good agreement with the experimental data.

In summary, the characteristic equations and finite difference approximations were used to satisfactorily model the flow of air through a tee. The results are in good agreement with published experimental data. The formulation can be extended to model flow through a branch point with four or more junctions by a simple extension of the equations for three junctions. It should be noted that considerable scatter in experimental data gathered by various authors was noted by Benson and Woollatt.<sup>75</sup> The construction of the flow branches (sharp or rounded edges) had a great effect on the observed pressure drops. These variations in tee construction can be accounted for by changing the velocity head multipliers (loss coefficients).

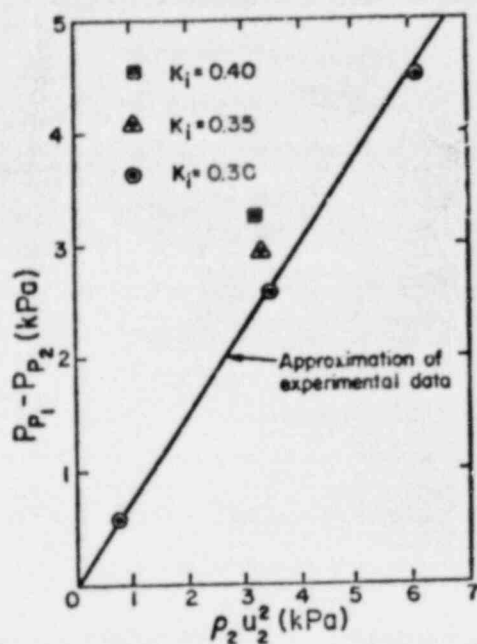


Fig. 102.

Static pressure drop through a tee (points with symbols are calculated values).

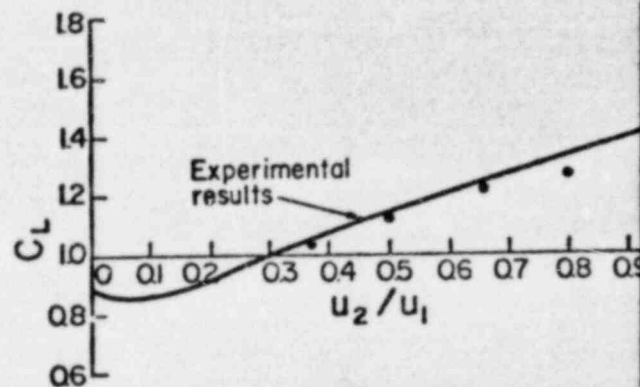


Fig. 103.

Total pressure loss coefficients through a tee (dots are calculated values).

#### B. Hydrogen Concentrations in Containment Compartments

(G. J. E. Willcutt, Jr., Q-6 and A. Koestel, IASL Consultant)

A previous study examined the separate effects of diffusion and natural convection on the movement and concentration of hydrogen in a closed containment compartment.<sup>76,77</sup> The source of hydrogen was the radiolytic decomposition of the water on the floor of the compartment following a LOCA. The objective of the work this fiscal year is to combine the effects of the diffusion and convection models by modifying the one-dimensional transient diffusion model to include effects of natural convection. Tasks involved are to:

1. include eddy diffusivity, based on the flow rate in the wall boundary layer,
2. include a convective term, based on the flow rate in the wall boundary layer,
3. modify the diffusion model boundary conditions to include hydrogen carried back down by the wall boundary layer, and

- compare results with the simple diffusion-only model for various compartment sizes, generation rates, and initial mixing periods.

An eddy diffusivity model was developed, based on the natural convection flow downward in the wall boundary layer. This flow produces an upward flow in the central core of the compartment outside the boundary layer. The mean velocity in this central core is used with the results of free jet analyses to determine the eddy diffusivity:<sup>78-82</sup>

$$\epsilon_d = 0.0922 U R,$$

where  $U$  is the average velocity at a given height in the central core and  $R$  is the compartment radius. For compartment circulation rates of greater than 3 volumes per hour, the peak concentration difference calculated by the diffusion model with the eddy diffusivity added is never greater than 0.5% for the base case  $283 \text{ m}^3$  ( $10,000 \text{ ft.}^3$ ) cube compartment. This result assumes a fixed core velocity based on the circulation rate indicated. A peak concentration difference of 4.8% was calculated without an eddy diffusivity term. A revised model is being developed, which will vary the eddy diffusivity as a function of height based on the core velocity variation with height.

### C. Containment Subcompartment Analysis

#### 1. Standard Modeling Procedures

(J. S. Gilbert, Q-6)

The objective of this task is the establishment of modeling procedure guidelines for reactor containment subcompartment analysis. These modeling procedures are being developed by determining the sensitivity of pressures, forces, and moments on the reactor vessel and other components to a variety of parameters. The parameters considered are:

1. friction flow loss coefficients defined by the coefficient of friction, length of flow path, and hydraulic diameter,
2. geometric flow loss coefficients accounting for contracting or expanding flow areas,
3. inertial form factors, which account for vent flows with inertia,
4. pipe break configuration assumptions yielding different break flow distributions,

5. representation of dynamic flow on obstructions such as displaced piping insulation, and
6. Moody<sup>83</sup> critical vent flow multipliers.

Each of these parameters will be varied within the range of its physical limits. This sensitivity study will be repeated for each of several reactor cavity and reactor piping geometries. The reactor lower cavity thickness is varied from 0.0508-0.6096 m (2 in.-2 ft.). The reactor cavity thickness in the region above and below the reactor nozzles is varied from 0.1524-0.9144 m (6 in.-3 ft.) while reactor lower cavity thickness is maintained at 0.1524 m (6 in.). This region around the nozzles extends 0.9144 m (3 ft.) below the centerline of the nozzles and to the top of the reactor cavity which is open. Finally, the thickness of the piping annulus is varied from 0.127-0.3048 m (5 in.-1 ft.). An alternate approach to the use of arbitrary geometric variations would be to use different actual plant geometries.

To supplement this sensitivity study, an investigation of the effects of vent geometry, compressibility, and two-phase flow on friction and geometric flow loss coefficients is being performed. The modeling procedures include the results of the recently completed containment subcompartment nodalization sensitivity study.<sup>2,70</sup>

Preliminary analysis of the sensitivity of pressures, forces, and moments on the reactor vessel to modified friction flow loss coefficients was performed during this quarter. The friction flow loss coefficients were all doubled resulting in minor changes in values of peak pressures, an approximately 15% reduction in the resultant force on the reactor vessel, and minor differences for the moments due to these forces. Because friction and geometric flow loss coefficients are summed to provide values for entrance and exit flow loss terms in COMPARE-Mod 1,<sup>64</sup> it was necessary to modify the code to input these quantities separately. Thus, for example, some or all of the friction contributions to the flow losses may be studied independently of contraction or expansion losses.

## 2. Calculation of the Comparative Analysis Standard Problem (CASP)

(W. S. Gregory, WX-8)

The Battelle-Frankfurt CASP for evaluation of containment subcompartment analysis codes has been calculated. The test (D10) was run on August 17, 1977, after which the test results for initial, and blowdown conditions were made available to

interested participants. Measured pressures and temperatures were not made publicly available. Participants in the U.S. were to calculate the transient pressure-temperature response and were to submit these to Battelle-Frankfurt for comparison with the measured results by way of the NRC.

For our calculations, CASP was represented for numerical analysis by means of 25 nodes. There were four nodes in Room 4 (R4), five nodes in R5, five nodes in R6 (the room in which blowdown occurred), four nodes in R7, four nodes in R8, two nodes in R9, and one node in the connection between R6 and R8. Nodes in a particular room have volumes that are within ~50% of each other. The main reason for the node size not being more uniform is that the model was originally set up for C-series test analysis where volumes were located, relative to potential orifice locations.<sup>66</sup>

Entrance head-loss coefficients for the junctions between nodes were calculated from the sum of upstream friction and the sum due to area change. The area change component due to flow contraction was always assumed to be 0.5 if there was an area change. Exit head-loss coefficients for the junctions between nodes were calculated from the sum due to area change and due to downstream friction. The area change component due to flow expansion was always assumed to be 1.0 if there was an area change. No turning losses were included.

Current licensing assumptions were used in the calculations. In particular, a Moody multiplier of 0.6, 100% entertainment, no heat sinks and homogeneous volume thermodynamics were used.

The COMPARE code<sup>84</sup> was used to perform the calculations.

#### D. Main Steam Line Break Inside Containment

(D. E. Lamkin, Q-6, and A. Koestel, LASL Consultant)

##### 1. Introduction

Recent analyses of postulated main steam line break (MSLB) accidents within the containment building have predicted containment atmosphere temperatures substantially higher than used in qualification testing of certain safety-related equipment. Consequently, a generic concern has arisen regarding the capability of these safety-related equipment to withstand the accident conditions.

preliminary consideration of the problem<sup>85</sup> has identified several areas of significant uncertainty and/or possible undue conservatism in these computations. The primary task for this quarter was to estimate the relative importance of these uncertainties and to evaluate the possibility of making significant progress toward their resolution within the time and funding available.

The problem areas can be divided into two broad categories:

1. considerations affecting the predicted containment atmosphere thermodynamic response and
2. considerations affecting the predicted thermal response of equipment to given atmospheric conditions.

They are discussed individually below.

## 2. Prediction of Containment Atmosphere Temperature Response

### a. Heat Transfer Coefficient for Energy Absorption by Heat Sinks

The industry standard for condensation heat transfer within reactor containments has for some time been the correlations proposed by Tagami<sup>86</sup> and Uchida.<sup>87</sup> These correlations were based upon very small-scale experimental conditions highly atypical of containment systems. The heat transfer coefficient predicted by these equations is conservative (low) by roughly a factor of four for the configuration of the Carolinas Virginia Tube Reactor (CVTR) test.<sup>88</sup> The CVTR test conditions are much more nearly representative of actual containment conditions than are the Japanese experiments cited above. Variation of the condensing heat transfer coefficient assumptions have been shown<sup>85</sup> to impact the predicted maximum atmosphere temperature by about 39 K.

The state of knowledge concerning condensation heat transfer under post-accident conditions is highly unsatisfactory, and this uncertainty has important implications for the problem at hand. The chief difficulty lies with the scaling uncertainty involved in extrapolating from small-scale experiments to containment conditions. Even if the Tagami/Uchida experimental results are accepted as valid, the correlation equations used are not obviously applicable to the vastly different conditions within a containment building. Indeed, the CVTR data indicate these equations are very conservative. There is no physical basis to believe that the correlation parameters used in these equations

correctly scale the results for the enormous extrapolation involved. It would be very helpful if more appropriate scaling relations could be discovered to reduce the ultra-conservatism of present practice.

Thorough resolution of this problem would best be accomplished by a rather involved analytical study to determine the correct scaling laws, together with some additional supporting experiments. However, it is doubtful whether this could be accomplished within the time and funding constraints of the present study. An alternative approach does offer some promise, however. Dimensional analysis of the governing differential equations reveals that the Nusselt number for condensing heat transfer is some unknown function of several classical dimensionless variables including the Reynolds number, Rayleigh number, Prandtl number, and the Schmidt number. Physical arguments can be advanced that the dependence upon several of these parameters should be of second-order importance. Therefore, it seems attractive to attempt a correlation of existing experimental data (Tagami,<sup>86</sup> CVTR,<sup>88</sup> Marviken,<sup>89</sup> and Battelle-Frankfurt<sup>90</sup>) in terms of these dimensionless variables. This should provide a much better basis for scaling.

#### b. Condensate Revaporization

Computations<sup>85</sup> with standard containment analysis codes have over-predicted the peak temperature measured in CVTR experiments. A possible explanation of this discrepancy was considered to be revaporization of condensate (formed early in the transient) during the superheated phase of the MSLB accident. It was found that assumption of revaporization of ~ 7.5% of the condensate produced approximate agreement with CVTR data. There was no mechanistic basis for this assumption, and therefore, no firm basis for applying it to the larger scale containment problem with different geometry and blowdown characteristics.

A very preliminary investigation has uncovered three possible mechanisms which could act to "desuperheat" the containment atmosphere:

1. radiation from the hot steam to the cooler walls,
2. recirculation into the bulk containment atmosphere and revaporization of small condensate droplets (fog) in the boundary layer near the wall, and
3. cooling of the atmosphere by falling drops of condensate from the ceiling of the building.

Crude estimates of the magnitudes of these effects indicates that, in sum, they may account roughly for the discrepancy found in the above computations. These matters require further evaluation and means of incorporating them into containment computations may need to be devised.

#### c. Liquid Entrainment in the Break Effluent

The entrainment of liquid water in the steam flowing from the broken steam line can have a significant effect upon the containment atmosphere thermodynamics. While this surely has important bearing upon the present problem, it lies wholly within the province of the NSSS vendor. Current containment analysis methods require no modification to accommodate this consideration, provided appropriate input is supplied. Therefore, this problem was judged to be outside the scope of the present study.

### 3. Prediction of Equipment Thermal Response

#### a. Temperature Variation Within Containment Atmosphere

CVTR measurements indicate that local atmosphere temperatures at various locations depart considerably ( $> 55$  K) from the "bulk" or mean temperature. This strongly suggests that the computed mean temperature may not be representative of the local ambient temperature adjacent to the safety-related equipment of concern.

The CVTR test geometry is not presently well enough understood to resolve this matter. However, examination of the test results is highly suggestive of the following interpretation: Early in the transient, the temperature differences may be due primarily to physical separation (by walls, equipment, etc.) of the containment into several regions with restricted flow between these volumes and fairly complete mixing within each one. Later in the transient, there appears to be significant "temperature stratification" due to thermally induced density differences within each region.

It should be possible to make some progress in this area. The physical separation of the containment into subregions presents a problem for which methodology is already available.<sup>64</sup> Within the separate regions, simple models can be devised to crudely estimate the temperature stratification effect.

#### b. Heat Transfer Coefficient for Equipment

It may be necessary to perform transient heat conduction analyses of the various pieces of safety equipment in order to determine the peak temperatures experienced by the critical components. Due to time lag in these

transients, it may well be that the equipment temperature peaks at considerably lower values than the atmosphere.

A necessary boundary condition for these calculations is an appropriate heat transfer coefficient to apply to the equipment surface. A condensing coefficient is needed when the surface temperature is lower than the saturated steam temperature, and a convection coefficient is required if the surface temperature exceeds the saturation temperature.

The work to be done regarding building heat sink coefficients should produce results which can also be applied to this problem. Alternatively, the equipment can perhaps be reasonably modeled as relatively small objects of simple shape (e.g., cylinders) and correlations available in the literature could be used. Whatever heat transfer correlations are used, it will be necessary to make estimates of the local velocity at the equipment locations. It is felt that conservative estimates can be made from classical results of fluid jet mechanics.

#### REFERENCES

1. K. A. Taggart and D. R. Liles, "POST - A Postprocessor Computer Code for Producing Three-Dimensional Movies of Two-Phase Flow in a Reactor Vessel" Los Alamos Scientific Laboratory report LA-NUREG-6954-MS (September 1977).
2. J. P. Jackson and M. G. Stevenson, "Nuclear Reactor Safety Quarterly Progress Report, July 1-September 30, 1977," Los Alamos Scientific Laboratory report LA-7039-PR (January 1978).
3. G. Kocumustafaogullari, "Thermo-Fluid Dynamics of Separated Two-Phase Flow," Ph.D. Thesis, School of Mechanical Engineering, Georgia Institute of Technology (Atlanta, GA, December 1971).
4. M. Ishii, Thermo-Fluid Dynamic Theory of Two-Phase Flow, Collection de la Direction des Etudes et Recherches D'Electricite de France (Byrolles, Paris, 1975).
5. F. H. Harlow and A. A. Amsden, "A Numerical Fluid Dynamics Calculation Method for All Flow Speeds," *J. Comp. Physics* 8, 197 (1971).
6. F. H. Harlow and A. A. Amsden, "KACHINA: An Eulerian Computer Program for Multifield Fluid Flows," Los Alamos Scientific Laboratory report LA-5680 (1975).
7. D. R. Liles and W. H. Reed, "A Semi-Implicit Method for Two-Phase Fluid Dynamics," Accepted for Publication in *J. of Comp. Physics*.
8. J. P. Jackson and M. G. Stevenson, "Nuclear Reactor Safety Quarterly Progress Report, April 1-June 30, 1977," Los Alamos Scientific Laboratory report LA-NUREG-6934-PR (August 1977).
9. J. G. Collier, Convective Boiling and Condensation (McGraw-Hill Co., New York, 1972).
10. S. Lekach, "Development of a Computer Code for Thermal Hydraulics of Reactors (THOR)," Brookhaven National Laboratory Quarterly Progress report BNL-19978 (1975).
11. W. C. Rivard and M. D. Torrey, "Numerical Calculation of Flashing from Long Pipes Using a Two-Field Model," Los Alamos Scientific Laboratory report LA-6104-MS (1975).
12. K. Lee and D. J. Ryley, "The Evaporation of Water Droplets in Superheated Steam," ASME paper 68-HT-11 (1968).
13. G. W. Govier and A. Aziz, The Flow of Complex Mixtures in Pipes (Van Nostrand Reinhold Co., New York, 1972).
14. G. B. Wallis, One-Dimensional Two-Phase Flow (McGraw-Hill, New York, 1969).
15. V. G. Levich, Physicochemical Hydrodynamics (Prentice-Hall, New York, 1962), pp. 430-432.

16. L. A. Bromley, "Heat Transfer in Stable Film Boiling," *Chemical Engineering Progress* 46, 221-227 (May 1950).
17. M. Abramowitz and I. A. Stegun, eds., *Handbook of Mathematical Functions*, National Bureau of Standards Applied Mathematics Series, Vol. 55 (May 1968).
18. C. J. Crowley, J. A. Block, and C. N. Cary, "Downcomer Effects in a 1/15-Scale PWR Geometry - Experimental Data Report," Create, Inc. report NUREG-0281 (May 1977).
19. "A Prediction of the Semiscale Blowdown Heat Transfer Test S-02-8 (NRC Standard Problem Five)," Electric Power Research Institute report EPRI NP-212 (October 1976).
20. H. C. Robinson, "LOFT Systems and Test Description (Loss-of-Coolant Experiments Using a Core Simulator)," EG&G Idaho, Inc. report TREE-NUREG-1019 (1976).
21. D. L. Batt, "Experimental Data Report for LOFT Nonnuclear Test L1-4," EG&G Idaho, Inc. report TREE-NUREG-1084 (1977).
22. W. L. Kirchner, "Reflood Heat Transfer in a Light Water Reactor," U.S. Nuclear Regulatory Commission report NUREG-0106 (August 1976).
23. L. M. Shotkin, U.S. Nuclear Regulatory Commission, personal communication (1977).
24. Commonwealth Edison Company, "Zion Nuclear Power Station, Unit 1, Startup Test Report," Docket No. 50-295, License No. DPR-39 (November 1974).
25. G. W. Johnson, F. W. Childs, and J. M. Broughton, "A Comparison of 'Best-Estimate' and 'Evaluation Model,' LOCA Calculations: The BE/EM Study," Idaho National Engineering Laboratory report PG-R-76-009 (December 1976).
26. Westinghouse Nuclear Energy Systems, "Reference Safety Analysis Report," RESAR 41 (December 1975).
27. "RELAP4/MOD5 User's Manual - Volume II," Idaho National Engineering Laboratory report ANCR-NUREG-1335 (September 1976).
28. D. G. Hall, "A Study of Critical Flow Prediction for Semiscale Mod-1 Loss-of-Coolant Accident Experiments," EG&G report TREE-NUREG-1006 (December 1976).
29. V. Esparza and K. E. Sackett, "Experimental Data Report for Semiscale MOD-1 Test S-06-5 (LOFT Counterpart Test)," EG&G report TREE-NUREG-1125 (June 1977).
30. W. C. Rivard and M. D. Tourey, "K-FIX: A Computer Program for Transient, Two-Dimensional, Two-Fluid Flow," Los Alamos Scientific Laboratory report LA-NUREG-6623 (1977).

31. J. K. Dienes, C. W. Hirt, and L. R. Stein, "Computer Simulation of the Hydroelastic Response of a Pressurized Water Reactor to a Sudden Depressurization," Los Alamos Scientific Laboratory report LA-NUREG-6772-MS (1977).
32. C. R. Bell, P. B. Bleiweis, J. E. Boudreau, F. R. Parker, and L. L. Smit, "SIMMER-I: An S. Implicit, Multifield, Multicomponent, Eulerian, Recriticality Code for IMPER Disrupted Core Analysis," Los Alamos Scientific Laboratory report LA-NUREG-6467-MS (1977).
33. C. R. Bell and J. E. Boudreau, "Application of SIMMER-I to the Postdisassembly Fluid Dynamic Behavior Within an IMPER Reactor Vessel," Los Alamos Scientific Laboratory report (to be published).
34. M. D. McKay, W. J. Conover, and D. E. Whiteman, "Report on the Application of Statistical Techniques to the Analysis of Computer Code," Los Alamos Scientific Laboratory report LA-NUREG-6526-MS (October 1976).
35. J. F. Jackson, "Nuclear Reactor Safety Quarterly Progress Report — January 1-March 31, 1977," Los Alamos Scientific Laboratory report LA-NUREG-6842-PR (May 1977).
36. R. J. Lawrence and D. S. Mason, "WINDY IV: A Computer Program for One-Dimensional Wave Propagation With Rezoning," Sandia Laboratories report SC-RR-710284 (August 1971).
37. L. D. Landau and E. M. Lifshitz, Fluid Mechanics (Addison-Wesley Publishing Co., Inc., Reading, MA, 1959), p. 359.
38. V. K. Dhir, "Quasisteady Laminar Film Condensation of Steam on Copper Spheres," J. Heat Transfer, 347-351 (August 1975).
39. D. K. Edwards, V. C. Denny, and A. F. Mills, Transfer Processes (Holt Rhinehart, Winston, NC, 1973).
40. A. E. Evans, J. D. Orndoff, and W. L. Talbert, "STF Diagnostic Instrumentation Evaluation with PARKA," Los Alamos Scientific Laboratory report LA-UR-77-2712, NEA Specialists Meeting on Fuel and Clad Motion Diagnostics for Fast Reactor Safety Test Facilities, Los Alamos, NM, (December 5-7, 1977).
41. C. L. Fink, R. P. Hosteny, A. DeVolpi, E. A. Rhodes, and A. E. Evans, "Analysis of the 91-Pin Subassembly Tests at PARKA," NEA Specialists Meeting on Fuel and Clad Motion Diagnostics for Fast Reactor Safety Test Facilities, Los Alamos, NM (December 5-7, 1977).
42. R. G. Behrens, "Thermodynamics of Transition Metal Carbonyls,  $\text{Fe}(\text{CO})_5$ ,  $\text{Ru}(\text{CO})_5$ ,  $\text{Os}(\text{CO})_5$ ," J. of the Less Common Metals 56, 55-58 (1977).
43. R. G. Behrens, "A Note on the Thermodynamics of Demanganese and Dirhenium Demanganese and Dirhenium Decacarbonyls," J. of Organometallic Chemistry 12, C63-C65 (1976).

44. "Reactor Safety Research Programs Quarterly Progress Report for the Period October 1-December 31, 1976," Depart. of Applied Science, Brookhaven National Laboratory report BNL-NUREG-50624 (February 1977).
45. J. L. Lunsford, "QUIL, A Chemical Equilibrium Code," Los Alamos Scientific Laboratory report LA-NUREG-6500 (February 1977).
46. W. L. Kirk, "HTGR Safety Research Program, January-March 1975," Los Alamos Scientific Laboratory report LA-5975-PR (June 1975).
47. W. L. Kirk, "HTGR Safety Research Program, April-June 1975," Los Alamos Scientific Laboratory report LA-6054-PR (September 1975).
48. W. A. Cook, "INGEN: A General-Purpose Mesh Generator for Finite Element Codes," Los Alamos Scientific Laboratory report LA-7135-MS (March 1978).
49. J. D. Reins, J. L. Quiros, W. C. Schnolbrich, and M. A. Sozen, "Shear Strength of End Slabs of Prestressed Concrete Nuclear Reactor Vessels," University of Illinois report ULLU-ENG-76-2022 (July 1976).
50. A. C. T. Chen and W. F. Chen, "Constitutive Relations for Concrete," J. of Engineering Mechanics Division, ASCE 101, EMI (August 1975).
51. B. Saugy, "Contributions to the Theoretical Study of the Nonlinear Behavior of Massive Reinforced Concrete Structures under Rapidly Applied Loads," Bulletin Technique de la Suisse Romande 22 (November 1969).
52. K. H. Gerstle, "Strength of Concrete Under Multiaxial Stress States," Proceedings of the McHenry Symposium sponsored by ACI (Mexico City, Mexico, October 1976).
53. C. A. Anderson, P. D. Smith, and J. T. P. Yao, "A Method of Reliability Assessment of Concrete Reactor Vessels," paper submitted for presentation at the June 1978 Pressure Vessel and Piping Conference, Montreal, Canada.
54. "Report to the AFS by the Study Group on Light Water Reactor Safety," David Pines, ed., Reviews of Modern Physics 47, Supp. 1 (1975).
55. K. D. Lathrop, "Reactor Safety and Technology Quarterly Progress Report, January 1-March 31, 1976," Los Alamos Scientific Laboratory report LAPR-NUREG-6317 (May 1976).
56. Yu. A. Zgsin, Fission Product Yields and Their Mass Distribution, Translation, Consultants Bureau (1964).
57. "Fission Product Data for Thermal Reactors," Electric Power Research Institute report EPRI NP-356, Parts 1 and 2 (December 1976).
58. M. Tošar, "Evaluation of High Temperature Gas-Cooled Reactor Fuel Particle Failure Models," U.S. Nuclear Regulatory Commission report NUREG-0001 (November 1976).

59. M. Schwartz, D. Sedgley, and M. Mendonca, "SORS: Computer Program for Analyzing Fission Product Release from HTGR Cores During Transient Temperature Excursions," General Atomic Company report GA-A12462 (April 1974).
60. L. Carruthers and C. Lee, "LARC-1: A Los Alamos Release Calculation Program for Fission Product Transport in HTGRs During the LOFC Accident," Los Alamos Scientific Laboratory report LA-NUREG-6563-MS (November 1976).
61. "Reactor Safety Study," U.S. Nuclear Regulatory Commission report WASH-1400 (NUREG-75/014), Appendix VI (October 1975).
62. "Effects of Sabotage on Nonpower Reactors," Quarterly Research and Development Status report No. 1, WX4-NRC-1 (November 1977).
63. T. E. Springer and O. A. Farmer, "TAF - A Steady-State, Frequency Response and Time Response Simulation Program," Proceedings, Fall Joint Computer Conference (San Francisco, CA, 1968).
64. R. G. Gido, J. S. Gilbert, R. G. Lawton, and W. L. Jensen, "COMPARE-Mod A Code for the Transient Analysis of Volumes with Heat Sinks, Flowing Vents, and Doors," Los Alamos Scientific Laboratory report (to be published).
65. G. J. E. Willcutt, Jr. and R. G. Gido, "Comparisons of CONTEMPT-LT Calculations with Marviken, LOFT, and Battelle-Frankfurt Blowdown Tests," Los Alamos Scientific Laboratory draft report (October 1977).
66. W. S. Gregory, J. R. Campbell, and R. G. Gido, "Comparisons of COMPARE/RELAP3 Subcompartment Calculations with Battelle-Frankfurt C-Series Test Results," Los Alamos Scientific Laboratory draft report (November 1977).
67. R. G. Gido, "Tagami Test Analysis," Los Alamos Scientific Laboratory draft report (November 1977).
68. A. Koestel and R. G. Gido, "Deposition and Entrainment in Two-Phase Flow," Los Alamos Scientific Laboratory draft report (November 1977).
69. D. E. Lamkin, A. Koestel, and R. G. Gido, "A Computational Model for Prediction of Condensation Heat Transfer within Reactor Containments," Los Alamos Scientific Laboratory draft report (November 1977).
70. J. S. Gilbert and R. G. Gido, "Containment Subcompartment Nodalization Sensitivity Study," Los Alamos Scientific Laboratory draft report (January 1978).
71. R. W. Meier and R. G. Gido, "One-Dimensional Calculation of Flow Branching Using the Method of Characteristics," Los Alamos Scientific Laboratory draft report (January 1978).
72. T. J. Merson and R. G. Gido, "Review of Subcompartment Analysis Codes," Los Alamos Scientific Laboratory draft report (February 1978).

73. A. H. Shapiro, The Dynamics and Thermodynamics of Compressible Flow, Sec. 24.7, Vol. II (Ronald Press, New York, 1954).
74. G. Rudinger, Nonsteady Duct Flow: Wave Diagram Analysis (Dover Publications, New York, 1969).
75. R. S. Benson and D. Woollatt, "Compressible Flow Loss Coefficients at Bends and T-Junctions," *The Engineer* (January 28, 1966).
76. G. J. E. Willcutt, Jr. and R. G. Gido, "Mixing of Radiolytic Hydrogen in Closed Containment Compartment Following a LOCA," ANS Topical Meeting on Thermal Reactor Safety (Sun Valley, ID, July 30-August 4, 1977) (Proceedings to be published).
77. G. J. E. Willcutt, Jr. and R. G. Gido, "Mixing of Radiolytic Hydrogen Produced from the Water on the Floor of a Closed Containment Compartment Following a LOCA-METHODS," Los Alamos Scientific Laboratory report (to be published).
78. S. S. Kutateladze, A. G. Kirdyashkin, and V. P. Ivakin, "Turbulent Natural Convection on a Vertical Plate and in a Vertical Layer," *International J. of Heat and Mass Transfer* 15, 193-202 (1972).
79. S. C. Kacker, B. R. Pai, and J. H. Whitelaw, "The Prediction of Wall Jet Flows with Particular Reference to Film Cooling," *Progress in Heat and Mass Transfer* 2, 163-186 (1969).
80. G. Abramovich, Theory of Turbulent Jets (MIT Press, Cambridge, MA, 1963).
81. H. Schlichting, Boundary Layer Theory, 4th ed. (McGraw-Hill Book Co., New York, 1960).
82. H. Rouse, ed., Advanced Mechanics of Fluids (John Wiley & Sons, Inc., New York, 1959).
83. F. J. Moody, "Maximum Flow Rate of a Single Component, Two-Phase Mixture," *J. of Heat Transfer, Trans. ASME, Series C* 87, 134-142 (February 1965).
84. R. G. Gido, C. I. Grimes, R. G. Lawton, and J. A. Kudrick, "COMPARE: A Computer Program for the Transient Calculation of a System of Volumes Connected by Flowing Vents," Los Alamos Scientific Laboratory report LA-NUREG-6488-MS (September 1976).
85. P. Baronowsky, U.S. Nuclear Regulatory Commission (private communication).
86. T. Tagami, "Interim Report on Safety Assessments and Facilities Establishment Project in Japan for Period Ending June 1965 (No. 1)," Unpublished report (February 28, 1966).
87. H. Uchida, A. Ogama, and Y. Togo, "Evaluation of Postincident Cooling Systems of Light-Water Power Reactors," Proceedings of the Third International Conference on the Peaceful Uses of Atomic Energy (Geneva, Switzerland, August 31-September 9, 1964); also Vol. 13, pp. 93-104, United Nations, A/CONF. 28/p. 436 (1965).

88. R. C. Schmitt, G. E. Bingham, and J. A. Norberg, "Simulated Design Basis Accident Tests of the Carolinas Virginia Tube Reactor Containment Final Report," Idaho Nuclear Corporation report IN-1403 (December 1970).
89. H. G. Thoren, L. Erickson, R. Hesbol, and W. Brandt, "Full-Scale Containment Experiments Performed in the Marviken Power Plant," Am. Nucl. Soc. National Topical Meeting on Water Reactor Safety (Salt Lake City, UT, March 26-28, 1973).
90. T. F. Kanzleiter, "Experimental Investigations of Pressure and Temperature Loads on a Containment After a Loss-of-Coolant Accident," Nucl. Engr. and Des. 38, 159-167 (1976).